Towards an Optimal Multi-query Framework based on Model-order Reduction for Non-linear Dynamics

Vers une Méthode de Réduction de Modèles Optimisée pour le Traitement d'un Grand Nombre de Simulations en Dynamique Non-linéaire

Thèse de doctorat de l'université Paris-Saclay

École doctorale n°579 : Sciences Mécaniques et Énergétiques, Matériaux et Géosciences (SMEMaG)
Spécialité de doctorat : Mécanique des solides et des structures
Graduate School : Sciences de l'ingénierie et des systèmes
Référent : ENS Paris-Saclay

Thèse préparée dans l'unité de recherche **LMPS** - Laboratoire de Mécanique Paris-Saclay (Université Paris-Saclay, CentraleSupelec, ENS Paris-Saclay, CNRS), sous la direction de **David Néron**, Professeur des universités, le co-encadrement de **Amélie Fau**, Maître de conférences et de **Pierre-Étienne Charbonnel**, Ingénieur-chercheur

Thèse soutenue à Paris-Saclay, le 1er décembre 2023, par

Alexandre Daby-Seesaram

THÈSE DE DOCTORAT

NNT : 2023UPAST157

Composition du jury

Membres du jury avec voix délibérative

Daniel RIXEN Professor, TU München	Président & Examinateur
Francisco CHINESTA Professeur des Universités, ENSAM Paris	Rapporteur & Examinateur
Anthony GRAVOUIL Professeur des Universités, INSA Lyon	Rapporteur & Examinateur
Udo NACKENHORST Professor, LU Hannover	Examinateur
Maria Paola SANTISI D'AVILA Maître de Conférences - HDR, Université Côte d'Azur	Examinatrice

université
PARIS-SACLAY

ÉCOLE DOCTORALE
Sciences mécaniques et
énergétiques, matériaux
et géosciences (SMEMAG)

Titre : Vers une Méthode de Réduction de Modèles Optimisée pour le Traitement d'un Grand Nombre de Simulations en Dynamique Non-linéaire

Mots clés : Réduction de modèle, Dynamique, Endommagement, Non-linéarité, LATIN, PGD

Résumé : Lorsque l'on cherche à prédire la probabilité de défaillance d'une structure soumise à un chargement incertain, il est nécessaire de réaliser un grand nombre de simulations hautement non-linéaires, jusqu'à la ruine, correspondant à une large famille de sollicitations plausibles. Il est alors nécessaire de travailler à diminuer le coût computationnel de ces études.

Aussi, cette thèse propose une stratégie visant à résoudre efficacement un grand nombre de problèmes de dynamique non-linéaire en basses fréquences. Cette stratégie repose sur l'utilisation d'un solveur efficace capable de résoudre une partie des équations du problème en utilisant la méthode de réduction de modèles PGD dans le domaine fréquentiel. Cette approche permet de réduire le nombre de problèmes globaux en espace à résoudre, tout en exploitant pleinement les architectures parallèles contemporaines lors de l'intégration de la composante temporelle des équations de mouvement. Une attention particulière a été portée à la minimisation des phénomènes de Gibbs dans les situations où la structure ne revient pas à son état initial (phénomènes irréversibles, régime transitoire, etc.) et pour lesquels la solution n'est donc pas périodique. À cette fin, une méthode reposant sur l'amortissement artificiel est proposée.

Le second aspect de cette méthodologie multi-requêtes consiste à exploiter les données issues des calculs déjà effectués pour accélérer les calculs suivants, diminuant ainsi le temps de calcul de l'étude globale. Afin de maximiser les bénéfices d'une telle approche, une méthode robuste et systématique a été développée pour déterminer l'ordre dans lequel les différentes simulations doivent être enchaînées. L'ensemble de la méthode est adaptée à un cadre dans lequel les nombreux chargements sont non paramétrés. Aussi, le choix des données précédentes à réutiliser ainsi que le choix de l'ordre pour la séquence des calculs s'appuient sur un indicateur basé sur la physique et ne nécessitent pas une paramétrisation préalable des chargements imposés à la structure. La méthode a montré des gains en temps de calcul allant jusqu'à un facteur quatre et des gains en stockage mémoire allant jusqu'à un facteur vingt.

université
PARIS-SACLAY

ÉCOLE DOCTORALE
Sciences mécaniques et
énergétiques, matériaux
et géosciences (SMEMAG)

Title : Towards an optimal multi-query framework based on model-order reduction for non-linear dynamics

Keywords : Reduced-order modelling, Dynamics, Non-linear, Damage, LATIN, PGD

Abstract : Predicting the probability of failure for a structure subjected to uncertain loading conditions requires conducting a large number of highly non-linear simulations, up to structural failure, across a wide range of plausible loadings.in order to make failure prediction readily accessible, it is crucial to reduce the numerical cost of these studies.

This thesis presents a strategy for efficiently solving numerous low-frequency non-linear dynamic problems. The proposed strategy relies on an efficient solver to find solutions to part of the problem's equations using the Proper Generalised Decomposition (PGD) model reduction method in the frequency domain. This minimises the number of global spatial problems to be solved while utilising current parallel architectures for handling the temporal part of the motion equations. Particular attention has been paid to mitigating Gibbs phenomena in cases where the structure does not return to its initial state (irreversible phenomena, transient regimes, etc.), and hence, the solution is not periodic. To address this, an artificial damping-based method is proposed.

The second aspect of the methodology involves utilising data from previously conducted calculations to speed up subsequent computations, thereby reducing the overall study's computation time. To maximise the benefits of such an approach, a robust and systematic method is employed to determine the order in which different simulations are chained together. The entire method is suited to a framework where the numerous loadings are non-parametric. Therefore, the choice of reusing previous data and the sequence of calculations rely on a physics-based indicator and do not require prior parametrisation of the loadings imposed on the structure. The method has demonstrated time savings of up to a factor of three and memory storage savings of up to a factor of twenty.

Acknowledgements

Une belle aventure débutée dans les murs de Cachan s'achève. Le moment est donc venu de me plonger dans l'exercice délicat de remercier toutes les personnes qui ont contribué à rendre mon cheminement scientifique de ces dernières années si plaisant. Cet exercice revêt une difficulté particulière, car la page qui se tourne annonce à la fois la fin d'une riche expérience au sein du LMT-LMPS et mon départ de l'ENS, où j'ai pu m'épanouir dans un cadre quasi familial pendant plus de 7 ans.

Je me lance en langue anglaise pour remercier les membres de mon jury. First and foremost, I would like to express my sincere gratitude to my two reviewers. Thank you, Francisco Chinesta, for allowing me to take a step back from my work, bringing an almost philosophical dimension into the discussion about the work accomplished and the directions still to be explored. Anthony Gravouil, your keen insights allowed me to delve more technically into my research during the jury discussion, confirming some of the perspectives envisioned for my work. A special thanks to Daniel Rixen, whose writings played a key role in shaping my understanding as a dynamicist. I am grateful that you accepted the role of the president, a role you warmly embodied, putting me in an idyllic position to present my work. I also extend my appreciation to Udo Nackenhorst for your meticulous questions, which enabled me to provide details on various aspects of my work. Finally, I'd like to thank Maria Paola Santisi D'Avila for your valuable insights and practical knowledge in the field of seismic engineering, providing a broader perspective.

Un immense merci à David, que j'ai tout d'abord eu la chance d'avoir comme enseignant et à qui je dois une grande partie de mes connaissances en mécanique, sans lesquelles ce manuscrit n'aurait jamais vu le jour. Durant mes années à l'ENS, tu nous as offert l'exemple parfait de ce qu'un cours magistral doit être : précis, fluide et captivant. J'espère un jour pouvoir tendre vers cette excellence. Merci bien sûr également d'avoir accepté d'embarquer dans l'aventure de la thèse avec moi, et, par la même occasion, de m'avoir ouvert les portes du monde passionnant de la réduction de modèles. Discuter avec toi, peu importe le sujet, est toujours un réel plaisir que j'espère pouvoir partager encore longtemps. Un sincère merci également à Amélie pour ton immense disponibilité qui a permis à cette aventure de débuter de la meilleure des manières malgré les conditions spécifiques du confinement et du Covid. Cette grande disponibilité, couplée à ton habitude du travail à distance, m'ont permis d'être parfaitement soutenu dans la difficile tâche d'entrer dans le monde de la recherche. Enfin, un grand merci à P-É qui m'a ouvert les portes du monde industriel et m'a toujours accueilli chaleureusement lors de mes visites sur site au CEA. Je termine par un grand merci à Charlène pour sa gestion impeccable et son sourire constant dans la prise en charge des aspects administratifs, contribuant au parfait déroulement de ces trois années.

Au risque de rendre mes remerciements interminablement longs, je ne peux omettre de mentionner les membres du DGM, qui ont fait de mes 7 années à l'ENS une expérience extraordinaire. PeeWee et Emeline, merci pour l'ambiance familiale que vous avez instaurée au sein du département. Sans vous, l'aventure à l'ENS aurait été bien triste. J'ai été très heureux de pouvoir prolonger l'expérience quelques années supplémentaire en vous croisant au café pendant la thèse ! Pour transitionner en douceur vers le laboratoire, je tiens à exprimer ma gratitude envers certains des permanents qui ont rendu ces années particulièrement agréables en insufflant vie et dynamisme dans mon quotidien de doctorant. Merci à François, PAG, Fédé, Ludo, Andréa pour votre présence quotidienne et votre joie de vivre, ainsi que pour les discussions, plus ou moins scientifiques, toujours très plaisantes.

Pour m'avoir accordé un peu de son temps pour une première pré-soutenance, un immense merci à PAB d'abord directeur du DGM lorsque j'étais élève, puis directeur du laboratoire pendant ma thèse. Ta constante disponibilité et tes conseils, qu'ils concernent la mécanique ou non, ont été des atouts précieux dont je m'estime chanceux d'avoir bénéficié. Merci également à Manu, pour tes remarques avisées en pré-soutenance, mais surtout pour tout ce que tu m'as apporté de manière plus générale. Tu as été le premier à m'accompagner dans une démarche de recherche lors du TER, confirmant ainsi mon goût pour la recherche et la mécanique numérique. Enfin, à l'instar de toute l'équipe mentionnée précédemment, te croiser au café pour discuter de tout et de rien était un véritable plaisir quotidien.

Lala, ces sept années auraient été bien fades sans ta présence quotidienne. Passer chaque jour au labo avec une complice merveilleuse, tant au labo qu'en dehors, a été une chance infinie. Partager un fût de bière, discuter des subtilités de LaTeX, ou simplement profiter de quelques instants avec toi a toujours été un réel plaisir ! Merci également de m'avoir fait découvrir un cercle d'amis qui compte désormais tout autant pour moi. Jason, merci pour ta grande patience et ta gentillesse infinie. Tom, l'imprévisible mouvement brownien, merci pour la touche de folie que tu apportes (et pour le café en haut des montagnes, j'espère que tu ne renonceras pas à la folle habitude d'apporter une Bialetti en rando de sitôt !). Claire, une personne formidable qui a le don d'égayer une journée en moins de temps qu'il ne faut pour le dire. Merci pour ta bonne humeur quotidienne et ton côté intrépide. Tu es la première à foncer tête la première dans la vie comme sur le vélo, j'espère avoir l'occasion de te voir charger sur ton gravel dans des chemins douteux encore quelques fois ! Je termine ces remerciements de groupe par Julien, un compagnon d'aventure incroyable toujours partant pour les expéditions les plus folles. Merci infiniment d'avoir rendu ces dernières années aussi agréables et joyeuses, toi qui a toujours le mot pour rire ! Toujours prêt à prendre notre revanche sur les Écrins.

Je ne peux terminer ces remerciements sans mentionner Ronan, investigateur du code ROMlab dans lequel il a toujours été très plaisant de développer les méthodes présentées dans ce manuscrit. Merci également pour le temps que tu m'as accordé lors d'une ultime répétition de ma soutenance. À Flavien, pour m'avoir accompagné dans la rédaction, samedis inclus, et pour avoir adopté puis nettoyé certaines de mes idées saugrenues quant au template latex utilisé pour le présent manuscrit. À toi et Breno pour les discussions plus ou moins locales parfois philosophiques et toujours passionnantes. À mes jeunes collègues devenus des amis, tout d'abord, Floriane, sans qui les trois semaines à Hanovre auraient été bien moins agréables. Merci de m'avoir laissé à mes pensées après une journée de canicule, offrant ainsi l'occasion de réfléchir et de donner naissance aux idées fondatrices du chapitre 4 du présent manuscrit. Je conclus en adressant mes remerciements au groupe des plus jeunes, Victor, Quentin et Pierrot. Merci infiniment d'avoir insufflé une nouvelle vie au CdS. Votre folie quotidienne, les discussions scientifiques ou non, ont véritablement animé mon quotidien. Merci également pour les moments hors laboratoire, sur les parois du viaduc des Fauvettes notamment.

Je souhaite maintenant adresser des remerciements aux amis qui ont partagé ce parcours avec moi, certains depuis longtemps. Théodore, compagnon de bien avant la thèse, je te suis reconnaissant pour nos discussions toujours captivantes, qu'elles soient d'ordre scientifique ou plus philosophique. En tant que source intarrissable de surprises, j'espère continuer à être agréablement étonné par tes aventures. D'autres m'ont accompagné depuis les débuts de cette aventure à l'ENS. À Alexis, sans qui le stage au Trinity College aurait été bien moins agréable, à Louis, Matthieu, Amandine, Héloïse que j'ai eu le plaisir de recroiser tout au long de la thèse. Merci Mahmoud pour ta gentillesse et ta disponibilité sans faille et enfin à Maxime, dont la propension au râlage dépasse même la mienne.

J'arrive à la fin de ces remerciements avec une pensée pour Fabrice qui m'a introduit au magnifique métier d'enseignant-chercheur en mécanique et qui m'a fait découvrir l'ENS Cachan. Je n'aurais pas embarqué dans cette belle aventure sans tes conseils avisés.

Enfin, je m'adresse à mes parents, sans qui je ne serais pas là aujourd'hui. Merci de m'avoir constamment encouragé à me dépasser ; cette réussite est autant la vôtre que la mienne. Merci d'avoir nourri ma curiosité et mon amour des sciences tout au long de mon enfance. Je reste aussi curieux aujourd'hui, et c'est pourquoi j'espère pouvoir continuer à apprendre encore longtemps. À Clara et Arnaud, ma sœur et mon frère, merci d'avoir été d'excellents complices au fil des années. Arnaud, la course A. Daby-Seesaram est lancée ☺.

Je ne saurais conclure ces remerciements autrement qu'avec une pensée émue et chaleureuse pour Marion. Je ne pourrais rêver d'une meilleure compagne, et je mesure la chance que j'ai de t'avoir à mes côtés depuis toutes ces années. Rentrer le soir et te retrouver est la plus grande joie qu'il m'ait été donnée de connaître. Tu as illuminé mon quotidien tout au long de l'aventure parfois vallonnée qu'a été la thèse. Ton soutien sans faille, notamment au cours des derniers mois, a été des plus précieux et j'espère pouvoir te rendre la pareille sous peu.

Gif-sur-Yvette, décembre 2023
Alexandre Daby-Seesaram

Foreword

This work was performed using HPC resources from the “Mésocentre” computing center of CentraleSupélec, École normale supérieure Paris-Saclay and Université Paris-Saclay supported by CNRS and Région Île-de-France (https://mesocentre.universite-paris-saclay.fr/)

Contents

Acknowledgements i
Foreword v
Contents ix
List of notations xi

Introduction **1**

I State of the art of Model-Order Reduction techniques for non-linear dynamics **11**

1 A non-linear dynamics problem **13**
1 Weak formulation of the dynamics problem 14
1.1 Kinematic description 14
1.2 Newton’s second law of motion 16
1.3 Linear elastodynamics 18
2 Time integration methods 19
2.1 Newmark scheme 20
2.2 Temporal finite element method 21
2.3 Frequency computations 22
3 Failure prediction with elastic models 22
4 Ductile damage model with crack-closure effect 23
4.1 Effective stress 23
4.2 State and evolution laws 24
5 Non-linear solvers 25
5.1 Newton-Raphson method 26
5.2 Arc-length solvers 28
5.3 Non-incremental solvers 28
✒ Chapter summary & perspectives 32

2 Model order reduction and multi-query approaches for non-linear mechanics **33**
1 Model-order reduction methods 34
1.1 Craig-Bampton method 36
1.2 Modes superposition 36

1.3 Proper Orthogonal Decomposition (POD) 37
1.4 Reduced-basis method 39
1.5 Proper Generalised Decomposition (PGD) 40
2 Multi-query context 43
2.1 Surrogate models 43
2.2 Enhanced multi-query solvers 44
✒ Chapter summary & perspectives 46

II Contributions to a MOR framework for multi-query studies 49

3 A hybrid frequency-temporal reduced-order method for non-linear dynamics 51
1 The LATIN-PGD method for dynamics problems 53
1.1 An iterative scheme with two alternated search directions 53
1.2 The non-linear ‘local’ stage 54
1.3 The linear ‘global’ stage 55
1.4 Reduced-order model implementation 55
2 Hybrid frequency-temporal reduced-order approach 56
2.1 Temporal calculations of the non-linear behaviour 57
2.2 Frequency calculations of the admissibility equation 58
3 Numerical results 63
3.1 Two-dimensional beam 65
3.2 Three-dimensional pipe 76
✒ Chapter summary & perspectives 80

4 Enhanced reduced-order model for efficient multi-load computations of non-linear dynamics problems 81
1 Multi-query context 83
2 LATIN-PGD scheme enhanced from a previous non-linear dynamics simulation 84
2.1 Initialisation of the PGD basis 84
2.2 Initialisation of the LATIN scheme 86
3 Proximity indicator 86
3.1 Singular value decomposition of each dynamic elastic solution 87
3.2 Proximity indicator between dynamics elastic solutions based on the singular value decomposition 88
4 Enhanced strategy in the multi-query context 90
4.1 Optimal path through the multi-load simulations 90
4.2 Choice of the parent-simulation computation 91
4.3 Overview 91
5 Numerical studies 93
5.1 Initialisation strategy in the multi-query context on the full order model 93
5.2 Reduced-order model improvements 94
5.3 Interpretation of the results in the parametric space 101

5.4 Influence of the number of computations in the multi-query study . . . 102
✒ Chapter summary & perspectives . . . 104

III Application of the novel framework for failure probability assessment 107

5 Multi-fidelity model-order reduction for fragility curves 109
1 Construction of the virtual chart . . . 110
2 Multi-fidelity solver . . . 111
2.1 Influence of the stopping criterion . . . 111
2.2 Multi-fidelity strategy . . . 114
2.3 Numerical results . . . 114
3 Fragility curves . . . 116
✒ Chapter summary & perspectives . . . 118

Conclusion & perspectives 119

Appendix 125

A Frequency derivation 127
1 Continuation method . . . 127
2 Example . . . 128

B ROMlab 131
1 History . . . 131
2 Principles . . . 131
3 Personal contributions . . . 132

C Industrial framework 135
1 Isotropic thermo-mechanical formulation . . . 135
2 Thermal damage assessment . . . 136
3 Fragility surfaces . . . 137
4 Overview of the framework . . . 137

D Extended abstract in French 139
1 Méthode de réduction de modèle hybride temps fréquence . . . 141
2 Cadre multi-requête proposé . . . 142
3 Extension multi-fidélité . . . 143

List of Figures 145

Bibliography 149

List of notations

LATIN-PGD quantities

$\hat{\square}_{n+1/2}$	Quantities related to the $n+1$-th local stage
$\square_{n+1}$	Quantities related to the $n+1$-th global stage
$\left(\mathbb{H}^+,\mathbb{H}^-\right)$	Two search directions
$\mathscr{A}_d$	The set of all admissible solutions
Γ	The set of all solutions of the nonlinear behaviour
$\overline{\boldsymbol{u}}_m$	m-th spatial mode
λ_m	m-th temporal mode
$\boldsymbol{\Delta u}$	Inelastic correction

Continuum mechanics

$\boldsymbol{\sigma}$	Cauchy's tensor
ε	Linearised strain tensor
$\boldsymbol{u}$	Displacement vector
$\mathbb{K}$	Elasticity tensor
D	Damage internal variable

Operators

$\nabla\cdot$	Divergence operator
$\cdot$	Scalar product
$:$	Tensor contraction
$\otimes$	Tensor product
Tr	Trace operator
$\langle\square\rangle$	Positive part of $\square$
$\square_d$	Deviatoric part of $\square$

Frequency space

ω	Angular frequency
$\jmath$	Imaginary unit
$\breve{\square}$	Fourier transform of $\square$
$\tilde{\square}$	Artificially damped quantity associated with $\square$

Multi-query aspects

$\square^{(k)}$	Quantity associated with the k-th computation
$\mathscr{B}$	PGD basis
$\mathscr{B}_0$	Initial PGD basis a computation start with
P	Path consisting of an indexed list of the order in which computations are performed

Introduction

> Nature cannot be fooled.
>
> Richard Feynman

The combustion of fossil fuels over the course of more than a century has already led to a global warming of 1.1 °C above pre-industrial levels. This discernible increase in temperature is illustrated in Figure 1 from [IPCC, 2021], which strongly demonstrates the substantial rise in global mean temperature over the past century, attributing this significant change to human activities.

Based on this existing warming, predictions can be made regarding its future trajectory. The Intergovernmental Panel on Climate Change (IPCC) made predictions based on five different scenarios [IPCC, 2021], which circumscribe a range of possibilities, including both pessimistic and optimistic outlooks concerning various sources of emissions. Figure 2 from [Chen et al., 2021] reveals that only the two most stringent scenarios enable reaching the target of limiting global warming to 1.5 °C, as established by the Paris Agreement during the COP21 of 2015.

Present and future global warming is not without consequences. The Working Group II Contribution to the Sixth Assessment Report of the IPCC emphasises the current disastrous consequences of climate change and predicts further deterioration in Earth's living conditions in the absence of robust adaptation measures [IPCC, 2022]. Most 'reasons for concern' already exhibit a significant impact at the current 1.1 °C of global warming, and their severity is expected to worsen. Moreover, the adverse effects of climate change are particularly pronounced in pessimistic scenarios associated with slow declines in greenhouse gas emissions. Those predictions justify the imperative to mitigate additional climate warming and the desire to align emissions with the two lowest-emission scenarios mentioned above.

In this regard, the Working Group III Contribution to the Sixth Assessment Report of the IPCC states that achieving the objective of restricting global warming to a level well below 2 °C requires significant transformations in the energy system within the next three decades [Clarke et al., 2022]. These transformations encompass a reduction in fossil fuel consumption, an augmented contribution from low- and zero-carbon energy sources, and *an increased reliance on electricity* and alternative energy vectors. As a result, the French National Low-carbon Strategy (NLCS) forecasts a 50% increase in the electricity consumption in France [RTE, 2021], as shown in Figure 3. Growing electricity demand implies that production systems

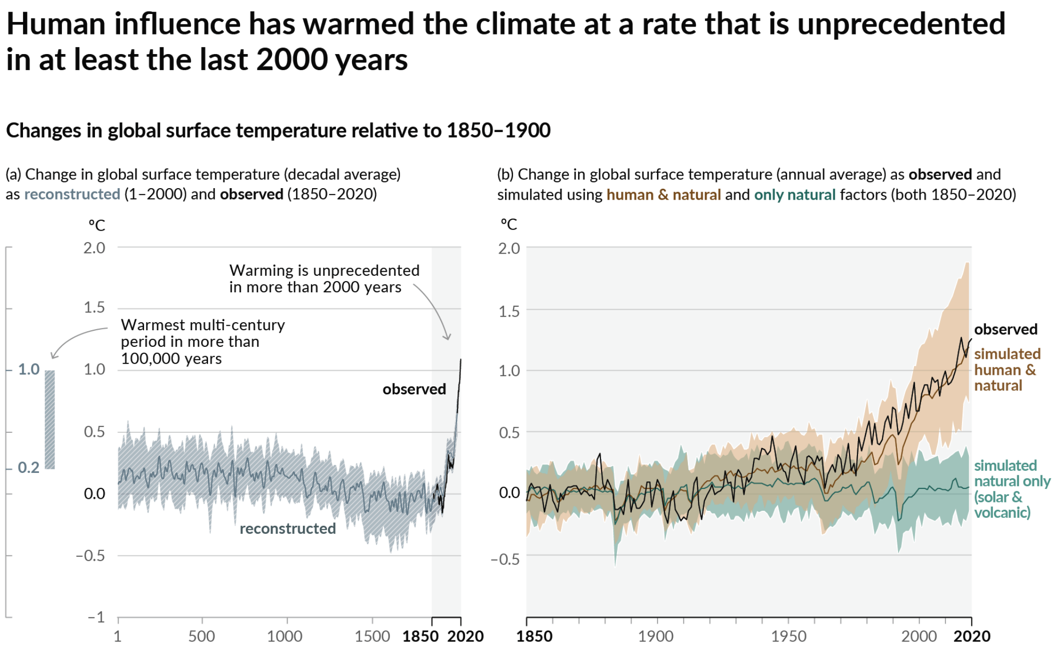

Figure 1 • Human influence on the global surface temperature. (Reproduction of Figure 1 from [IPCC, 2021])

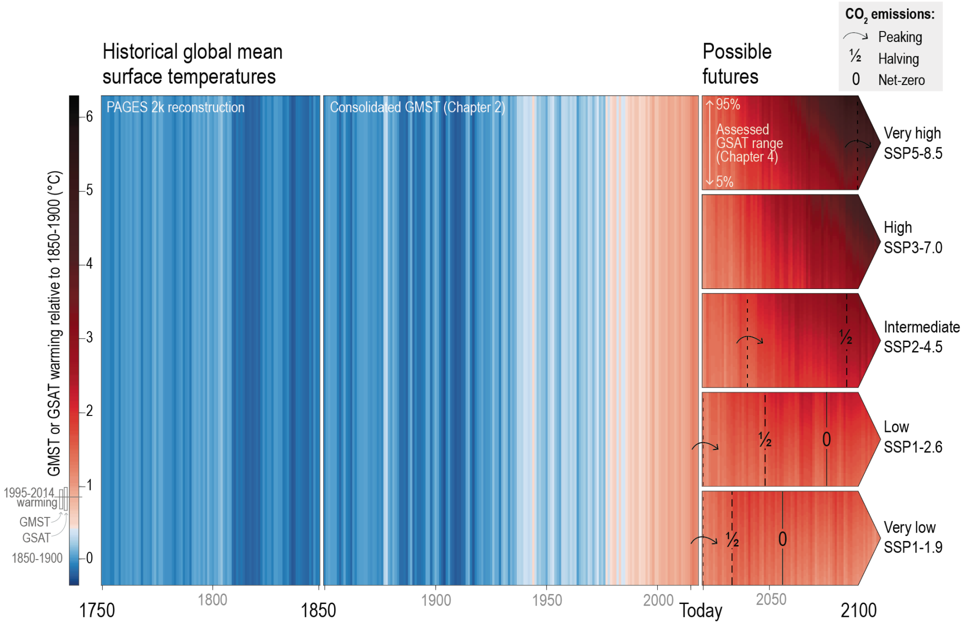

Figure 2 • Global mean surface air temperature (GSAT) illustrated as warming stripes from blue (cold) to red (warm) over three different time periods. From 1750–1850 based on PAGES 2K reconstructions (PAGES 2k Consortium, 2017, 2019). (Reproduction of Figure 1.25 from [Chen et al., 2021])

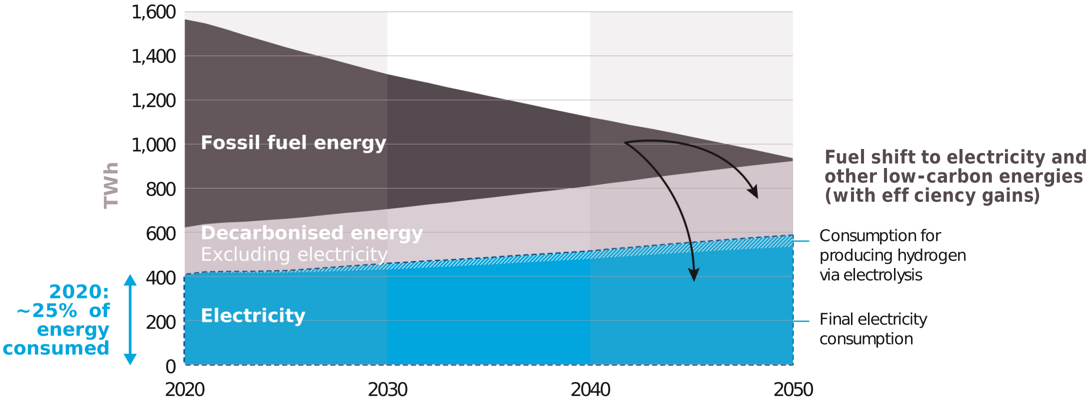

Figure 3 • Projected final energy consumption in the NLCS in France from 2020 to 2050. Reproduced from [RTE, 2021]

must be highly resilient to avoid blackouts if demand exceeds production. In the meantime, the IPCC states that the effects of climate change will influence the future prospects of local and national low-carbon energy systems. Nonetheless, these impacts' precise nature and extent remain uncertain, particularly when considered at the regional scale [Clarke et al., 2022]. This source of risk due to extreme weather is closely investigated in the context of nuclear safety in work package 1 "*Characterization of potential physical threats due to different external hazards and scenarios*" of the NARSIS project[1], of which the CEA is a part.

In addition to those climate-change-related uncertain loadings, seismic risk also emerges as a significant source of uncertain loading, which poses a substantial threat to the structural integrity and operational stability of power generation facilities. Earthquakes, characterised by their unpredictable occurrence and varying magnitudes, can induce complex dynamic forces and ground motions that apply significant stress to the components and infrastructure of these facilities. The potential consequences of seismic activity include structural damage, equipment malfunction, and disruptions to the supply of electricity, thus emphasising the criticality of addressing and mitigating the impact of seismic risk on power generation facilities. Furthermore, the inherent unpredictability of seismic hazards motivates comprehensive studies and assessments, even in countries with historically low seismic activity. Recent events, such as the earthquake in western France on 16th June 2023, provide a stark reminder that seismic events can happen unexpectedly.

For those combined reasons, there is a pressing requirement to enhance the capacity for predicting the failure of electrical production systems in the face of uncertain risks. Indeed, detecting power plant failures enables proactive prevention of such failures before they occur. It also allows for the possibility of postponing maintenance operations if they are unnecessary, thereby minimising the offline period of these crucial sources of electricity. While the climate crisis exacerbates the need for predictions regarding the failure of electric production systems, such necessity was underscored in the broader context of nuclear safety by the Fukushima accident in 2011. Within this broader framework, the work of the CEA, through projects such as NARSIS, contributes to improving the safety of nuclear installations.

---

[1] NARSIS is a European project focused on enhancing the safety of nuclear power plants. The project's list of deliverables is available at http://www.narsis.eu/page/deliverables, with a specific deliverable addressing extreme weather and flooding hazards.

Predicting failure probabilities requires conducting numerous computationally intensive simulations to account for multiple loading scenarios. For instance, one approach to account for this variability is by building virtual charts known as fragility curves, which describe the probability of structural failure [Zentner et al., 2017; Rohmer et al., 2020; Sainct et al., 2020]. When building fragility curves, boundary conditions are specified as indexed time series, as illustrated in Figure 4a. These indexed time series represent non-parametrised loading, such as earthquake recordings for seismic hazard assessment. A specific scalar quantity, denoted α, describes the severity of the loading. It can, for instance, represent the peak ground acceleration in the case of an earthquake. The signals are then grouped based on the shared value of α. Next, using a defined failure criterion, the probability of failure P_f of the structure is computed for various values of severity α. This requires running simulations on different signals sharing the same α. The resulting probabilities are plotted on a graph, with the y-axis representing the probability of structural failure and the x-axis corresponding to the severity, as depicted in Figure 4b. Interpreting this curve provides the probability of structural failure under different levels of loading criticality, characterised by the scalar α.

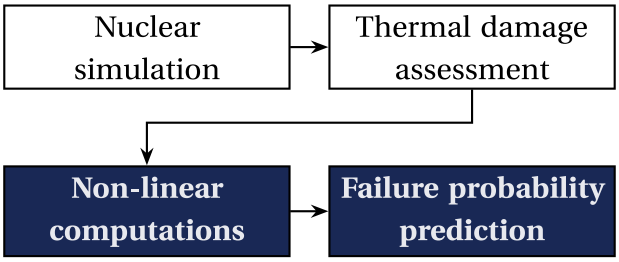

Figure 5 • Industrial framework

In practice, several hundred signals must be considered to construct a single fragility curve, each requiring a non-linear computation. Moreover, in industrial scenarios, multiple fragility curves are often needed to account for the variability in the health of a structure at different times during its life cycle *i.e.*, for different pre-damage levels. In the context of studying power plant piping components, the industrial workflow comprises several stages, as summarised in Figure 5, with detailed information provided in Appendix C. Initially, a nuclear simulation is conducted to generate physical input variables for a thermo-mechanical simulation, which assesses the damage level resulting from thermal fatigue during nominal pipe operation. The pre-damage assessment is then input into a non-linear solver to model the structure's non-linear response to numerous various hazards, such as seismic events. Subsequently, this response is utilised to analyse the structural failure probability. This thesis specifically focuses on a subset of this methodology, which is highlighted in Figure 5. The substantial computational costs associated with such studies pose a significant barrier. Indeed, in addition to including many computations, the cost of each calculation is very high since simulation up to the ruin of the structure requires highly non-linear behaviour to be taken into account. Therefore, there is a severe need to develop specific numerical strategies that effectively reduce the computational burden, thereby enhancing the accessibility and

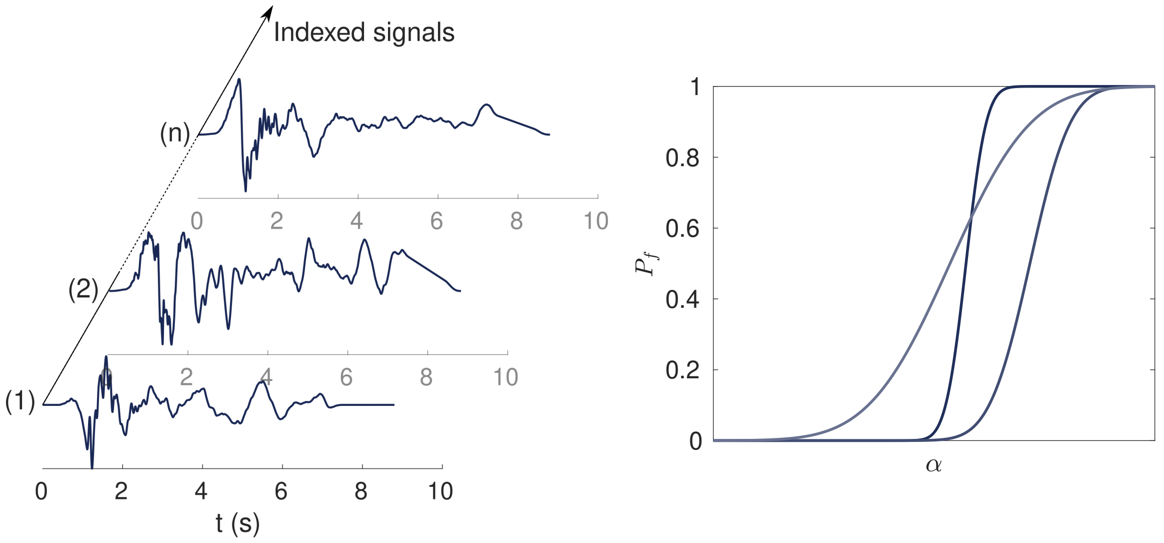

(a) Non-parametrised indexed loading scenarios **(b)** Example of fragility curves

Figure 4 • Fragility curves and seismic ground motions examples

feasibility of comprehensive risk assessment studies. Improved numerical strategies hold the potential to make failure probability prediction more readily available and applicable across a wide range of engineering applications.

In order to decrease the computational cost of fatigue failure predictions, studies propose simpler modelling based on an elastic solution post-processing [H. Wu et al., 2019; Proso et al., 2016; Marsh et al., 2016]. However, such methods do not give a detailed description of the non-linearities nor take the temporal specifics of the loading into account. Accurately predicting the failure of structures requires a fine description of their non-linear behaviour until failure. Therefore, specific efficient solvers for those detailed problems are of particular interest.

Various methods such as Domain Decomposition Methods (DDM) [Gravouil & Combescure, 2003; Farhat & Li, 2005] or adaptative mesh refinement [Zeoli et al., 2020] have been proposed in the literature to decrease the cost of non-linear computations. Model simplification can also achieve similar ends using super elements in dynamics, for example [Morin et al., 2018]. Model-order reduction methods offer an alternative by not simplifying the physical problem itself but reducing the cost of solving it by looking for low-rank solutions. Such methods are an effective mean to lower the numerical cost of expensive computations. *A posteriori* methods such as Proper Orthogonal Decomposition (POD) rely on an offline stage consisting of prior full non-linear computations for several sets of parameters [Chatterjee, 2000]. The reduced-order basis built from the snapshots is then used in the online stage to find low-cost solutions to the non-linear problem for a new set of parameters. Automation of snapshot selection has been proposed in the Reduced Basis method [Maday et al., 2002]. Conversely, *a priori* reduced-order methods such as Proper Generalised Decomposition (PGD) [Néron & Ladevèze, 2010a; Chinesta et al., 2011] avoid the offline phase as the reduced-order basis is constructed on the fly during computations. The PGD has already proven to be effective for dynamics problems in linear [Boucinha et al., 2014] and non-linear [Germoso et al., 2016; Quaranta et al., 2019] contexts. On the one hand, parametric studies can include parameters as additional coordinates of the reduced-order model [Chinesta et al., 2011; Lu et al., 2018; Paillet et al., 2018] as done in stochastic finite element methods [Anders & Hori, 1999]. This approach does not require multiple calls to the solver, but a higher-dimensional problem is constructed. This approach also requires specific solvers for each new parametric problem. On the other hand, the PGD can be used to separate time-space variables only, keeping potential other parameters outside of the solver and relying on a specific multi-query strategy to optimally handle multiple calls to the space-time PGD solver [Nachar et al., 2020; Néron et al., 2015]. Leaving the extra parameters outside of the PGD decomposition allows to rely on more generic PGD solvers, enabling the development of non-intrusive solvers [Scanff et al., 2022]. It is worth mentioning that, while the set of boundary conditions can be seen as discrete extra-coordinates [Courard, 2016], in cases where the multi-query study involves indexed non-parametrised time-series instead of sets of parameters, an external multi-query framework offers more flexibility. The PGD space-time basis is built explicitly for the problem at hand. Therefore, the PGD ensures a relevant basis for the current problem and eliminates the need for expensive full-order computations and the tedious selection of snapshots [Tegtmeyer et al., 2017]. The use of the PGD method requires the handling of global solutions over space and time. In a non-linear context, the use of a non-incremental solver is therefore required. The PGD is thus inherently embedded in the LATIN method, a non-incremental iterative scheme [Ladevèze, 1999]. After the initialisation of the solution, each LATIN iteration consists in solving the non-linear equations on one side and the global problem on the other side, therefore iteratively converging towards the solution of the non-linear dynamics problem. The separation of variables between time and space is easily written for the global problem, which remains linear even for non-linear problems. The LATIN-PGD method has been applied to many non-linear contexts, including the damage evolution of quasi-brittle materials subjected to low-cycle and high-cycle quasi-static fatigue loading [Bhattacharyya et al., 2018b; Bhattacharyya et al., 2019] or under dynamic conditions [Iturra, 2021; Daby-Seesaram et al., 2023]. Two leverage points have improved the LATIN-PGD in the multi-query context for material variability. First, the iterative scheme is initialised with the space-time solution of a previous computation to reduce the number of iterations needed for convergence. Second, the reduced-order basis generated for another simulation is provided to the new simulation as in the POD framework. Thus, the computational effort to evaluate the spatial modes to be added on the fly is reduced in a parametric context [Heyberger et al., 2012]. Some of these advances could be used in the case of load variability, but the fact that the different simulations do not share the same admissibility requires further development.

The numerical benefit of reduced-order modelling techniques can be paired with building a surrogate model to reduce the number of calls to the solver, thus decreasing the numerical cost of the study. Moreover, in a context where the full solutions associated with every computation are not useful but where only specific quantities of interest are needed, the intermediate simulations can be performed with coarse convergence criterion. This is particularly relevant for optimisation studies for instance. In such a context, multi-fidelity kriging methods coupled with the PGD have been successfully employed for a parametric visco-plastic study [Nachar et al., 2020]. Using such methods, however, requires the problem to be parametrised with a low enough number of parameters. These methods are, therefore, not directly applicable to the problem addressed in this doctoral thesis, given that the focus is on tackling non-parametrised problems.

* * *

This doctoral thesis introduces a promising framework that offers a cost-effective approach to estimating the probability of structural failure under uncertain loading conditions.

As mentioned previously, the investigation was initially motivated by the case of seismic hazard in the context of nuclear safety but extends to various studies where multiple non-linear dynamics computations need to be performed. The objective is to develop a method that works favourably when each non-linear computation is associated with load supplied as a non-parametrised indexed temporal signal. The number of computations to perform is, therefore, given and cannot be decreased to mitigate the computational cost. Moreover, in the following, we will refrain from relying on prior knowledge of any load parametrisation as the framework is expected to be robustly used in cases where such a parametrisation is not readily available.

More precisely, this work offers a framework that consists of an efficient non-linear dynamics solver seamlessly paired with a novel multi-query strategy that exploits the similarities from one computation to another and offers a robust procedure to determine an optimal path through the loading scenarios space. This doctoral thesis is structured into three parts. The first part provides an overview of the state of the art for dynamics non-linear computations, while the second part presents the new ingredients at the core of the proposed methodology. Finally, the third part offers an application case of this methodology for predicting the probability of failure of a structure subjected to seismic hazards. This doctoral thesis comprises a total of five chapters, the contents of which are detailed below.

◇ **PART I - STATE OF THE ART**

- **Chapter** 1 sets out the different notations used and presents the non-linear dynamics problem, which lies at the core of the methodology proposed in this thesis. An overview of some of the main time integration methods for solving dynamics problems is given. Chapter 1 also presents an overview of non-linear solvers.
- **Chapter** 2 presents commonly used reduced-order model methods that can help decreasing the high computational costs induced by the computation of the non-linear dynamics solutions. It provides an initial overview of the *Proper Generalised Decomposition* (*PGD*), an *a posteriori* method that will be further employed in the proposed solver. The existing tools to tackle multi-query problems are also discussed, and the main idea on which the proposed framework relies is presented.

◇ PART II - MULTI-QUERY ROM CONTRIBUTIONS

- **Chapter** 3 presents the solver used in the study. In order to decrease the high numerical cost associated with solving the non-linear dynamics problem, an efficient solver based on space-time model-order reduction techniques is proposed. Given the objective of employing the solver within a multi-query framework, the LATIN method appeared as a natural choice so that we could later rely on its non-incremental nature to smartly initialise computations. Moreover, its architecture allowed the combined use of temporal and frequency computations. Solving dynamics problems in the frequency domain gives significant advantages compared with solutions fully computed in the temporal domain, but history-dependent non-linear behaviour is an obstacle to employing that strategy. A hybrid approach is proposed to solve the non-linear behaviour in the temporal domain while the mechanical equilibrium is solved using a frequency strategy coupled with model-order reduction methods. In order to employ the Fast Fourier Transform (FFT) robustly for the transient regime, artificial numerical damping is used. The reduced-order hybrid temporal-frequency approach appears as a robust and proficient technique to simulate structures under transient dynamic loadings until failure. This chapter is derived from the work presented in [Daby-Seesaram et al., 2023].
- **Chapter** 4 shows how a specific multi-query framework has been built around the LATIN-PGD solver. Predicting the failure risk of a mechanical structure under dynamic loadings requires running non-linear computations for a large number of load scenarios. Reduced-order models provide relatively cheap simulation for each load case. Assuming that previous computations have been performed, this chapter exploits the similarities between the different simulations to further decrease the computational cost. The new simulation benefits from previous simulations to initialise the non-linear scheme and the reduced basis. Looking for the parent-simulation, i.e., the best computation to accelerate the new computation, is particularly challenging in cases where the loading is non-parametrised. A physical-based strategy using the elastic responses is proposed. A genetic algorithm designs an optimal sequence to perform the simulations.

◇ PART III - APPLICATION TO THE EARTHQUAKE ENGINEERING CONTEXT

- **Chapter** 5 further builds on the non-incremental strategy by exploiting the multi-fidelity aspect of the methodology. Relying on the distance indicator developed in Chapter 4, an upgraded strategy is proposed where the stopping criterion of the LATIN solver is chosen on the fly depending on the level of non-linearity expressed in the close computation highlighted by the indicator. Non-critical cases therefore lead to cheaper computations. Consequently, the total computational cost of the study is decreased without losing the fine knowledge needed to decide whether or not a loading leads to the ruin of the structure. This extended

> methodology is showcased in an earthquake engineering context where loadings are not parametrised but consist of indexed signals. Examples of fragility curves are built from the multi-query study showcasing the numerical benefits offered by the new framework in an earthquake engineering context.

The methodology is visually represented in Figure 6 as a flowchart, illustrating its sequential steps. Each contribution is linked to its respective chapter, providing readers with a convenient reference to locate detailed information about each specific contribution within the doctoral dissertation.

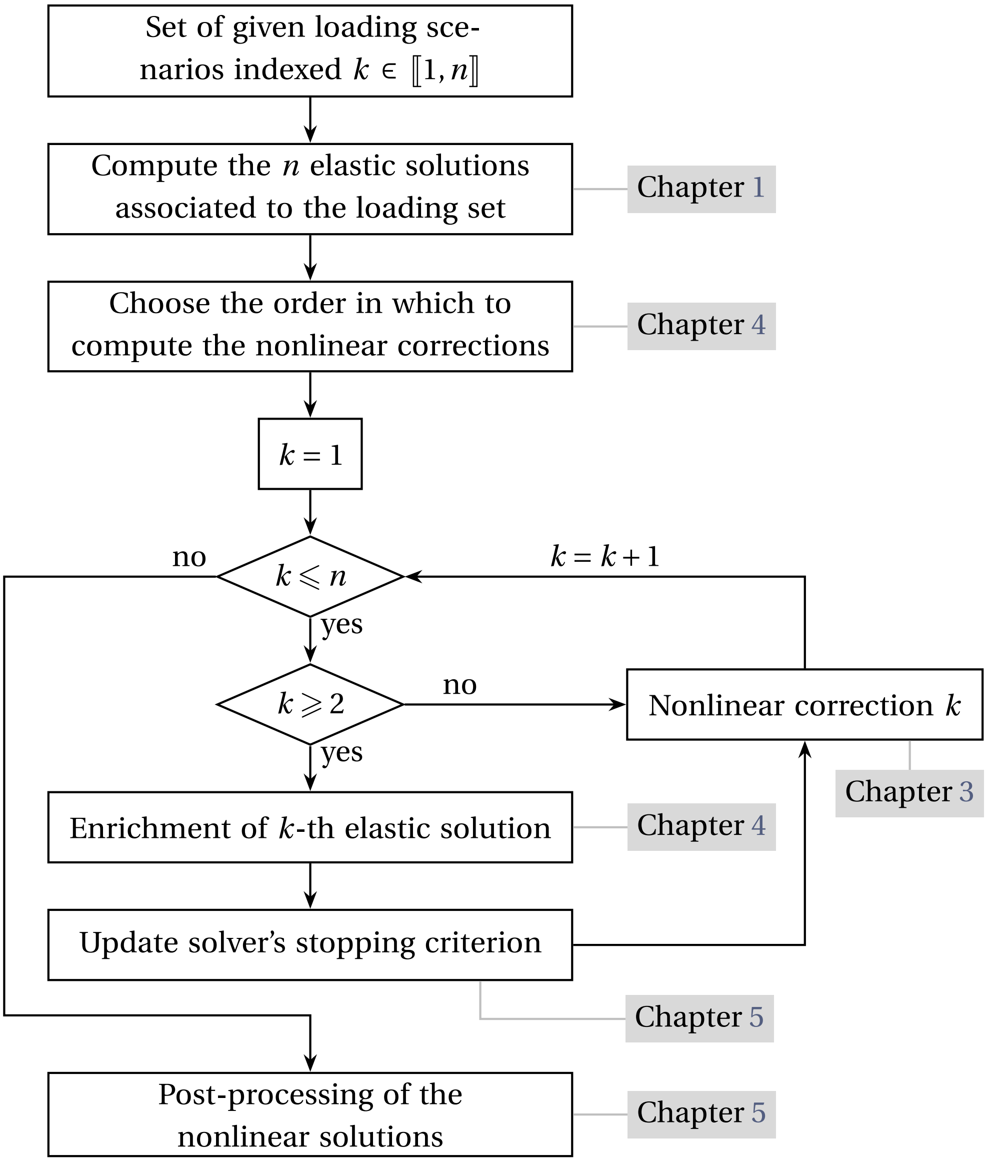
Set of given loading scenarios indexed $k \in [\![1, n]\!]$
Compute the n elastic solutions associated to the loading set
Chapter 1
Choose the order in which to compute the nonlinear corrections
Chapter 4
$k = 1$
no
$k \leqslant n$
$k = k + 1$
yes
$k \geqslant 2$
no
Nonlinear correction k
yes
Chapter 3
Enrichment of k-th elastic solution
Chapter 4
Update solver's stopping criterion
Chapter 5
Post-processing of the nonlinear solutions
Chapter 5

Figure 6 • Flow chart of the proposed methodology

Part I

State of the art of Model-Order Reduction techniques for non-linear dynamics

Chapter 1

A non-linear dynamics problem

> When we, system dynamicists, see a pattern persist in many parts of a system over long periods, we assume that it has causes embedded in the feedback loop structure of the system.
>
> Donella H. Meadows

This chapter introduces the non-linear dynamics problem at the core of the proposed methodology and presents key numerical integration methods for structural dynamics. Additionally, linear-based methods for assessing fatigue damage in mechanical structures are discussed, highlighting their limitations. In contrast, a comprehensive description of the plasticity-driven damageable behaviour is provided to address these limitations. Standard non-linear numerical solvers are then presented to solve the non-linear mechanical problem.

Contents

1 Weak formulation of the dynamics problem 14
  1.1 Kinematic description 14
  1.2 Newton's second law of motion 16
  1.3 Linear elastodynamics 18
2 Time integration methods 19
  2.1 Newmark scheme 20
  2.2 Temporal finite element method 21
  2.3 Frequency computations 22
3 Failure prediction with elastic models 22
4 Ductile damage model with crack-closure effect 23

4.1 Effective stress . . . 23
4.2 State and evolution laws . . . 24
5 Non-linear solvers . . . 25
5.1 Newton-Raphson method . . . 26
5.2 Arc-length solvers . . . 28
5.3 Non-incremental solvers . . . 28
Chapter summary & perspectives . . . 32

1 Weak formulation of the dynamics problem

The dynamics aspects of the problem, notations and hypothesis are introduced in this section. The kinematic description and equilibrium are first presented before giving the weak formulation of the dynamics problem. In an ambient space $\mathscr{E}$, let one consider during the time interval $I = [0, T_0]$ a body of density ρ with spatial domain denoted Ω submitted to body forces $\boldsymbol{f}_d$ and surface forces $\boldsymbol{F}_d$ on Ω and $\partial\Omega_2$ respectively, as represented in Figure 1.1. Displacements $\boldsymbol{u}_d$ are prescribed on the edge $\partial\Omega_1$.

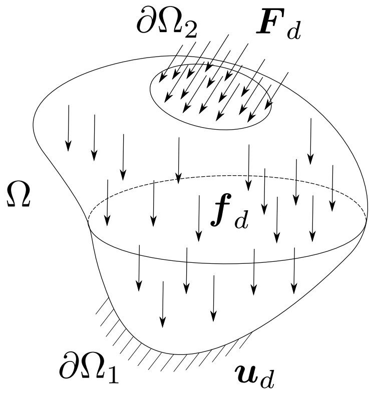

Figure 1.1 • Reference problem

1.1 Kinematic description

This section is devoted to the kinematic description of the transformation of a continuum medium described in Figure 1.2. In a given frame of reference $\mathscr{R}$ the movement from a initial configuration Ω_0 and the current configuration $\Omega(t)$ is described through the mapping $\phi(\boldsymbol{X}, t)$ such that

$$\begin{aligned} \phi : \Omega_0 &\longrightarrow \Omega(t) \\ \boldsymbol{X} &\longmapsto \boldsymbol{x} = \phi(\boldsymbol{X}, t), \end{aligned} \tag{1.1}$$

with $\boldsymbol{X}$ the vector of Lagrangian coordinates of each point $M_0 \in \Omega_0$ and $\boldsymbol{x}$ the vector of Eulerian coordinates of each point $M(t) \in \Omega(t)$.

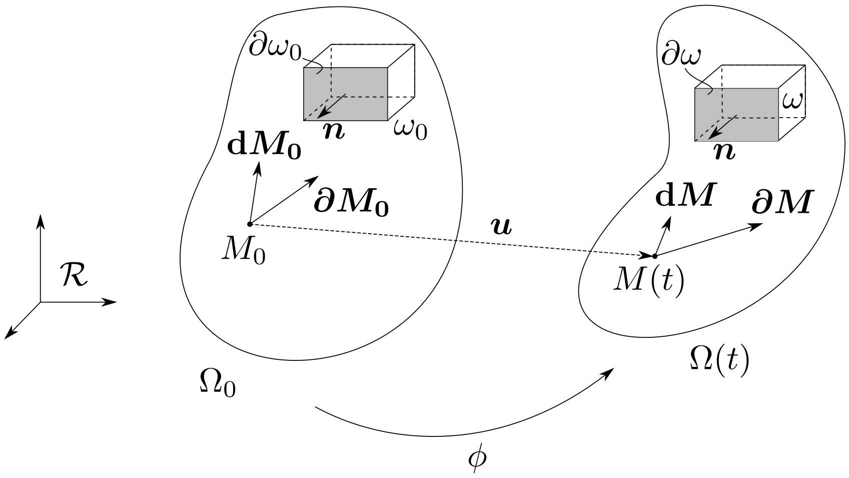

Figure 1.2 • Kinematic transformation of a continuum medium

The kinematic description of the transformation must account for the relative variations of angle and length between two infinitesimal vectors $\mathbf{d}\boldsymbol{M_0}$ and $\boldsymbol{\partial M_0}$ from the initial configuration to their counter part $\mathrm{d}\boldsymbol{M}$ and $\boldsymbol{\partial M}$ in the current configuration. To achieve this, after having introduced the dilatation tensor

$$\mathbb{C} = \boldsymbol{g}\mathbb{F}^T\mathbb{F}, \tag{1.2}$$

with $\mathbb{F} = \frac{\partial\phi}{\partial \boldsymbol{X}}$ the gradient of the transformation and $\boldsymbol{g}$ a metric of the ambient space $\mathscr{E}$, a measure of strain is introduced. An example of which, for instance, is the Green-Lagrange tensor

$$\mathbb{E}\left(\boldsymbol{X}, t\right) = \frac{1}{2}\left(\mathbb{C} - \boldsymbol{g}\right), \tag{1.3}$$

a second-order covariant tensor defined on the initial configuration Ω_0.

Remark In the context of continuum mechanics, it is very common to work within a Euclidean space of dimension $\mathrm{d} \in \{1,2,3\}$, *e.g.* $\mathscr{E} = \mathbb{R}^{\mathrm{d}}$. In the absence of curvature, the previously described tensors are more simply redefined as

$$\begin{cases} \mathbb{E}\left(\boldsymbol{X}, t\right) = \frac{1}{2}\left(\mathbb{C} - \mathbb{1}\right) \\ \mathbb{C} = \mathbb{F}^T\mathbb{F}. \end{cases} \tag{1.4}$$

The gradient of the transformation $\mathbb{F} = \frac{\partial\phi}{\partial \boldsymbol{X}}$ can also be defined directly from the displacement field $\boldsymbol{u}$. In the frame of reference $\mathscr{R}$, the displacement field $\boldsymbol{u}\left(\boldsymbol{X}, t\right)$ describes the movement of a particle point from the location $M_0 \in \Omega_0$ at $t = 0$ that moved to $M(t) \in \Omega(t)$ at $t > 0$. The displacement field $\boldsymbol{u}$ is therefore defined as

$$\boldsymbol{u} = \boldsymbol{M_0 M} = \phi\left(\boldsymbol{X}, t\right) - \boldsymbol{X}. \tag{1.5}$$

Introducing the displacement field, the gradient of the transformation $\mathbb{F}$ thus reads,

$$\mathbb{F}\left(\boldsymbol{X}, t\right) = \mathbb{1} + \frac{\partial \boldsymbol{u}}{\partial \boldsymbol{X}}. \tag{1.6}$$

Accounting for the initial and boundary conditions described in Figure 1.1, the set of kinematically admissible displacements denoted $\mathscr{U}$ is finally defined as

$$\mathscr{U} = \Big\{ \boldsymbol{u} \mid \boldsymbol{u}\left(\boldsymbol{x}, t\right) \in \mathscr{H}^1\left(\Omega, \mathbb{R}^{\mathrm{d}}\right) \otimes \mathscr{L}^2\left(I, \mathbb{R}\right), \\ \dot{\boldsymbol{u}}\big|_{t=0} = \boldsymbol{0},\ \boldsymbol{u}|_{t=0} = \boldsymbol{0} \text{ in } \Omega,\ \boldsymbol{u} = \boldsymbol{u}_d \text{ and } \dot{\boldsymbol{u}} = \dot{\boldsymbol{u}}_d \text{ on } \partial\Omega_1 \Big\}, \tag{1.7}$$

where $\boldsymbol{u}$ is the displacement vector, $\dot{\boldsymbol{u}}$ the velocity and $\varepsilon(\boldsymbol{u})$ the strain tensor and with $\mathrm{d} \in \{1, 2, 3\}$ depending on the spatial dimension of the problem. The corresponding homogeneous space is denoted $\mathscr{U}^0$, where $\boldsymbol{u}_d$ and $\dot{\boldsymbol{u}}_d = 0$. In the end, kinematic admissibility amounts to

$$\begin{cases} \boldsymbol{u} \in \mathscr{U} \\ \mathbb{E}\left(\boldsymbol{X}, t\right) = \frac{1}{2}\left(\mathbb{C} - \mathbb{1}\right). \end{cases} \tag{1.8}$$

In case of small strain, displacements and small rotations, the linear approximation $\varepsilon\left(\boldsymbol{u}, t\right)$ of the Green-Lagrange tensor is much greater than the higher order terms which can be neglected. The strain tensor ε then reads

$$\varepsilon\left(\boldsymbol{u}, t\right) = \frac{1}{2}\left(\frac{\partial \boldsymbol{u}}{\partial \boldsymbol{X}} + \frac{\partial \boldsymbol{u}}{\partial \boldsymbol{X}}^T\right) \tag{1.9}$$

The kinematic description of the transformation between the initial and current configuration being finalised, a representation of the forces within the body Ω is now needed to further complete the description of the mechanical state of the structure.

1.2 Newton's second law of motion

Cauchy's postulates [Cauchy, 1827] state that there are two types of forces in the studied structures:

- volumic forces defined through a volumic force density $\boldsymbol{f}_v\left(\boldsymbol{x}, t\right)$ such that
  - $\mathrm{d}\boldsymbol{F} = \boldsymbol{f}_v \mathrm{d}\omega$
- contact forces defined through a surfacic force density $\boldsymbol{T}\left(\boldsymbol{x}, \partial\omega, t\right)$ such that
  - $\mathrm{d}\boldsymbol{F} = \boldsymbol{T}\left(\boldsymbol{x}, \partial\omega, t\right)\partial\omega$

Cauchy's second postulate stipulates that the stress vector $\boldsymbol{T}$ only depends form the external normal vector $\boldsymbol{n}$, therefore,

$$\boldsymbol{T}\left(\boldsymbol{x},\partial\omega,t\right)=\boldsymbol{T}\left(\boldsymbol{x},\boldsymbol{n},t\right). \tag{1.10}$$

Moreover, Cauchy's theorem allows introducing Cauchy's tensor $\boldsymbol{\sigma}\left(\boldsymbol{x},t\right)$, a second-order contravariant and symmetric tensor defined on the deformed configuration $\Omega\left(t\right)$ such that

$$\boldsymbol{T}\left(\boldsymbol{x},\boldsymbol{n},t\right)=\boldsymbol{\sigma}\left(\boldsymbol{x},t\right)\boldsymbol{n}\left(\boldsymbol{x},t\right). \tag{1.11}$$

Under those assumptions and in a continuum medium, *Newton's second law of motion* reads

$$\begin{aligned} \frac{\mathrm{d}}{\mathrm{d}t}\int_{\omega}\rho\boldsymbol{v}\mathrm{d}\omega &= \int_{\omega}\boldsymbol{f_d}\mathrm{d}\omega+\int_{\partial\omega}\boldsymbol{T}\partial\omega, \quad \forall\omega\subset\Omega \\ \Longleftrightarrow \int_{\omega}\rho\boldsymbol{\gamma}\mathrm{d}\omega-\int_{\omega}\boldsymbol{f_d}\mathrm{d}\omega &= \int_{\partial\omega}\boldsymbol{T}\partial\omega=\int_{\omega}\nabla\cdot\boldsymbol{\sigma}\mathrm{d}\omega, \quad \forall\omega\subset\Omega \end{aligned} \tag{1.12}$$

Hence locally, the equation of motion reads,

$$\nabla\cdot\boldsymbol{\sigma}+\boldsymbol{f_d}=\rho\boldsymbol{\gamma} \quad \forall\boldsymbol{x}\in\Omega,\forall t\in I. \tag{1.13}$$

This equation, coupled with prescribed forces described in 1.1, defines the set $\mathscr{S}$ which contains the Cauchy stress tensors denoted $\boldsymbol{\sigma}$ that are dynamically admissible and an acceleration $\boldsymbol{\gamma}$, which is linked to the primal displacement variable $\boldsymbol{u}$ via the equation

$$\boldsymbol{\gamma}=\ddot{\boldsymbol{u}}, \tag{1.14}$$

i.e.,

$$\mathscr{S}=\left\{\left(\boldsymbol{\sigma},\boldsymbol{\gamma}\right)\mid\nabla\cdot\boldsymbol{\sigma}+\boldsymbol{f}_d=\rho\boldsymbol{\gamma}\text{ in }\Omega,\ \boldsymbol{\sigma}\ \boldsymbol{n}=\boldsymbol{F}_d\text{ on }\partial\Omega_2\right\} \tag{1.15}$$

with $\boldsymbol{n}$ the normal vector to $\partial\Omega_2$.

Newton's law can be formally re-written under the so-called *weak formulation* which is a formulation at the heart of the finite element method (FEM), widely used to solve mechanics problems numerically. The weak formulation of Newton's second law of motion corresponds to the virtual power principle (VPP) of continuum mechanics.

The virtual power principle reads:

$$\mathscr{P}^*_{\text{ext}}+\mathscr{P}^*_{\text{int}}=\mathscr{P}^*_{\text{acc}} \tag{1.16}$$

with,

$$\begin{cases} \mathscr{P}^*_{\text{ext}}=\displaystyle\int_{\Omega}\boldsymbol{f_d}\cdot\boldsymbol{v}^*\mathrm{d}\Omega+\int_{\partial\Omega}\boldsymbol{T}\cdot\boldsymbol{v}^*\partial\Omega, \\ \mathscr{P}^*_{\text{int}}=-\displaystyle\int_{\Omega}\boldsymbol{\sigma}:\varepsilon(v^*)\mathrm{d}\Omega, \\ \mathscr{P}^*_{\text{acc}}=\displaystyle\int_{\Omega}\rho\boldsymbol{\gamma}\cdot\boldsymbol{v}^*\mathrm{d}\Omega;\forall\boldsymbol{v}^*\in\mathscr{U}^0. \end{cases} \tag{1.17}$$

The solution to the problem $s = \left(\boldsymbol{u}, \left(\boldsymbol{\sigma}, \boldsymbol{\gamma}\right)\right) \in \mathscr{U} \times \mathscr{S}$ thus includes both the displacement and stress fields that satisfy the weak formulation of the dynamic equilibrium

$$
\begin{aligned}
-\int_{\Omega \times I} \boldsymbol{\sigma} : \boldsymbol{\varepsilon}\left(\boldsymbol{u}^*\right) \mathrm{d}\Omega \mathrm{d}t + \int_{\Omega \times I} \boldsymbol{f_d} \cdot \boldsymbol{u}^* \mathrm{d}\Omega \mathrm{d}t + \int_{\partial\Omega \times I} \boldsymbol{F_d} \cdot \boldsymbol{u}^* \mathrm{d}S \mathrm{d}t \\
= \int_{\Omega \times I} \rho\, \boldsymbol{\gamma} \cdot \boldsymbol{u}^* \mathrm{d}\Omega \mathrm{d}t, \ \forall \boldsymbol{u}^* \in \mathscr{U}^0,
\end{aligned}
\quad (1.18)
$$

as well as the constitutive relations corresponding to the material of the body. The constitutive relation of the material is yet to be defined to complete the mechanical problem to be solved. The behaviour equations provide a link between the aforementioned kinetic quantities and forces.

1.3 Linear elastodynamics

In the section and in the remainder of the thesis, the small strain hypothesis is adopted. Under such an assumption, the current and initial configuration are considered identical and the linearised strain tensor $\boldsymbol{\varepsilon}$ can be used in preference to the Green-Lagrange tensor. The kinematic quantity given by the strain tensor and the dual quantity described by Cauchy's tensors can be linked directly even though the former lives in the initial configuration while the latter lives in the current configuration. The simplest way of linking those two quantities it to assume a linear dependency between the two. In this case the behaviour is reversible and consider *elastic*. The behaviour then simply reads

$$
\boldsymbol{\sigma}^e = \mathbb{K} : \boldsymbol{\varepsilon}, \quad (1.19)
$$

where $\boldsymbol{\sigma}^e$ is the elastic Cauchy's stress tensor. If a Kelvin-Voigt description is considered, viscous forces can be introduced in parallel to the elastic behaviour as shown in Figure 1.3. The stress tensor then reads $\boldsymbol{\sigma} = \boldsymbol{\sigma}^e + \boldsymbol{\sigma}^v$ where $\boldsymbol{\sigma}^v = \mathbb{D} : \dot{\boldsymbol{\varepsilon}}$ with $\mathbb{D}$ being a tensor describing all viscosity phenomena [Chevreuil et al., 2007; Eugeni et al., 2021; Chouaki et al., 1998].

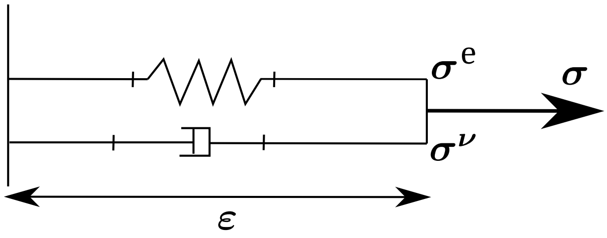

Figure 1.3 • Kelvin-Voigt linear model

In the context of linear elasticity, the weak form of Newton's second law of motion given in Equation 1.16 reads,

$$
\begin{aligned}
-\int_{\Omega\times I}\varepsilon:\mathbb{K}:\varepsilon\left(\boldsymbol{u}^*\right)\mathrm{d}\Omega\mathrm{d}t-\int_{\Omega\times I}\dot{\varepsilon}:\mathbb{D}:\varepsilon\left(\boldsymbol{u}^*\right)\mathrm{d}\Omega\mathrm{d}t+\int_{\Omega\times I}\boldsymbol{f_d}\cdot\boldsymbol{u}^*\mathrm{d}\Omega\mathrm{d}t+\int_{\partial\Omega\times I}\boldsymbol{T}\cdot\boldsymbol{u}^*\mathrm{d}S\mathrm{d}t&\\
=\int_{\Omega\times I}\rho\,\boldsymbol{\gamma}\cdot\boldsymbol{u}^*\mathrm{d}\Omega\mathrm{d}t,\ \forall\boldsymbol{u}^*\in\mathcal{U}^0,&
\end{aligned}
\tag{1.20}
$$

The numerical integration of a linear elastic problem has widely been discussed in the literature and a presentation of the main methods is proposed in Section 2.

2 Time integration methods

The weak form of the dynamics problem can be semi-discretised in space using a Galerkin approximation. Because this particular study consists in low-frequency dynamics, the finite element method is employed to construct the basis functions $\left\{N_i^x(\boldsymbol{x})\right\}_{i\in[\![1,N]\!]}$ onto which the desired solution is projected. The displacement field $\boldsymbol{u}$ therefore reads

$$
\boldsymbol{u}\left(\boldsymbol{x},t\right)\approx\sum_{i=1}^{N}N_i^x(\boldsymbol{x})\left\{U_i\right\}(t)\,,
\tag{1.21}
$$

where $\left\{U_i\right\}$ is the i-th component of the nodal displacements vector $\left\{U\right\}$ and $N_x^i(\boldsymbol{x})$ is the associated spatial shape function. Once semi-discretised in space using the finite element method, the equation reads

$$
\left[M\right]\left\{\ddot{U}\right\}+\left[D\right]\left\{\dot{U}\right\}+\left[K\right]\left\{U\right\}=\left\{F\right\},
\tag{1.22}
$$

where $\left[M\right]$, $\left[D\right]$ and $\left[K\right]$ are the mass, damping and stiffness matrices respectively. The vector $\left\{U\right\}(t)\in\mathbb{U}^N$ represents the displacement vector, which is the solution to the resulting second-order differential equation. The discrete kinematic admissible subspace $\mathbb{U}^N$ is defined as

$$
\mathbb{U}^N=\left\{\left\{U\right\}\in\mathbb{R}^{N\times N_t}\mid\boldsymbol{u}\in\mathcal{U}\right\},
\tag{1.23}
$$

with N_t the number of time steps.

Remark It can be noted that the previously introduced tensor $\mathbb{D}$ describes viscous phenomena locally and therefore mostly describes material viscosity while the damping matrix $\left[D\right]$ can also provide a broader description of dissipating phenomena. This includes friction in joints and the dissipation arising from the structure's interactions with surrounding fluids. The introduction of the viscous forces in the continuum mechanics problem is mainly interesting for mapping the role of damping throughout the equations in the developments to follow.

In the literature, several integration methods allow to get an approximation of that displacement vector in a given finite number of instants $\{t_n\}_{n\in[\![1,N_t]\!]}$ called time steps.

2.1 Newmark scheme

The most common integration method for structural dynamics is the *Newmark* scheme [Newmark, 1959] that is implemented in most commercial finite element software. This integration method is based on the following approximation of displacement and velocity fields,

$$\begin{cases} \{\dot{U}\}\left(t_{n+1}\right) = \{\dot{U}\}\left(t_n\right) + \Delta t \, \{\ddot{U}\}_{\gamma}, \\ \{U\}\left(t_{n+1}\right) = \{U\}\left(t_n\right) + \Delta t \, \{\dot{U}\}\left(t_n\right) + \tfrac{1}{2} \, \Delta t^2 \, \{\ddot{U}\}_{\beta}, \end{cases} \tag{1.24}$$

with,

$$\begin{cases} \{\ddot{U}\}_{\gamma} = (1-\gamma)\,\{\ddot{U}\}\left(t_n\right) + \gamma\{\ddot{U}\}\left(t_{n+1}\right), \quad \gamma \in [0,1] \\ \{\ddot{U}\}_{\beta} = (1-2\beta)\,\{\ddot{U}\}\left(t_n\right) + 2\beta\{\ddot{U}\}\left(t_{n+1}\right), \quad \beta \in \left[0, \tfrac{1}{2}\right]. \end{cases} \tag{1.25}$$

Relying on Equation 1.24 and Equation 1.25, the variation in acceleration $\left\{\delta\ddot{U}\right\} = \{\ddot{U}\}\left(t_{n+1}\right) - \{\ddot{U}\}\left(t_n\right)$ and the variation in velocity $\left\{\delta\dot{U}\right\} = \{\dot{U}\}\left(t_{n+1}\right) - \{\dot{U}\}\left(t_n\right)$ read

$$\begin{cases} \left\{\delta\ddot{U}\right\} = \tfrac{1}{\beta \, \Delta t^2} \underbrace{\left(\{U\}\left(t_{n+1}\right) - \{U\}\left(t_n\right)\right)}_{\{\delta U\}} - \tfrac{1}{\beta \, \Delta t}\{\dot{U}\}\left(t_n\right)\left(\tfrac{1}{2\beta}\right)\{\ddot{U}\}\left(t_{n+1}\right) \\ \left\{\delta\dot{U}\right\} = \tfrac{\gamma}{\beta \, \Delta t}\,\{\delta U\} - \tfrac{\gamma}{\beta}\{\ddot{U}\}\left(t_n\right) - \Delta t \, \left(1 - \tfrac{\gamma}{2\beta}\right)\{\ddot{U}\}\left(t_n\right). \end{cases} \tag{1.26}$$

Differentiating Equation 1.22 between two consecutive time steps leads to the correction equation

$$[M]\left\{\delta\ddot{U}\right\} + [D]\left\{\delta\dot{U}\right\} + [K]\,\{\delta U\} = \{\delta F\}. \tag{1.27}$$

Injecting equations given in 1.26 in the correction dynamics Equation 1.27 yields

$$\begin{aligned} \left[\frac{[M]}{\beta \, \Delta t^2} + \frac{[D]\,\gamma}{\beta \, \Delta t} + [K]\right]\{\delta U\} = \{\delta F\} + \frac{1}{\beta\Delta t}\,[M]\,\{\dot{U}\}\left(t_n\right) + \frac{1}{2\beta}\,[M]\,\{\dot{U}\}\left(t_n\right) \\ + \frac{\gamma}{\beta}\,[D]\,\{\dot{U}\}\left(t_n\right) - \Delta t\left(1 - \frac{\gamma}{2\beta}\right)[D]\,\{\dot{U}\}\left(t_n\right). \end{aligned} \tag{1.28}$$

From this equation, the displacement correction $\{\delta U\}$ can be retrived and the velocity and acceleration corrections $\left\{\delta\dot{U}\right\}$ and $\left\{\delta\ddot{U}\right\}$ can be post-processed from Equation 1.26.

The choice of parameters γ and β drives the behaviour of the integration scheme. Table 1.1 gives an overview of the expected behaviour of Newmark scheme for different ranges of values for its parameters.

Some pairs of hyper-parameters are widely used. For instance, the pair $\left(\gamma = 1/2, \beta = 0\right)$ enables reducing the problem to an explicit scheme that is conditionally stable. Conversely, the pair $\left(\gamma = 1/2, \beta = 1/4\right)$ leads to the most accurate unconditionally stable scheme.

Table 1.1 • Newmark scheme hyper-parameters

Parameters range	Behaviour
$\gamma \leqslant 1/2$	Instable
$1/2 \leqslant \gamma$ $2\beta \leqslant \gamma$	Conditionnally stable
$1/2 \leqslant \gamma \leqslant 2\beta$	Inconditionnaly stable

2.2 Temporal finite element method

Similarly to what is classically done in space, the finite element method can be used to solve the temporal partial differential equation. Using time finite element method, the continuous in time displacement $\{U\}(t)$ is approximated by interpolating its values at N_t temporal nodes as

$$\{U\}(t) = \sum_{i=1}^{N_t} N_i^t(t) \{U\}(t_i), \tag{1.29}$$

with $N_i^t(t)$ being the temporal shape function associated with the i-th temporal node. Similarly, on each temporal element comprising N_{te} nodes, the velocity can be approximated as

$$\{\dot{U}\}(t) = \sum_{i=1}^{N_{te}} \frac{\partial N_i^t(\tau)}{\partial \tau} \frac{\partial \tau}{\partial t} \{U\}(t_i), \tag{1.30}$$

with τ being the time coordinate on the 1D isoparametric time element. $\frac{\partial x}{\partial t}$ is then computed using the same shape function leading to

$$\frac{\partial \tau}{\partial t} = \left(\sum_{i=1}^{N_{te}} \frac{\partial N_i^t(\tau)}{\partial \tau} t_i \right)^{-1} = [J]^{-1} \tag{1.31}$$

with $\{t_i\}$ begin the coordinate of the temporal element on the temporal mesh and $[J]$ being the Jacobian matrix associated with the temporal shape functions.

The Galerkin method can be applied to either the displacement field alone or to both the displacement and velocity fields. Moreover, the chosen elements can be either continuous or discontinuous. The time finite element method using discontinuous Galerkin has for instance been applied to structural dynamics [Hulbert, 1992]. A comparison of single and double field discontinuous Galerkin method and continuous Galerkin method is presented in [Boucinha et al., 2013] in the case of elastodynamics. Wang and Zhong, 2017 proposed a novel weak form of the structural dynamics equation to be solved with a single field continuous Galerkin formulation without any regularisation term. Directly solving the assembled problem using a continuous Galerkin method can however be costly, thus reverting to an incremental solving scheme is often proposed.

2.3 Frequency computations

Using the frequency domain allows for very efficient computations in dynamics [Hall, 1982] thanks to the Fast Fourier Transform (FFT) algorithm described in [Cooley & Tukey, 1965]. Indeed, frequency-based calculations can easily be performed in parallel due to the independence of the frequency steps from one another. Therefore, the computations associated with each frequency can be done simultaneously without the need for specific temporal domain decomposition strategies. In addition, relying on frequency calculations may be the natural resort when dealing with parameters that depend on the loading frequency, such as hysteric damping [Bishop, 1955]. With $\left\{\breve{U}\right\}$ the Fourier counterpart of the displacement vector $\{U\}$, ω the angular frequency and j the imaginary unit, the semi-discretised dynamics equation reads

$$\left[-\omega^2\left[M\right]+j\omega\left[D\right]+\left[K\right]\right]\left\{\breve{U}\right\}=\left\{\breve{F}\right\}. \tag{1.32}$$

> **Remark** The FFT algorithm introduced in [Cooley & Tukey, 1965] required that the number time steps was a power of two. Since then this requirement has been lifted by various extension of the algorithm but the FFT remains more efficient if the temporal discretisation leads to a number of time steps that is a power of two.

In case of non-smooth function, the Fourier representation leads to unwanted artefact called Gibbs phenomenon [Carslaw, 1925]. In practice, sharp variations of the function or discontinuity therefore appear as an obstacle to employ the FFT algorithm. In particular if a function f is described over a temporal interval I and $f(\min(I)) \neq f(\max(I))$, then the non-periodicity of the function would incur Gibbs phenomenon. In particular, if a structure is weakly damped or prevented in some way from returning to its initial state such that its final state differs from its initial state, Gibbs phenomena will be observed. Chapter 3 presents a method based on artificial damping [Humar & Xia, 1993] to reduce unwanted aliasing effects arising in such cases.

3 Failure prediction with elastic models

Based the elastodynamic solution, a first estimation of the potential failure of the structure can be performed. Indeed, simple models allow to rely on the elastic response alone to predict the failure of a structure. There are many variants that can be used to predict the level of damage to a structure based on the elastic response alone. This section aims at giving a brief overview of the ideas that are commonly found.

The endurance limit of a given structure, defined as the number of cycles N_f it can withstand under cyclic loading with a specific mean stress σ_m and stress amplitude σ_a, can be determined by S-N curves derived from experimental fatigue tests. A typical example of S-N curve is presented in Figure 1.4. For non-cyclic loading scenarios, the loading can be represented as an equivalent number of cycles using the rainflow cycle counting method [Socie, 1992]. Then, under the assumption that fatigue damage is equal to the accumulated cycle ratio, the endurance of the structure can be determined using the Palmgren-Miner linear damage rule [Hashin & Rotem, 1978; Miner, 1945]. This assumption is translated as

$$D = \sum_i \frac{n_i}{N_{fi}}, \tag{1.33}$$

with D the cumulative fatigue damage of the structure, n_i is the number of cycle associated with the load σ_i and N_{fi} is the endurance of the structure associated with the load σ_i. Faillure happens when $D = 1$. Those method based on the sole elastic solution have already been applied to structural dynamics [H. Wu et al., 2019; Proso et al., 2016; Marsh et al., 2016].

S-N curves provide a general approach but may not accurately capture the specific behaviour of a structure in all scenarios. Indeed, using such curves lack of sensitivity to localized effects and they do not account for loading history and its influence on fatigue damage accumulation. Accurately predicting the failure of structures under complex loading requires a fine description of their non-linear behaviour until failure. The behaviour can alternatively be described using the evolution of history-dependent non-linear internal variables [Lemaitre, 1996].

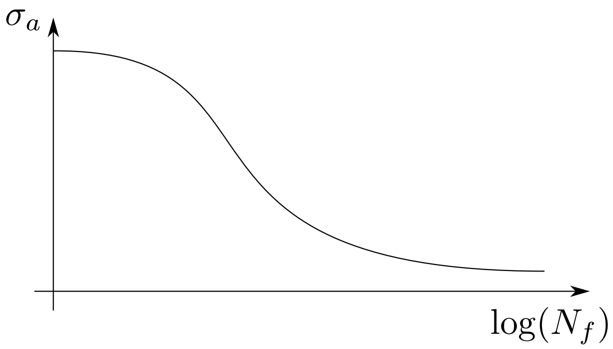

Figure 1.4 • Example of an S-N curve

4 Ductile damage model with crack-closure effect

In order to get a detailed description of the failure phenomenon, the elastic hypothesis is dropped in favour of a damageable plastic behaviour in this thesis. The resulting non-linear behaviour is described in this section.

Similarly to a Kelvin-Voigt model, the non-linear elasto-plastic damage model studied herein is taken in parallel with the material damping properties (see Figure 1.5). The total stress $\boldsymbol{\sigma}$ can therefore be decomposed into a damageable elasto-plastic part $\boldsymbol{\sigma}^\delta$ and a viscous part $\boldsymbol{\sigma}^\nu$ so that it reads $\boldsymbol{\sigma} = \boldsymbol{\sigma}^\delta + \boldsymbol{\sigma}^\nu$. Non-linearities arise from the contribution of the elasto-plastic damage branch, including crack-closure effects. The ductile non-linear behaviour is yet to be described.

4.1 Effective stress

Damage growth is governed by plasticity, which is modelled using linear kinematic and isotropic hardening as introduced in [Lemaitre & Chaboche, 1994]. Isotropic damage is characterised by the scalar variable D. Crack-closure effects [Lemaitre & Desmorat, 2005;

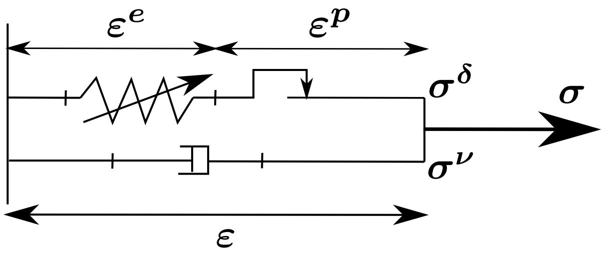

Figure 1.5 • Kelvin-Voigt non-linear model

Lemaitre, 1996] are described by introducing the effective damageable elasto-plastic stress tensor $\boldsymbol{\sigma}^{\boldsymbol{\delta}}_{\boldsymbol{eff}}$ [Bhattacharyya et al., 2019] as

$$\boldsymbol{\sigma}^{\boldsymbol{\delta}}_{\boldsymbol{eff}} = \frac{\boldsymbol{\sigma}^{\delta}_{d}}{1-D} + \left[\frac{\langle\sigma^{\delta}_{H}\rangle}{1-D} - \langle -\sigma^{\delta}_{H}\rangle\right]\mathbf{1}, \tag{1.34}$$

where $\sigma^{\delta}_{H} = \frac{1}{3}\mathrm{Tr}(\boldsymbol{\sigma}^{\delta})$ and $\boldsymbol{\sigma}^{\delta}_{d} = \boldsymbol{\sigma}^{\delta} - \sigma^{\delta}_{H}\mathbf{1}$ are the hydrostatic stress and the deviatoric part of the Cauchy stress tensor, respectively. The operator $\langle\square\rangle = \max\left(\square, 0\right)$ gives the positive part of the quantity of interest. $\mathbf{1}$ denotes the identity tensor and $\mathrm{Tr}(\square)$ gives the trace of $\square$. Thus, the Hooke relation is conveyed by a linear relationship between the effective damageable elasto-plastic stress and the elastic strain $\boldsymbol{\varepsilon}^{e}$ as

$$\boldsymbol{\sigma}^{\boldsymbol{\delta}}_{\boldsymbol{eff}} = \mathbb{K} : \boldsymbol{\varepsilon}^{e} \tag{1.35}$$

with $\mathbb{K}$ representing the Hooke's tensor.

4.2 State and evolution laws

The limit of the elastic domain is defined by the yield function f_p as

$$f_p = J_2\left(\frac{\boldsymbol{\sigma}^{\boldsymbol{\delta}}}{1-D} - \boldsymbol{X}\right) - \sigma_y - R, \tag{1.36}$$

where $J_2\left(\square\right)$ is the von Mises equivalent stress operator and σ_y is the material yield stress. When hardening occurs, the isotropic hardening variable and the kinematic hardening tensor are denoted R and $\boldsymbol{X}$. The yield function f_p satisfies

$$f_p \leqslant 0, \tag{1.37}$$

with an elastic domain defined by $f_p < 0$. Otherwise, when $f_p = 0$, plasticity occurs and the internal variables are updated.

The plasticity model considered here is a Marquis-Chaboche model [Lemaitre & Chaboche, 1994]. The strain tensor is composed of an elastic part $\boldsymbol{\varepsilon}^{e}$ and a plastic part $\boldsymbol{\varepsilon}^{p}$ such that

$$\boldsymbol{\varepsilon} = \boldsymbol{\varepsilon}^{e} + \boldsymbol{\varepsilon}^{p}. \tag{1.38}$$

The cumulative plastic strain p is a strictly increasing internal variable introduced to describe the plasticity level. Linear hardening is given by the linear state equations

$$\begin{cases} R = hp, \\ \boldsymbol{X} = \frac{2}{3}C\boldsymbol{\alpha}, \end{cases} \tag{1.39}$$

where h and C are two material coefficients and $\boldsymbol{\alpha}$ is the kinematic internal variable.

Normality rule leads to the following plasticity evolution laws

$$\begin{cases} \dot{\boldsymbol{\varepsilon}}^p = \dot{p}\dfrac{3}{2}\dfrac{\left(\boldsymbol{\sigma}^{\delta}_{eff}-\boldsymbol{X}\right)_d}{J_2\left(\boldsymbol{\sigma}^{\delta}_{eff}-\boldsymbol{X}\right)}, \\ \dot{\boldsymbol{\alpha}} = \dot{p}\left(1-D\right)\left[\dfrac{3}{2}\dfrac{\left(\boldsymbol{\sigma}^{\delta}_{eff}-\boldsymbol{X}\right)_d}{J_2\left(\boldsymbol{\sigma}^{\delta}_{eff}-\boldsymbol{X}\right)}\right]. \end{cases} \tag{1.40}$$

Damage evolution law [Lemaitre & Desmorat, 2005] is given by

$$\dot{D} = \begin{cases} \dot{p}\left(\frac{Y}{S}\right)^{s_d}, & \text{if } w_s > w_D \\ 0, & \text{otherwise} \end{cases} \tag{1.41}$$

where s_d and S are material parameters and Y is the elastic energy density defined as

$$Y = \frac{1}{2}\boldsymbol{\varepsilon}^e : \mathbb{K} : \boldsymbol{\varepsilon}^e = R_\nu \frac{J_2\left(\boldsymbol{\sigma}^{\delta}_{eff}\right)^2}{2E}, \tag{1.42}$$

with $R_\nu = \frac{2}{3}\left(1+\nu\right) + 3\left(1-2\nu\right)\langle\frac{\sigma^{\delta}_{eff,H}}{J_2\left(\boldsymbol{\sigma}^{\delta}_{eff}\right)}\rangle^2$ the triaxiality function, ν the Poisson ratio, E the Young's modulus and $\sigma^{\delta}_{eff,H}$ the hydrostatic part of the effective damageable elasto-plastic stress tensor. w_s denotes the corrected stored energy density [Lemaitre & Desmorat, 2005] defined as

$$w_s = \int_I \left(R\dot{p} + \boldsymbol{X} : \dot{\boldsymbol{\alpha}}\right)\mathrm{d}t. \tag{1.43}$$

This energy density is compared with an energy density threshold w_D, which is a material parameter. The non-linear behaviour is modelled using this plasticity-driven damage model until the damage variable reaches the critical value D_c at least at one integration point; macrocracks are initiated once this value is reached and classical continuum mechanics is no longer adapted to describe damage phenomena. In the following, the generic expression of the behaviour will be referred to as $\boldsymbol{\sigma}^{\delta} = \mathscr{H}\left(\boldsymbol{\varepsilon}\left(\boldsymbol{u}\right)\right)$.

5 Non-linear solvers

A wide range of solvers is available to solve non-linear mechanical problems. The main idea of those solvers is to rely on two-alternated search directions. The idea is to alternate between solving non-linear equations and the VPP. Search directions allow going back and forth between the local quantities and the solutions of the admissibility problem.

Remark

Vocabulary: Specific terminology is used for two-alternated search directions solvers. A search direction

- is said to be *vertical* when the local and global strain are kept the same, *i.e.* when the numerical computation is stress-controlled,
- is said to be *horizontal* when the local and global stress are kept the same, *i.e.* when the numerical computation is strain-controlled.

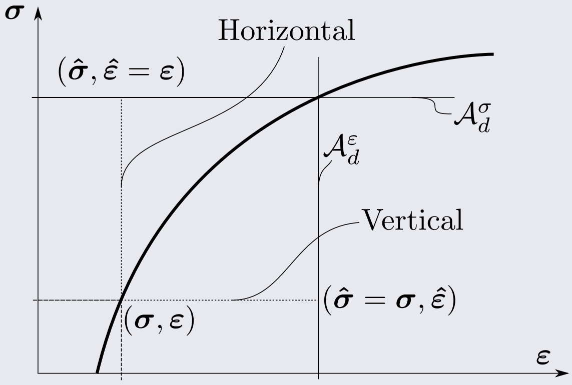
$\boldsymbol{\sigma}$
Horizontal
$(\hat{\boldsymbol{\sigma}}, \hat{\varepsilon} = \varepsilon)$
$\mathcal{A}_d^{\sigma}$
$\mathcal{A}_d^{\varepsilon}$
Vertical
$(\hat{\boldsymbol{\sigma}} = \boldsymbol{\sigma}, \hat{\varepsilon})$
$(\boldsymbol{\sigma}, \varepsilon)$
ε

Among non-linear solvers, the Newton–Raphson method and its derivatives are the most commonly used.

5.1 Newton-Raphson method

The Newton-Raphson method, based on Newton's work [Newton, 1736], is an iterative approach used to solve non-linear equations. It works by incrementally approximating the solution through successive iterations, relying on the first-order approximation of the equation around previous step. The temporal domain is discretised into a finite number of time steps. By performing the iterative process for each time step, the method converges towards the solution at these specific instants. Once the solution for one time step is converged in the sense of a given criterion, the incremental algorithm moves to the next time step and the iterative convergence process is repeated.

In practical terms, from a converged solution $\boldsymbol{u}_i$ at time step i, the solution $\boldsymbol{u}_{i+1}$ for the next time step $i+1$ is is calculated so as to cancel a residual $\mathscr{R}\left(\boldsymbol{u}_{i+1}\right)$. Such residual is defined as

$$\begin{aligned}\mathscr{R}(\boldsymbol{u}) = -\int_{\Omega\times I} \boldsymbol{\sigma} : \boldsymbol{\varepsilon}\left(\boldsymbol{u}^*\right) \mathrm{d}\Omega \mathrm{d}t + \int_{\Omega\times I} \boldsymbol{f_d} \cdot \boldsymbol{u}^* \mathrm{d}\Omega \mathrm{d}t + \int_{\partial\Omega\times I} \boldsymbol{F_d} \cdot \boldsymbol{u}^* \mathrm{d}S \mathrm{d}t \\ - \int_{\Omega\times I} \rho\, \boldsymbol{\gamma} \cdot \boldsymbol{u}^* \mathrm{d}\Omega \mathrm{d}t,\ \forall \boldsymbol{u}^* \in \mathscr{U}^0.\end{aligned} \tag{1.44}$$

In practice, several corrections $\boldsymbol{\Delta u}_{i+1}^{k}$, so that $\boldsymbol{u}_{i+1}^{n} = \boldsymbol{u}_i + \sum\limits_{k=1}^{n} \boldsymbol{\Delta u}_{i+1}^{k}$, are computed until the residual is smaller than a chosen stopping criterion η_{NR}

$$\left\| \mathscr{R}\left(\boldsymbol{u}_i + \sum_{k=1}^{n} \boldsymbol{\Delta u}_{i+1}^{k}\right) \right\| \leqslant \eta_{NR}, \tag{1.45}$$

and the displacement is initialised using the previous converged value such that $\boldsymbol{u}_{i+1}^{1} = \boldsymbol{u}_i$. The corrections are computed in an iterative process. Each step aims at finding a displacement correction $\boldsymbol{\Delta u}_{i+1}^{k+1}$ so that

$$\mathscr{R}\left(\boldsymbol{u}_i + \sum_{l=1}^{k+1} \boldsymbol{\Delta u}_{i+1}^{l}\right) = 0, \tag{1.46}$$

which, at the first-order, translates to the equation

$$\mathscr{R}'\left(\boldsymbol{u}_{i+1}^{k}\right) \boldsymbol{\Delta u}_{i+1}^{k+1} = -\mathscr{R}\left(\boldsymbol{u}_{i}^{k}\right), \tag{1.47}$$

where $\mathscr{R}'$ is the derivative of the residual with respect to the displacement. Once semi-discretised in space, the operator $\mathscr{R}'$ is the Jacobian matrix of the residual matrix and corresponds to the tangent stiffness matrix. The method is graphically illustrated in Figure 1.6. Numerous variants of this algorithm have been developed to reduce its computational cost. Such an approach, called the *modified Newton scheme*, involves treating the stiffness operator as a constant over a specified number of steps. Although this may negatively impact convergence, it enables skipping the computation of the expensive stiffness operator thus decreasing the numerical cost.

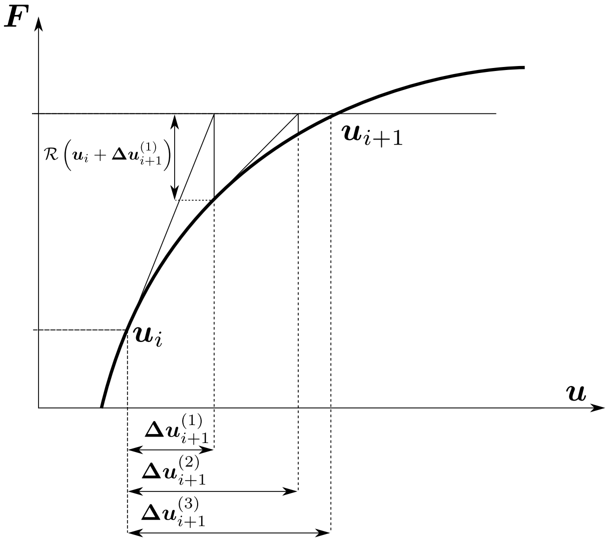
$\boldsymbol{F}$
$\mathcal{R}\left(\boldsymbol{u}_i + \boldsymbol{\Delta u}_{i+1}^{(1)}\right)$
$\boldsymbol{u}_{i+1}$
$\boldsymbol{u}_i$
$\boldsymbol{u}$
$\boldsymbol{\Delta u}_{i+1}^{(1)}$
$\boldsymbol{\Delta u}_{i+1}^{(2)}$
$\boldsymbol{\Delta u}_{i+1}^{(3)}$

Figure 1.6 • Newton-Raphson scheme applied to mechanics

One limitation of these schemes is their inability to handle situations where the overall stiffness of a system reaches zero. In such cases, when a global softening occurs, the method fails to achieve convergence. To solve problems in which such phenomena appear, so called *arc-length* methods can be used.

5.2 Arc-length solvers

The arc-length method is an alternative approach used to solve problems involving situations where the overall stiffness of a system reaches zero, causing a global softening. Its iterative principle is similar to that of Newton's method, as it also relies on an incremental approach and most of the concepts presented in Section 5.1 applies. The main idea is that the increment is no longer a displacement nor a force but a mixed of primal and dual quantities.

In practice, the arc-length method involves considering both displacement increments and a load scaling parameter λ, commonly referred to as the arc-length parameter. This parameter allows for tracking the behaviour of the system as it undergoes softening. By introducing the arc-length parameter, the method effectively bypasses the issue of zero stiffness. Because a new parameter is added, an extra-equation is needed to solve the problem thus introducing the so called *arc-length equation* [Riks, 1979] that takes the form of an *arc-following constraint*

$$g\left(\boldsymbol{u_i}, \lambda_i, \boldsymbol{\Delta u}, \Delta\lambda, \Delta l\right) = 0, \tag{1.48}$$

where Δl is the path length increment and g represents a chosen hypersurface that intersects with the displacement-force cuve. Several arc-length equations have been proposed in the literature, thus introducing different variations of the arc-length method. The most common schemes are Riks [Riks, 1979] Crisfield [Crisfield, 1981; 1983] and Ramm [Ramm, 1981]. A more recent approach suggests using the energy to drive the computations [Gutiérrez, 2004].

The spherical Riks method is illustrated in Figure 1.7 derived from [Crisfield, 1983]. This figure shows the method in the case where the hypersurface g is chosen to be an hypersphere. Note that arc-length increment does not have a physical signification on the contrary of displacement or force increment when discretising the load in the Newton's algorithm.

5.3 Non-incremental solvers

In addition to the previously mentioned incremental methods, there also exist non-incremental non-linear solvers. In such cases, the iterative convergence process occurs over complete space-time solutions. At each iteration, a solution over the entire space-time is computed. The difference between incremental and non-incremental solvers is illustrated in Figure 1.8. These so-called non-incremental schemes are so called because they lead to the manipulation of spatio-temporal fields at each iteration, unlike incremental schemes which build the solution time step by time step. However, this does not prevent time-based partial differential equations from being solved after a temporal discretisation of the problem.

The LATIN method is a non-incremental solver which makes it particularly well suited to *a priori* model-order reduction methods that will be latter presented. The core idea of

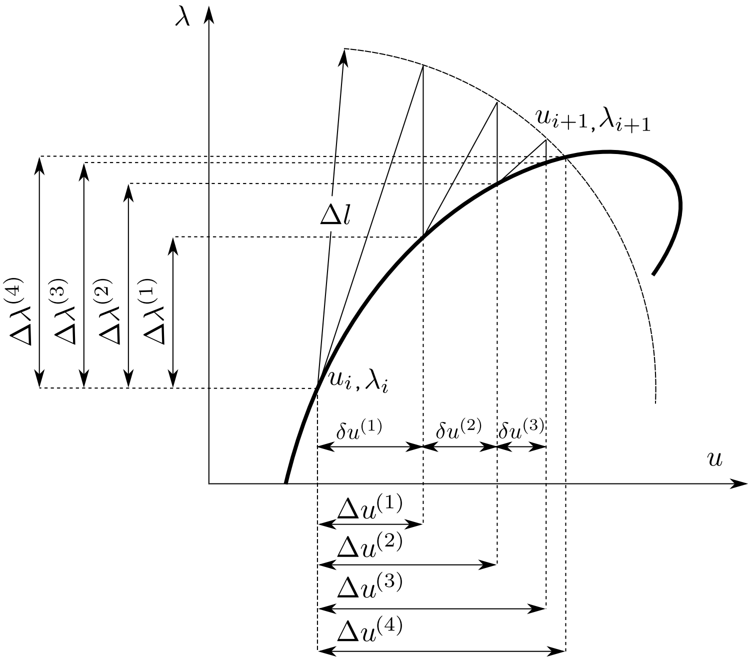
λ
u_{i+1}, λ_{i+1}
Δl
$\Delta\lambda^{(4)}$
$\Delta\lambda^{(3)}$
$\Delta\lambda^{(2)}$
$\Delta\lambda^{(1)}$
u_i, λ_i
$\delta u^{(1)}$
$\delta u^{(2)}$
$\delta u^{(3)}$
u
$\Delta u^{(1)}$
$\Delta u^{(2)}$
$\Delta u^{(3)}$
$\Delta u^{(4)}$

Figure 1.7 • Spherical Riks method, reproduced from [Crisfield, 1983].

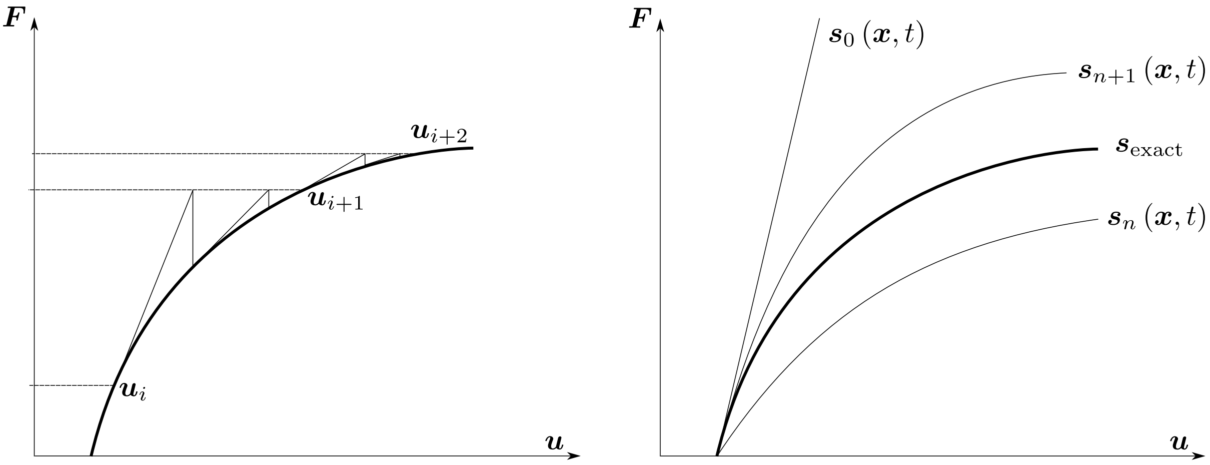
$\boldsymbol{F}$
$\boldsymbol{u}_{i+2}$
$\boldsymbol{u}_{i+1}$
$\boldsymbol{u}_i$
$\boldsymbol{u}$
$\boldsymbol{F}$
$\boldsymbol{s}_0\left(\boldsymbol{x}, t\right)$
$\boldsymbol{s}_{n+1}\left(\boldsymbol{x}, t\right)$
$\boldsymbol{s}_{\text{exact}}$
$\boldsymbol{s}_n\left(\boldsymbol{x}, t\right)$
$\boldsymbol{u}$

(a) Incremental method

(b) Non-incremental method

Figure 1.8 • Comparison between incremental and non-incremental schemes the method is to separate the local equations (which may be non-linear) from the global, linear equations. The solutions of those two sets of equations define the two manifolds Γ and $\mathscr{A}_d$ respectively which are linked by two user-defined search directions $\mathbb{H}^+$ and $\mathbb{H}^-$. The LATIN method therefore falls in the scope of the two-alternated search directions schemes. The exact solution s_{exact} of the problem is both a solution of the local and global equations and therefore lies at the intersection of those two manifolds, $s_{\text{exact}} = \Gamma \cap \mathscr{A}_d$. In practice, the method consists in an iterative process to estimate the solution by alternately considering the local and global aspects as shown in Equation 1.49. A graphical illustration of the method is given in Figure 1.9.

$$s_0 \in \mathscr{A}_d \rightarrow \hat{s}_{1/2} \in \Gamma \rightarrow s_1 \in \mathscr{A}_d \dashrightarrow \underbrace{\overbrace{\hat{s}_{n+1/2} \in \Gamma}^{\text{Local stage}} \rightarrow \overbrace{s_{n+1} \in \mathscr{A}_d}^{\text{Global stage}}}_{\text{Iteration } n+1} \dashrightarrow \dots \tag{1.49}$$

Remark In a sense, arc-length methods are closer to the LATIN method than Newton-Raphson is as the LATIN methods allows a great variablity of search directions therefore does not require the local aspect of the computation to be strain or stress controlled but allows for a mix of both as do arc-length methods. Such a parallel is, for instance, drawn in [Vandoren et al., 2013a].

The LATIN method has been used in a wide range of applications. It has first been developed to tackle non-linear problems, which is the intended application in this work, but its concepts have been extended to several computational methods since then. The LATIN has for instance been used as a domain decomposition methods as a mixed strategy [Ladevèze & Dureisseix, 1999; Champaney et al., 1997; Oumaziz et al., 2017; Ruda et al., 2022]. Using the method in a domain decomposition framework allowed coupling the XFEM methods and multi-scale approaches [Guidault et al., 2007]. As mentioned, besides domain decomposition approaches, the LATIN is used as a powerful non-linear solver that has proven effective for a wide range of highly non-linear problems. It has for instance been used for hyper elasticity problems [Boisse et al., 1990] or large strain with plasticity

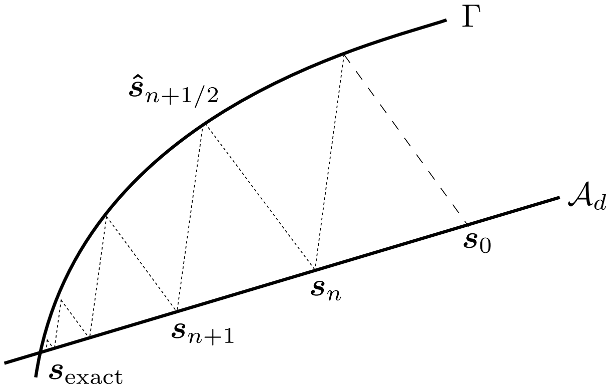

Figure 1.9 • Graphical illustration of the LATIN method reproduced from [Ladevèze, 1999]

[Boucard et al., 1997] as well as for quasi-brittle materials [Vandoren et al., 2013a]. In the context of this thesis, the main advantages of the LATIN scheme are the separation of local and possibly non-linear equations from global but linear equations and its non-incremental aspect. First, separating local and global equations, allows to use different tools for the non-linear local equations and for the linear global equations, which in the context of the thesis are a return mapping algorithm for solving the "local" equations and frequency computations for the global linear equation. Second, the non-incremental aspect of the LATIN solvers combined with the previously mentioned separation of the linear equations allows using reduced-order methods to solve the global equations of a non-linear problem. This has proven advantageous in numerous non-linear cases such as viscoplastic cases [Relun et al., 2015], fatigue computations [Bhattacharyya et al., 2018b], and strongly coupled problems [Néron & Dureisseix, 2008]. Third, the non-incremental aspect of the LATIN allow a wise initialisation of the iterative process, thus decreasing the numerical cost of simulations [Boucard & Champaney, 2003; Néron et al., 2015]. This last aspect also allows access to multi-fidelity solutions. Indeed, stopping the iterative process still gives a whole space-time solution for a coarser convergence criterion [Nachar et al., 2020] thus giving access to low fidelity solution in cases where the required precision for the solution is low.

Remark The LATIN method leads to an algorithm that gives access at each iteration to a spatio-temporal approximation of the solution. In this respect, it is often described as a "non-incremental" method. This non-incremental nature of the LATIN method can be perceived as a drawback in certain cases. While it is highly convenient to have access to a semi-converged spatio-temporal solution at each iteration of the method in certain cases, such as for optimisation purposes, it can also be detrimental not to incrementally solve the numerical problem. In a scenario where the structure would reach failure within the studied time interval, an incremental method would allow for a converged solution until the structure's failure and then stop the computation. In a similar scenario, the LATIN method would fail to provide a solution.

Chapter summary

The mechanical problem of interest consists in solving two types of equations. On the one hand it consists in dynamics equations that are linear but global in the sense that they couple all the spatial degrees of freedom of the studied structure. Those equations can be solved with several time integration schemes. In the reminder of the thesis, a frequency solver is used. On the other hand, the solution to the whole problem must also satisfy the non-linear behaviour. Besides the global dynamics equation, the set of local, possibly non-linear equations characterising the behaviour of the material must, therefore, also be solved. However, these equations are local and can, therefore, be solved independently on each Gauss point of the structure. The non-linear model describes the plasticity and damage evolution of the structure, taking into account the crack-closure effect. The numerical treatment of the non-linear aspect of the problem has also been described. Several non-linear solvers allow the computation of solutions to those non-linear mechanical problems. A strength of the non-incremental LATIN method is its ability to encompass an *a priori* reduced-order model method natively. Such methods require global equations over the space-time domain, which is exactly the general framework offered by the LATIN method.

* * *

Perspectives

The previously described numerical model allows a physically detailed description of the material evolution during loading. However, it results in a strongly non-linear problem with a large number of degrees of freedom as it relies on a fine description of the structural behaviour. It has been shown in [Bhattacharyya et al., 2018a] that in a quasi-static context the LATIN-PGD method allows to finely describe the response of a damageable structure with few PGD modes. The great reducibility of such problems in quasi-statics has motivated the investigation of their usage in a low-frequency dynamics context. The use of such methods requires the linearisation of the non-linearities; the LATIN-PGD method has proven to be an efficient way to decouple the non-linear behaviour from the linear admissibility equations [Ladevèze, 1999; Néron & Ladevèze, 2010a], allowing the usage of reduced-order methods on the latter. Such decoupling also gives a high degree of modularity to the method that is exploited in chapter 3.

Chapter 2

Model order reduction and multi-query approaches for non-linear mechanics

> Science is what we have learned about
> how to keep from fooling ourselves.
>
> Richard Feynman

The use of reduced-order model techniques is one possible way of reducing the prohibitive cost of non-linear studies. This chapter provides an overview of key reduced-order modelling techniques and the efficiency of the Proper Generalised Decomposition is exemplified on a data compression example. Additionally, typical treatments of multi-query problems are presented, highlighting the LATIN solver's potential in this context.

Contents

1 Model-order reduction methods . . . 34
  1.1 Craig-Bampton method . . . 36
  1.2 Modes superposition . . . 36
  1.3 Proper Orthogonal Decomposition (POD) . . . 37
  1.4 Reduced-basis method . . . 39
  1.5 Proper Generalised Decomposition (PGD) . . . 40
2 Multi-query context . . . 43
  2.1 Surrogate models . . . 43
  2.2 Enhanced multi-query solvers . . . 44
✒ Chapter summary & perspectives . . . 46

The main drawback of a detailed non-linear description is that it raises the need for a fine spatial and temporal discretisation, leading to a large number of degrees of freedom, whereas the computation cost of these calculations needs to be relatively low to make non-linear studies feasible. Thus, solving a non-linear dynamics problem requires the use of an efficient solver that can handle both the dynamics and the non-linear aspects for a modest calculation cost. Moreover, in the context of risk assessment, multiple non-linear computations are required. The solver must, therefore, be efficient and multi-query friendly. The combined use of reduced-order modelling and non-linear solver can help decrease the cost of the non-linear simulations while providing a solution that takes into account complex material behaviour.

1 Model-order reduction methods

In order to decrease the computational costs associated with the search for discretised mechanical fields, model-order reduction methods rely on the separated-variable representation of the quantities of interest. In particular, the displacement field $\boldsymbol{u}\left(\boldsymbol{x}, t\right)$, can be expressed as

$$\boldsymbol{u}\left(\boldsymbol{x}, t\right) = \sum_{i=1}^{\infty} \Lambda_i\left(\boldsymbol{x}\right) \otimes \lambda_i\left(t\right), \tag{2.1}$$

where $\otimes$ denotes the tensor product. In cases where the Kolmogorov width of the field to be reduced is small, the above equation can be approximated with a small number m of pairs. In this scenario, the rank-m approximation $\boldsymbol{u}_m$ of the displacement field reads

$$\boldsymbol{u}\left(\boldsymbol{x}, t\right) \approx \boldsymbol{u}_m\left(\boldsymbol{x}, t\right) = \sum_{i=1}^{m} \Lambda_i\left(\boldsymbol{x}\right) \otimes \lambda_i\left(t\right). \tag{2.2}$$

In the structural dynamics context, after discretising the problem using a Galerkin approximation, which already transforms the solution from being sought in an infinite space to being sought in a spatial space of finite dimension N, the objective is to further reduce the dimension of the space in which the solution is sought.

Remark The Galerkin approximation used when using the finite element method already leads to a separated-variable representation of the displacement field. A temporal function is associated to each shape functions which, in fact, are very local spatial modes. Reducing the dimensionality of the discretised problem can be seen as replacing the very local modes associated with each node, i.e. the finite element shape functions, with more global modes constituting the reduced-order basis.

After discretisation of the problem, the essence of reduced-order modelling is to seek the solution within a smaller subset $\mathbb{R}^{m\times N_t} \subset \mathbb{R}^{N\times N_t}$, where $m \ll N$. The goal is not to simplify the model itself, but rather to reduce the dimensionality m of the subspace in which the solution is sought.

Let $\{\Lambda_k\}_{k\in[\![1,N]\!]}$ and $\{\Lambda_k\}_{k\in[\![1,m]\!]}$ be two bases of $\mathbb{R}^N$ and $\mathbb{R}^m$ respectively. In the context of a time-space displacement field for instance, the idea is to approximate a solution $\{U\}$ such that

$$\{U\} = \sum_{i=1}^{N} \{\Lambda_i\}\{\lambda_i\}^T \approx \sum_{i=1}^{m} \{\Lambda_i\}\{\lambda_i\}^T, \tag{2.3}$$

thus relying on the space-time separability of the displacement field ensured by a thin *Kolmogorov width* d_m defined as

$$d_m = \inf_{\mathbb{R}^{m\times N_t}\subset\mathbb{R}^{N\times N_t}} \left[\sup_{\{U\}\in\mathbb{U}^N} \left(\inf_{\{U_m\}\in\mathbb{R}^{m\times N_t}} \left\| \{U\} - \{U_m\} \right\| \right) \right], \tag{2.4}$$

where $\mathbb{U}^N$, defined in Equation 1.23, is a restriction of $\mathbb{R}^{N\times N_t}$ to the discrete displacement fields that satisfy the dynamics equation.

Remark A visual representation of the compression benefits offered by the separation of variables is showcased on a discrete two-dimensional field. The information content reduces from $N \times N_t$ to $m \times (N + N_t)$, a significantly smaller amount as long as m remains small.

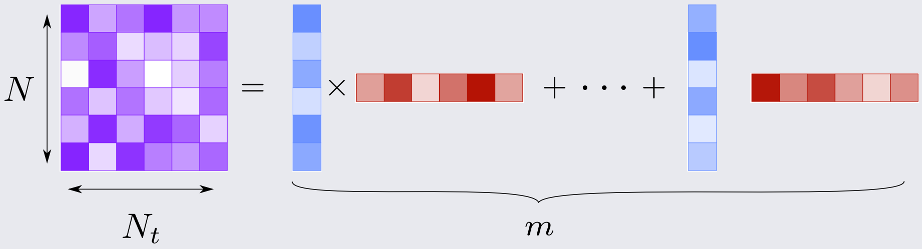

Under a discretised form, the m-th order reduced approximation $\{U_m\}$ of the displacement $\{U\}$ reads

$$\{U\} = [\Pi]\{U_m\}, \tag{2.5}$$

with $[\Pi]$ a projection matrix on subspace of dimension m. $[\Pi]$ is a $N \times m$ matrix whose columns are span the subspace in which the reduced solution is searched for. Once this operator is chosen, *i.e.* once the reduced-basis is chosen, the equation of motion can be projected onto the subspace as

$$[M_m]\left\{\ddot{U}_m\right\} + [D_m]\left\{\dot{U}_m\right\} + [K_m]\{U_m\} = \{F_m\}, \tag{2.6}$$

where

$$\begin{cases} [M_m] = [\Pi]^T [M] [\Pi], \\ [D_m] = [\Pi]^T [D] [\Pi], \\ [K_m] = [\Pi]^T [K] [\Pi], \\ \{F_m\} = [\Pi]^T [F], \end{cases} \tag{2.7}$$

thus decreasing the numerical cost associated to the computation of its solution.

A major difficulty consists of finding a suitable reduced-order basis for the problem of interest, *i.e.* finding the best subspace $\mathbb{R}^{m\times N_t}$ so that corresponding to the Kolmogorov width defined in 2.4. Various methods of reduced-order modelling exist, each leading to different approaches for obtaining a reduced-order basis. This section aims to present the primary methods employed in computational mechanics to obtain such a reduced-order basis.

1.1 Craig-Bampton method

In the case of the Craig-Bampton (CB) method [Craig & Bampton, 1968], the idea is to reduce part of the internal degrees of freedom of the structure on interfaces. In practice, the Craig-Bamptom method classifies degrees of freedom into two categories: boundaries degrees of freedom $_B$ and internal degrees of freedom $_I$ of the subsystems. The stiffness matrix can therefore be decomposed as four sub-matrices as

$$[K] = \begin{bmatrix} [K_{II}] & [K_{IB}] \\ [K_{BI}] & [K_{BB}] \end{bmatrix}, \tag{2.8}$$

where the submatrices $[K_{II}]$ and $[K_{BB}]$ represent the stiffness of the internal subsystems and of the boundary respectively. The matrices $[K_{IB}]$ and $[K_{BI}]$ couple interface and internal degrees of freedom. The projection matrix $[\Pi]$ then reads

$$[\Pi] = \begin{bmatrix} [1] & [0] \\ -[K_{II}]^{-1}[K_{IB}] & [\Lambda] \end{bmatrix}, \tag{2.9}$$

with $[\Lambda]$ the truncated vibration modes matrix where only a limited number of vibration modes $\{\Lambda\}_i$ are retained. The number of vibration modes required can, for instance, be chosen based on *a posteriori* error estimation [Jakobsson et al., 2011].

In practical terms, the reduced basis is therefore made up of all the static modes on the boundaries that ensure the admissibility of the displacement field, and a truncation of the clamped structure's vibration modes. Those vibration modes are obtained by solving the the eigenproblem of the substructure

$$\left[[K_{II}] - \omega^2 [M_{II}]\right]\{\Lambda\} = \{0\}. \tag{2.10}$$

Several variations of the CB method exist. In particular the dual Craig-Bampton approach [Rixen, 2004] assembles the substructures using interface forces instead of displacement continuity.

1.2 Modes superposition

The eignevectors of the structure can also be used in a more direct manner without substructuring the structure. The modal projection method [Hansteen & Bell, 1979; Avitabile, 2003], is a model reduction technique where the modal basis of the structure directly serves as the reduced basis. The eigenfrequencies ω_i and the eigenmodes $\{\Lambda_i\}$ of the structure are the solution of

$$\left[[K]-\omega^2[M]\right]\{\Lambda\}=\{0\}. \tag{2.11}$$

In practice, only few eigenvectors are kept to describe the solution of the dynamics problem. The aforementioned reduction matrix $[\Pi]$ is therefore composed of the m first eigenvectors of the previous problem.

> **Remark** In scenarios involving non-linear behaviour leading to small localised variations in the displacement field, the inclusion of very short wavelength modes becomes essential to address these localised effects. Capturing those modes requires computing high-frequency-associated modes, despite the loading resulting in a low-frequency response.

In order to avoid solving an eigenvalue problem to find the eigenmodes of the structure, the latter can instead be approximated by Ritz-vectors [Idelsohn & Cardona, 1985; AL-Shudeifat & Butcher, 2010]. The eigenvalue problem can also be solved on the reduced domain given by the Craig-Bampton method to decrease the associated computational cost.

> **Remark** The described methods so far are solely based on the knowledge of the structure but do not account for the specificities of the loading applied to it. Taking into account knowledge from the loading to which the structure is subjected can help better choose the reduced-basis that best describe the solution and may help decreasing the number of modes needed.

The reduced-order basis on which the solution is sought after can also be composed of modes other than the Linear Normal Modes (LNM).

The Proper Orthogonal Decomposition (POD) has also been used in a dynamics context [Eftekhar Azam & Mariani, 2013] where some authors showed better approximation results than LNM superposition [Radermacher & Reese, 2013].

1.3 Proper Orthogonal Decomposition (POD)

The Proper Orthogonal Decomposition (POD), also known as Principal Component Analysis (PCA), is a model-order reduction technique used in an *a posteriori* manner. It involves computing POD modes from previously obtained solution fields called snapshots. The POD modes form the reduced basis. The snapshots are typically generated in an *off-line* stage through a small number n of simulations that produce solutions close to the desired reduced solutions. Once the POD basis is constructed from these snapshots, following computations can be performed *online* with a significantly reduced numerical cost, using the POD reduced basis.

This section focuses on the method employed to compute the POD basis from a collection of snapshots. The objective is to find a reduced basis $\{\Lambda_k\}_{k\in[\![1,m]\!]}$ of dimension m that best represents the snapshots $\{\boldsymbol{u}^i\}_{i\in[\![1,n]\!]}\mathbb{R}^{d\times n}$ with $d \in \{1,2,3\}$ depending on the dimension of the problem. This objective is translated into solving the minimisation problem

$$\left\{\{\Lambda_k\}\right\}_{k\in[\![1,m]\!]} = \underset{\substack{\left\{\{\Lambda_k\}\right\}_{k\in[\![1,m]\!]} \in \mathbb{R}^{N\times m} \\ \left(\{\Lambda_k\},\{\Lambda_j\}\right) = \delta_k^j}}{\text{argmin}} \left[\underbrace{\sum_{i=1}^{n} \| u^i - \sum_{j=1}^{m}\left(u^i,\{\Lambda_j\}\right)\{\Lambda_j\}\|^2}_{J\left(\left\{\{\Lambda_k\}\right\}_{k\in[\![1,m]\!]}\right)}\right]. \tag{2.12}$$

Remark As that the cost function also reads

$$J\left(\left\{\{\Lambda_k\}\right\}_{k\in[\![1,m]\!]}\right) = \sum_{i=1}^{n} \| u^i \|^2 - \sum_{i=1}^{n}\sum_{k=1}^{m}\left(u^i,\{\Lambda_k\}\right)^2, \tag{2.13}$$

the minimisation problem reverts to maximisation problem. On a discretised problem, and for the scalar product associated to the $\mathscr{L}_2$ norm, the latter reads

$$\left\{\{\Lambda_k\}\right\}_{k\in[\![1,m]\!]} = \underset{\substack{\left\{\{\Lambda_k\}\right\}_{k\in[\![1,m]\!]} \in \mathbb{R}^{N\times m} \\ \left(\{\Lambda_k\},\{\Lambda_j\}\right) = \delta_k^j}}{\text{argmax}} \left[\sum_{i=1}^{n}\sum_{k=1}^{m}\left(\left\{U^i\right\}^T\{\Lambda_k\}\right)^T\left(\left\{U^i\right\}^T\{\Lambda_k\}\right)\right], \tag{2.14}$$

Introducing the snapshot matrix $[X] = \text{Col}\left(\left\{U^i\right\}\right)$ and its auto-correlation matrix $[S] = [X]^T[X]$, the problem becomes

$$\left\{\{\Lambda_k\}\right\}_{k\in[\![1,m]\!]} = \underset{\substack{\left\{\{\Lambda_k\}\right\}_{k\in[\![1,m]\!]} \in \mathbb{R}^{N\times m} \\ \left(\{\Lambda_k\},\{\Lambda_j\}\right) = \delta_k^j}}{\text{argmax}} \left[\sum_{k=1}^{m}\{\Lambda_k\}^T[S]\{\Lambda_k\}\right]. \tag{2.15}$$

Solving that leads to finding the stationarity of the Rayleigh quotient associated with the auto-correlation matrix $[S]$. A discrete version of the POD thus closely relates to the Singular Values Decomposition (SVD) [C. Wu et al., 2003]. With the introduced notations, seeking for the eigenvalues of the correlation matrix $[S]$ is the same as seeking for the singular values of the data matrix $[X]$.

The described POD method enables significant data size reduction and leads to a reduced-order basis on which a costly numerical problem can be projected to decrease its dimensionality. However, the quality of this basis is closely linked to the chosen snapshots. For example, in a spatio-temporal problem, if all snapshots come from a stationary part of the evolution, the basis may poorly represent the transitional regime. Additionally, the *a posteriori* aspect of the method implies that it relies on prior possibly costly computations. The obtention of the reduced-basis might therefore be very costly while not being well suited to the study of the current problem.

1.4 Reduced-basis method

Like the POD method, the Reduced-Basis (RB) method [Maday & Rønquist, 2002] is a technique that aims at building a reduced-order basis onto which the problem is then projected to reduce its dimensionality. The RB method, however, offers a robust strategy for the selection of snapshot thus overcoming a major drawback of the POD method. In case of an equation parametrised by a vector $\mu \in \mathscr{D}$, selecting suitable snapshots amounts to choosing a finite number of samples $\{\mu_i\}_{i\in[\![1,n]\!]} \in \mathscr{D}^n$.

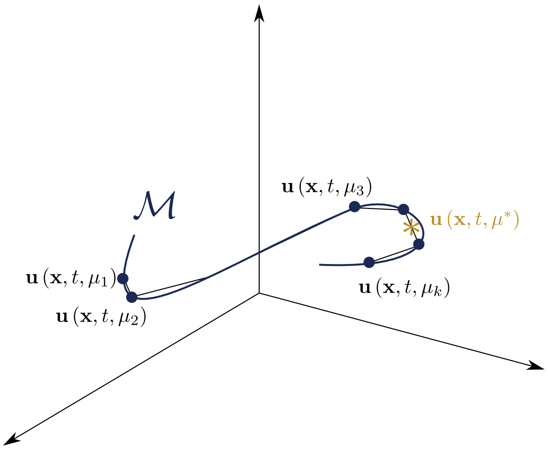
$\mathcal{M}$
$\mathbf{u}(\mathbf{x},t,\mu_3)$
$\mathbf{u}(\mathbf{x},t,\mu^*)$
$\mathbf{u}(\mathbf{x},t,\mu_1)$
$\mathbf{u}(\mathbf{x},t,\mu_k)$
$\mathbf{u}(\mathbf{x},t,\mu_2)$

Figure 2.1 • Parametric manifold $\mathscr{M}$ and approximation of the solution associated to the parameter μ^*. Reproduced from [Rozza, 2014]

The RB method progressively enriches the reduced basis by incrementally selecting snapshots, *i.e.* new samples μ_i, that maximise the quality of the solution. The greedy algorithm building the reduced-order basis consists in identifying the snapshot with the largest projection error Ξ onto the current reduced basis and adding the corresponding missing information by enlarging the reduced basis to better represent the solution. Once an $m-$rank reduced basis has been built relying on k snapshots $\left\{\boldsymbol{u}^{(i)}\right\}_{i\in[\![1,k]\!]}$, the $k+1$-th snapshot $\boldsymbol{u}^{(k+1)} = \boldsymbol{u}\left(\boldsymbol{x}, t, \mu_{k+1}\right)$ is selected by finding the parameters maximising the projection error, *i.e.*

$$\mu_{k+1} = \arg\max_{\mu_{k+1}\in\mathscr{D}} \underbrace{\left\| \boldsymbol{u}^{(k+1)} - \boldsymbol{u}_m^{(k+1)} \right\|}_{\Xi}, \tag{2.16}$$

with $\boldsymbol{u}_m^{(k+1)}$ the $k+1$-th snapshot's projection onto the current reduced basis. Since the solution $\boldsymbol{u}^{(k+1)}$ for the new snapshot is unknown prior to computation, this projection error remains dependent on the selection of an error estimator. Suitable error estimators must be used to avoid the high cost of browsing the whole parametric space [Prud'homme et al., 2001; Rozza et al., 2008].

Once the quality of the reduced-order basis is considered sufficient, the *online* phase during which the smaller-dimension projected problem is solver is similar to what is achieved using the POD. The solution of the problem for any new $\mu^* \in \mathscr{D}$ is then computed as a combination of the previous snapshots. A graphical representation of the manifold

$$\mathscr{M} \triangleq \left\{ \boldsymbol{u}\left(\boldsymbol{x}, t, \mu\right) | \boldsymbol{x} \in \Omega,\ t \in I,\ \mu \in \mathscr{D} \right\} \tag{2.17}$$

and of the approximation of $\boldsymbol{u}\left(\boldsymbol{x}, t, \mu^*\right)$ is given in Figure 2.1.

The RB method still relies on previous full computation in order to build the reduced-order basis and is designed for problems involving explicit dependence on the parameters.

1.5 Proper Generalised Decomposition (PGD)

To avoid the drawbacks of prior (possibly costly) computations of an *offline* phase, dedicated modes can be calculated on the fly thanks to *a priori* methods, therefore optimising the number of modes computed to get a solution. The Proper Generalised Decomposition (PGD), initially referred to as the *approximation radiale* by [Ladevèze, 1985], is distinct from the Proper Orthogonal Decomposition (POD) in that it is an *a priori* method. Unlike the POD, which derives the reduced-order basis from existing snapshots, the PGD involves directly computing the different modes that comprise the reduced-order basis using a greedy algorithm for instance. This greedy algorithm iteratively adds modes that best capture the desired solution until the appropriate level of approximation is achieved. Such *a priori* methods have already shown interesting results when applied to dynamics problems. For example a space-time PGD [Néron & Ladevèze, 2010a; Chinesta et al., 2011] was successfully applied to transient problems [Ammar et al., 2007] and space-time dynamics [Boucinha et al., 2013; Boucinha et al., 2014]. Reduced-order modelling methods generally require linear equations but the PGD, along side non-linear solvers, has already been applied to dynamics in a frequency context for non-linear elastic applications [Quaranta et al., 2019] and non-linear contact forces [Germoso et al., 2016]. A linearisation process can also rely on a static-dynamic hybrid scheme for updating non-linear geometrical forces under a static assumption while applying those forces in a dynamics framework [Yang et al., 2019].

In addition to remove the burden associated with obtaining snapshots, the PGD offers the advantage of providing a low-order approximation with a specified error level, without requiring prior knowledge of the number of modes needed to achieve that error. This specific feature sets the PGD apart from *a posteriori* methods, where the number of modes necessary to attain a certain level of accuracy must be estimated in advance. In contrast, the PGD's greedy algorithm dynamically determines the number of modes required to meet the desired error tolerance during the approximation process.

In addition to being used directly to solve equations, PGD can, like POD, be used to compress data. While the application of PGD for solving partial differential equations will be explored in detail in Chapter 3, this section will concentrate on illustrating the fundamental principles of the PGD method specifically for data compression applied to a bi-parametric function $\boldsymbol{f}\left(\boldsymbol{x}, \boldsymbol{y}\right)$ defined as

$$
\begin{aligned}
\boldsymbol{f} \colon \Omega_x \times \Omega_y &\longrightarrow \mathbb{R} \\
(\boldsymbol{x}, \boldsymbol{y}) &\longmapsto \boldsymbol{f}(\boldsymbol{x}, \boldsymbol{y}) .
\end{aligned}
\tag{2.18}
$$

The aim is to find the families $\{\Lambda_i\}_{i \in [|1,m|]}$ and $\{\lambda_i\}_{i \in [|1,m|]}$ so that the m-order approximation $\boldsymbol{f}_m$ of $\boldsymbol{f}$ reads

$$
\boldsymbol{f}_m = \sum_{i=1}^{m} \Lambda_i(\boldsymbol{x}) \lambda_i(\boldsymbol{y}). \tag{2.19}
$$

The approximation $\boldsymbol{f}_m$ is computed so that

$$
\boldsymbol{f}_m(\boldsymbol{x}, \boldsymbol{y}) = \underset{\boldsymbol{\Lambda}_i, \lambda_i}{\arg\min} \left[\int\limits_{\Omega_x \times \Omega_y} \left(\boldsymbol{f}(\boldsymbol{x}, \boldsymbol{y}) - \sum_{i=1}^{m} \boldsymbol{\Lambda}_i(\boldsymbol{x}) \lambda_i(\boldsymbol{y}) \right)^2 \mathrm{d}\boldsymbol{x} \mathrm{d}\boldsymbol{y} \right] . \tag{2.20}
$$

When adding the k-th mode, the minimisation presented in 2.20 leads to finding Λ_k and λ_k such that

$$
\int\limits_{\Omega_x \times \Omega_y} \left(\delta \boldsymbol{f} - \lambda_k \Lambda_k \right) \left(\lambda^* \Lambda_k + \lambda_k \Lambda^* \right) \mathrm{d}\boldsymbol{x} \mathrm{d}\boldsymbol{y} = 0, \ \forall \left(\lambda^*, \Lambda^* \right) \in \mathscr{I} \times \mathscr{V}, \tag{2.21}
$$

where $\delta \boldsymbol{f} = \boldsymbol{f} - \boldsymbol{f}_{k-1}$ and with $\mathscr{I} = \mathscr{L}^2 \left(\Omega_y \right)$ and $\mathscr{V} = \mathscr{L}^2 \left(\Omega_x \right)$. Equation 2.21 stands $\forall \left(\lambda^*, \Lambda^* \right) \in \mathscr{I} \times \mathscr{V}$. Getting the PGD pair $\left(\Lambda_k, \lambda_k \right)$ thus results in solving the following two-equation system

$$
\left\{
\begin{aligned}
&\int_{\Omega_x} \left(\delta \boldsymbol{f} - \lambda_k \Lambda_k \right) \Lambda_k \mathrm{d}\boldsymbol{x} = 0, \\
&\int_{\Omega_y} \left(\delta \boldsymbol{f} - \lambda_k \Lambda_k \right) \lambda_k \mathrm{d}\boldsymbol{y} = 0.
\end{aligned}
\right.
\quad \Leftrightarrow \quad
\left\{
\begin{aligned}
\lambda_k &= \left(\int_{\Omega_x} \delta \boldsymbol{f} \Lambda_k \mathrm{d}\boldsymbol{x} \right) \left(\int_{\Omega_x} \Lambda_k^2 \mathrm{d}\boldsymbol{x} \right)^{-1}, \\
\Lambda_k &= \left(\int_{\Omega_y} \delta \boldsymbol{f} \lambda_k \mathrm{d}\boldsymbol{y} \right) \left(\int_{\Omega_y} \lambda_k^2 \mathrm{d}\boldsymbol{y} \right)^{-1}.
\end{aligned}
\right.
\tag{2.22}
$$

In practice, norming Λ_k or λ_k insures the uniqueness of the solution. The previous system is solved using a fixed-point algorithm alternating between solving one equation of the system and the other.

Remark The reason why a non-incremental scheme is required to use the PGD comes from the need to integrate over the whole domain at each iterations. With an incremental solver, the solution is only known on the whole domain at the end of the iterative process, rendering the computation of those integrals impossible.

The function $\boldsymbol{f}$ can for instance be a surface or an image made of pixels. To get a quantifiable idea of how much data can be compressed using such a decomposition, the previously described algorithm has been implemented on an image (see Figure 2.2) and the results are shown in the following graphs and figures.

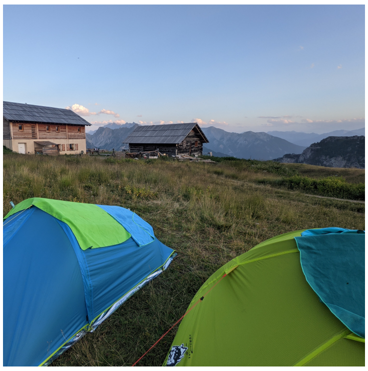

Figure 2.2 • Uncompressed image - Furfande, GR 58

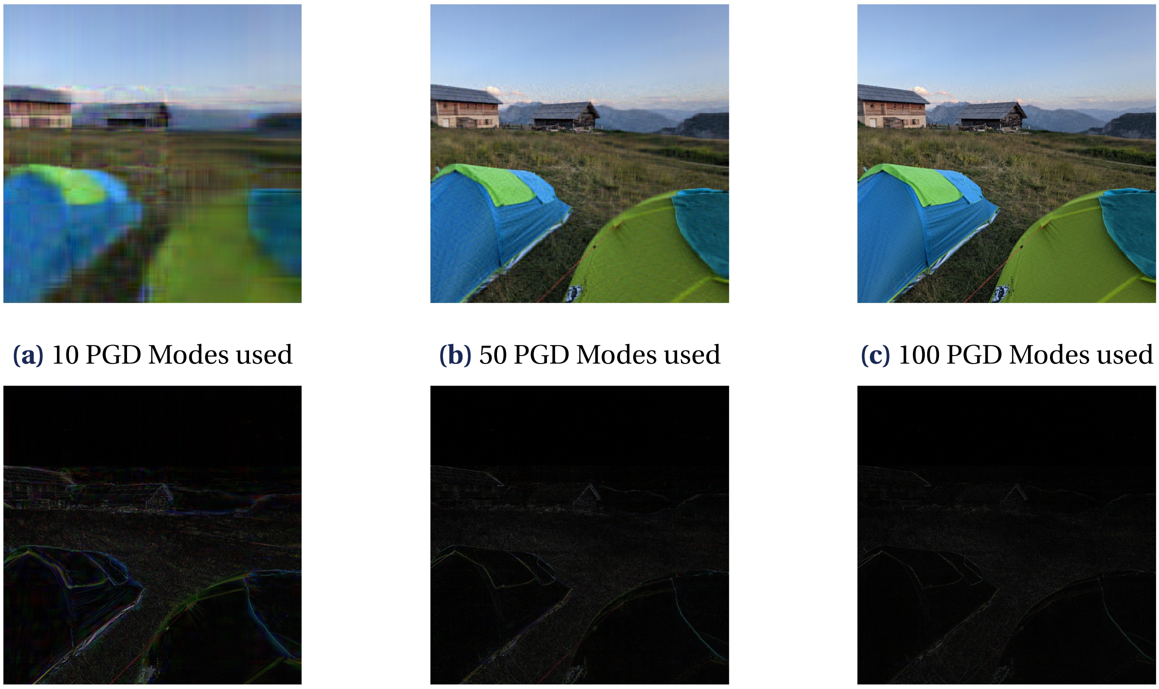

(a) 10 PGD Modes used

(b) 50 PGD Modes used

(c) 100 PGD Modes used

(d) Error with 10 PGD Modes

(e) Error with 50 PGD Modes

(f) Error with 100 PGD Modes

Figure 2.3 • Compressed images and their respective errors

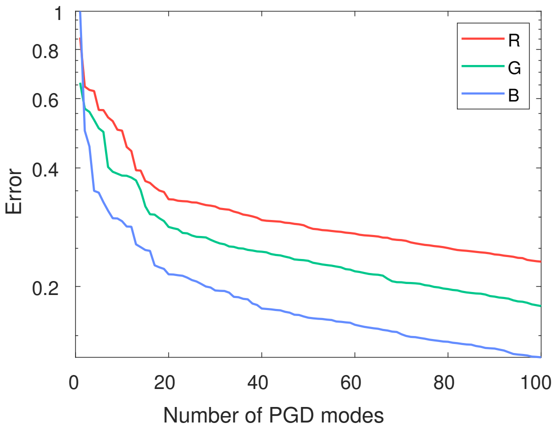

Figure 2.4 • Error function of the number of PGD modes for each colour canal

In that example, the picture described using 100 modes in Figure 2.3f is still 93 % lighter to store than the original picture. The data reduction applied to a function f that is expensive to store has thus been illustrated. Such computations do also lead to having a reduced basis just as the POD did which could also be used for future other computations. The PGD shows similar numerical cost-reduction results in the context of partial differential equation solving that will be presented in Chapter 3.

2 Multi-query context

In a multi-query context where a solver is called numerous times, having an efficient solver relying on reduced-order model helps decreasing the high computational cost but other levers exist to further decrease the numerical burden associated with such study. The number of calls required for the study can for instance be decreased. In some cases the number of calls to the solver is fixed. In those cases, an efficient multi-query framework can still lead to significant decrease of then numerical cost of the study.

2.1 Surrogate models

In a parametric context, surrogate models give an approximation of a given quantity of interest (QoI) based on a finite sample of possibly costly solutions constituting the *training set*. Knowing the input parameter of the problem the surrogate model provides a mapping to the quantity of interest. Once the surrogate model has been built, it allows predicting the value of the quantity of interest for a new set of parameters that is not part of the training set without the need to call the solver. Evaluation of the response of the structure regarding a given QoI therefore becomes very cheap as it only requires reading the value out of the surrogate model.

Based on a training set of observations $\left\{(\boldsymbol{\theta_i}, D_i) \in \Theta \times \mathbb{R}\right\}_{i\in[\![1,n]\!]}$, where $\boldsymbol{\theta}_i$ are input parameters and D_i the maximum damage of the structure for those parameters, and using a

Gaussian process regression (GPR) for instance [Hensman et al., 2010; Deringer et al., 2021], the maximum damage D of a structure as a function of new parameter set $\boldsymbol{\theta} \in \Theta$ can be interpolated as

$$D\left(\boldsymbol{\theta}\right) = \sum_{i=1}^{n} \omega_i k\left(\boldsymbol{\theta}, \boldsymbol{\theta_i}\right) \forall\, \boldsymbol{\theta} \in \Theta, \tag{2.23}$$

where k is a kernel function and $\{\omega_i\}_{i \in [\![1,n]\!]}$ are the weights associated with each previous observation in the training data set. Those coefficients are found by minimising a loss function penalising the distance of estimation of known points with their real value. Such minimisation leads to

$$\{\omega\} = \left(\left[C\right] + \left[\Sigma\right]\right)^{-1} \left\{D\right\}, \tag{2.24}$$

where $\{\omega\}$ and $\left\{D\right\}$ are the vectors whose coefficients are the weights and the values of damage for the known data points. The matrix $\left[\Sigma\right]$ is a diagonal matrix that allows to tune the strength of the fitting of the estimation to the known data points. The covariance matrix $\left[C\right]$ reads

$$\left[C\right]_{i,j} = k(\boldsymbol{\theta_i}, \boldsymbol{\theta_j}). \tag{2.25}$$

Based on this interpolation method, new data points can be gradually added to the training dataset until the standard deviation over the expected input parameter range becomes acceptable. The rules governing the addition of new points can be tailored for specific applications, such as classification. For example, employing the kriging algorithm for classifying between failure and non-failure can achieve high precision when sampling rules are carefully designed accordingly [Fuhg & Fau, 2022]. The surrogate model enables the creation of a virtual chart where the quantity of interest can be estimated inexpensively once the training set is sufficiently rich, although its initial creation requires costly numerical computations as each entry in the training dataset represents a call to the non-linear solver. To further reduce the cost of the parametric study, some points can be computed using a coarse solver stopping criterion, resulting in low fidelity points. By combining the multi-fidelity aspect provided by the non-incremental nature of LATIN and kriging, significant numerical advantages can be achieved [Nachar et al., 2020]. Those surrogate models however require the entries of the problem to be easily parametrised and would not work to account for uncertainty of indexed time series.

2.2 Enhanced multi-query solvers

One of the main advantages of the LATIN method in a multi-query context is its non-incremental nature. This key element incurs that the numerical scheme is initialised using a space-time solution. This solution is usually taken to be the elastic solution associated with a non-linear problem but in the case of multiple calls to the solver, the initial solution can be chosen as a previous non-linear solution that is guessed to be close to the current computation. Doing so allows to start the iterative process closer to the exact solution of the problem, thus decreasing the number of iterations needed to reach convergence. A wise initialisation of the LATIN scheme has already proven very effective without reduced-order method in the case of contact non-linearities where several dozen calculations were performed for various sets of parameters [Boucard & Champaney, 2003]. As the methodology is very versatile, it has latter been reused for different applications and extended to work favourably paired with the PGD [Néron et al., 2015; Heyberger et al., 2012]. The method has proven effective at decreasing the number of iterations required for thermal and visco-plastic problems where both the previous solution and previous PGD bases were reused. Shared PGD modes are thus only computed once and used through out different computations as shown in [Néron et al., 2015].

It is worth mentioning however that in the existing literature, the variability from one computation to the other lies in the change of behaviour. The different solutions of the multi-query problem therefore share admissibility. Using one whole solution to wisely initialise the LATIN scheme is therefore possible because all solution are points on the same manifold $\mathscr{A}_d$. The idea of wise initialisation is therefore graphically presented in Figure 2.5 where a first computation (j) is performed and its solution is used to initialise a second computation (k) thereby decreasing the number of iterations needed to reach the converged solution.

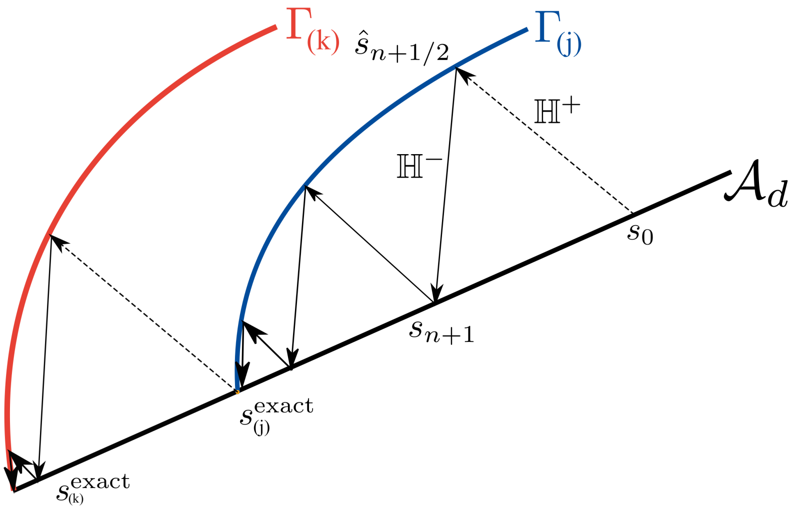

Figure 2.5 • Wise initialisation strategy

Although PGD bases are shared, during the numerous calls to the solver, the number of PGD modes generated can however become quite large. In order to decrease the number of modes needed to represent the solution works have shown that introducing an SVD decomposition instead of a Gram-Schmidt algorithm helps getting an optimal basis of lower-rank [Giacoma et al., 2015; Alameddin et al., 2019].

Chapter summary

Directly solving non-linear problems often incurs a high computational cost. To decrease that numerical cost, model-order reduction techniques can be used. Most of those methods rely on prior costly computations to build a reduced basis on which the problem is then projected. The modal projection method provides insight into the structure's specifics through an eigenvalue computation but overlooks loading and other features. The POD utilises snapshots, *i.e.* full-order model calculations to account for features like loading and non-linear responses. The PGD, on the other hand, offers a method to build a reduced basis on-the-fly during the computation of the solution, eliminating the need for prior computations. The reduced-order basis thus directly incorporates all specific features of the current calculation. The use of such a method, however, requires the solver to be non-incremental. To that aim, the LATIN method offers a compelling choice, allowing the use of the PGD in a non-linear context. The solver also proved very effective in a multi-query context as it allows for a wise initialisation of the non-linear computations based on previous results. Lastly, the LATIN solver also gives access to multi-fidelity solutions which can be used to build precise virtual charts at a lower cost.

* * *

Perspectives

The LATIN scheme can be extended to allow frequency computations in a non-linear context paired with model-order reduction techniques. The reduced-order model hybrid temporal-frequency solver is described in chapter 3. Building on the wise initialisation idea in a multi-query context, a specific framework needs to be built in cases where the variability lies in the loading scenarios. Indeed, with such variabilities, the different solutions no longer share admissibility therefore, they cannot be used directly to initialise the LATIN iterative scheme. Such a framework is presented in chapter 4. Lastly, when building virtual charts for failure assessment, the multi-fidelity aspect offered by the LATIN can be utilised to further decrease the numerical cost of the risk study. This aspect is presented in chapter 5.

Part II

Contributions to a MOR framework for multi-query studies

Chapter 3

A hybrid frequency-temporal reduced-order method for non-linear dynamics

> It is simple, and therefore it is beautiful.
>
> Richard P. Feynman

A hybrid approach is proposed to solve the non-linear dynamics problem. It offers frequency-computation and ROM advantages while allowing for solving the history-dependent non-linear behaviour. Artificial damping is introduced to handle non-periodic solutions arising from non-linear effects or transient regimes.

Contents

1 The LATIN-PGD method for dynamics problems . . . 53
- 1.1 An iterative scheme with two alternated search directions . . . 53
- 1.2 The non-linear 'local' stage . . . 54
- 1.3 The linear 'global' stage . . . 55
- 1.4 Reduced-order model implementation . . . 55

2 Hybrid frequency-temporal reduced-order approach . . . 56
- 2.1 Temporal calculations of the non-linear behaviour . . . 57
- 2.2 Frequency calculations of the admissibility equation . . . 58

3 Numerical results . . . 63
- 3.1 Two-dimensional beam . . . 65
- 3.2 Three-dimensional pipe . . . 76

✎ Chapter summary & perspectives . . . 80

This chapter focuses on the method used to efficiently solve the non-linear dynamics problem of interest. The proposed solver is a LATIN-based hybrid approach consisting of computations done partially in the frequency and temporal domains. The frequency domain may not be suited for the description of non-linearities inherent to the behaviour. Evolution laws often rely on the knowledge of temporal quantities [Lemaitre & Desmorat, 2005] since describing material non-linearities is incremental by nature: the mechanical state of a medium depends on the previous state of the latter and on the current load applied. A specific effort must be made to take advantage of frequency domain computations when dealing with non-linear materials and one of the objectives of the present chapter is to describe the linearisation strategy that will be used in this work.

An alternating frequency-temporal approach [Cameron & Griffin, 1989] has already been carried out to find periodic steady-state solutions on structures with few degrees of freedom [Zhu et al., 2022; Kappauf et al., 2022] or where only few degrees of freedom were impacted by non-linear forces, such as dry-friction or contact forces [Nacivet et al., 2003; Von Groll & Ewins, 2001; Leine & Schreyer, 2016]. In order to take into account damage-induced non-linearities in dynamics, the proposed method relies similarly on an alternative scheme, but it is embedded within an efficient linearisation framework, called the LATIN method [Ladevèze, 1999], already used for many history-dependent non-linear problems involving internal variables. It thus allows complex material non-linearities to be taken into account robustly within a naturally non-incremental framework. Contrary to other alternating-temporal approaches, the foundation of the proposed strategy is to offer a reduced-order model embedded in the solver. As mentioned, separating variables reduces computational costs in solving non-linear dynamics. Furthermore, it's worth noting that the LATIN method's previously mentioned suitability in a parametric framework [Boucard & Champaney, 2003] was a key factor in its selection. This method has been applied for dynamics problems with visco-plastic behaviour [Rodriguez et al., 2019] as well as for a wide range of behaviour non-linearities for statics problems, including, among others, the study of plasticity, damage evolution for quasi-brittle materials, and fatigue prediction [Vandoren et al., 2013b; Vitse et al., 2019; Bhattacharyya et al., 2018b; Bhattacharyya et al., 2019; Iturra, 2021] where computations were totally dealt with in the temporal domain. The LATIN approach is traditionally equipped with an efficient *a priori* model-order reduction method, using a space-time separation of variables, the aforementioned PGD; the resulting method is the LATIN-PGD. The proposed methodology does not use a classical space-time decomposition but relies on a space-frequency separation of variables that is well suited for dynamics problems. The PGD already proved to be effective in a linear space-frequency context for acoustic problems [Barbarulo et al., 2014; de Brabander, 2021] as well as for structural dynamics [Chevreuil & Nouy, 2012; Malik et al., 2018].

The efficiency of frequency computations relies heavily on the Fast Fourier Transform (FFT) performances. To avoid Gibbs phenomena [Humar & Xia, 1993] in the case of poorly damped or in the eventuality of the structure not returning to its rest position due to non-linear effect, artificial damping [Humar & Xia, 1993] is used in both the transfer function and the right-hand side of the problem.

1 The LATIN-PGD method for dynamics problems

The essence of the LATIN-PGD method is to separate the equations driving the behaviour from those corresponding to the admissibility of the solution.

1.1 An iterative scheme with two alternated search directions

The LATIN method [Ladevèze, 1999] consists of an iterative scheme with two alternated search directions which estimates the solution on the whole time-space domain at each iteration. A graphical illustration is proposed in Figure 3.1 and gives a schematisation of the numerical strategy. Solutions of the non-linear equations (Equations (1.35), (1.37), (1.39), (1.40), (1.41)) on one side and of the linear equations (Equation (3.8) imposing the respect of Equation (1.18)) on the other side define the two manifolds Γ and $\mathscr{A}_d$, respectively. The exact solution s_{exact} lies at the intersection of these two manifolds. The consecutive approximations of this solution are computed alternately in Γ and $\mathscr{A}_d$ through the iterative scheme

$$s_0 \in \mathscr{A}_d \rightarrow \hat{s}_{1/2} \in \Gamma \rightarrow s_1 \in \mathscr{A}_d \dashrightarrow \underbrace{\overbrace{\hat{s}_{n+1/2} \in \Gamma}^{\text{Local stage}} \rightarrow \overbrace{s_{n+1} \in \mathscr{A}_d}^{\text{Global stage}}}_{\text{Iteration } n+1} \dashrightarrow \ldots \tag{3.1}$$

This iterative scheme shaping the LATIN method is first initialised by a dynamically admissible elastic solution s_0. Then, each iteration comprises two stages, a local stage and a global stage. The non-linear part of the constitutive behaviour is solved on the whole time-space domain during the local stage, while the global stage consists of solving a linear problem based on admissibility conditions, also imposed on the whole time-space domain. Knowing the estimation of the quantities s_n at iteration n the solution $\hat{s}_{n+1/2}$ of the local problem is estimated in Γ from the search direction $\mathbb{H}^+$. From $\hat{s}_{n+1/2}$ the solution s_{n+1} of the global problem is sought after in $\mathscr{A}_d$ based on the search direction $\mathbb{H}^-$, as follows

$$\begin{cases} \left(\boldsymbol{\sigma}^{\delta}_{n+1} - \hat{\boldsymbol{\sigma}}^{\delta}_{n+1/2}\right) - \mathbb{H}^- : \left(\boldsymbol{\varepsilon}_{n+1} - \hat{\boldsymbol{\varepsilon}}_{n+1/2}\right) = \mathbf{0}, \\ \left(\hat{\boldsymbol{\sigma}}^{\delta}_{n+1/2} - \boldsymbol{\sigma}^{\delta}_{n}\right) + \mathbb{H}^+ : \left(\hat{\boldsymbol{\varepsilon}}_{n+1/2} - \boldsymbol{\varepsilon}_{n}\right) = \mathbf{0}. \end{cases} \tag{3.2}$$

Those search directions provide a link between the damageable elasto-plastic stress $\boldsymbol{\sigma}^{\delta}$, computed when solving the non-linear behaviour during the local stage and the dynamically admissible stress $\boldsymbol{\sigma}$ corrected during the global stage. The iterative scheme continues until the quantity

$$\eta = \left(\frac{\|\hat{s}_{n+1/2} - s_{n+1}\|^2}{1/2\|s_{n+1}\|^2 + 1/2\|\hat{s}_{n+1/2}\|^2} \right)^{1/2} \tag{3.3}$$

is lower than a user-defined threshold η_c. The norm $\|s\|$ is defined as

$$\|s\|^2 = \int_{\Omega\times I} \boldsymbol{\varepsilon} : \mathbb{K} : \boldsymbol{\varepsilon} \, \mathrm{d}\Omega \mathrm{d}t + \int_{\Omega\times I} \boldsymbol{\sigma}^{\boldsymbol{\delta}} : \mathbb{K}^{-1} : \boldsymbol{\sigma}^{\boldsymbol{\delta}} \, \mathrm{d}\Omega \mathrm{d}t. \tag{3.4}$$

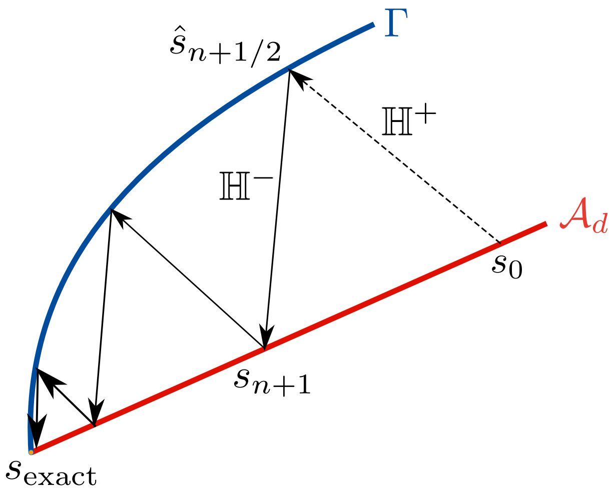

Figure 3.1 • Working principle of the LATIN method, modified from [Ladevèze, 1999]

The interested reader can refer to [Ladevèze, 1999] for the choice of the search directions and a detailed description of the methodology. The following subsections give an overview of the stages of the iterative scheme.

1.2 The non-linear 'local' stage

The local stage estimates all internal and state variables such that the constitutive behaviour detailed in Section 4 of Chapter 1 is satisfied. Considering the two previously-defined manifolds, the local stage gives $\hat{s}_{n+1/2} \in \Gamma$ knowing $s_n \in \mathscr{A}_d$ using the search direction given in Equation (3.2) and the behaviour description. Herein, the search direction $\mathbb{H}^+$ is chosen such that $\hat{\varepsilon}_{n+1/2} = \varepsilon_n$ i.e. $\mathbb{H}^+ = \infty$.

Knowing $\hat{\varepsilon}_{n+1/2}$, finding $\hat{s}_{n+1/2} \in \Gamma$ leads to solving the system

$$\begin{cases} \hat{\varepsilon}_{n+1/2} = \hat{\varepsilon}^e_{n+1/2} + \hat{\varepsilon}^p_{n+1/2} \\ \hat{\boldsymbol{\sigma}}^{\boldsymbol{\delta}}_{\boldsymbol{eff}\,n+1/2} = \mathbb{K} : \hat{\varepsilon}^e_{n+1/2} \\ \hat{\sigma}^{\delta}_{n+1/2} = \mathscr{H}\left(\hat{\varepsilon}_{n+1/2}\right). \end{cases} \tag{3.5}$$

A traditional return mapping algorithm [Lee & Fenves, 2001] is set up so that the damage variable D, as well as the plastic multiplier p driving the evolution of the isotropic hardening R, the kinematic hardening $\boldsymbol{X}$ and the plastic strain ε^p satisfy the Equations (1.37), (1.40), (1.41). Because those equations are local, they are solved independently on each Gauss point of the considered structure.

Remark Note that the above framework is general and versatile, and that any other behaviour could be solved at the local stage.

1.3 The linear ‘global’ stage

From the elastic initialisation $s_0 \in \mathscr{A}_d$ giving displacement prediction $\boldsymbol{u}_0(\boldsymbol{x},t) \in \mathscr{U}$, displacement corrections $\boldsymbol{\Delta u_j} \in \mathscr{U}^0$ are computed at each following global stage to ensure that dynamic admissibility given by Equation (1.18), is achieved. The displacement field is approximated as

$$\boldsymbol{u}\left(\boldsymbol{x},t\right) \approx \boldsymbol{u}_0(\boldsymbol{x},t) + \underbrace{\sum_{j=1}^{n} \boldsymbol{\Delta u_j}}_{\boldsymbol{\Delta u}} . \tag{3.6}$$

Introducing the operator $\Delta\square_{n+1}$ defined as the correction between two successive estimations, i.e. $\Delta\square_{n+1} = \square_{n+1} - \square_n$, the admissibility equation in terms of correction reads

$$-\int_{\Omega\times I} \boldsymbol{\Delta\sigma}_{n+1} : \varepsilon(\boldsymbol{u}^*)\mathrm{d}\Omega\mathrm{d}t = \int_{\Omega\times I} \rho\boldsymbol{\Delta\gamma}_{n+1}\cdot\boldsymbol{u}^*\mathrm{d}\Omega\mathrm{d}t,\ \forall\boldsymbol{u}^* \in \mathscr{U}^0. \tag{3.7}$$

Using Equation (1.14) and the search direction as defined by Equation (3.2), we obtain

$$\begin{aligned}
&\int_{\Omega\times I} \mathbb{H}^- : \varepsilon(\boldsymbol{\Delta u_{n+1}}) : \varepsilon(\boldsymbol{u}^*)\mathrm{d}\Omega\mathrm{d}t + \int_{\Omega\times I} \mathbb{D} : \varepsilon(\boldsymbol{\Delta \dot{u}_{n+1}}) : \varepsilon(\boldsymbol{u}^*)\mathrm{d}\Omega\mathrm{d}t \\
&+ \int_{\Omega\times I} \rho\boldsymbol{\Delta\ddot{u}}_{n+1}\cdot\boldsymbol{u}^*\mathrm{d}\Omega\mathrm{d}t \\
&= \int_{\Omega\times I} \underbrace{\left[\left(\sigma_n^\delta - \hat{\sigma}_{n+1/2}^\delta\right) - \mathbb{H}^- : \left(\varepsilon_n - \hat{\varepsilon}_{n+1/2}\right)\right]}_{\hat{\boldsymbol{f}}^{n+1}} : \varepsilon(\boldsymbol{u}^*)\mathrm{d}\Omega\mathrm{d}t,\ \forall\boldsymbol{u}^* \in \mathscr{U}^0.
\end{aligned} \tag{3.8}$$

One may notice that terms in the right-hand side $\hat{\boldsymbol{f}}^{n+1}$ of that equation are known quantities at this stage. The displacement field $\boldsymbol{\Delta u_{n+1}}$ is the only unknown at this stage, which consists basically of solving a linear dynamics problem.

1.4 Reduced-order model implementation

The PGD model-order reduction method can naturally be introduced in the global stage of the LATIN method, which deals with linear equations over the space-time domain. Doing so means that the displacement correction $\boldsymbol{\Delta u} \approx \sum_{j=1}^{n+1}\boldsymbol{\Delta u_j}$ computed at the $n+1$-th global stage is sought after as a sum of modes defined as products of space functions $\overline{\boldsymbol{u}}^i$ and temporal functions $\lambda^i(t)$. After having added m PGD pairs, the displacement reads

$$\boldsymbol{\Delta u}(\boldsymbol{x},t) \approx \sum_{i=1}^{m} \lambda_i(t)\overline{\boldsymbol{u}}_i(\boldsymbol{x}). \tag{3.9}$$

Once $m \geqslant 1$ PGD modes have been added, a preliminary substep of the global stage can be inserted between both the local stage and the addition of a new PGD pair. The substep consists of updating the previously computed temporal modes $\{\lambda_i\}_{i\in[\![1,m]\!]}$ in order to achieve dynamic admissibility while the spatial modes $\{\overline{\boldsymbol{u}}_i\}_{i\in[\![1,m]\!]}$ are considered fixed. If this updating step proves to be sufficient, the next LATIN iteration can be performed; if it is insufficient, a new PGD pair is added.

Remark Due to the updating stage, the number of PGD pairs might be lower than that of LATIN iterations. In Equation 3.6, n LATIN iterations lead to n corrections $\boldsymbol{\Delta u}_i$ to be computed and Equation 3.9 shows that the full inelastic correction $\boldsymbol{\Delta u}(\boldsymbol{x}, t)$ consists of a sum of m modes with $m \leqslant n$. Indeed, some LATIN stages only consists in updating the time functions without adding new PGD pairs.

The reader can refer to [Nouy, 2010] for an overview of the methods to solve a linear problem using the PGD. Section 2 details the calculations arising from the PGD paradigm for the application of the methodology in the frequency domain.

2 Hybrid frequency-temporal reduced-order approach

The main Equation (3.8) of the problem corresponds to a linear dynamics equation that, when semi-discretised in space, reads

$$[M]\{\ddot{U}\} + [D]\{\dot{U}\} + [K]\{U\} = \{F\}. \tag{3.10}$$

In addition to which, initial and boundary conditions need to be specified. It consists of a finite element problem where $[M]$, $[D]$ and $[K]$ are the mass, damping and stiffness matrices respectively. Thus, its computation can easily be performed in the frequency domain, as traditionally done in the literature [Hall, 1982], in order to benefit from all corresponding computational advantages. Indeed, frequency-based calculations, for instance, allow for easy parallelisation of the computations. Contrary to time steps, frequency steps are not interdependent, and the computation for each frequency step may easily be done simultaneously on different threads of a multi-threaded chip without the need to use specific temporal domain decomposition techniques [Lions et al., 2001; Chartier & Philippe, 1993]. Moreover, it appears that much fewer frequency steps than time steps are needed to describe the signals dealt with. For those two combined reasons, a frequency-based method leads to cheaper computations. In addition, the use of a frequency-based methodology may, in some cases, be required to deal with some *frequency dependency* of the material behaviour, such as hysteric damping [Bishop, 1955] where the damping matrix $[D]$ would depend on the frequency. However, the description of the non-linear behaviour of the material can only be achieved in the temporal domain. Thus, the decoupling feature of the LATIN method, introduced in Section 1, is employed to jointly use the temporal and frequency domains. Note that the FFT algorithm is very efficient. Thus, numerous transfers between temporal and frequency domains do not represent a bottleneck. The time associated with alternating between the temporal domain and the frequency domain using the FFT and iFFT algorithms is insignificant compared to the numerical cost of a given computation, i.e. a few tenths or hundredths of percent of the total computational time. Technicalities of LATIN iterations and the specific Fourier and inverse Fourier transforms involved in the method are schematised in Figure 3.2. First, the elastic problem is solved on the frequency domain. Then, after an inverse Fourier transform, the non-linear behaviour (manifold Γ) is approximated on the temporal domain and the dynamic admissibility equation (manifold $\mathscr{A}_d$) is solved based on a frequency strategy. This step is enhanced with the implementation of the PGD. Again an inverse Fourier transform is performed before the successive iteration and the algorithm goes on until reaching convergence.

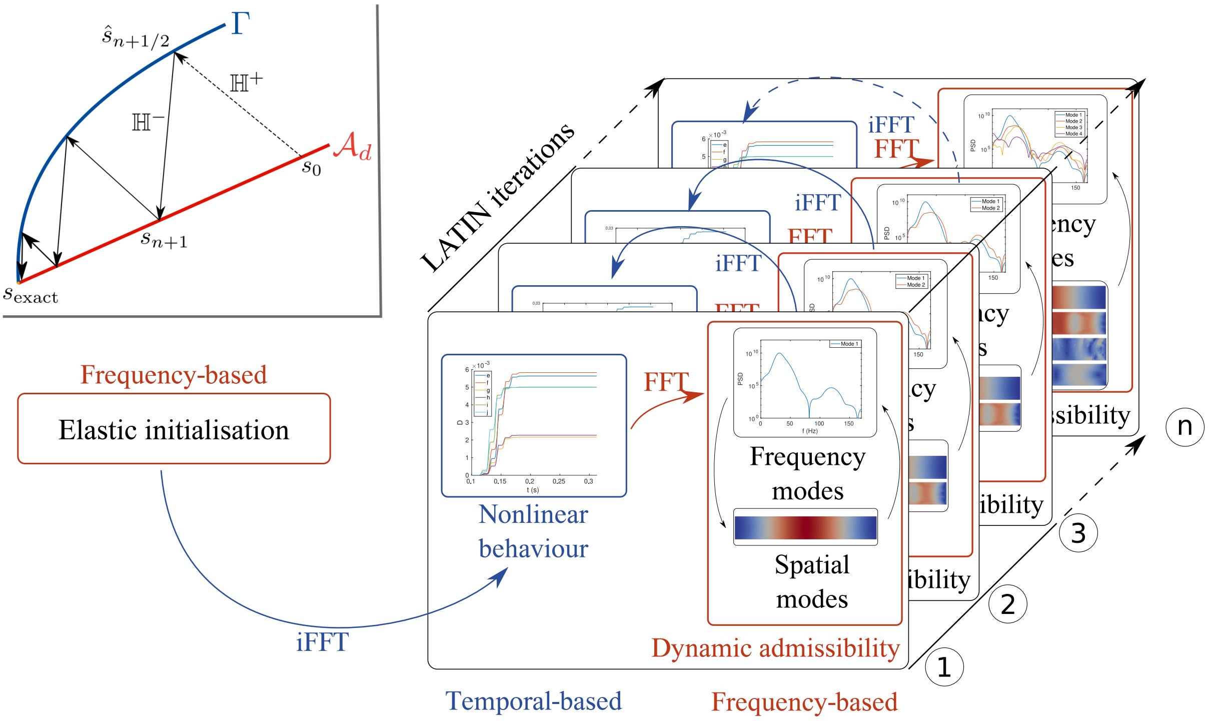
$\hat{s}_{n+1/2}$
Γ
$\mathbb{H}^+$
$\mathbb{H}^-$
A_d
s_0
s_{n+1}
s_{exact}
LATIN iterations
Frequency-based
Elastic initialisation
iFFT
FFT
Nonlinear behaviour
Frequency modes
Spatial modes
Dynamic admissibility
Temporal-based
Frequency-based
1
2
3
n

Figure 3.2 • Scheme of the hybrid frequency-temporal strategy

2.1 Temporal calculations of the non-linear behaviour

The constitutive behaviour presented in Section 4 of Chapter 1 gives a history-dependent description of the material properties evolution. Ensuring the validity of the von Mises yield criterion given in Equation (1.37) at a given instant, for instance, requires the knowledge of the isotropic and kinematic hardening R and $\boldsymbol{X}$ at that particular instant, which depend on the loading history up to the moment in question. Similarly, knowledge of the damage variable D, which also depends on the loading history, is needed to compute the effective damageable elasto-plastic stress $\boldsymbol{\sigma}^{\delta}_{eff}$ described in Equation (1.34). Solving the behaviour equations must therefore be done in the time domain. The LATIN local stage consists precisely in solving the problem given by Equation (3.5), which groups the constitutive equations as already explained. For our reference problem, Equations (1.37), (1.40), (1.41) are solved using a backward Euler integration scheme and a return mapping algorithm. It can be noted that the size of the problem depends on the number of degrees of freedom. However, these equations can be straightforwardly parallelised as they are independent for each Gauss point.

2.2 Frequency calculations of the admissibility equation

The dynamics part of the problem lies in the global equations leading to the solutions on the manifold $\mathscr{A}_d$. Those linear dynamics equations are well-suited to a frequency approach which allows for very efficient calculations. Therefore, the global stage of the LATIN scheme will take advantage of that framework.

Elastic initialisation

The iterative scheme begins with initialising the estimation considering an elastic behaviour. The goal is to solve the weak form of the dynamics problem, which was previously defined in the temporal domain by Equation (1.18). It is now turned into the following frequency problem:

$$
\begin{aligned}
-\int_\Omega \varepsilon(\breve{\boldsymbol{u}}):\mathbb{K}:\varepsilon(\breve{\boldsymbol{u}}^*)\mathrm{d}\Omega - \jmath\omega\int_\Omega \varepsilon(\breve{\boldsymbol{u}}):\mathbb{D}:\varepsilon(\breve{\boldsymbol{u}}^*)\mathrm{d}\Omega + \int_\Omega \boldsymbol{f_d}\cdot\breve{\boldsymbol{u}}^*\mathrm{d}\Omega \\
+\int_{\partial\Omega} \boldsymbol{F_d}\cdot\breve{\boldsymbol{u}}^*\mathrm{d}S = -\omega^2\int_\Omega \rho\,\breve{\boldsymbol{u}}\cdot\breve{\boldsymbol{u}}^*\mathrm{d}\Omega,\ \forall\boldsymbol{u}^*\in\mathscr{U}^0,\forall\omega\in\mathbb{R}^+,
\end{aligned}
\tag{3.11}
$$

where the angular frequency is denoted ω and $\breve{\boldsymbol{u}}(\boldsymbol{x},\boldsymbol{\omega})$ is the Fourier transform of the displacement $\boldsymbol{u}(\boldsymbol{x},\boldsymbol{t})$, as follows

$$
\breve{\boldsymbol{u}}(\boldsymbol{x},\omega) = \int_{-\infty}^{+\infty} \boldsymbol{u}(\boldsymbol{x},t)e^{-\jmath\omega t}\mathrm{d}t. \tag{3.12}
$$

When solving such a problem numerically, only a finite number N_t of time steps and therefore of angular frequency steps is considered. Let $\Phi = \{\omega_i\}_{i=[\![1,N_t]\!]}$ be the finite set of angular frequencies. Then for each ω_i in Φ, one needs to solve Equation (3.11), leading to N_t independent problems that can be solved separately. Hence, computations can be sped up using parallelisation. Moreover, if the external load happens to be zero for some of these angular frequencies, the computations for these particular frequencies can be skipped, leading to supplementary calculation gains.

Calculation of the displacement correction

Once the elastic initialisation has been performed, the global stage of the iterative scheme consists of adjusting a displacement correction $\boldsymbol{\Delta u}$ that is dynamically admissible to zero as given by Equation (3.8) such that the displacement field solution of the problem reads $\boldsymbol{u}(\boldsymbol{x},t) = \boldsymbol{u}_0(\boldsymbol{x},t) + \boldsymbol{\Delta u}(\boldsymbol{x},t)$ with the correction being improved at each iteration such that it reads $\boldsymbol{\Delta u} \approx \sum_{j=1}^{n+1}\boldsymbol{\Delta u_j}$ at the $(n+1)$-th global stage. Similarly to the elastic initialisation, those steps are written in the frequency domain. Equation (3.8) is turned into

$$
\begin{aligned}
\int_\Omega \mathbb{H}^-:\varepsilon(\boldsymbol{\Delta\breve{u}_{n+1}}):\varepsilon(\breve{\boldsymbol{u}}^*)\mathrm{d}\Omega + \jmath\omega\int_\Omega \varepsilon(\boldsymbol{\Delta\breve{u}_{n+1}}):\mathbb{D}:\varepsilon(\breve{\boldsymbol{u}}^*)\mathrm{d}\Omega \\
-\omega^2\int_\Omega \rho\boldsymbol{\Delta\breve{u}_{n+1}}\cdot\breve{\boldsymbol{u}}^*\mathrm{d}\Omega = \int_\Omega \breve{\hat{\boldsymbol{f}}}_{n+1}:\varepsilon(\breve{\boldsymbol{u}}^*)\mathrm{d}\Omega\ \forall\breve{\boldsymbol{u}}^*\in\mathscr{U}^0,\forall\omega\in\mathbb{R}^+,
\end{aligned}
\tag{3.13}
$$

which is solved as multiple decoupled spatial problems. Moreover, this step is well-suited for using model-order reduction techniques such as the PGD, which further helps lowering calculation cost by reducing drastically the number of degrees of freedom.

A greedy algorithm is set up in order to find the increment of the displacement field $\boldsymbol{\Delta\breve{u}}$ under a PGD form

$$\boldsymbol{\Delta\breve{u}}(\boldsymbol{x},\omega) \approx \sum_{i=1}^{m} \overline{\boldsymbol{u}}_i(\boldsymbol{x})\breve{\lambda}_i(\omega), \tag{3.14}$$

where m represents the number of PGD modes used to describe the solution.

Addition of a new PGD pair

When adding a new PGD pair at the LATIN iteration $n+1$, the displacement correction corresponds to the estimation of the $m+1$ pair comprising a space and a frequency function. One gets

$$\boldsymbol{\Delta\breve{u}_{n+1}} = \overline{\boldsymbol{u}}_{m+1}\breve{\lambda}_{m+1}.$$

Thus, considering the addition of a PGD pair, Equation (3.13) leads to the two coupled equations that define the new spatial and frequency modes $\{\overline{\boldsymbol{u}}_{m+1}, \breve{\lambda}_{m+1}\}$

$$\begin{cases} \displaystyle\int_\Omega \varepsilon(\overline{\boldsymbol{u}}_{m+1})\boldsymbol{H^\lambda}_{m+1}\ \varepsilon(\overline{\boldsymbol{u}}^*) + \int_\Omega \varepsilon(\overline{\boldsymbol{u}}_{m+1})\boldsymbol{D^\lambda}_{m+1}\ \varepsilon(\overline{\boldsymbol{u}}^*) + \int_\Omega \overline{\boldsymbol{u}}_{m+1}\boldsymbol{M^\lambda}_{m+1}\overline{\boldsymbol{u}}^*\mathrm{d}\Omega \\ \qquad\qquad\qquad \displaystyle = \int_\Omega\int_I \lambda_{m+1}\hat{\boldsymbol{f}}_{n+1}\mathrm{d}t : \varepsilon(\overline{\boldsymbol{u}}^*)\mathrm{d}\Omega, \quad \forall\overline{\boldsymbol{u}}^* \in \mathscr{U}^0 \\ \left(a_{m+1} + \jmath\omega b_{m+1} - \omega^2 c_{m+1}\right)\breve{\lambda}_{m+1} = \breve{g}_{m+1}, \forall\omega \in \mathbb{R}^+ \end{cases} \tag{3.15}$$

solved using a fixed-point algorithm initialised by a user-chosen temporal function, with,

$$\begin{cases} \boldsymbol{H^\lambda}_{m+1} = \displaystyle\int_I (\lambda_{m+1})^2\,\mathbb{H}^-\mathrm{d}t \\ \boldsymbol{D^\lambda}_{m+1} = \displaystyle\int_I \dot{\lambda}_{m+1}\mathbb{D}\lambda_{m+1}\mathrm{d}t \\ \boldsymbol{M^\lambda}_{m+1} = \displaystyle\int_I \rho\ddot{\lambda}_{m+1}\lambda_{m+1}\mathrm{d}t \\ a_{m+1} = \displaystyle\int_\Omega \varepsilon\left(\overline{\boldsymbol{u}}_{m+1}\right) : \mathbb{H}^- : \varepsilon\left(\overline{\boldsymbol{u}}_{m+1}\right)\mathrm{d}\Omega \\ b_{m+1} = \displaystyle\int_\Omega \varepsilon\left(\overline{\boldsymbol{u}}_{m+1}\right) : \mathbb{D} : \varepsilon\left(\overline{\boldsymbol{u}}_{m+1}\right)\mathrm{d}\Omega \\ c_{m+1} = \displaystyle\int_\Omega \rho\overline{\boldsymbol{u}}_{m+1}\cdot\overline{\boldsymbol{u}}_{m+1}\mathrm{d}\Omega \\ \breve{g}_{m+1} = \displaystyle\int_\Omega \varepsilon\left(\overline{\boldsymbol{u}}_{m+1}\right) : \breve{\hat{\boldsymbol{f}}}_{n+1}\mathrm{d}\Omega. \end{cases} \tag{3.16}$$

Estimating the new frequency modes involves spatial integrals, whereas the estimation of the new space mode is based on temporal integrals. Indeed, for the sake of simplicity, usual temporal integral operators are employed here as the considered damping does not depend on the frequency. Thus the new frequency mode is transformed back to its temporal counterpart at each iteration, which is straightforward using the inverse FFT algorithm. The operators $\boldsymbol{H}^{\boldsymbol{\lambda}}$, $\boldsymbol{D}^{\boldsymbol{\lambda}}$ and $\boldsymbol{M}^{\boldsymbol{\lambda}}$ of the spatial problem in Equation (3.15) are therefore similarly obtained by injecting the PGD form of the displacement correction from Equation (3.9) to Equation (3.8) as it has been detailed for the frequency modes in Equations (3.13) and (3.14). One may notice that the contribution of the previous PGD modes is taken into account in the right-hand-side of those equations where the quantity $\hat{\boldsymbol{f}}_{n+1}$ links the quantities computed in the LATIN global stage n and the following local stage $n+1/2$ as follows

$$\hat{\boldsymbol{f}}_{\boldsymbol{n+1}} = \left(\boldsymbol{\sigma}_n^{\delta} - \hat{\boldsymbol{\sigma}}_{n+1/2}^{\delta}\right) - \mathbb{H}^- : \left(\boldsymbol{\varepsilon}_n - \hat{\boldsymbol{\varepsilon}}_{n+1/2}\right). \tag{3.17}$$

Remark 1 An orthogonalisation step is carried out once a new mode has been added. This step allows the previously computed modes to form a basis without losing the newly computed information. Moreover, projecting a new mode onto the basis provides additional insights: the extent to which it adds new information. For instance, if its projection is zero, it indicates that the previous modes already represent this mode, rendering it irrelevant. In practical terms, when generating a new pair of modes $(\overline{\boldsymbol{u}}_{m+1}, \lambda_{m+1})$, we “eliminate" from $\overline{\boldsymbol{u}}_{m+1}$ the projection of the new mode onto the preceding modes, yielding $\mathring{\overline{\boldsymbol{u}}}_{m+1}$. Consequently, we adjust the λ_i values accordingly to avoid information loss, resulting in $\mathring{\lambda}_i$. Subsequently, we normalise this new mode $\mathring{\overline{\boldsymbol{u}}}_{m+1}$ using equations (3.18), (3.19), (3.20), and (3.21).

$$\boldsymbol{u}_{m+1} = \sum_{i=1}^{m} \underbrace{(\lambda_i + \lambda_{m+1}\, \overline{\boldsymbol{u}}_i^T \overline{\boldsymbol{u}})}_{\mathring{\lambda}_i} \overline{\boldsymbol{u}}_i + \lambda_{m+1} \underbrace{\left(\overline{\boldsymbol{u}}_{m+1} - \sum_{i=1}^{m} (\overline{\boldsymbol{u}}_i^T \overline{\boldsymbol{u}}) \overline{\boldsymbol{u}}_i\right)}_{\mathring{\overline{\boldsymbol{u}}}_{m+1}} \tag{3.18}$$

$$\overline{\boldsymbol{u}}_{m+1} \longleftarrow \frac{\mathring{\overline{\boldsymbol{u}}}_{m+1}}{\|\mathring{\overline{\boldsymbol{u}}}_{m+1}\|_{\mathbb{K}}} \tag{3.19}$$

$$\lambda_{m+1} \longleftarrow \lambda_{m+1} \|\mathring{\overline{\boldsymbol{u}}}_{m+1}\|_{\mathbb{K}} \tag{3.20}$$

$$\{\lambda_i\}_{i\in[\![1,m]\!]} \leftarrow \{\mathring{\lambda}_i\}_{i\in[\![1,m]\!]} \tag{3.21}$$

Remark 2 Alternatively, time vectors can also be compressed as proposed in [Giacoma et al., 2015], converging towards the SVD decomposition of the displacement field, thus avoiding reduncdancy in temporal vectors.

Updating the frequency modes

Before adding a new PGD pair to the decomposition already including m pairs, a simple update of the frequency functions $\breve{\lambda}^i(\omega)$ is performed considering the associated spatial modes $\overline{\boldsymbol{u}}^i$ as fixed. Such a step is achieved by solving the problem

$$\left(\boldsymbol{A}^{\text{Update}} + \jmath\omega\boldsymbol{B}^{\text{Update}} - \omega^2\boldsymbol{C}^{\text{Update}}\right)\breve{\boldsymbol{\Lambda}} = \breve{\boldsymbol{F}}^{\text{Update}}, \forall\omega \in \mathbb{R}^+, \tag{3.22}$$

with, for any $(k,l) \in [\![1,m]\!]^2$,

$$\begin{cases} \boldsymbol{A}_{kl}^{\text{Update}} = \displaystyle\int_\Omega \varepsilon\left(\overline{\boldsymbol{u}}^k\right) : \mathbb{H}^- : \varepsilon\left(\overline{\boldsymbol{u}}^l\right) \mathrm{d}\Omega \\ \boldsymbol{B}_{kl}^{\text{Update}} = \displaystyle\int_\Omega \varepsilon\left(\overline{\boldsymbol{u}}^k\right) : \mathbb{D} : \varepsilon\left(\overline{\boldsymbol{u}}^l\right) \mathrm{d}\Omega \\ \boldsymbol{C}_{kl}^{\text{Update}} = \displaystyle\int_\Omega \rho\overline{\boldsymbol{u}}^k \cdot \overline{\boldsymbol{u}}^l \mathrm{d}\Omega \\ \breve{\boldsymbol{F}}^{\text{Update}} = \displaystyle\int_\Omega \varepsilon\left(\overline{\boldsymbol{u}}^k\right) : \breve{\hat{\boldsymbol{f}}}^{n+1} \mathrm{d}\Omega \end{cases} \tag{3.23}$$

and,

$$\breve{\boldsymbol{\Lambda}} = \left[\breve{\lambda}^1, \breve{\lambda}^2, \cdots, \breve{\lambda}^m\right]^T. \tag{3.24}$$

Starting by updating the frequency functions may allow skipping the addition of a new PGD pair if the updating step allows sufficient progress in the iterative scheme. Then, the LATIN iteration is significantly less expensive than adding a new pair. A new mode is only added if the updated functions $\{\lambda^{i,\text{ Update}}\}_{i\in[\![1,m]\!]}$ are considered too similar compared to their counterpart $\{\lambda^i\}_{i\in[\![1,m]\!]}$ prior to the updating step, i.e.

$$\max_{i\in[\![1,m]\!]} \left(\frac{\int_I |\lambda^i - \lambda^{i,\text{ Update}}| \mathrm{d}t}{1/2 \int_I |\lambda^i + \lambda^{i,\text{ Update}}| \mathrm{d}t} \right) \leqslant \xi_c \tag{3.25}$$

with ξ_c a user-defined threshold.

The proposed method relies heavily on multiple Fourier transforms. However, the FFT algorithm is known for not being robust for signals which do not vanish at the end of the time window. Indeed, when the damping rate is low or if the temporal observation window is short, one may face the transient regime where FFT can lead to temporal overlapping [Humar, 1990]. To avoid this numerical artefact, artificial damping is included to the global equations.

Artificial damping in the frequency calculation strategy

Artificial damping can be added temporarily as a computational step to overcome the overlapping issue. This method, which offers numerical robustness for any scenario, is inspired by the Prony transform [Van Blaricum & Mittra, 1978] which corresponds to a damped Fourier transform.

Consider the case where a PGD pair is added, i.e. when solving Equation (3.15). The frequency problem can be written as

$$\breve{\lambda}_{m+1}(\omega) = \breve{H}_{m+1}(\omega)\breve{g}_{m+1}(\omega) \tag{3.26}$$

by introducing H_{m+1} as the response function of the system and g_{m+1} as the forcing function as follows

$$\begin{cases} g_{m+1}(t) = \displaystyle\int_{\Omega} \hat{\boldsymbol{f}}^{\boldsymbol{n+1}}(t,\boldsymbol{x})\,\varepsilon\left(\overline{\boldsymbol{u}}_{m+1}\right)\mathrm{d}\Omega, \\ \breve{H}_{m+1}(\omega) = \left(a_{m+1} + \jmath\omega b_{m+1} - \omega^2 c_{m+1}\right)^{-1}. \end{cases} \tag{3.27}$$

Artificial damping is introduced through a modified response function

$$\tilde{H}_{m+1}(t) = e^{-a_d t} H_{m+1}(t) \tag{3.28}$$

with $a_d \in \mathbb{R}_*^+$, a user-chosen parameter that will further be discussed. The damped response function can also be evaluated without an explicit temporal formulation but directly from its frequency counterpart [Humar & Xia, 1993] as

$$\breve{\tilde{H}}_{m+1}(\omega) = \breve{H}_{m+1}(\omega - \jmath a_d) \tag{3.29}$$

with $\jmath$ the imaginary unit. Equation 3.29 is directly derived from equation 3.28. Indeed,

$$\begin{aligned} \breve{\tilde{H}}_{m+1}(\omega) &= \int_{-\infty}^{+\infty} \tilde{H}(t) e^{-\jmath\omega t}\mathrm{d}t \\ &= \int_{-\infty}^{+\infty} e^{-a_d t} H(t) e^{-\jmath\omega t}\mathrm{d}t \\ &= \int_{-\infty}^{+\infty} H(t) e^{-\jmath(\omega - \jmath a_d)t}\mathrm{d}t \\ &= \breve{H}_{m+1}(\omega - \jmath a_d). \end{aligned} \tag{3.30}$$

Then, the temporal solution $\lambda_{m+1}(t)$ of Equation (3.15) satisfying

$$\lambda_{m+1}(t) = \int_{\mathbb{R}} H_{m+1}(t-\tau) g_{m+1}(\tau)\mathrm{d}\tau \tag{3.31}$$

also satisfies the following modified relationship

$$\lambda_{m+1}(t) = e^{a_d t} \int_{\mathbb{R}} \tilde{H}_{m+1}(t-\tau)\tilde{g}_{m+1}(\tau)\mathrm{d}\tau, \tag{3.32}$$

with $\tilde{g}_{m+1}(\tau) = e^{-a_d \tau} g_{m+1}(\tau)$ the modified forcing function. Because $\tilde{H}_{m+1}$ is inherently damped, the convolution product $\tilde{g}_{m+1} \star \tilde{H}_{m+1}$ can be easily performed numerically in the frequency domain. Thus, the problem of interest consists in evaluating the modified Fourier response $\breve{\tilde{\lambda}}_{m+1}(\omega)$ through the following problem

$$\breve{\tilde{\lambda}}_{m+1}(\omega) = \breve{\tilde{H}}_{m+1}(\omega)\breve{\tilde{g}}_{m+1}(\omega), \tag{3.33}$$

which is robust and accurate even in cases where the response function H_{m+1} is poorly or even not damped.

Then the initial unknown $\lambda_{m+1}(t)$ is retrieved as

$$\lambda_{m+1}(t) = e^{a_d t}\tilde{\lambda}_{m+1}(t). \tag{3.34}$$

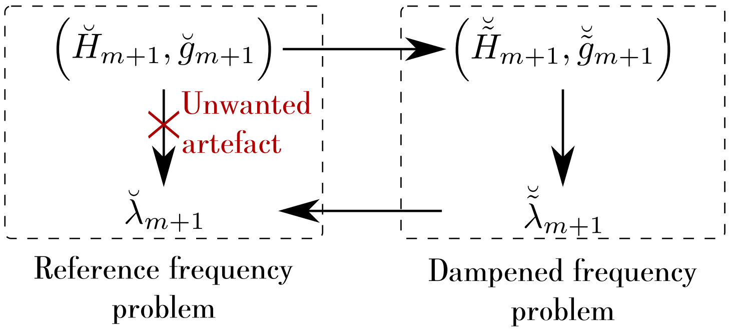
$(\breve{H}_{m+1}, \breve{g}_{m+1})$
$(\breve{\breve{H}}_{m+1}, \breve{\breve{g}}_{m+1})$
Unwanted artefact
$\breve{\lambda}_{m+1}$
$\breve{\breve{\lambda}}_{m+1}$
Reference frequency problem
Dampened frequency problem

Figure 3.3 • Frequency modes calculation strategy based on artificial damping

The artificial damping strategy can be summarised by Figure 3.3.

Similar strategy is used for the elastic initialisation and for each LATIN iteration, either updating frequency modes or adding a new pair. It allows for the accurate calculation of a transient solution on an observation time $I = [0, T_0]$ at the end of which the structure shall still be vibrating.

Remark Artificial damping also helps to avoid Gibbs phenomena in a non-linear context where residual displacements due to plasticity, for instance, prevents the structure from returning completely to its initial state even after an extended period.

3 Numerical results

The hybrid LATIN-PGD presented herein is investigated for two structures. All the numerical examples were carried out using ROMlab [Scanff et al., 2020], an in-house software written in MATLAB® language (see Appendix B). The meshes were obtained using the software GMSH. The graphical post-processing was done with the software Paraview. For both cases, the material parameters are defined in Table 3.1.

The damping of the structure is represented via a damping matrix $[D]$. Herein, a Rayleigh damping matrix expressed as a linear combination of the mass and stiffness matrices $[M]$ and $[K]$ is chosen such that it reads $[D] = \alpha_r [K] + \beta_r [M]$. The parameters α_r and β_r are chosen so that the damping rate defined from the projection of the dynamic admissibility on the eigenmodes [Géradin & Rixen, 2015] as

$$\xi = \frac{1}{2}\left(\alpha_r \omega_{0i} + \frac{\beta_r}{\omega_{0i}}\right), \tag{3.35}$$

is equal to 5% for the first two eigenfrequencies $f_1 = 30\,\text{Hz}$ and $f_2 = 78\,\text{Hz}$. An example of the evolution of the damping rate ξ as a function of the frequency is shown in Figure 3.4 where both f_1 and f_2 are circled out.

In the methodology, multiple user-defined thresholds have been introduced. In the following results, the stopping criterion was chosen such that $\eta_c = 2 \times 10^{-3}$. To improve

Young modulus:	$E = 70\,\mathrm{GPa}$
Poisson ratio:	$\nu = 0.3$
Density:	$\rho = 7000\,\mathrm{kg/m^3}$
Yield stress:	$\sigma_y = 200\,\mathrm{MPa}$
Kinematic hardening modulus:	$C = 2.211 \times 10^4\,\mathrm{MPa}$
Isotropic hardening ratio:	$h = 0\,\mathrm{MPa}$
Damage threshold energy:	$w_D = 0\,\mathrm{Jm^3/kg}$
Damage law exponent:	$s_d = 2$
Parameter for damage evolution:	$S = 0.6\,\mathrm{MPa}$
Critical damage:	$D_c = 0.5$

Table 3.1 • Material parameters

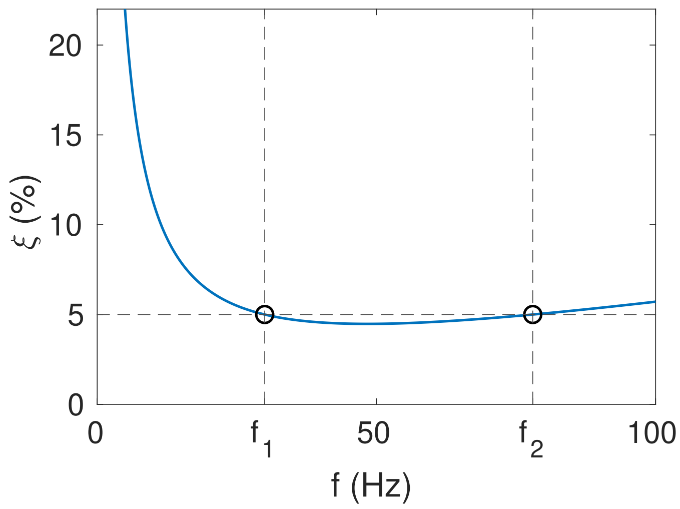

Figure 3.4 • Evolution of the damping rate as a function of the frequency. A Rayleigh damping matrix is used with a damping rate fixed at 5 % for the first two eigenfrequencies $f_1 = 30\,\mathrm{Hz}$ and $f_2 = 78\,\mathrm{Hz}$.

convergence, a relaxation coefficient of $\mu_r = 0.8$ was also used, as inspired by [Heyberger et al., 2012]; the global stage is therefore modified so that, from the solution $\mathring{s}_{n+1}$ given at the end of the PGD process, the relaxed solution at the end of the global stage reads $\mu_r \mathring{s}_{n+1} + (1-\mu_r)\, s_n$. The criterion ξ_c driving the update or the addition of a new mode is adaptive with the size of the PGD basis. Initially, it equals 1; once 5 modes have been included in the basis, it is fixed to 0.15. This evolution allows a quick expense of the basis at the beginning of the LATIN steps.

3.1 Two-dimensional beam

A fixed-end beam of length $L_b = 9\,\text{m}$ and width $W_b = 80\,\text{cm}$ as illustrated in Figure 3.5 is investigated. It is meshed with 9,080 T3 elements of mean size equal to 4 cm.

Its end section is submitted to an oscillatory load U_d.

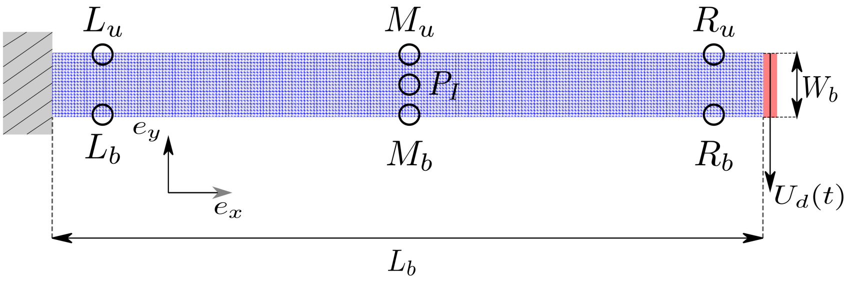

Figure 3.5 • Two-dimensional fixed-end beam

Single-frequency load

First, a single-frequency load plotted in Figure 3.6 and defined by

$$U_d(t) = U_d^{\max} \exp\left(-\left(10\frac{(t-\frac{T_0}{2})}{T_0}\right)^2\right) \sin\left(2\pi f\ t\right) \tag{3.36}$$

is considered, where the final time is $T_0 = 0.3125\,\text{s}$. $N_t = 1{,}024$ time steps with uniform $\delta t \approx 3\times10^{-4}\,\text{s}$ were employed, a number of time steps which is a power of two allows to benefit at best from the FFT numerical efficiency. In the below application, the values of the loading parameters are $f = 40\,\text{Hz}$ and $U_d^{\max} = 100\,\text{mm}$.

The damage field in the beam at different instants is given in Figure 3.7. From the initial time step, which corresponds to an undamaged structure, it can be seen that the damage field increases first close to the solicited extremity of the beam where the bending moment is maximum. In response to that loading scenario, the beam tends to oscillate along a first-mode type of movement therefore damage also grows close to the middle of the beam , which corresponds to the location of an anti-node, where the displacement is therefore important.

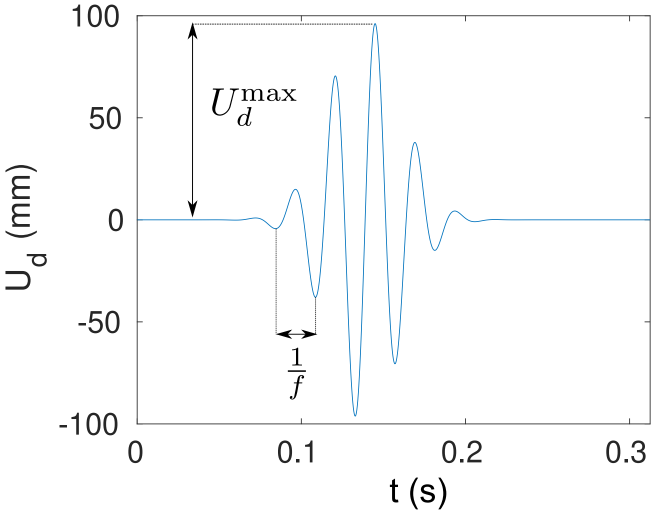

Figure 3.6 • Temporal load 1 - mono-frequency case

The temporal evolution of damage for six Gauss points located on the left side, the middle part and the right side of the beam (see Figure 3.5) can be seen in Figure 3.8. It can be highlighted that up to around 0.15 s the points on the right side (near to the application points of the load) were the most damaged, but afterwards the critical points are the points on the left side, near to the embedding zone. The delay is due to the time required by stress waves to reach that zone.

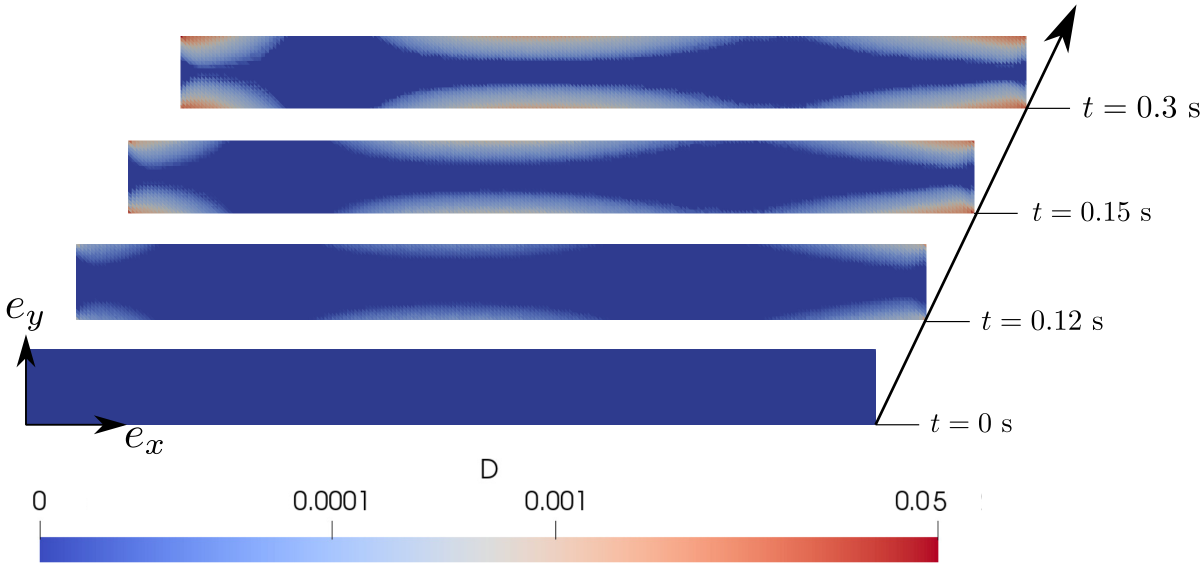

Figure 3.7 • Evolution of the damage field for the beam solicited with load 1 - $f = 40$ Hz and $U_d^{\max} = 100$ mm

Only nineteen iterations were required for the LATIN hybrid algorithm to reach the convergence criterion $\eta_c = 2 \times 10^{-3}$ (Figure 3.9). Note that the error does not decrease monotonously. Such an error decay is a traditional result when using a Galerkin formulation

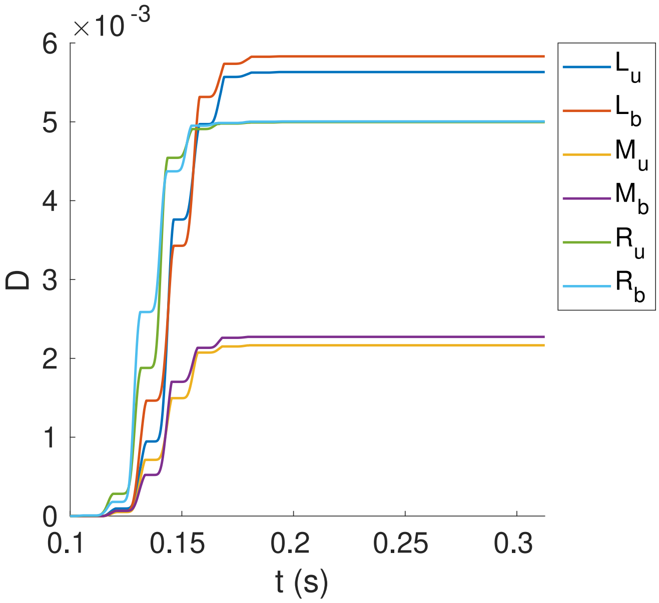

Figure 3.8 • Damage evolution at different points of the beam (Figure 3.5) solicited with load 1 - $f = 40\,\text{Hz}$ at $U_d^{\max} = 100\,\text{mm}$

for the PGD implementation as it is done here. The interested reader can refer to [Nouy, 2010] for further information on how the PGD implementation can impact the error decay. The resulting reduced model comprises only six modes. Thus, most iterations were very cheap as they consisted in updating the frequency modes and, for only less than a third of the iterations, spatial computations were performed.

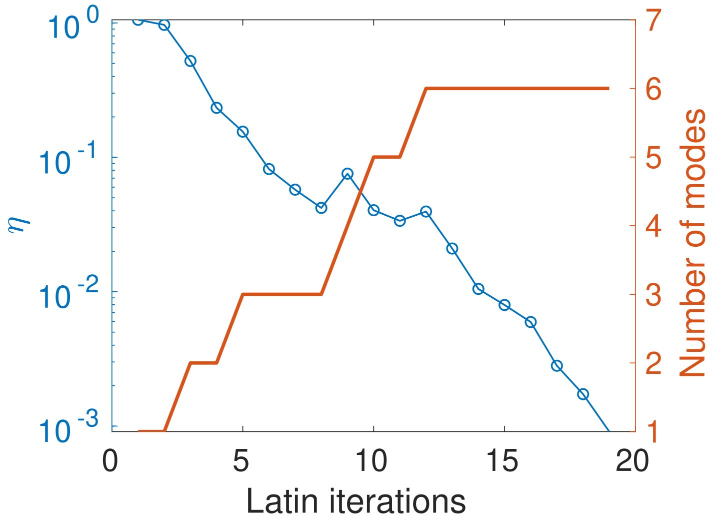

Figure 3.9 • Convergence of the error indicator and evolution of the number of PGD modes with LATIN iteration for the beam solicited with load 1 - $f = 40\,\text{Hz}$ and $U_d^{\max} = 100\,\text{mm}$

The six obtained spatial modes are shown in Figure 3.10. The first two modes lead to global corrections whereas the following modes, shown for instance in Figures 3.10g and 3.10k, highlight patterns at each end of the beam that follow patterns depicted by the damage field (Figure 3.7). The PGD modes therefore target corrections specific to the non-linearities appearing in the structure. To highlight the fact that the strategy allows to build modes that are specific to the problem, the spatial PGD modes can be compared to the 6 (energetically) predominant classical linear modes; they are smoother and don't exhibit localised patterns.

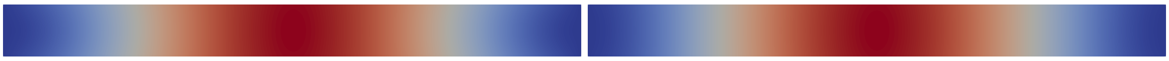

(a) PGD mode n°1 **(b)** Eigenmode n°1

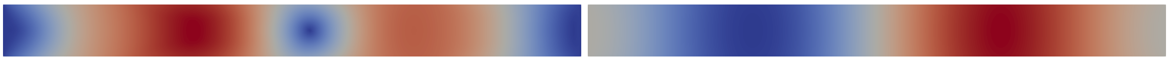

(c) PGD mode n°2 **(d)** Eigenmode n°2

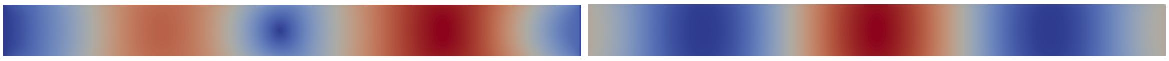

(e) PGD mode n°3 **(f)** Eigenmode n°3

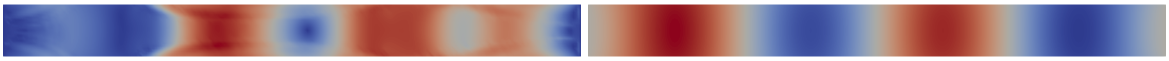

(g) PGD mode n°4 **(h)** Eigenmode n°4

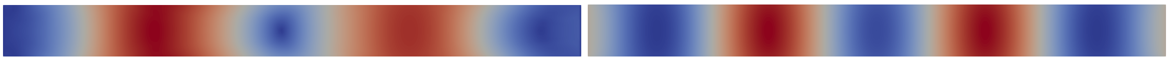

(i) PGD mode n°5 **(j)** Eigenmode n°5

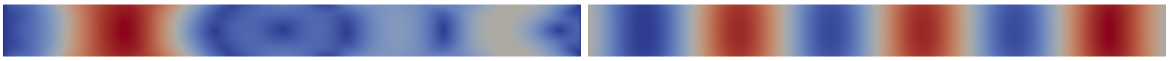

(k) PGD mode n°6 **(l)** Eigenmode n°6

Figure 3.10 • Magnitude of PGD modes for the beam solicited with load 1 - $f = 40\,\text{Hz}$ and $U_d^{\max} = 100\,\text{mm}$ compared to energetically predominant eigenmodes

Similarities between the spatial PGD modes and the natural eigenvectors of the beam can be quantified through their energetic scalar product. The obtained values are represented within the Modal Assurance Criterion (MAC) matrix [Allemang & Brown, 1987] shown in Figure 3.11. The first PGD mode matches closely the first eigenvector. The second PGD mode, as well as the third and fifth PGD modes have similarities with the second eigenmode while the fourth and sixth PGD modes don't share significantly similar information with the eigenmodes, as they rather focus on local non-linear behaviour.

It is also interesting to compare LATIN computations associated with an adaptive PGD basis or with a fixed basis comprising the first 100 eigenvectors. To do so, a relative error Ξ is evaluated for any iteration n of the LATIN by comparing a reference solution $U_{overkill}$ being an overly converged LATIN-PGD solution considering $\eta_c = 2 \times 10^{-4}$ with U_n the current solution at the $n-th$ iteration either with a PGD approach or with a projection onto the eigenvectors basis, as follows

$$\Xi = \frac{\left(U_{overkill} - U_n\right)^T [K] \left(U_{overkill} - U_n\right)}{U_{overkill}^T [K] U_{overkill}}. \tag{3.37}$$

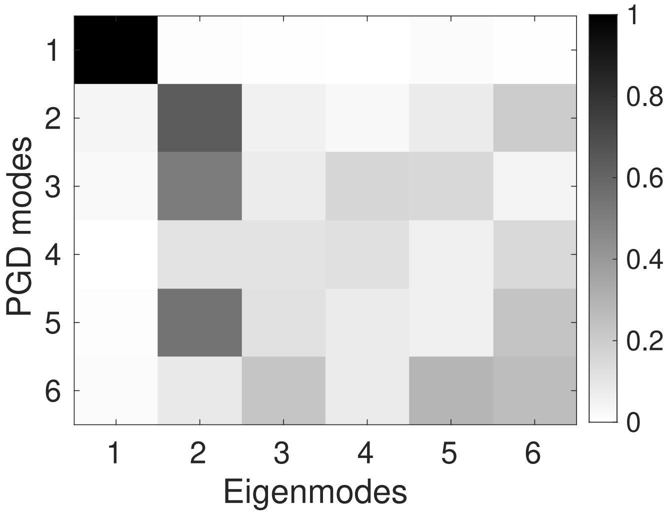

Figure 3.11 • Modal Assurance Criterion Matrix of the PGD modes and the eigenmodes for the beam solicited with load 1 - $f = 40\,\text{Hz}$ and $U_d^{\max} = 100\,\text{mm}$

The evolution of these errors with LATIN iteration is shown in Figure 3.12. During the first iteration, the error is mostly attributable to the two-alternated search direction scheme that is far from the converged solution therefore the error given by both computations based on the eigenvector basis and the one using the PGD is the same. But, the PGD basis provides quickly a better estimation than the fixed basis. After ten iterations, the LATIN computation based on the eigenbasis leads to a stagnating error. It seems that the method does not appear to be able to decrease below that plateau. However, using the PGD basis, the error decreases significantly below that plateau by generating new optimised modes.

The temporal functions associated with the spatial PGD modes are shown in Figure 3.13; their frequency counterparts are given in Figure 3.14. It can be seen in both figures that the first mode significantly outperforms the following modes. On the temporal domain (Figure 3.13), the temporal information of the damage evolution (Figure 3.8) can be clearly seen on the PGD modes. The non-linear behaviour is significant only after 0.1 s and stagnation of some modes such as mode 4 can be observed after 0.2 s. It can be highlighted that this stagnation is not for a zero-value, conveying a permanent perturbation due to the non-linear behaviour. Note that artificial damping is therefore needed. Indeed, even in cases where the steady state is reached within the considered temporal window, special care must be paid to avoid Gibbs phenomena due to the existence of possible residual displacements associated with non-linear phenomena. The frequency modes (Figure 3.14) show that even a simple mono-frequency load can lead to a complex spectrum of the non-linear response. The first mode exhibits a main contribution around 30 Hz, which corresponds to the first eigenfrequency of the structure (second and third eigenfrequencies are 78 Hz and 142 Hz), but the following modes show less and less this predominant frequency band and the last modes are distributed over the frequency domain with a tortuous spectrum as shown in Figure 3.13. Note that the study of damage evolution is mainly interesting during the transient regime, the

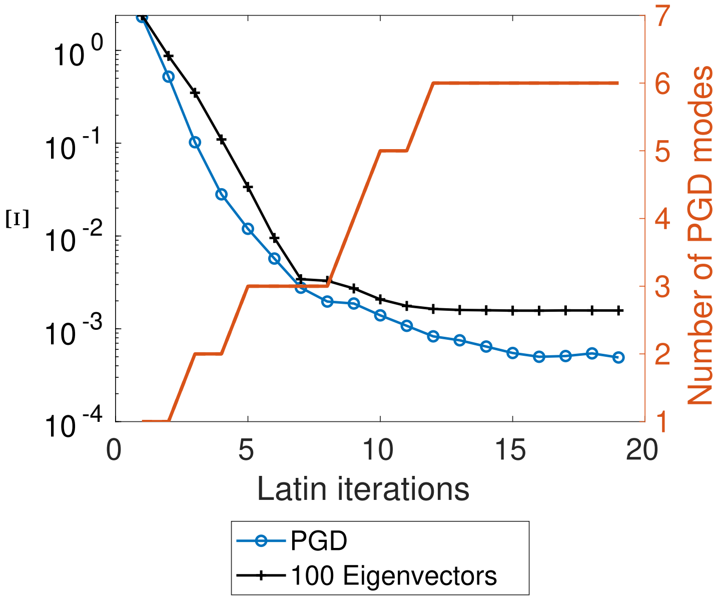

Figure 3.12 • Evolution of the error with LATIN iteration using an adaptive PGD basis or a fixed basis comprising the first 100 eigenmodes for the beam solicited with load 1 - $f = 40\,\text{Hz}$ and $U_d^{\max} = 100\,\text{mm}$

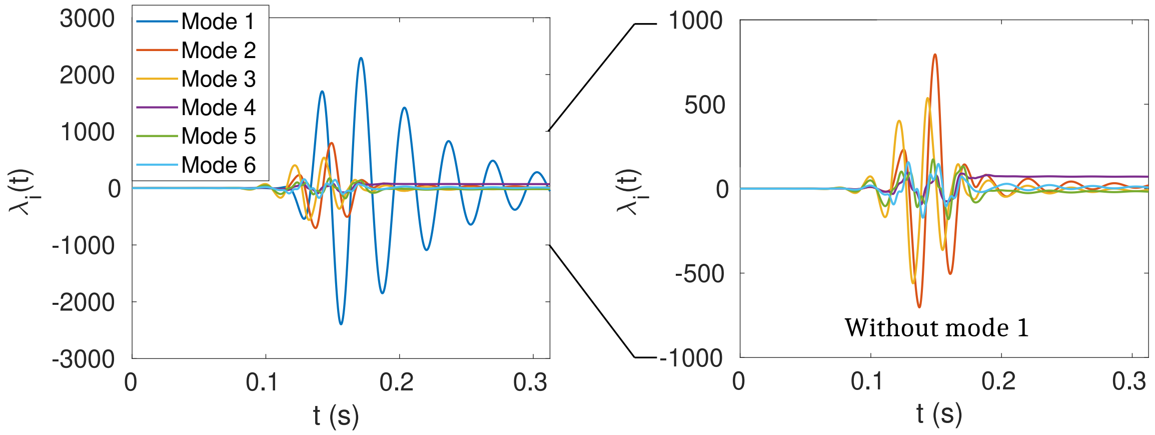

Figure 3.13 • Six estimated temporal PGD modes for the beam solicited with load 1 - $f = 40\,\text{Hz}$ and $U_d^{\max} = 100\,\text{mm}$

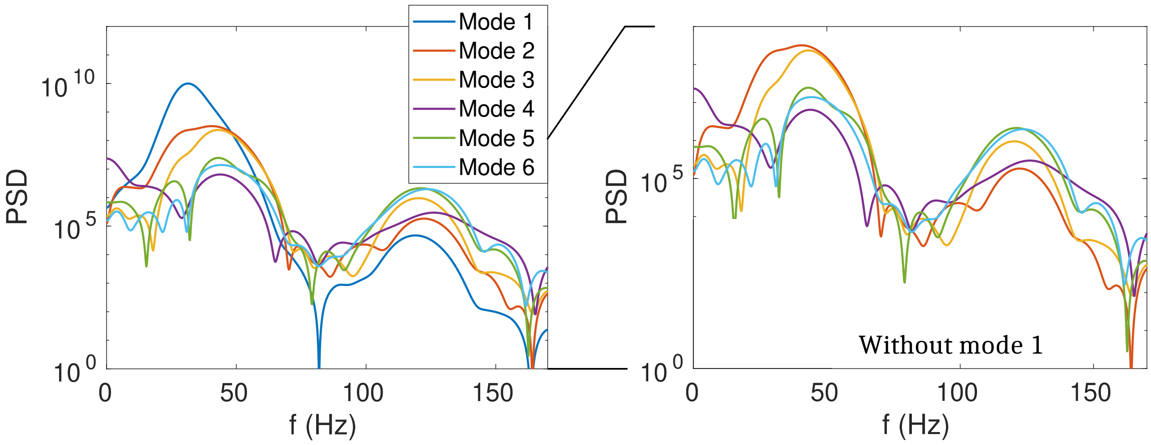

Figure 3.14 • Power spectral densities (PSD) of the six estimated frequential PGD modes for the beam solicited with load 1 - $f = 40\,\mathrm{Hz}$ and $U_d^{\max} = 100\,\mathrm{mm}$

study has therefore been narrowed down to such a window (see Figure 3.8). The importance of the artificial damping in that context is exposed in Figure 3.15 where the displacement along the y-axis at point P_I with $x_{P_I} = L_b/2$ and $y_{P_I} = W_b/2$ given by the elastic initialisation is shown. Considering a temporal computation given by a classic Newmark scheme (Figure 3.15a), the steady-state displacement is not reached at the end of the considered temporal window. A frequency computation without artificial damping (Figure 3.15b) leads to unwanted temporal overlap rendering the solution acausal. Adding artificial damping (Figure 3.15c) provides proficient results, which is illustrated by the comparisons exposed in Figure 3.15d.

In details, the artificial damping relies on the damping rate a_d (see equation (3.28)). That parameter value is derived from the choice of a value for the damping coefficient d at the end of the temporal loading with $a_d = \log(d)/T_0$. The numerical influence of d has been investigated for the elastic initialisation for the same point of interest P_I in terms of an overlapping error defined by comparing the vertical displacement components of a temporal reference solution U^{ref} with a dampened frequency estimation U^{freq}, as follows

$$\zeta = \max_{t\in I} \frac{|U^{freq} - U^{ref}|}{\max_{t\in I} U^{ref}} \tag{3.38}$$

The evolution of the overlapping error with the value of the damping coefficient (Figure 3.16) shows a strong and maximum error with the value $d = 1$, which corresponds with $a_d = 0$, i.e. without considering artificial damping. The addition of numerical damping only improves the solution by compensating the artefact introduced by the temporal overlapping. The decrease of error is strong by increasing the value from 1 to 100, then, it tends to stagnate. The very weak dependence of the damping coefficient above $d = 100$ proves the robustness of the method with respect to high damping values. A minimum appears for $d = 1 \times 10^3$, which has then been used for all numerical results shown in this article.

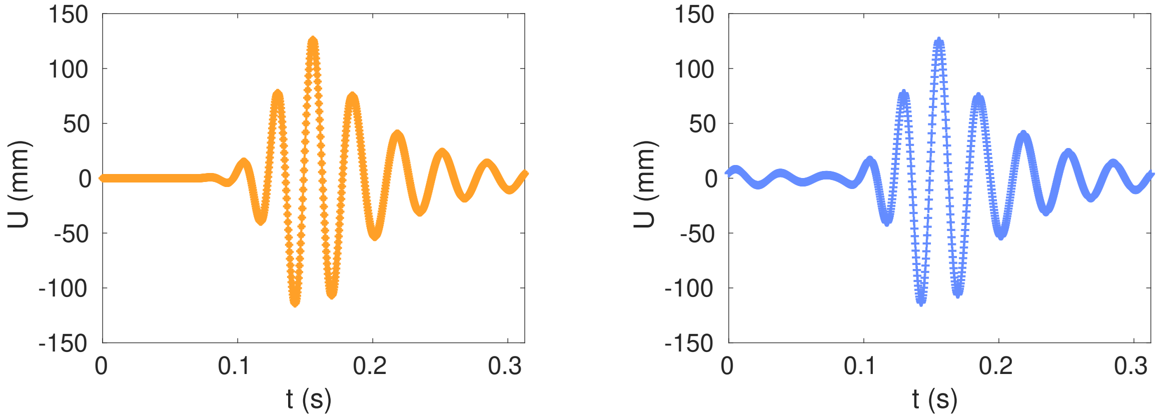

(a) $U(t)$ temporal computation **(b)** $U(t)$ frequency computation

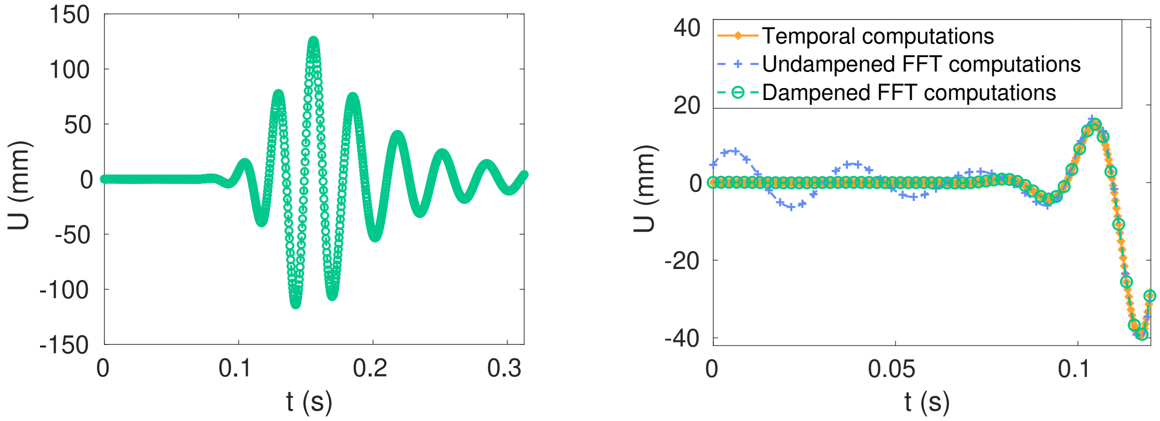

(c) $U(t)$ dampened frequency computation **(d)** Comparison of the three methods

Figure 3.15 • Numerical effect of the artificial damping: comparison of the temporal, non-dampened (showing unwanted artefacts) and dampened frequency computations for the elastic initialisation at point P_I of the beam solicited with load 1 - mono-frequency Gaussian load with $f = 40\,\mathrm{Hz}$ and $U_d^{\max} = 100\,\mathrm{mm}$

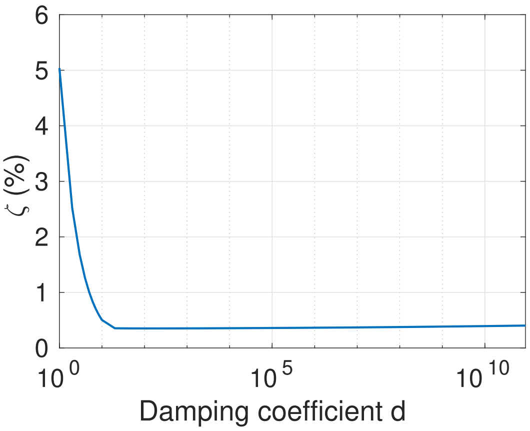

Figure 3.16 • Evolution of the overlapping error ζ for dampened frequency computation with regard to the damping coefficient d for the beam solicited with load 1 - mono-frequency Gaussian load with $f = 40\,\mathrm{Hz}$ and $U_d^{\max} = 100\,\mathrm{mm}$

Bi-frequency loading

A second loading case (Figure 3.17), which is the sum of two sinus functions with different frequencies, as follows

$$U_d(t) = U_d^{\max} \exp\left(-\left(10\frac{(t-\frac{T_0}{2})}{T_0}\right)^2\right)\left(\sin\left(2\pi f_a\ t\right) + \sin\left(2\pi f_b\ t\right)\right) \tag{3.39}$$

is considered such that the robustness and behaviour of the method for various frequency spectra of the load can be studied. The final time is $T_0 = 0.3125\,\mathrm{s}$ and $N_t = 1024$ time steps were employed. The values of the loading parameters are $f_a = 40\,\mathrm{Hz}$, $f_b = 80\,\mathrm{Hz}$ and $U_d^{\max} = 30\,\mathrm{mm}$.

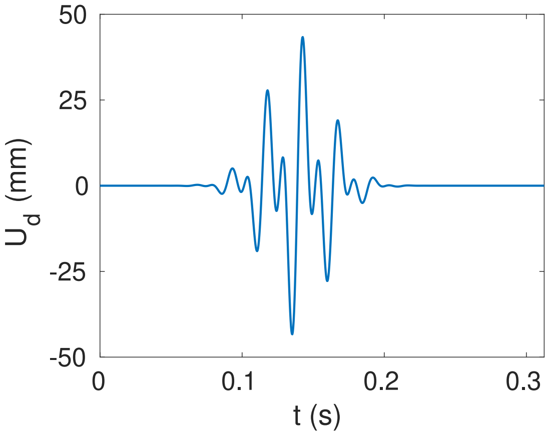

Figure 3.17 • Temporal load 2 - bi-frequency Gaussian case

Similar convergence behaviour as for the mono-frequency load has been observed. It is interesting to look at the new spectrum of frequency modes in Figure 3.18. Comparing with the mono-frequency case, the contribution of the different modes is more distributed over the frequency domain, particularly the first mode, which is composed of a large bump. It is remained that the two first eigenfrequencies are $f_1 = 32\,\text{Hz}$ and $f_2 = 78\,\text{Hz}$. Following modes tend to correct the response more locally over the frequency space. Besides, the different modes seem to equally contribute to the solution, whereas the first mode was far more prominent than the others for the previous loading scenario.

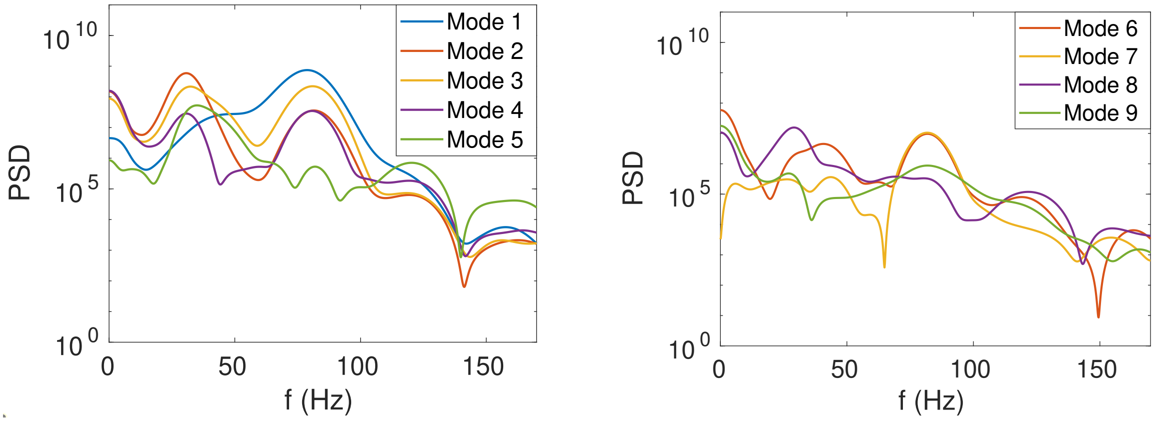

(a) Frequency modes 1 to 5

(b) Frequency modes 6 to 9

Figure 3.18 • Power Spectral Density of the nine estimated PGD modes for the beam solicited with load 2 - bi-frequency load with $f_a = 40\,\text{Hz}$, $f_b = 80\,\text{Hz}$ at $U_d^{\text{max}} = 30\,\text{mm}$

Complex loading

In order to evaluate the versatility of the proposed method, a modified earthquake load shown in Figure 3.19 has been considered. This loading lies over $I = [0\,\text{s}, 3\,\text{s}]$ and it has been discretised uniformly with 4400 time steps ($\delta t \approx 7 \times 10^{-4}\,\text{s}$).

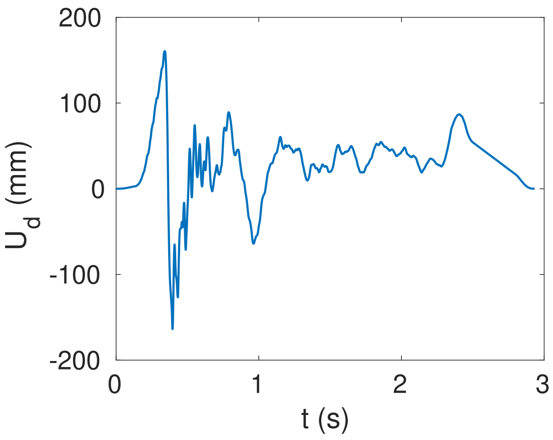

Figure 3.19 • Temporal load 3 - a complex load

The load frequency fluctuates, it is high in the first second of the signal, whereas it is relatively slow in the following two seconds. It is interesting to see that the corrections given by the temporal modes shown in Figure 3.20 grasp that information, as they give high-amplitude correction in the first second of the simulation. The rest of the temporal domain shows rather stagnating correction as the non-linearities tend to stop evolving.

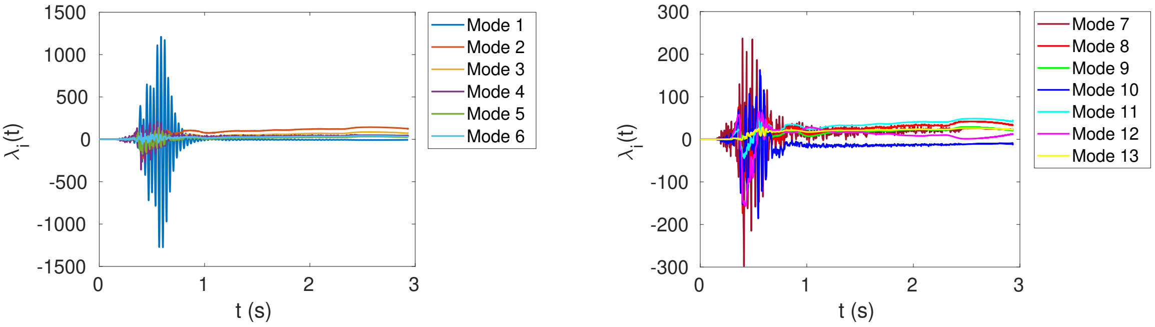

(a) Temporal modes n°1 to n°6

(b) Temporal modes n°7 to n°13

Figure 3.20 • Temporal PGD modes for the beam solicited with load 3 - a complex load

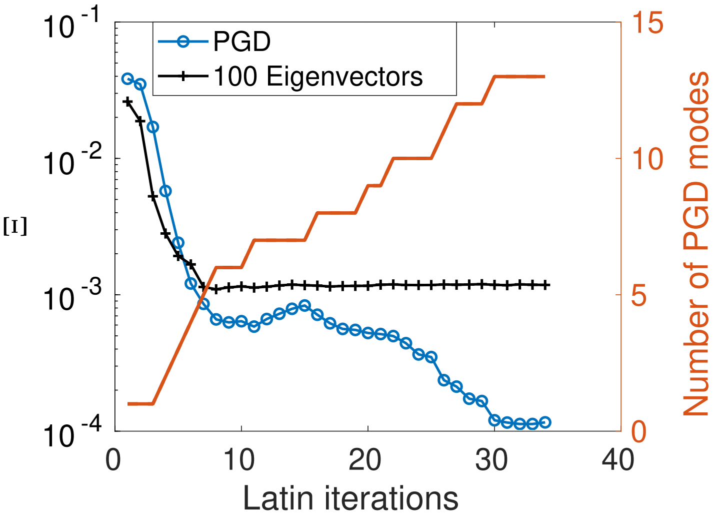

Figure 3.21 • Evolution of the error with LATIN iteration using an adaptive PGD basis or a fixed basis comprising the first 100 eigenmodes for the beam solicited with load 3 - a complex load

Thirteen PGD modes and 35 LATIN iterations are needed to reach the stopping criterion $\eta_c = 2 \times 10^{-3}$. Comparing the PGD basis with the eigenbasis of 100 vectors in Figure 3.21, a similar behaviour as for the mono-frequency load 1 is observed. After eight iterations, the accuracy of the LATIN method based on the eigenbasis stagnates to a plateau. The non-linear behaviour is ultimately much better described with a small number of PGD modes (5 to 13 modes) computed on the fly than with 100 eigenvectors.

The MAC matrix (Figure 3.22) between the PGD modes and the eigenmodes confirms the difference between the PGD basis and the eigenbasis. Except from the first and fifth PGD modes which are very similar to the first and third eigenmodes, respectively, most PGD modes largely differ from the first 13 eigenvectors.

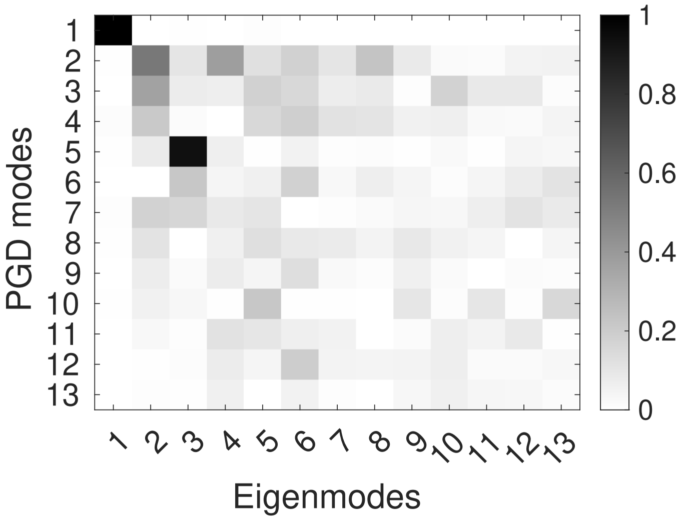

Figure 3.22 • Modal Assurance Criterion (MAC) matrix comparing the basis of PGD modes with classical LNMs for the beam solicited with load 3 - a complex load

3.2 Three-dimensional pipe

A three-dimensional L-shaped pipe, as schematised in Figure 3.23, has also been studied. The dimensions of the structure are given in Table 3.2. This structure has been meshed with 119, 682 second-order tetrahedral elements.

Middle pipe height:	$H_1 = 3\,\mathrm{m}$
Top pipe height:	$H_2 = 0.5\,\mathrm{m}$
Pipe mid-length:	$L_1 = 1.86\,\mathrm{m}$
Pipe top length:	$L_2 = 2\,\mathrm{m}$
Pipe external diameter:	$D_e = 0.5\,\mathrm{m}$
Pipe internal diameter:	$D_i = 0.48\,\mathrm{m}$
Pipe bending radius:	$R_c = 0.25\,\mathrm{m}$

Table 3.2 • Geometrical parameters of the pipe

The pipe is submitted to a moving-support type of loading (Figure 3.23). A three-dimensional load whose components are plotted in Figure 3.24 is imposed to the bottom section through the boundary conditions of the pipe, as shown in Figure 3.23. More compliant conditions

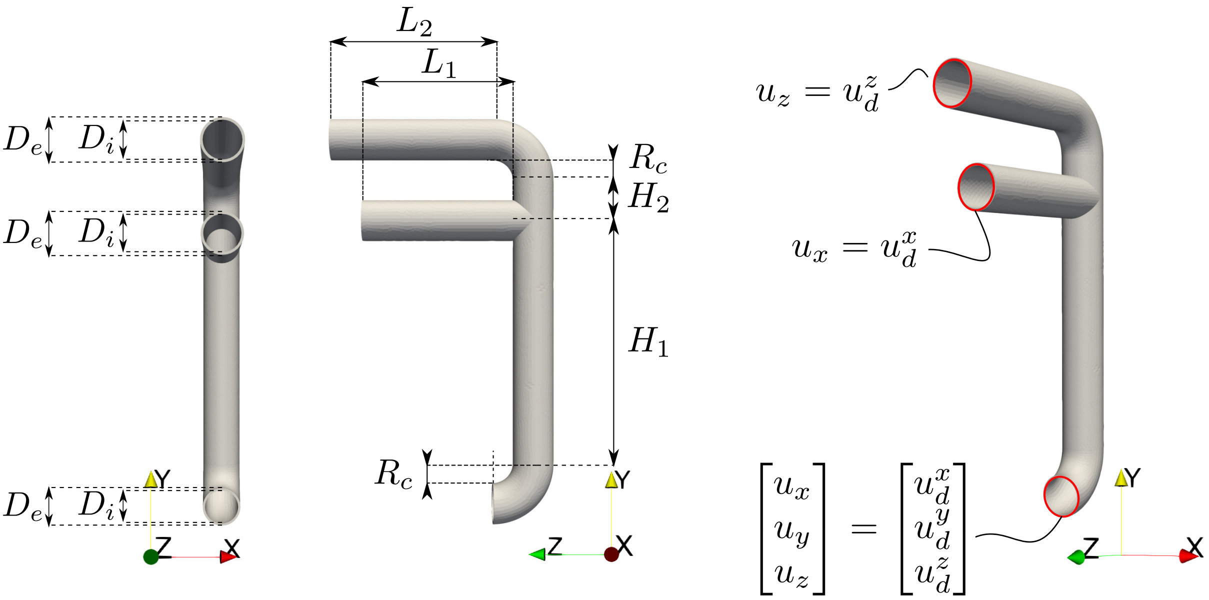
D_e
D_i
D_e
D_i
D_e
D_i
Y
Z
X
L_2
L_1
R_c
H_2
H_1
R_c
Y
Z
X
$u_z = u_d^z$
$u_x = u_d^x$
$\begin{bmatrix} u_x \\ u_y \\ u_z \end{bmatrix} = \begin{bmatrix} u_d^x \\ u_d^y \\ u_d^z \end{bmatrix}$
Y
Z
X

Figure 3.23 • Three-dimensional structure with boundary conditions

are applied to the top and middle sections where displacement is only imposed in the z-direction and in the x-direction respectively. This loading lies over $I = [0\,\mathrm{s}, 9\,\mathrm{s}]$ and it has been discretised uniformly with 4,400 time steps ($\delta t \approx 2 \times 10^{-3}\,\mathrm{s}$).

Convergence behaviour is given in Figure 3.25. It is interesting to note that, in that case too, only a few PGD modes, exactly 13 modes, are sufficient to represent accurately the solution. These modes are evaluated after 35 LATIN iterations. Therefore, more than half of the iterations simply consist of updating the frequency modes without adding new spatial modes.

Finally, the quantity of interest, namely the damage field, can be extracted as shown in Figures 3.26 and 3.27. It appears on the three-dimensional fields shown in Figure 3.26 that damage mostly grows at the T-junction of the pipe where a stress concentration occurs. We can observe in Figure 3.27 that damage grows between 1.2 s and 2 s which corresponds to the time of occurrence of the dominant peak in the load. After $t = 2\,\mathrm{s}$ the non-linearities stop evolving because the structure is only stressed such that the stored energy remains below the damage threshold. Figure 3.27 also shows the final damage field in the pipe on the deformed structured at time $t = 2\,\mathrm{s}$ with a magnification factor of 10.

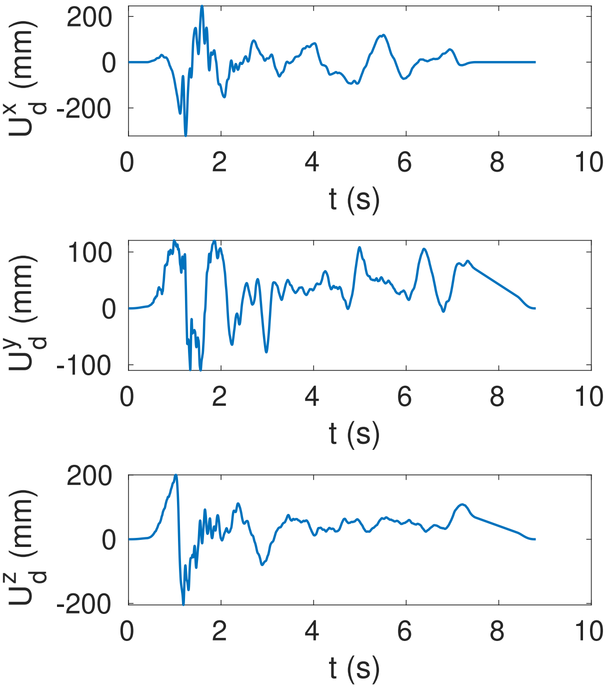

Figure 3.24 • Three-dimensional complex load applied to the pipe's boundary conditions

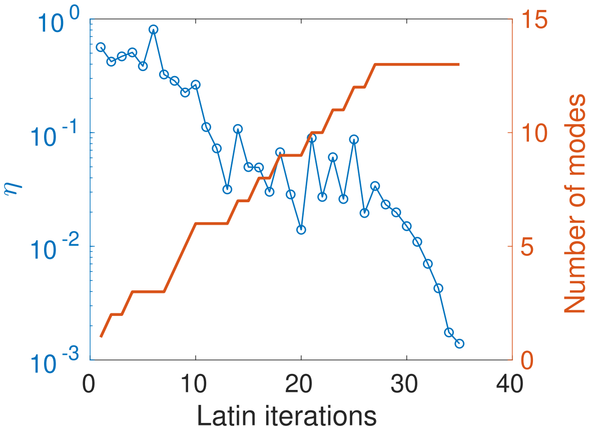

Figure 3.25 • Evolution of the error indicator and the number of PGD modes for the three-dimensional pipe structure solicited with a complex load

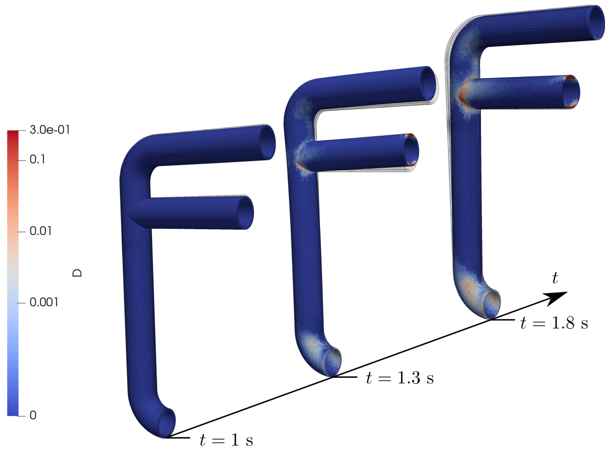
3.0e-01
0.1
0.01
0.001
0
D
t
$t = 1.8$ s
$t = 1.3$ s
$t = 1$ s

Figure 3.26 • Evolution of the damage field for the pipe solicited with a complex loading

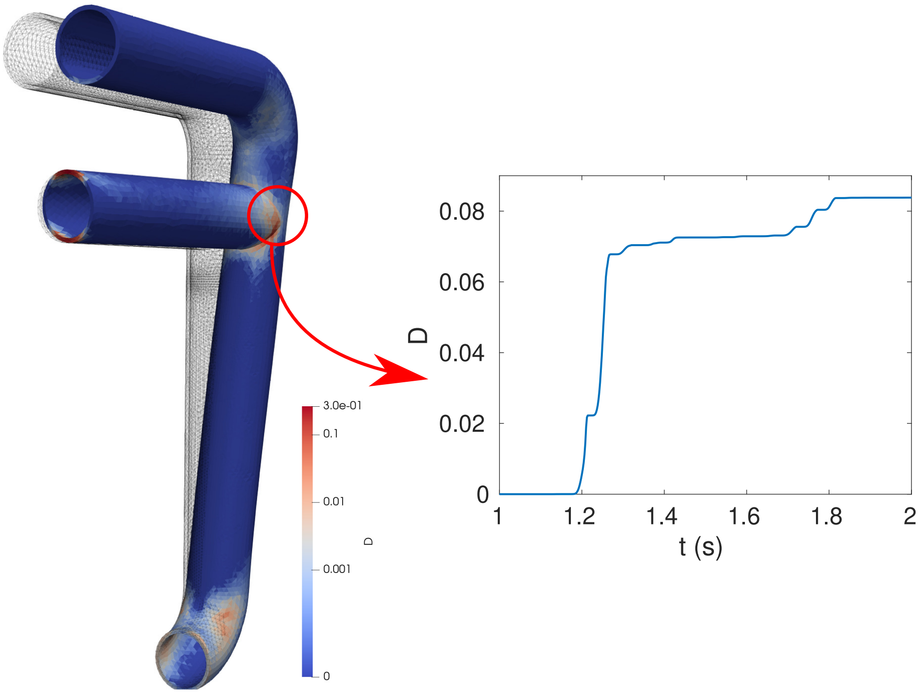

Figure 3.27 • Damage field in the three-dimensional pipe structure solicited with a complex load at time $t = 2$ s and damage evolution at the T-junction between the tube and the middle branch over time

Chapter summary

An original hybrid LATIN-PGD framework has been proposed for damageable materials in dynamics. The computations of the dynamics aspect are handled in the frequency domain while still solving for the non-linear behaviour in the temporal domain. Predicting the damage evolution of a damageable plastic structure under dynamic loading has been shown for various load conditions. This work successfully implements a hybrid time-frequency approach for continuous damage mechanics. The FFT algorithm is used even with residual displacements due to plasticity by introducing artificial damping to avoid Gibbs phenomena. The results also highlight the great reducibility of low-frequency dynamics problems with a plasticity-driven damage behaviour. Indeed, few PGD modes are needed to represent the solution to the different problems tackled in this chapter. Fewer modes lead to fewer spatial problems, ultimately reducing numerical cost. The method appears versatile with reduced computational cost due to the adaptive PGD basis, and it offers rich information with the prediction of a large set of internal variables over the full time-space domain.
This chapter thus presents an initial partial answer to the general problem addressed in this doctoral thesis by providing a method to decrease the computational burden associated with each calculation of the study.

* * *

Perspectives

It then remains to address the multi-query context, using the redundancy between the different calculations. In such a multi-query framework, generating PGD modes is advantageous since these modes can be reused for different calculations. Furthermore, in a multi-query context, the non-incremental aspect of the solver is also a strength as it allows to initialise the non-linear scheme with a converged space-time solution that may be close to the exact solution sought, thus decreasing the computational time associated with new simulations after a first computation has been performed.
This solver appears as a building block that can be judiciously used in a specific multi-query framework yet to be defined. The next chapter will focus on detailing such a framework for multiple-loading scenarios.

Chapter 4

Enhanced reduced-order model for efficient multi-load computations of non-linear dynamics problems

> The only true and sustainable prosperity is shared prosperity.
>
> Joseph E. Stiglitz

This chapter presents a robust multi-query framework for uncertainty loadings study. Previous solutions are used to wisely initialise the non-incremental solver, thus decreasing the numerical cost of the multi-query study. A physical-based strategy using the mechanical content of elastic responses is proposed to find the most relevant previous computations to boost the current simulation. The optimal computation sequence, i.e. *the optimal path, is designed using a genetic algorithm based on the physical-based distance indicator.*

Contents

1 Multi-query context 83
2 LATIN-PGD scheme enhanced from a previous non-linear dynamics simulation 84
  2.1 Initialisation of the PGD basis 84
  2.2 Initialisation of the LATIN scheme 86
3 Proximity indicator 86
  3.1 Singular value decomposition of each dynamic elastic solution 87
  3.2 Proximity indicator between dynamics elastic solutions based on the singular value decomposition 88

4 Enhanced strategy in the multi-query context 90
4.1 Optimal path through the multi-load simulations 90
4.2 Choice of the parent-simulation computation 91
4.3 Overview 91
5 Numerical studies 93
5.1 Initialisation strategy in the multi-query context on the full order model 93
5.2 Reduced-order model improvements 94
5.3 Interpretation of the results in the parametric space 101
5.4 Influence of the number of computations in the multi-query study . . 102
Chapter summary & perspectives 104

One goal of this work consists in efficiently computing the evolution of plasticity-driven damage non-linearities under multiple dynamic loading scenarios, which can then be applied to risk assessment for instance. The idea is to exploit the model-order reduction method presented in Chapter 3 as a foundation for setting up an optimised strategy for conducting simulations corresponding to each of the loading scenarios. At this point, we should remind the reader that the method presented in this chapter is designed for the case of seismic risk prediction, where a prior parametrisation of the loadings is inaccessible, the latter being supplied as a list of indexed time series as illustrated in Figure 4.1. Particular attention is therefore paid to the fact that the methodology does not rely on such parametrisation, *i.e.* on an explicit parametric definition of the signals.

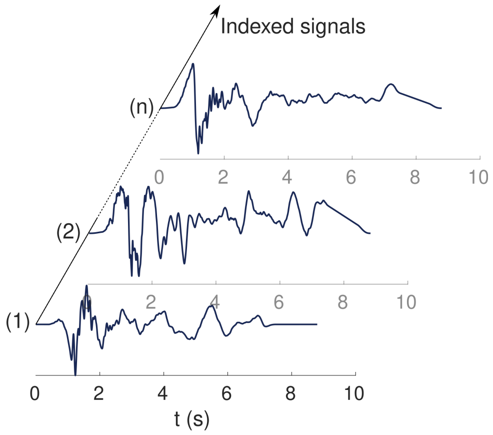

Figure 4.1 • Non-parametrised indexed loading scenarios

As in the case of material variability [Boucard & Ladevèze, 1998], the reduced basis and the solution from a previous computation nourish the new calculation. The reuse of the reduced basis is straightforward. However, initialising the solution requires a specific strategy because the problems associated with the different loading scenarios do not share the same boundary conditions. Thus, the displacement field of a previous load case cannot be used directly to initialise the LATIN scheme since it does not satisfy the admissibility equations of the new problem. The proposed initialisation consists in superposing the elastic calculation corresponding to the loading conditions of interest and the inelastic homogeneous correction associated with a well-suited non-linear solution already evaluated. While the choice of such previous computation to accelerate the current simulation was straightforward for parametrised variable material parameters using a distance in the parametric space, new tools are needed to assess the distance between one computation and another when it comes to boundary conditions variability in a non-parametrised context. We propose to select the best candidate based on the distance between the elastic solutions of different loading scenarios. The elastic responses of the structure contain some decisive mechanical information for the distance estimation between the associated damage evolution. Each elastic response is decomposed by a Singular Value Decomposition (SVD). The distance between subspaces can be determined on the Grassmann manifolds, which comprise spaces spanned by the basis of singular vectors of each computation, using the Grassmann distance, *e.g.* [Shigenaka et al., 2012; Ryckelynck et al., 2011]. However, this distance does not provide information about the response magnitude. Therefore, an original indicator is proposed to assess the proximity between calculations based on singular values and vectors. From this indicator, the calculations are performed in an order which maximises the proximity between them using the latest developments in genetic algorithms.

The chapter is organised as follows. Section 2 details the acceleration of the non-linear scheme by smart initialisation and the reuse of an existing reduced basis in a bi-computations context where two computations are performed sequentially. Section 3 details the physics-based distance indicator between two computations to extend that work in a multi-query context. This distance indicator allows setting up the multi-query framework shown in Section 4, where a robust strategy is proposed to find an optimal sequence for the multiple computations. Finally, Section 5 outlines the numerical results obtained using the proposed framework in a simple multi-query context.

1 Multi-query context

The ROM hybrid frequency-temporal LATIN-PGD scheme has been presented in Chapter 3 and is referred to as the standard LATIN-PGD scheme. The LATIN simulation usually begins with an empty initial basis $\mathscr{B}_0 = \emptyset$ of space functions. Once a space function has been estimated, the displacement correction is first looked for by only updating the frequency modes while keeping the space functions unchanged. In detail, at iteration $n+1$, for instance, if m modes are already in the reduced basis, the frequency modes $\{\check{\lambda}_i(\omega)\}_{i\in[\![1,m]\!]}$ are updated while $\{\overline{\boldsymbol{u}}_i(\boldsymbol{x})\}_{i\in[\![1,m]\!]}$ remain unchanged. If sufficient, this update stage decreases computational costs. If not, the space basis is enlarged by computing a new pair comprising one space and one frequency mode such that $\boldsymbol{\Delta u_{n+1}} = \lambda_{m+1}(t)\overline{\boldsymbol{u}}_{m+1}(\boldsymbol{x})$. Each following LATIN stage begins with an update of frequency functions. The algorithm thus increases the dimension of the PGD reduced basis adaptively so that the displacement correction reads

$$\boldsymbol{\Delta u}(\boldsymbol{x},t) = \sum_{i=1}^{m} \lambda_i(t)\overline{\boldsymbol{u}}_i(\boldsymbol{x}). \tag{4.1}$$

The problem of interest concerns situations where the prescribed forces $\boldsymbol{F}_d$ on $\partial\Omega_2$ or displacements $\boldsymbol{u}_d$ on $\partial\Omega_1$ are uncertain or consist of a set of different loading scenarios. Loading uncertainty is particularly crucial when building response surfaces or for risk assessment. Extensive literature exists about the best representation of the response surfaces using adaptive sampling [Fuhg et al., 2020], or innovative strategies dedicated explicitly to risk assessment [Gidaris et al., 2015; Fuhg & Fau, 2022].

Here the goal is not to reduce the number of simulations required for the multi-query study but to efficiently compute a given set of non-linear dynamic simulations. The enhanced methodology is designed for computations associated with various Dirichlet boundary conditions with a fixed spatial distribution, which means that the surface $\partial\Omega_1$ remains the same for all computations. Uncertainty in terms of displacement conditions can be either expressed as raw input data i.e., a set of samples $\left\{\boldsymbol{u}_d^{(i)}(t)\right\}$ with $i \in [\![1; n]\!]$ and n the number of experiments included in the design of experiments, or a parametrised displacement $\boldsymbol{u}_d(t, \boldsymbol{\alpha}^{(i)})$ with $\left\{\boldsymbol{\alpha}^{(i)}\right\}$ a set of parameter samples.

> **Remark** Uncertainty in terms of material parameters or in terms of Neumann boundary conditions could also be included. Uncertain Neumann boundary conditions can even include changes of the surface $\partial\Omega_2$. However, the proposed strategy would not be required; the parametric approach exposed in [Heyberger et al., 2012] would be efficient for such cases.

2 LATIN-PGD scheme enhanced from a previous non-linear dynamics simulation

Let computation (k) be the current LATIN-PGD computation, which can be nourished by the previous simulation (j). Two perspectives are used to reduce the computational cost for computation (k) as proposed in [Boucard & Ladevèze, 1998] for material parameters. The strategy is illustrated in Figure 4.2. First, the LATIN-PGD for the current computation (k) is initialised with an admissible solution improved by the non-linear corrections of the so-called parent-simulation (PS) denoted (j). Second, the PGD basis built for computation (j) is employed as an initial basis for computation (k). It is hoped that these two ingredients provide an initialisation closer to the solution than the naive initialisation.

The enhanced variant of the LATIN solver only modifies the initialisation and the initial global stage. The following iterations are classically performed with the non-linear hybrid LATIN-PGD algorithm proposed in [Daby-Seesaram et al., 2023].

2.1 Initialisation of the PGD basis

The LATIN-PGD method relies on a reduced-order description of the displacement field. The global dynamics problem given in (1) is solved using a frequency-space separation of variables. Thus, the current simulation (k) is fed with the reduced basis

$$\mathscr{B}^{(j)} = \left\{\overline{\boldsymbol{u}}_i^{(j)}(\boldsymbol{x})\right\} \tag{4.2}$$

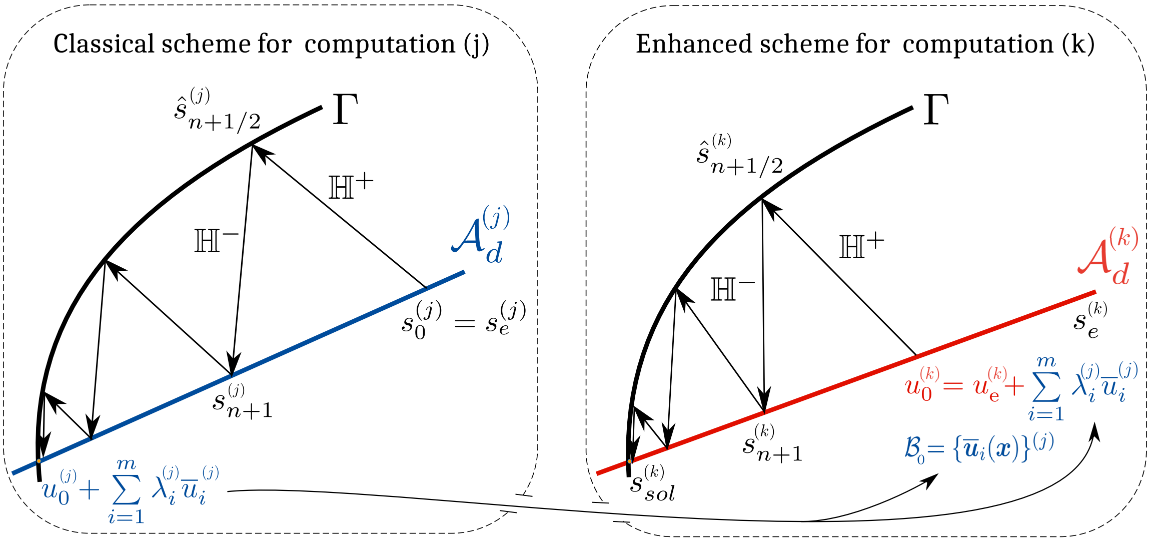
Classical scheme for computation (j)
$\hat{s}^{(j)}_{n+1/2}$
Γ
$\mathbb{H}^+$
$\mathbb{H}^-$
$\mathcal{A}_d^{(j)}$
$s_0^{(j)} = s_e^{(j)}$
$s^{(j)}_{n+1}$
$u_0^{(j)} + \sum_{i=1}^{m} \lambda_i^{(j)} \overline{u}_i^{(j)}$
Enhanced scheme for computation (k)
$\hat{s}^{(k)}_{n+1/2}$
Γ
$\mathbb{H}^+$
$\mathbb{H}^-$
$\mathcal{A}_d^{(k)}$
$s_e^{(k)}$
$u_0^{(k)} = u_e^{(k)} + \sum_{i=1}^{m} \lambda_i^{(j)} \overline{u}_i^{(j)}$
$s^{(k)}_{n+1}$
$\mathcal{B}_0 = \{\overline{u}_i(x)\}^{(j)}$
$s^{(k)}_{sol}$

Figure 4.2 • Standard and enhanced non-linear LATIN-PGD schemes

from the parent non-linear simulation so that the initial basis for (k) reads

$$\mathscr{B}_0^{(k)} = \mathscr{B}^{(j)}. \tag{4.3}$$

Therefore, even the first *global stage* of computation (k) begins with an update of the frequency functions. Updating requires low computational costs and memory, and providing pertinent initial reduced bases to parametric simulations, the LATIN method can then mainly behave as a cheap *a posteriori* method. In [Heyberger et al., 2012], the PGD basis established for the first value of the material parameter is transferred to the computations for all other material parameter values, which converge without requiring any additional mode.

The LATIN-PGD method is *per se* an *a priori* method. Therefore, if the provided reduced basis is not suited to describe the displacement field of the non-linear simulation (k), the reduced basis is automatically extended along with the LATIN iterations. The adaptivity of the method provides a robust and accurate solver. However, for damage simulations under variable loading, the PGD basis tends to increase drastically [Alameddin et al., 2020]. Efficient basis compression using a randomised singular value decomposition has been proposed in [Alameddin et al., 2019] to retain small-sized optimal PGD bases. Along the same line, even with a large set of previously computed solutions, the PGD basis of a single previous simulation is employed in the enhanced LATIN-PGD scheme. Besides, the unexploited PGD modes are automatically excluded after the updating stage. If a frequency mode vanishes as

$$\int_I \lambda_i^2(t)\mathrm{d}t \leqslant \eta_\lambda \tag{4.4}$$

with η_λ a user-chosen threshold, the associated spatial mode $\overline{\boldsymbol{u}}_i(\boldsymbol{x})$ is removed from the reduced basis of (k).

2.2 Initialisation of the LATIN scheme

The LATIN-PGD method is a time-space approach, which needs to be initialised with an admissible displacement field on the whole time-space domain. Instead of the traditional elastic solution, computation (k) starts from the displacement field $\boldsymbol{u}_0^{(k)}$ defined as

$$\boldsymbol{u}_0^{(k)}\left(\boldsymbol{x}, t\right) = \boldsymbol{u}_e^{(k)} + \boldsymbol{\Delta u}^{(j)}, \tag{4.5}$$

where $\boldsymbol{u}_e^{(k)}$ is the elastic solution corresponding to loading (k) and $\boldsymbol{\Delta u}^{(j)}$ denotes the inelastic corrections of the parent-solution. Because the elastic solution $\boldsymbol{u}_e^{(k)}$ is kinematically admissible and the inelastic correction $\boldsymbol{\Delta u}^{(j)}$ is kinematically admissible to zero, the displacement field $\boldsymbol{u}_0^{(k)}\left(\boldsymbol{x}, t\right)$ is kinematically admissible, even though the boundary conditions of computations (j) and (k) differ. Using the initialisation based on computation (k), it is hoped that the initial trial is closer to the exact solution than the elastic trial. Therefore, the number of iterations to reach convergence is expected to be reduced.

After the initialisation, the iterative scheme is classically performed. The frequency functions are updated to improve the solution at each global stage, and if needed, the PGD reduced basis grows.

> **Remark** Note that starting the computation with a reduced basis which includes the PGD modes associated with the non-linear initial correction, is crucial. Otherwise, the algorithm would require at least as many iterations as there are temporal functions requiring updating, only to rebuild the associated spatial functions.

In the multi-query context, more than one non-linear computation is available to enhance computation (k). Therefore, the need to decide which previous simulation is the best suited to initialise the current computation, *i.e.* to be the parent-simulation, arises.

3 Proximity indicator to evaluate the best candidate between previous non-linear simulations

In practice, from a set of $k-1$ loading scenarios for which the non-linear responses are already solved, the best provider (j) of both the reduced basis and the initial solution for computation (k) has to be selected. Computations associated with a small distance between loading properties under dynamic loading can lead to a significant distance between the damage responses due to resonance effects. Therefore, the distance between the loading scenarios or parameters cannot effectively discriminate the parent-simulation contrary to material variability under quasi-static loading where distances in the material parameters space appear relevant [Boucard & Ladevèze, 1998]. As illustrated in Figure 4.3, an indicator based on the dynamic elastic responses is proposed to determine the parent-simulation computation (j) corresponding to the closest non-linear response among the set of $k-1$ loading scenarios to that of the problem of interest (k). Then, the non-linear solution (j) will be employed for initialising the displacement field and the reduced basis for the non-linear scheme of computation (k) as exposed in Section 2.

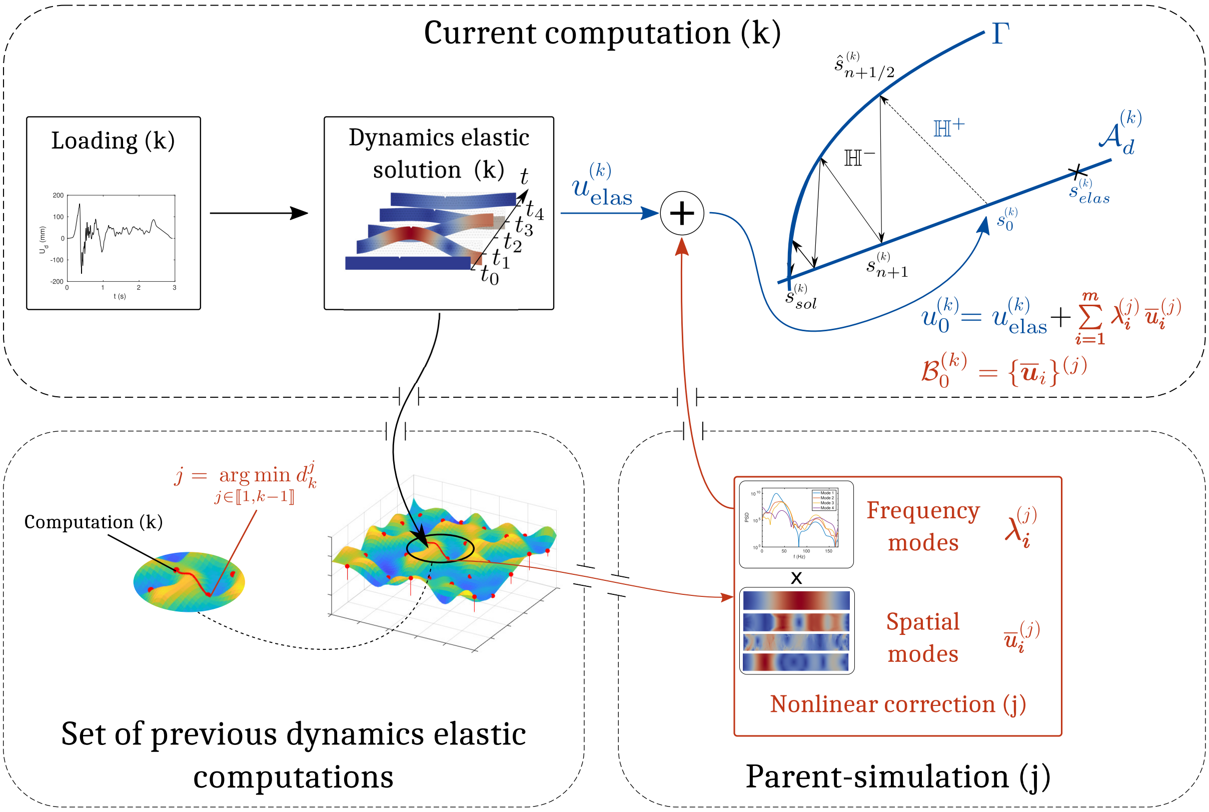
Current computation (k)
Loading (k)
200
100
0
-100
-200
U_d (mm)
0
1
2
3
t (s)
Dynamics elastic solution (k)
t
t_4
t_3
t_2
t_1
t_0
$u_{\text{elas}}^{(k)}$
$+$
Γ
$\hat{s}_{n+1/2}^{(k)}$
$\mathbb{H}^+$
$\mathbb{H}^-$
$\mathcal{A}_d^{(k)}$
$s_{elas}^{(k)}$
$s_0^{(k)}$
$s_{n+1}^{(k)}$
$s_{sol}^{(k)}$
$u_0^{(k)} = u_{\text{elas}}^{(k)} + \sum_{i=1}^{m} \lambda_i^{(j)} \overline{u}_i^{(j)}$
$\mathcal{B}_0^{(k)} = \{\overline{\boldsymbol{u}}_i\}^{(j)}$
$j = \arg\min_{j \in [\![1,k-1]\!]} d_k^j$
Computation (k)
Frequency modes
$\lambda_i^{(j)}$
x
Spatial modes
$\overline{u}_i^{(j)}$
Nonlinear correction (j)
Set of previous dynamics elastic computations
Parent-simulation (j)

Figure 4.3 • Computation (k) enhanced from a chosen parent-simulation

The distances between the non-linear responses associated with various loads are estimated from the distance between the dynamic elastic responses of the structure under these loads. Indeed, the elastic structure response contains a rich mechanical content contrary to the raw loading signals. Each elastic response is factorised by a singular value decomposition.

3.1 Singular value decomposition of each dynamic elastic solution

Each elastic space-time displacement field is discretised using a number n_Ω of degrees of freedom and a number n_t of time steps. Thus, the elastic displacement field associated with loading (k) is represented by a $n_\Omega \times n_t$ matrix $\boldsymbol{U}_e^{(k)}$. The features of each elastic response are extracted from the truncated singular value decomposition (SVD) of the matrix such that

$$\boldsymbol{U}_e^{(k)} \approx \boldsymbol{S}_\Omega^{(k)} \boldsymbol{\Sigma}^{(k)} \boldsymbol{S}_t^{(k)^T}, \tag{4.6}$$

where $\boldsymbol{\Sigma}^{(k)}$ is a $\ell \times \ell$ matrix containing the first ℓ singular values of $\boldsymbol{U}_e^{(k)}$. The $n_\Omega \times \ell$ matrix $\boldsymbol{S}_\Omega^{(k)}$ and the $n_t \times \ell$ matrix $\boldsymbol{S}_r^{(k)}$ contain ℓ left-singular vectors and ℓ right-singular vectors of $\boldsymbol{U}_e^{(k)}$, respectively. The number ℓ is chosen to be significantly smaller than n_Ω and n_t. The decomposition is performed efficiently using a randomised SVD [Halko et al., 2011; Alameddin et al., 2019]. The very low computational cost is crucial because the number of decompositions is equal to the number of load cases, which may be large.

The randomised singular value decomposition offers a direct truncation of the SVD as it involves randomly sampling the matrix columns. The truncation is based on the number of independent sampled columns, similar to the randomised range-finder method [Falini, 2022].

3.2 Proximity indicator between dynamics elastic solutions based on the singular value decomposition

The proximity indicator between two dynamic elastic solutions is based on comparing their singular values and vectors. Therefore, if the number of singular values and vectors differ between the two computations to compare, the computation with the maximum number of singular terms is further truncated to comprise the same number of terms as the other computation.

Besides, to compare singular values and vectors from computation (j) with computation (k), we first ensure that the order of the two factorisations is such that each singular vector of the decomposition (j) is compared with the most similar vector of the decomposition (k). Thus, given decomposition (k), decomposition (j) is reordered to estimate the rearranged singular vectors $\tilde{\boldsymbol{S}}_\Omega^{(j)}$ and $\tilde{\boldsymbol{S}}_t^{(j)}$ and the rearranged matrix of singular values $\tilde{\boldsymbol{\Sigma}}^{(j)}$ with

$$\boldsymbol{U}_e^{(j)} \approx \tilde{\boldsymbol{S}}_\Omega^{(j)} \, \tilde{\boldsymbol{\Sigma}}^{(j)} \, \tilde{\boldsymbol{S}}_t^{(j)^T}, \tag{4.7}$$

such that the scalar products between the left-singular vectors associated with spatial features of both decompositions are maximised, i.e.,

$$\tilde{\boldsymbol{S}}_\Omega^{(j)}(:,i) = \boldsymbol{S}_\Omega^{(j)}\left(:, \arg\max_{j\in[\![1,\ell]\!]}\left(\langle \boldsymbol{S}_\Omega^{(k)}(:,i)\boldsymbol{S}_\Omega^{(j)}(:,j)\rangle\right)\right), \forall\, i \in [\![1,\ell]\!] \tag{4.8}$$

subject to the condition that each column of $\boldsymbol{S}_\Omega^{(j)}$ appears only once in the matrix $\tilde{\boldsymbol{S}}_\Omega^{(j)}$. The matrix $\boldsymbol{\Sigma}^{(j)}$ containing the singular vectors is also sorted accordingly to build $\tilde{\boldsymbol{\Sigma}}^{(j)}$.

The proximity indicator between the elastic responses of computations (k) and (j) is estimated by the following L^2-norm

$$d_{(k)}^{(j)} \triangleq \left\| \left| \mathrm{diag}\left(\tilde{\boldsymbol{\Sigma}}^{(j)}\right) \odot \exp\left(\jmath \boldsymbol{\Theta}_{(k)}^{(j)}\right) - \mathrm{diag}\left(\boldsymbol{\Sigma}^{(k)}\right) \right| \right\|_2, \tag{4.9}$$

where $\odot$ represents the Hadamard or Schur product and the operator denoted by $|\bullet|$ gives a vector containing the modulus of each component of the argument vector. The vector $\boldsymbol{\Theta}_{(k)}^{(j)}$ defined as

$$\boldsymbol{\Theta}_{(k)}^{(j)} = \mathrm{diag}(\boldsymbol{W}) \tag{4.10}$$

contains the *principal angles* between the subspaces of dimension ℓ spanned by the singular vectors of the elastic solutions (k) and (j), respectively. The operator diag gives the vector comprising the diagonal terms of a matrix. Matrix $\boldsymbol{W}$ is computed as the singular-values matrix of $S_\ell^{(k)^T} \tilde{S}_\ell^{(j)}$ as explained in [Mohammadi, 2014]. We remark that the L^2-norm of the vector $\boldsymbol{\Theta}_{(k)}^{(j)}$ provides the Grassmann distance [Deutsch, 1995; Miao & Ben-Israel, 1992] denoted d_{Gr}

$$\left\|\boldsymbol{\Theta}_{(k)}^{(j)}\right\|_2 = d_{Gr}\left(\mathscr{S}^{(k)}, \mathscr{S}^{(j)}\right) \tag{4.11}$$

between the subspaces $\mathscr{S}^{(k)} = \mathrm{Span}(S_\Omega^{(k)})$ and $\mathscr{S}^{(j)} = \mathrm{Span}(S_\Omega^{(j)})$. The Grassmann distance gives the distance between two points $\mathscr{S}^{(j)} \in Gr\left(\ell, n_\Omega\right)$ and $\mathscr{S}^{(k)} \in Gr\left(\ell, n_\Omega\right)$ on the Grassmann manifold $Gr\left(\ell, n_\Omega\right)$ where points $\mathscr{S}^{(j)}$ and $\mathscr{S}^{(k)}$ are defined by the subspaces spanned by the singular vectors of the elastic computations (j) and (k), respectively. Two similar subspaces correspond with a distance equal to 0, while two orthogonal subspaces correspond with a distance equal to $\frac{\pi}{2}$. The Grassmann distance gives insight into the modal proximity of two elastic solutions but ignores the magnitude similarity or discrepancy between both solutions.

On the contrary, the proposed distance indicator given by eq.(4.9) merges information from singular values, i.e., vectors $\mathrm{diag}\left(\tilde{\boldsymbol{\Sigma}}^{(j)}\right)$ and $\mathrm{diag}\left(\boldsymbol{\Sigma}^{(k)}\right)$ and singular vectors.

Remark 1 When the two subspaces spanned by the singular vectors are co-linear, the exponential term equals 1, which recasts the indicator into a comparison of the singular values. Thus, the indicator quantifies the proximity between the elastic energies of the solutions. When the two subspaces spanned by the singular vectors are orthogonal, the exponential term equals $-\jmath$. The indicator also includes the amplitudes of singular values. Thus, it increases with the solutions' elastic energy.

Remark 2 It can be noted that the proximity indicator is based on elastic solutions, whatever the loading. Thus, it can tackle parametrised or random loads generated without straightforward apparent parameters.

The parent-simulation computation is looked for in the subset of non-linear computations that have already been performed, i.e. among scenarios (1) to $(k-1)$. Thus, the pertinence of the PS computation depends on the sequence in which the n loading scenarios are solved. Indeed, the smaller the distance $d_{(k)}^{(j)}$ between the current computation (k) and the PS (j), the more efficiently the PS computation (j) is expected to enhance computation (k). Therefore, we aim to minimise the distance between successive computations by designing an adequate order for the simulations.

4 Enhanced reduced-order model for non-linear dynamic simulations in case of multiple loading scenarios

To efficiently solve a set of non-linear computations corresponding to loading (1) to (n), the knowledge acquired by the first computations is exploited to initialise the current computation smartly. The numerical scheme comprises five major steps. First, the elastic dynamic responses of the structure associated with all the loading are computed. Second, a proximity indicator between them is estimated from the singular value decomposition of each response as exposed in Section 3. Third, an optimal order in which non-linear simulations will be performed is designed from a genetic algorithm based on the proximity indicator between the elastic responses. Fourth, the parent-simulation for the current computation is looked for among the non-linear computations already computed. Finally, the parent-simulation simulation (j) enhances the computation (k) of interest as introduced in Section 2.

4.1 Optimal path through the multi-load simulations

The enhancement of non-linear simulations is optimal if the most pertinent simulations are included in the set where the parent-simulation is sought. Thus, knowing all the two-by-two distances between the elastic solutions, i.e. the following distance matrix

$$\boldsymbol{D}_{i,j} = d_{(j)}^{(i)}, \forall \left(i, j\right) \in [\![1, n]\!]^2, \tag{4.12}$$

we aim at minimising the distance between two consecutive calculations, establishing an optimal path P_{optimal} for the whole set of computations. The *optimal path* in this context is defined as the sequence among the n scenarios which minimises the total path length traversed by the set of n calculations defined as

$$\mathscr{L}(P) = \sum_{k=2}^{n} d_{P(k-1)}^{P(k)}, \tag{4.13}$$

with the path P consisting of the ordered sequenced in which computations are performed and $P(i)$ giving the $i-$th computations of the path P. This problem corresponds to the well-known “Travelling Salesman Problem" (TSP), where the goal is to determine the shortest route so that the total travel distance passing through each city once and only once for a given number of cities is minimal. In practice, the optimal path comprises a sequential order of calculations, which minimises the distances between consecutive computations under the constraint that all computations are performed once and only once. Thus, ordering the simulations boils down to solving the following minimisation problem.

$$P_{\text{optimal}} = \arg \min_{P \in \sigma\left([\![1, n]\!]\right)} \mathscr{L}(P) \tag{4.14}$$

with $\sigma\left([\![1, n]\!]\right)$ being the set of all permutations of the n first integers. Obtaining the exact minimum can be highly computationally intensive. Genetic Algorithms (GAs) are very efficient in addressing this challenge. They provide a suitable solution with a relatively modest computational cost [Hussain et al., 2017]. Our study employs a GA proposed by Zhang et al. [Zhang et al., 2022], incorporating recently proposed crossover operators demonstrating excellent convergence performances. It can be noted that the entire sequence is designed by the algorithm, including the initial point.

Once an enhanced sequence that differs from the initial indexed list has been found, the computations to be performed must be re-indexed as follow

$$(\ell) \leftarrow \left(P_{\text{optimal}}(\ell)\right) \forall \ell \in [\![1, n]\!] \tag{4.15}$$

during a so-called *re-indexation stage*.

4.2 Choice of the parent-simulation computation

The first simulation is performed using the standard LATIN-PGD. Computation (2) uses the enhanced scheme from the parent-simulation (1). Before computing any non-linear case (k) with $k \geq 3$, the parent-simulation computation (j) is looked for among the set of $k-1$ previous scenarios, which is the closest to computation (k) i.e.,

$$j = \underset{j \in [\![1, k-1]\!]}{\arg\min}\, d_{(k)}^{(j)}. \tag{4.16}$$

The appropriate parent-simulation enhances the LATIN-PGD scheme for computation (k) as detailed in Section 2. The obtained non-linear correction is saved so that it can be employed to speed-up further simulations.

4.3 Overview

The Algorithm 1 outlines the various steps to enhance the LATIN-PGD scheme for computing non-linear dynamic responses across multiple loadings. This strategy is founded on three core principles.

Principle I. Smart initialisation of the space-time solution and reduced basis

This first principle makes it possible to start the iterative scheme closer to the exact solution, thereby reducing the initial error and the number of iterations needed to reach convergence. Initialising the reduced-order basis prevents redundant LATIN steps for computing pre-existing modes.

Principle II. Selection of a well-suited parent-simulation

Relying on elastic solutions to find the optimal PS calculation allows to robustly find an ideal prior computation for initialising the current one. This approach draws from solid mechanical knowledge rather than relying on parametrised loading descriptions, for instance, ensuring method robustness for non-parametrised loading signals.

Principle III. Find an optimal computation sequence

This last step ensures that a suitable parent-simulation is found within the pool of prior solutions, even at the beginning of the multi-query context, when few computations have yet been performed.

```
Algorithm 1: Multi-query method
Loading: $\{\boldsymbol{u_d}^{(i)}\}, i \in [\![1,n]\!]$
for $k \in [\![1,n]\!]$ do                                /* Compute all elastic solutions */
    $\boldsymbol{u}_{\boldsymbol{e}}^{\boldsymbol{k}} \leftarrow \boldsymbol{u}| \begin{cases} \nabla \cdot \sigma + \boldsymbol{f}_d = \rho \ddot{\boldsymbol{u}}, \\ \dot{\boldsymbol{u}}\big|_{t=0} = \boldsymbol{0},\ \boldsymbol{u}|_{t=0} = \boldsymbol{0} \text{ in } \Omega, \\ \boldsymbol{u} = \boldsymbol{u}_d^{(k)} \text{ and } \dot{\boldsymbol{u}} = \dot{\boldsymbol{u}}_d^{(k)} \text{ on } \partial\Omega_1, \\ \sigma\, \boldsymbol{n} = \boldsymbol{F}_d^{(k)} \text{ on } \partial\Omega_2, \end{cases}$
end
$\boldsymbol{D}_{i,j} \leftarrow d_{(j)}^{(i)}, \forall \left(i,j\right) \in [\![1,n]\!]^2$      /* Compute the distance matrix */
$P_{\text{optimal}} \leftarrow \arg\min \mathscr{L}(P)$                /* Find the optimal path using the GA */
$(\ell) \leftarrow \left(P_{\text{optimal}}\left(\ell\right)\right) \forall \ell \in [\![1,n]\!]$                /* Re-indexation stage */
for $k \in [\![1,n]\!]$ do
    $j \leftarrow \underset{j \in [\![1,k-1]\!]}{\arg\min}\, d_{(k)}^{(j)}$                  /* Find the parent-simulation */
    $\mathscr{B}_0^{(k)} \leftarrow \mathscr{B}^{(j)}$                    /* Initialise the reduced PGD basis */
    $\boldsymbol{u}_0^{(k)} \leftarrow \boldsymbol{u}_e^{(k)} + \boldsymbol{\Delta u}^{(j)}$               /* Initialise the LATIN-PGD scheme */
    while $\eta \leqslant \eta_c$ do                          /* Call the LATIN-PGD solver */
        LATIN-PGD iterations
    end
    Save $\boldsymbol{\Delta u}^{(k)}$                     /* Save the $k$-th non-linear correction */
end
```

5 Numerical studies

The problem consists of a notched fixed-end beam of length $L_b = 9\,\mathrm{m}$ and width of $W = 80\,\mathrm{cm}$ as shown in Figure 4.4a, which is submitted to a bi-parametric load plotted in Figure 4.4b.

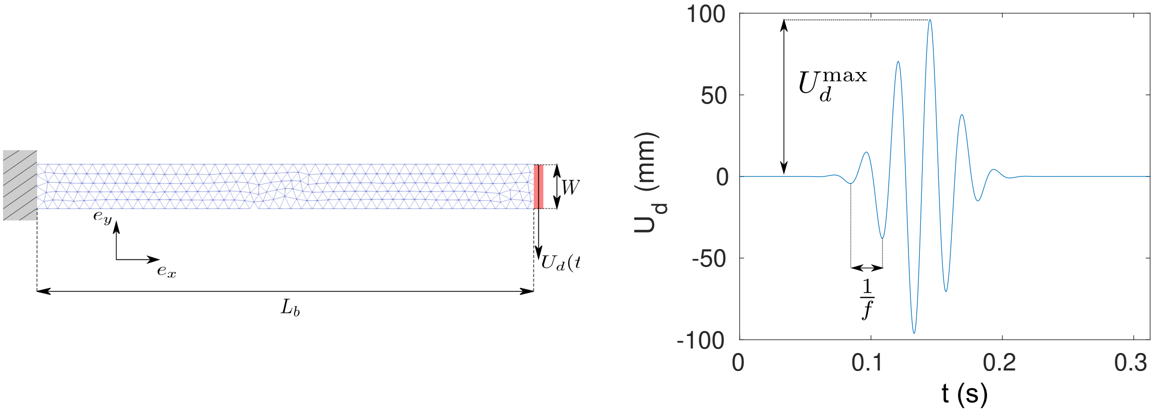

(a) Notched beam

(b) Bi-parametric loading

Figure 4.4 • Reference problem

The multi-query study proposed to illustrate the method consists of finding the structure's response for a set of 600 pairs of parameters. The parameter space was uniformly sampled in a grid of 20 samples in the amplitude direction and 30 samples in the frequency direction. The frequency range spans across a wide range of frequencies, including the first eigenfrequency, starting at 5 Hz and ending at 90 Hz. The amplitude of the loading goes from 2 mm to 60 mm. In this context, the number of computations is fixed. All the 600 computations associated with the set of parameters must be solved. The final study's results give the full space-time non-linear solution of the structure subjected to the multiple-loading scenarios.

The maximum damage value reached in the structure over the whole time domain is shown in Figure 4.5. It can be seen that the maximum damage largely depends on the load parameters. It regularly increases with the amplitude. The dependence with frequency fluctuates with two peaks. Indeed, the frequency range is centred on the first eigenfrequency of the structure $f_1 = 44\,\mathrm{Hz}$ and comes close to the second natural frequency $f_2 = 98\,\mathrm{Hz}$.

5.1 Initialisation strategy in the multi-query context on the full order model

This section illustrates the part of the methodology within the intended use case scenario, *i.e.* where many computations are performed across a wide range of parameters using the full-order model. Notably, this section focuses solely on the space-time solution initialisation aspect of the proposed framework without investigating the model-order reduction techniques aspects. Consequently, the results presented herein exclusively concern the

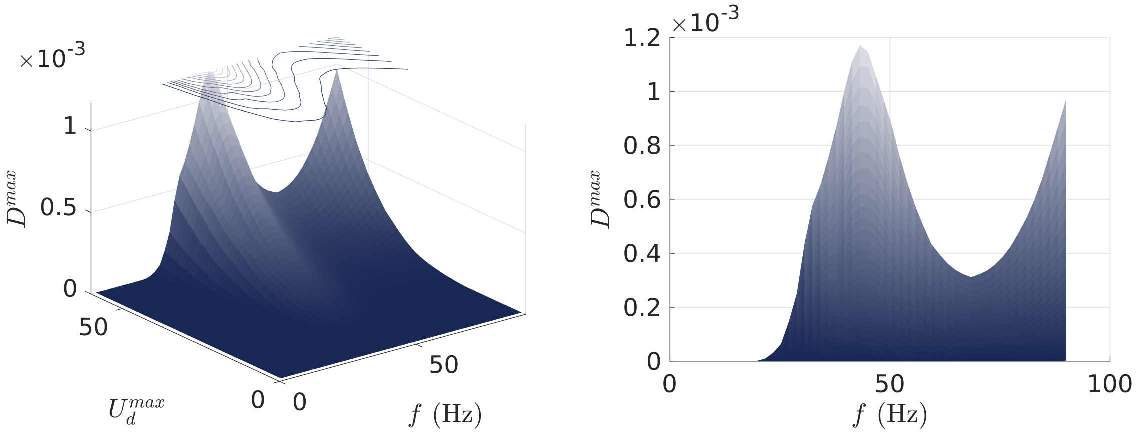

(a) Side view of the response surface **(b)** Front view of the response surface

Figure 4.5 • Maximum damage as a function of the loading parameters

initialisation of the solution within the non-incremental computation strategy. The partially enhanced strategy presented in this section will be referred to as the *semi-enhanced* strategy. The semi-enhanced strategy comprises the principles two and three described in the overview 4.3, but as it involves full-order computations, only half of the first principle is applicable. A comparative analysis is conducted between the standard method, involving independent execution of the 600 computations, and the semi-enhanced methodology. Figure 4.6 demonstrates that a noteworthy 30% reduction in the total number of iterations required to reach convergence across all 600 computations is achieved by employing the semi-enhanced approach. Initially, both the standard and the semi-enhanced methods exhibit comparable results as they produce elastic solutions during the early computations. However, as non-linearities come into play, the semi-enhanced methodology outperforms the standard method by demonstrating a lower computational cost.

These results highlight the potential of the smart initialisation technique to speed up the convergence process when non-linearities emerge, ultimately enhancing the computational efficiency of the overall analysis.

The first aspects of the proposed method have been shown on full-order computations to grasp the magnitude of the improvement offered by the sole initialisation process. The full methodology, however, also relies on generating fewer modes in a reduced-order model context by reusing the previously computed reduced-order basis for the current computations.

5.2 Reduced-order model improvements

The whole methodology is shown in this section, where both the initialisation and the reuse of reduced bases help decrease the computational cost. The method is first presented in the case of two successive computations. A multi-query application is then investigated to showcase the full potential of the proposed methodology.

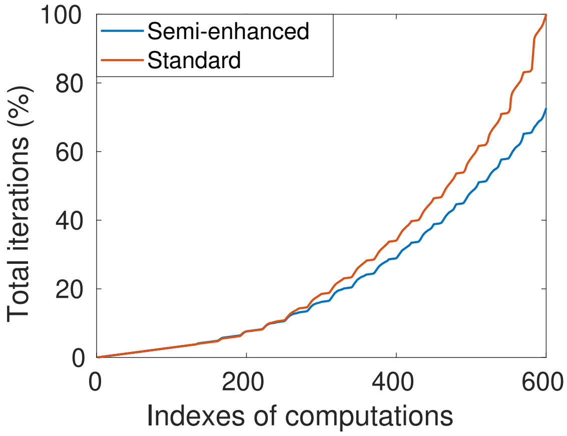

Figure 4.6 • Comparison of the number of total iterations required for the semi-enhanced and the standard methods

Two successive computations

The enhanced strategy, which includes reduced-order model aspects, is first investigated in the case of two successive computations (j) and (k).

Computation (k) is performed with a loading of $f = 40\,\mathrm{Hz}$ and $U_d^{max} = 30\,\mathrm{mm}$. It is then accelerated with computation (j) that has previously been carried out with $f = 41\,\mathrm{Hz}$ and $U_d^{max} = 35\,\mathrm{mm}$.

Figure 4.7 gives an overview of the evolution of the size of the basis and the number of iterations when solving both the PS computation (j) and the current simulation (k) sequentially. The enhanced method is compared to the classical scheme. When using the classical scheme, both the parent-simulation and current computations lead to roughly the same number of iterations to reach the convergence criterion $\eta = 2 \times 10^{-3}$ and require generating more than 15 modes. In contrast, as shown by figure 4.7, the second calculation leads to significantly fewer iterations when using the enhanced framework. The number of iterations of computation (k) is reduced from 25 for the classic method to 11 for the new method. This drop is due to the combined effect of the smart initialisation highlighted by a lower initial error and the use of the previous reduced-order basis as an initial basis, allowing the generation of fewer new modes, further decreasing the number of iterations.

Furthermore, Figure 4.7 highlights the fact that the PGD basis in the case of the enhanced scheme gradually increases, adding only the missing modes from one computation to the other, contrary to the classical scheme that needs to rebuild from scratch a satisfactory PGD basis for each computation. Indeed, only 5 PGD modes are added during the enhanced current computations to reach 22 modes, while 21 modes are needed and generated for the standard scheme. Finally, Figure 4.7 suggests that the more computations there will be, the more efficient the enhanced methodology will be. Indeed, the more computations there are, the less the initial cost of the first computation will be significant. The proposed approach is all the more interesting in a multi-query context.

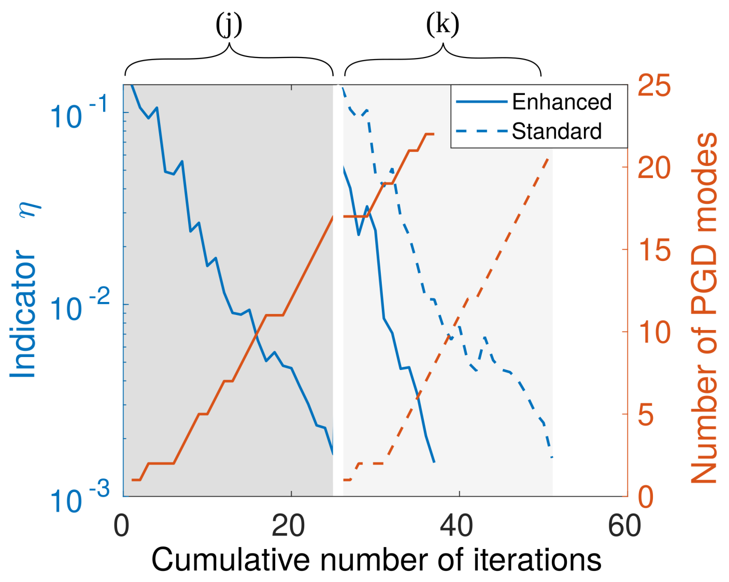

Figure 4.7 • Parent-simulation and enhanced current computations sequence compared with parent-simulation and standard current sequences

In the multi-query context

In a multi-query application, the proposed enhanced strategy leads not only to a decrease in the number of iterations required but also to a drastic decrease in the number of PGD modes generated during all the calculations carried out through the multi-query process.

> **Remark** The maximum number of iterations for the reference methodology using reduced-order model computations differ from those needed without model-order reduction techniques. However, the comparison between the enhanced and semi-enhanced methods helps to understand that both the initialisation of the reduced-order basis and the initialisation of the solution allow the number of iterations required to reach convergence for all 600 computations to decrease.

Figure 4.8a shows that while the number of generated modes grows indefinitely for the standard LATIN-PGD method where all computations are tackled independently, it rapidly stagnates to a low number when using the enhanced LATIN-PGD proposed in this paper. A significant improvement is also apparent when we look at the number of iterations required to reach convergence of the 600 calculations. Indeed, Figure 4.8b shows that the enhanced LATIN-PGD leads to 2.9 times fewer iterations, thus significantly decreasing the computational cost of the multi-query study.

> **Remark** Without specific work to decrease the cost of the local stage and when considering numerous time steps, the local stage can be numerically expensive. Using

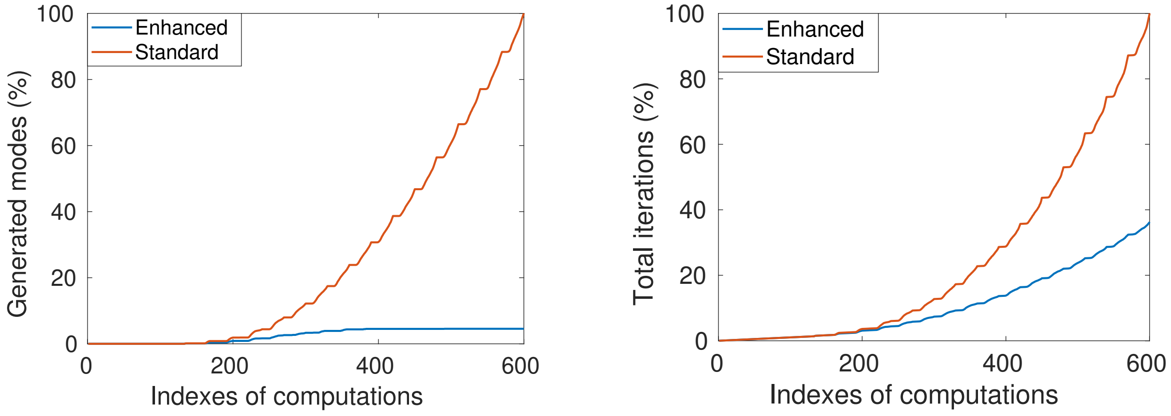

(a) Growth of the PGD basis size

(b) Number of iterations

Figure 4.8 • Comparison of the standard method with the enhanced strategy.

> the PGD at the global stage increases the number of LATIN iterations to reach convergence and, therefore, increases the number of local stages to be solved. However, the PGD also allows for drastically decreasing the number of iterations in the proposed multi-query framework, thus decreasing the numerical burden associated with the study in a multi-query framework.

The strategy relies heavily on the fact that a calculation close to the current calculation can be found in the set of calculations already carried out. Therefore, the order of the calculations plays a crucial role in obtaining significant results.

Influence of the computation sequence

In order to investigate the influence of the order in which computations are performed plays in the results previously showcased, several random sequences have been run. For those random runs, the enhanced methodology has been carried out without the optimal path aspect. Only the order of the computations changes. 5 random sequences have been generated to get an idea of how significant of an impact the order of the computations has. Figure 4.9b compares those random runs to the optimal path obtained from the genetic algorithm as presented in Section 4.1. The grey area outlines the worst and the best of the five random runs. The genetic algorithm introduced allows finding a cumulative path through the computations significantly shorter than the one obtained by a random route. Such a decay is shown in Figure 4.9a, which highlights a quick convergence of the genetic algorithm.

For clarity, in post-processing, the results of different runs have been sorted to align with the corresponding computations in all plotted cases. As a result, the computation labelled as the ‘i-th’ may not have occurred at the ‘i-th’ position in all sequences.

The comparison of the random runs with the optimal path clearly shows that even though random runs still manage to yield a significant decrease in the number of modes generated

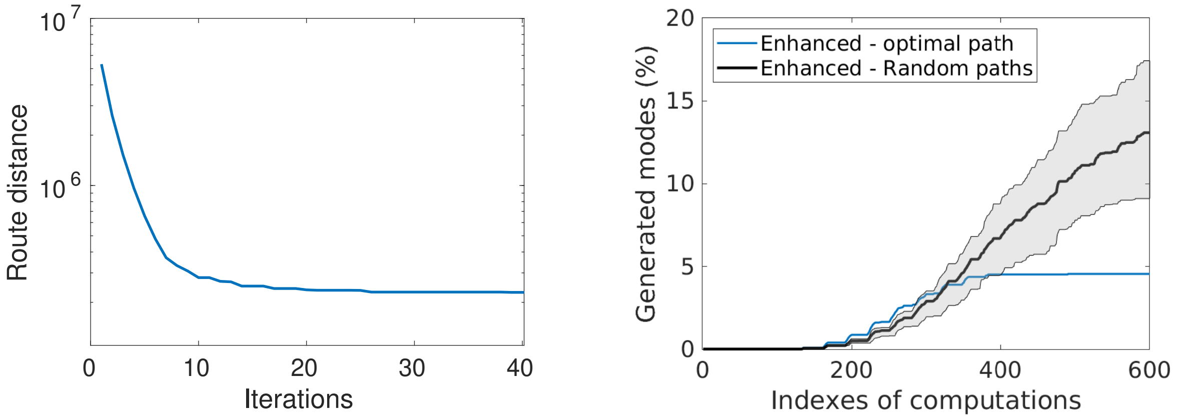

(a) Shortening of the path through the GA iterations

(b) Optimal path compared to random paths

Figure 4.9 • Optimal path strategy illustration

(between 5 to 10 times less than the standard method), significant variability is to be expected from one random run to another. Moreover, the optimal path offers a robust way to achieve significantly better results as the number of generated modes using the optimal sequence leads to 2 times less mode than the better random runs. The optimal path leads to a drastic reduction in the number of modes needed for all 600 computations. Indeed, the optimal path leads to 20 times less mode generated than the standard method. All non-linear computations converge with a number of PGD modes comprised between 5 and 49, and a rSVD decomposition of each computation leads to the same number of modes as the number of PGD modes needed to reach convergence in most cases. However, in the proposed methodology, because only the basis of the parent-simulation is reused, a total of 253 modes have been generated, and an SVD compression of all those modes (which do not form a basis as they are never used all at once), lead to only 54 modes. The PGD, therefore, leads to an optimal-sized basis for each computation. However, even though the methodology leads to a massive improvement in the number of modes being generated, the compressed optimal basis is smaller than the number of generated modes.

Figure 4.10a demonstrates that the optimal pathway given by the genetic algorithm does not invariably result in utilising the immediately preceding computation as the parent-simulation. The optimal path may need to locally provide a sequence of computations further from one another to decrease the overall length of the path. Consequently, the additional step in looking for the closest computation from the set of previously computed solutions while executing the optimal sequence instead of relying solely on the preceding computation guarantees the selection of the most pertinent parent-simulation. Figure 4.10a, however, shows that relying on an optimal path contributes, on average, to the reduction of the parent-simulation width (PSW)

$$\mathscr{W}^{(k)} = k - j, \tag{4.17}$$

between the current computation (k) and the parent-simulation (j) identified from previous

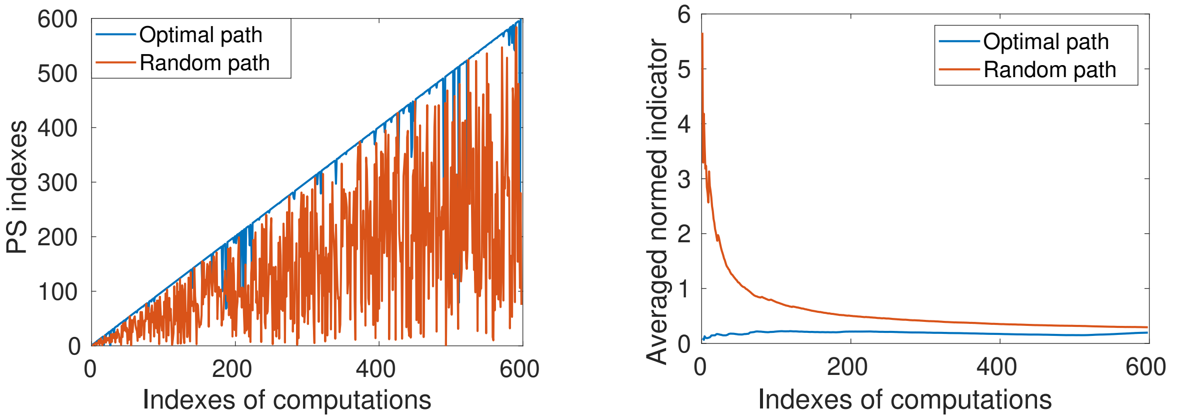

(a) Indexes of the parent-simulation for each computation

(b) Averaged normed distance to the parent-simulation

Figure 4.10 • Indexes and distances indicators values of PS computations for the optimal path strategy compared with those of a random path

computations. Indeed, when relying on an optimal sequence, the PS index consistently exhibits proximity to the index of the ongoing simulations. In contrast, the PS index in a random sequence is randomly distributed in the integer range $[\![1, k-1]\!]$. Table 4.1 details a comparison of the PSW between a random and optimal sequence given by the GA. The GA yields a substantial reduction in PSW, with 82 % of computations resulting in an PSW of 1 within the optimal sequence framework. In contrast, the random sequence scenario leads to 94 % of computations with an PSW higher than 5. The Cumulative distribution function of

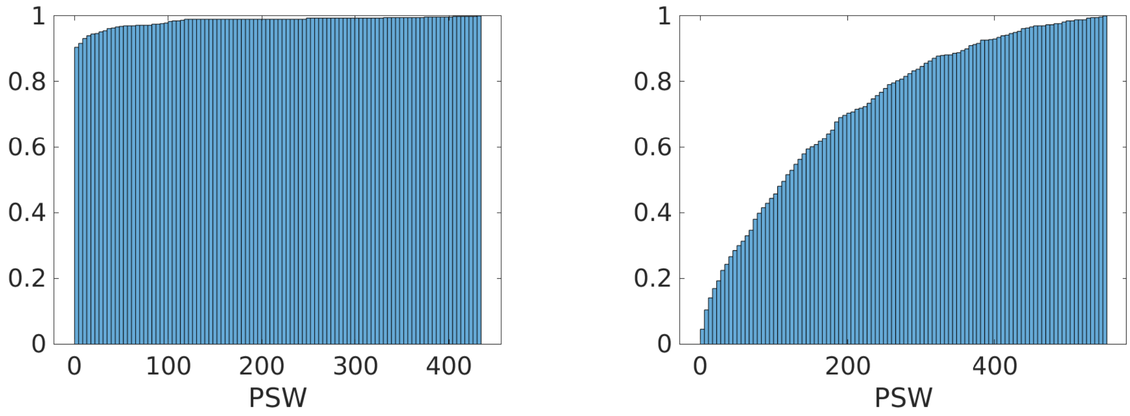

(a) Cumulative distribution function of the PS width for the optimal path

(b) Cumulative distribution function of the PS width for a random path

Figure 4.11 • Comparison of Cumulative distribution function of the PS width for the optimal path and a random path

PSW for both an optimal and a random sequence are presented in Figures 4.11a and 4.11b, respectively. These figures describe the distribution of simulations resulting in a width below different values in both scenarios. While the optimal sequence scenario predominantly corresponds to shallow PSW values across most computations, the random sequence is associated with a significant proportion of computations exhibiting a broader PSW.

$\forall k \in [\![1,600]\!]$	$\#\left\{\mathscr{W}^{(k)} = 1\right\}$	$\#\left\{\mathscr{W}^{(k)} \leqslant 5\right\}$	$\#\left\{\mathscr{W}^{(k)} \geqslant 500\right\}$	$\mu_{1/2}\left(\mathscr{W}^{(k)}\right)$
Optimal path	495	546	0	1
Random path	6	27	10	116

Table 4.1 • Comparison of the indexes of the PS computations for the optimal path and a random path

> **Remark** In a limited memory scenario, using an optimal sequence given by the GA may allow deleting some previous results and keeping only a small buffer of previous computations, while a random sequence may lead to the early results still being needed for new computations therefore making it impossible to delete any previous computation.

The main goal of relying on an optimal sequence of computations is to identify a close PS computation (j) for each current computation (k) therefore keeping the value of the distance indicator d_j^k low for all $k \in [\![1, n]\!]$. Figure 4.10b illustrates the average of the normalised value of d_j^k relative to the maximum value of that indicator when using the optimal sequence, which is defined as

$$d_j^{k\,\text{Normed}} = \frac{d_j^k}{d^{\text{up}}}, \tag{4.18}$$

where $d^{\text{up}} = \max_{k\in[\![1,n]\!]} d_j^k$ in the case of the optimal path. For each computations, the average on all previous computations

$$\overline{d_j^k} = \frac{1}{k}\sum_{i=1}^{k} d_j^{i\,\text{Normed}} \tag{4.19}$$

of the normed distance is then plotted. The GA effectively ensures low distances between computations and their respective PS across the whole set of simulations. That statement holds even in the initial stages, with a few simulations performed. Conversely, when using a random sequence, the distance from a computation to its associated PS can be up to six times larger than the worst-case scenario observed in the optimal sequence. The mean distance decreases when the number of simulations increases, given the broader pool of potential parent-simulations from previously computed solutions. The optimal path, however, consistently yields superior performance across the entire batch of computations. Table 4.2 provides a detailed comparison of a random sequence with an optimal sequence, revealing, for instance, that, despite similar minimal distance indicator values in both cases, the mean value of the indicator is sixteen-fold higher in the context of the random sequence thus proving that the optimal path allows the selection of more suitable parent-simulations.

	$\min\left(d_j^{k\text{Normed}}\right)$	$\max\left(d_j^{k\,Normed}\right)$	$\text{mean}\left(d_j^{k\,Normed}\right)$	$\mu_{1/2}\left(d_j^{k\,Normed}\right)$
Optimal path	7.5×10^{-3}	1	1.9×10^{-1}	1.5×10^{-1}
Random path	7.5×10^{-3}	8.3	3.0	1.7×10^{-1}

Table 4.2 • Comparison of the normalised distance indicator from PS computations to the current simulations for the optimal path and a random path

5.3 Interpretation of the results in the parametric space

To further understand how the strategy impacted the different computations, Figure 4.12 shows maps of the number of generated modes for each parametric pair for both the standard method and the enhanced strategy. Figure 4.12a shows that the more non-linear a computation is, the more modes are needed to reach convergence. On the contrary, Figure 4.12b highlights that the PGD basis only expands around areas where new damage patterns arise. Once these places in the parametric space have been explored and the PGD basis has been extended accordingly, the following computations are done using the given PGD basis as if they just consisted of POD computation. The PGD method, therefore, reverts to being used as an *a posteriori* reduced-order method. In this context, the PGD is therefore used both as an *a priori* and an *a posteriori* model-order reduction technique, demonstrating its versatility. The PGD basis is extended when further knowledge is needed. However, when the PGD basis is well suited for the current computation, only the temporal modes are updated, and the basis size remains unchanged. This way, new information is built on the fly when needed without having to choose the suitable snapshots and without paying the numerical cost of building from scratch a new basis for each computation.

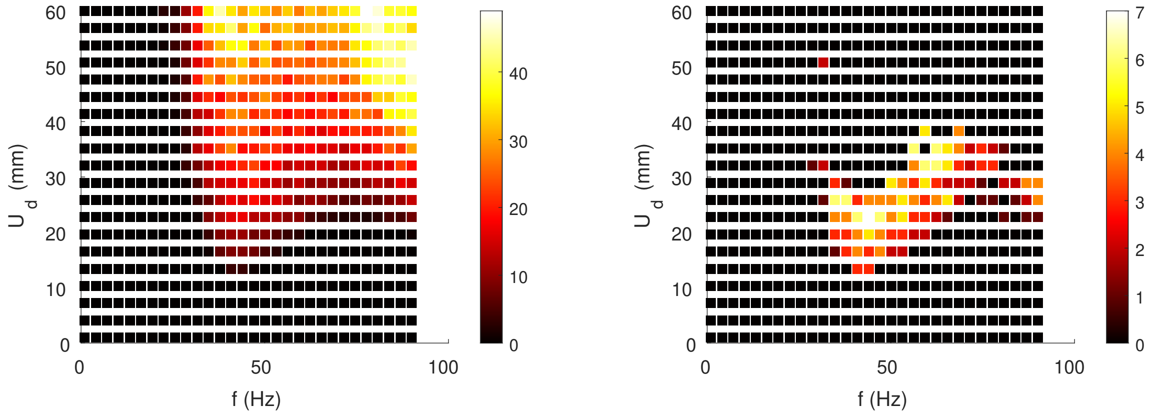

(a) PGD Modes - standard **(b)** PGD Modes - enhanced

Figure 4.12 • Number of generated modes in the parametric space

Similar maps are presented in Figure 4.13 where the number iterations are shown for the different parameter pairs. Figure 4.13a shows that the number of iterations needed to converge for highly non-linear computations is greater than that for weakly non-linear simulations. Figure 4.13b showcases the numerical gains made possible by the enhanced strategy. Indeed, the most complex computations only require 30 iterations to converge using the proposed strategy, while it needs 100 iterations to reach convergence using the standard LATIN-PGD method. Building a suited PGD basis beforehand and wisely initialising the non-linear scheme, therefore, helps decrease all the non-linear computations.

> **Remark** To have visible results on the graph showcasing the enhanced results, the colour scales for the enhanced and the standard LATIN-PGD method are different. The enhanced scheme requires new modes for fewer scenarios, and the number of modes added is also significantly smaller.

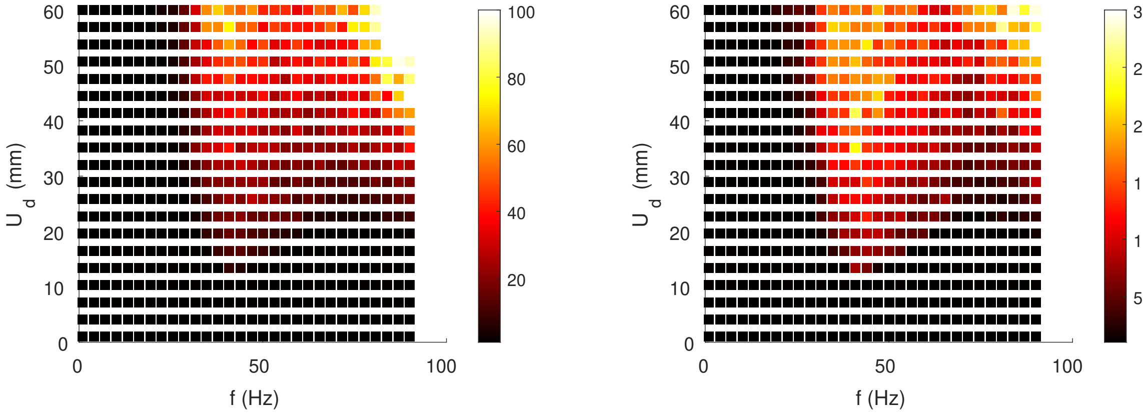

(a) Iterations - standard

(b) Iterations - enhanced

Figure 4.13 • Number of iterations in the parametric space

5.4 Influence of the number of computations in the multi-query study

The numerical benefits of such a framework heavily depend on the number of computations to be performed. Figure 4.14 investigates the relation between the benefits given by the enhanced methodology and the number of simulations in the study, *i.e.* the number of queries to the solver. It appears that numerical benefits arise rapidly, even with a relatively low number of simulations. After 70 computations, the numerical cost is at least halved and the benefits of the framework keep improving with the number of queries; the more computations are needed, the more benefits the proposed methodology will offer. Between 150 and 600 simulations, a steady behaviour of the framework is reached where the numerical benefits of the methodology increase linearly with the number of queries of the study.

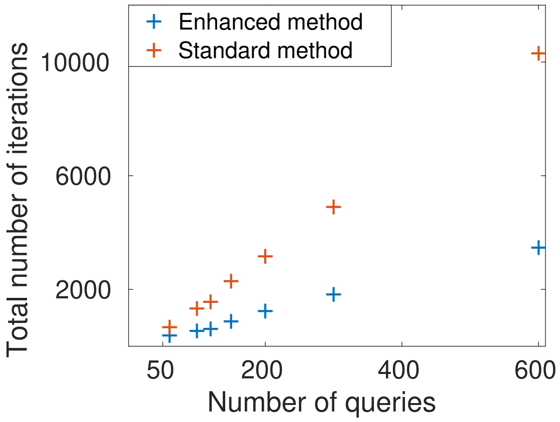

Figure 4.14 • Speed-up as a function of the number of computations in the multi-query study

Remark 1 The benefits of the method also heavily depend on the level of non-linearity of the different solutions of the multi-query study. The more non-linearities the results exacerbate, the more benefits the new framework will bring. If linear simulations happen to be included in the design of the study, no benefit will appear for these calculations.

Remark 2 For a large number of queries, this variability is averaged. However, when few queries are considered, accounting for the variability while assessing the benefits of the method would require the raw results presented in Figure 4.14 to be average on simulations sample sets.

Chapter summary

An original multi-query framework for non-linear dynamics has been proposed. This framework successfully takes advantage of similarities between computations to reduce the computation cost of a multiple-loading study significantly. It has proven to be very effective at decreasing the number of iterations needed to reach convergence for a large number of computations sequentially performed. Similarly, when coupled with a reduced-order solver, the proposed strategy offers significant computation gains by drastically decreasing the number of modes to generate. A comparison of the semi-enhanced and enhanced strategies showed that both aspects of the method (reusing the previous basis and reusing the previous converged solution) play a significant role in the final decrease of the computation cost. Moreover, it has been shown that the order in which the computations are performed can significantly change the performance of the proposed framework. An additional step of finding an optimal sequence of computations has been proposed, leading to a robust framework that achieves optimal performances. The ingredients of this new framework are deliberately not based on an a priori parametrisation of inputs, making the methodology transferable to studies with non-parametrised inputs.

* * *

Perspectives

If the requirement for a precise solution across all mechanical fields is relaxed and the objective shifts, for instance, to merely classifying computations based on the scalar value of a given quantity of interest, low-fidelity calculations may be adequate to achieve satisfactory classification at a reduced computational cost. A multi-fidelity strategy is therefore being investigated. It relies on the proposed distance to employ coarse convergence criteria for computations leading to non-critical damage values, *i.e.* damage values that are far from the classification threshold and for which a slight estimation error would, therefore, not bias the classification outcome.

Part III

Application of the novel framework for failure probability assessment

Chapter 5

Multi-fidelity model-order reduction for fragility curves

This chapter presents an extension of the multi-query framework where the LATIN solver's multi-fidelity capability is exploited to decrease further the computational cost associated with the risk study. The framework is tested on indexed signals whose prior parameterisation is not exploited. As announced in the introduction, a fragility curve is built using the proposed methodology.

Contents

1 Construction of the virtual chart 110
2 Multi-fidelity solver 111
  2.1 Influence of the stopping criterion 111
  2.2 Multi-fidelity strategy 114
  2.3 Numerical results 114
3 Fragility curves 116
✎ Chapter summary & perspectives 118

This chapter aims at extending the multi-query framework developed in Part II of this thesis to a context where the interest is no longer to compute the whole non-linear solution but rather to get access to a given quantity of interest (QoI), based on which specific operations are performed. In certain situations where several calculations are carried out, it is not always necessary to precisely know the value of the quantity of interest for each simulation. When trying to optimise a structure, for example, the value of the quantity of interest only needs to be precisely known close to the optimum. In the application illustrated in this chapter, the operation to be performed based on the quantity of interest is a classification of calculations depending on whether the quantity of interest is above or below a given threshold. Some of the calculations that lead to a QoI value close to the threshold will be regarded as critical because a small error in estimating the QoI would lead to a classification error. In contrast, others for which the QoI is far from the threshold could be known coarsely without impinging on the classification operation.

In practical terms, this chapter gives a methodology to build a fragility curve associated with a given loading scenario set. For each scenario, the maximum damage value in the structure is computed to calculate a failure probability

$$P_f(\alpha) = 1 - P\left(D(\boldsymbol{x}, t, \alpha) < D_c, \forall \boldsymbol{x} \in \Omega, \forall t \in I\right), \tag{5.1}$$

with D_c a chosen damage threshold and α is a scalar parameter describing the severity of the loading.

1 Construction of the virtual chart

Referring to the example from the previous chapter for conceptual clarity, Figure 5.1 is derived, illustrating the response surface of normalised maximum damage intersected by a horizontal plane dividing the computations into two categories. One category leads to structural failure, corresponding to points above this plane, while another involves simulations preserving structural integrity, corresponding to points below this surface. The objective of this chapter shifts from obtaining the complete mechanical fields of the nonlinear response of the structure to achieving a cost-effective and precise classification of these computations. Indeed, as long as the classification of simulations remains accurate, the accuracy of other mechanical quantities is of little significance to construct a fragility curve, *i.e.* computing the probability given in Equation 5.1.

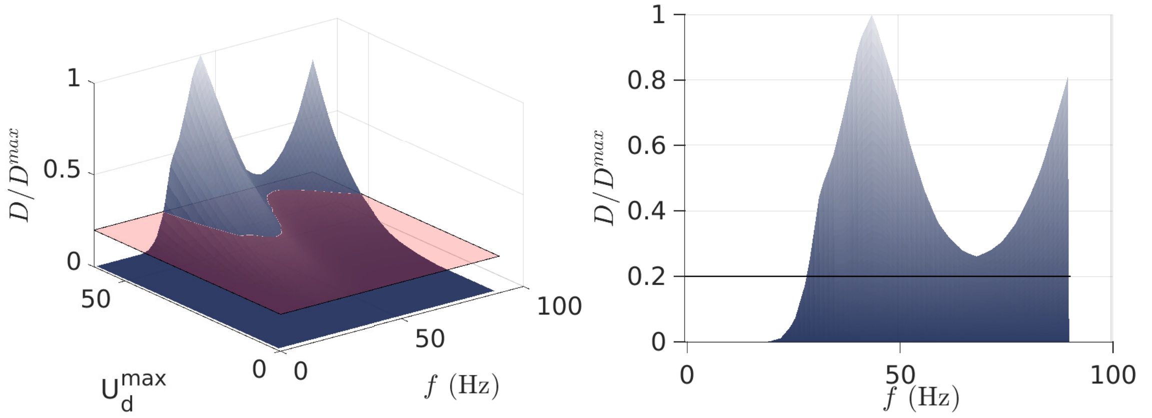

(a) Side view of the response surface showing the normalised maximum damage in the structure.

(b) Front view of the response surface showing the normalised maximum damage in the structure.

Figure 5.1 • Normalised response surface of damage in the structure with the critical damage D_c plane

Classifying each computation based on the value of a single quantity only requires that quantity to be accurately known for critical cases. Therefore, less expensive low-fidelity solutions are often sufficient. Such low-fidelity solutions being numerically cheaper, relying on coarse computations helps decreasing the numerical cost of the multi-query classification study. This chapter aims at taking advantage of this observation without impacting the classification operation and, therefore, the resulting fragility curve. To achieve this goal, the idea is to use different convergence thresholds for the simulations included in the study to reduce the computational cost without affecting the result.

2 Multi-fidelity solver

The non-incremental aspect of the LATIN solver gives access to multiple levels of fidelity for the solution. The current section investigates the impact of a coarser stopping criterion η_c^ℓ on the quantity of interest *e.g.* the damage value. Varying the level of convergence changes the precision of the damage value obtained from the computation; therefore, assessing the error made when using a low-fidelity solution is crucial.

2.1 Influence of the stopping criterion

In the following scenarios, the reference damage map has been obtained using a stopping criterion

$$\eta_c^h = 2 \times 10^{-3}. \tag{5.2}$$

Several coarser criteria have then been used, leading to solutions with varying degrees of error. The maximum damage error maps obtained for each coarse stopping criterion value are shown in Figure 5.2. The error

$$\Xi_{\eta_c^\ell} = \frac{\left| D_{\max}^{(k)}\left(\eta_c^\ell\right) - D_{\max}^{(k)}\left(\eta_c^h\right) \right|}{\max_{j \in [\![1,n]\!]} D_{\max}^{(j)}\left(\eta_c^h\right)} \tag{5.3}$$

shown corresponds to the approximation error made using a low-fidelity solution relative to the maximum damage value of all studies. Figures 5.2b and 5.2c respectively show the error made when considering $\eta_c = 2 \times 10^{-2}$ and $\eta_c = 5 \times 10^{-2}$ while figure 5.2a shows the reference damage map in the parametric space.

Increasing the stopping criterion by an order of magnitude only leads to a 3 % error for the maximum damage assessment.

Figure 5.3 shows that the classification goal is even less impacted by using a lower fidelity solution than the complete response surface. Table 5.1 summarises the classification error made using each coarse stopping criterion. Only 0.6 % of the computations are ill-classified when an order of magnitude coarser stopping criterion is used.

While classification is only slightly affected by the choice of a much coarser stopping criterion, the numerical benefits of doing so are substantial. Figure 5.4 shows the number of iterations required when using a fine stopping criterion and the difference in the number of

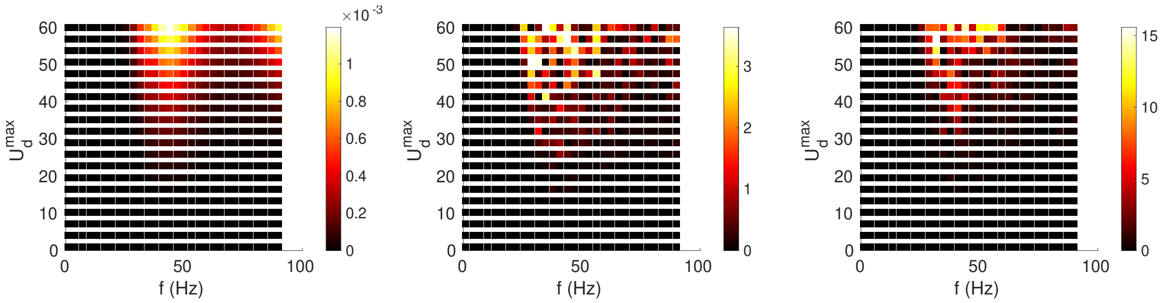

(a) $D^{\max}$ - $\eta_c = 2\times10^{-3}$ **(b)** Approximation error $\Xi_{\eta_c^\ell}$, $\eta_c^\ell = 2\times10^{-2}$ **(c)** Approximation error $\Xi_{\eta_c^\ell}$, $\eta_c^\ell = 5\times10^{-2}$

Figure 5.2 • Approximation error for different values of coarse stopping criterion η_c^ℓ

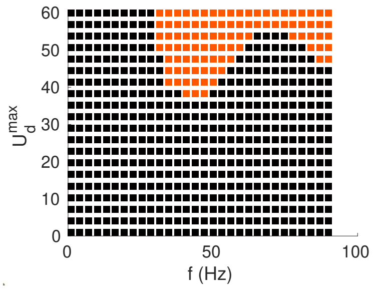

(a) Classification surface with $\eta_c = 2\times10^{-3}$

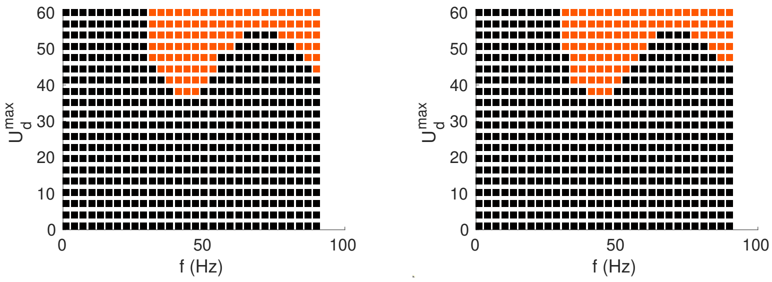

(b) Classification surface with $\eta_c^\ell = 2\times10^{-2}$ **(c)** Classification surface with $\eta_c^\ell = 5\times10^{-2}$

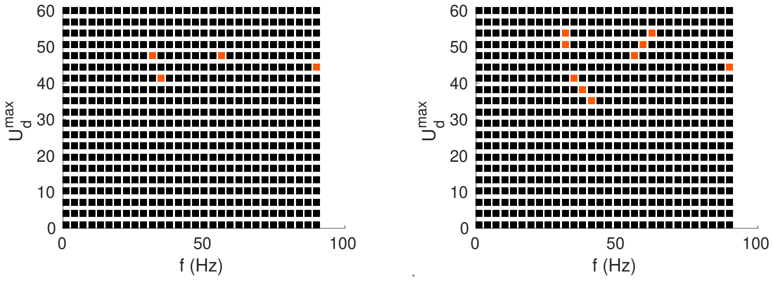

(d) Ill-classified simulations with $\eta_c^\ell = 2\times10^{-2}$ **(e)** Ill-classified simulations with $\eta_c^\ell = 5\times10^{-2}$

Figure 5.3 • Influence of the stopping criterion on the classification precision between computations leading to failure (red) and safe results (black).

η_c	Error max	Number of ill-classified simulations
2×10^{-2}	3.5 %	4
5×10^{-2}	15 %	9

Table 5.1 • Relative error in maximum damage and classification error for different values of stopping criterion η_c.

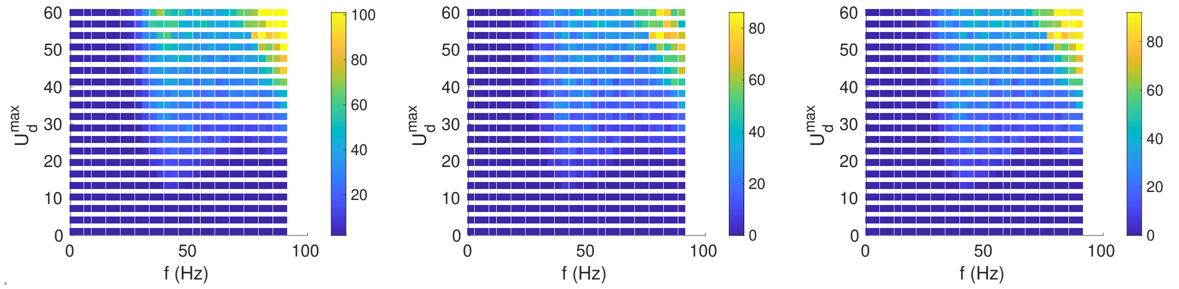

(a) Number of iterations for $\eta_c^h = 2 \times 10^{-3}$

(b) Difference in the number of iterations $\Delta n_{\eta_c^\ell}$, $\eta_c^\ell = 2 \times 10^{-2}$

(c) Difference in the number of iterations $\Delta n_{\eta_c^\ell}$, $\eta_c^\ell = 5 \times 10^{-2}$

Figure 5.4 • Difference in the number of iterations for different values of stopping criterion η_c.

modes

$$\Delta n_{\eta_c^\ell} = n_{\eta_c^h} - n_{\eta_c^\ell} \tag{5.4}$$

between a simulation relying on a fine and coarser stopping criterion. For the most demanding scenario, the number of iterations required to reach convergence can drop from up to 80 %. In general, Figures 5.4b and 5.4c show that the difference in the number of iterations is of the same magnitude as the number of iterations required with the fine criterion shown in Figure 5.4a, indicating a general significant decrease in the number of iterations needed to reach convergence for low-fidelity simulation.

Similarly, Figure 5.5 shows the number of modes required when using a fine stopping criterion and the difference in the number of modes

$$\Delta m_{\eta_c^\ell} = m_{\eta_c^h} - m_{\eta_c^\ell} \tag{5.5}$$

between a simulation relying on a fine and coarser stopping criterion. For the fine stopping criterion, 50 modes are generated for the most complicated cases, and those simulations converge with up to 40 modes less when using coarser criteria. More generally, the calculations converge with fewer modes when relying on a coarse stopping criterion.

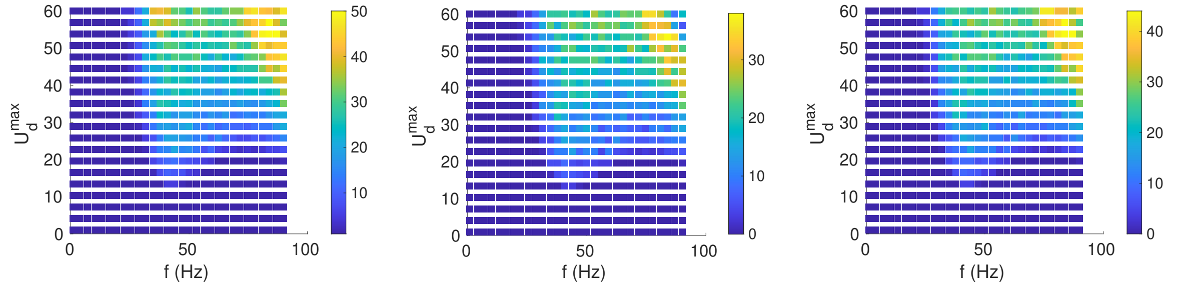

(a) Number of modes for $\eta_c^h = 2 \times 10^{-3}$

(b) Difference in the number of modes $\Delta n_{\eta_c^\ell}$ for $\eta_c = 2 \times 10^{-2}$

(c) Difference in the number of modes $\Delta n_{\eta_c^\ell}$ for $\eta_c = 5 \times 10^{-2}$

Figure 5.5 • Difference in the number of modes for different values of stopping criterion η_c.

Numerical benefits from low-fidelity solutions are more important for high frequency and high amplitude, *i.e.* highly non-linear loading scenarios. At the same time, the classification errors appear to be localised towards the decisive regions where the maximum damage $D^{\max}$ is close to the damage threshold D_c. Utilising different values of stopping criterion for those two cases would decrease the numerical cost while keeping an accurate classification between simulations leading to failure and those that do not.

2.2 Multi-fidelity strategy

To achieve the most accurate classification, this chapter proposes to dynamically adjust the stopping criterion of LATIN, allowing reliance on lower-quality solutions when the outcome of the ongoing classification is almost certain. Additionally, it suggests employing refined simulations for points with a more critical classification due to their proximity to the failure threshold D_c. The proximity indicator

$$d_{(k)}^{(j)} \triangleq \left\| \left| \operatorname{diag}\left(\tilde{\boldsymbol{\Sigma}}^{(j)}\right) \odot \exp\left(J \boldsymbol{\Theta}_{(k)}^{(j)}\right) - \operatorname{diag}\left(\boldsymbol{\Sigma}^{(k)}\right) \right| \right\|_2 \tag{5.6}$$

presented in Chapter 4 is used to select a suited stopping criterion. If the PS associated with the current computation lead to a maximum damage value $D^{\max}$ that is further than a given value Ξ_η from the threshold D_c then we assume that the current calculation will output maximum damage that is also far from the threshold. Therefore, this simulation is not critical to the classification process and does not require a fine knowledge of the exact value of $D^{\max}$. The stopping criterion for such a computation can be relatively coarse. Conversely, a fine stopping criterion is used if a simulation is paired with a PS, highlighting a damage value close to the failure threshold. Figure 5.6 depicts a region confined between two horizontal blue planes, within which lies the red plane $D^{\max} = D_c$. This region highlights simulations that demand fine computations. In this zone, $\eta = \eta_c^h$ is employed; conversely, outside this region, η_c^ℓ is utilised.

The method for dynamically selecting the stopping criterion is graphically sumarised in Figure 5.7.

> **Remark** Although rather naive, this approach should be studied to verify its relevance. Indeed, the advantages of a coarse stopping criterion could be offset by lesser benefits when reusing the weakly converged inelastic corrections in the enhanced framework.

2.3 Numerical results

This section shows the numerical results associated with the multi-fidelity strategy that has been coupled with the enhanced framework presented in Chapter 4.

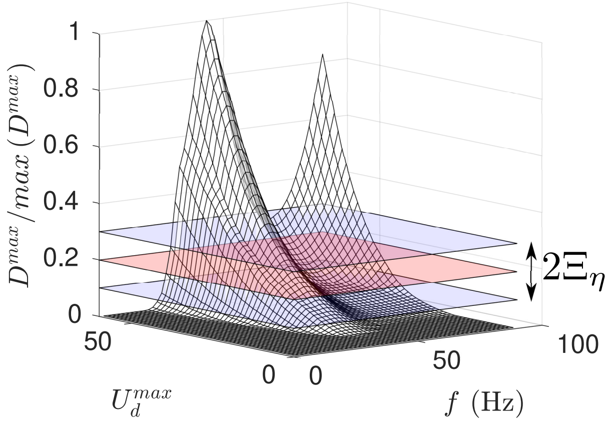

Figure 5.6 • Demarcation of low and high fidelity computations

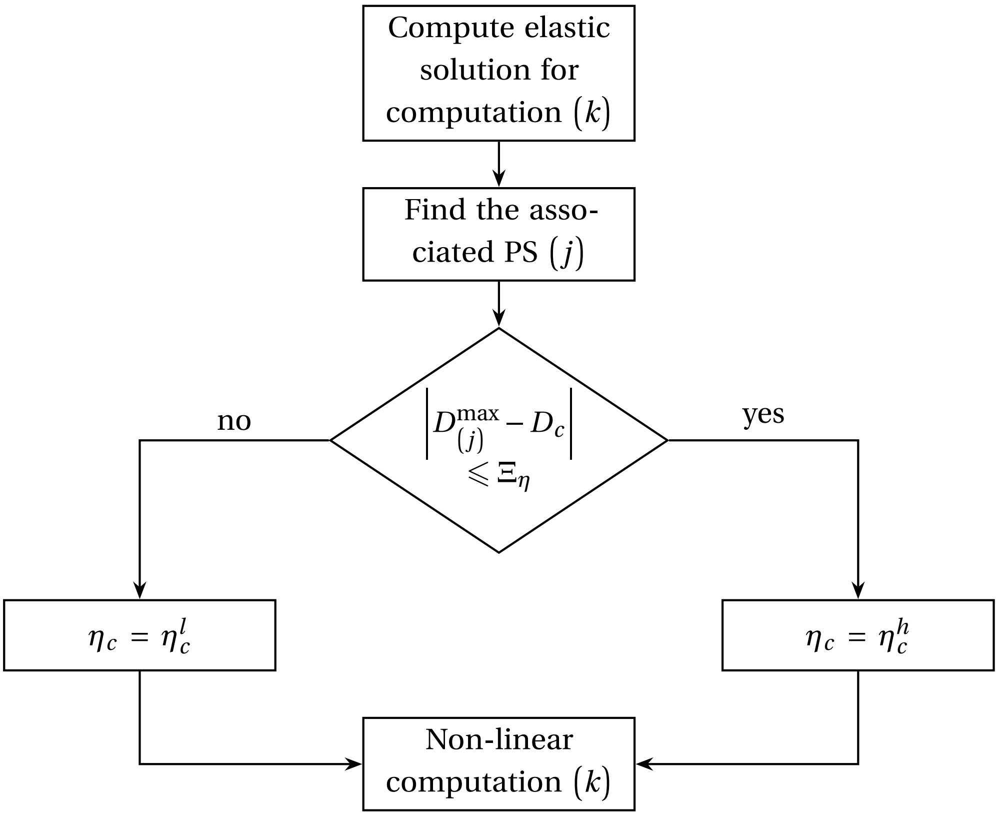
Compute elastic solution for computation (k)
Find the associated PS (j)
$\left|D^{\max}_{(j)} - D_c\right| \leqslant \Xi_\eta$
no
yes
$\eta_c = \eta_c^l$
$\eta_c = \eta_c^h$
Non-linear computation (k)

Figure 5.7 • Flow chart of the dynamic update of the stopping criterion methodology

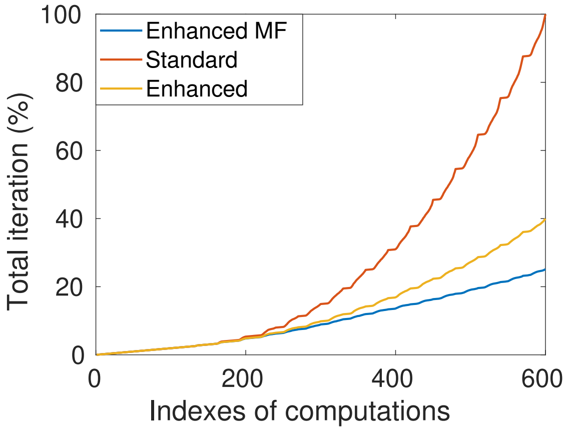

Figure 5.8 • Comparison of the number of iterations for the standard method, the enhanced method and the enhanced multi-fidelity method

Figures 5.8 compares the new multi-fidelity strategy with the sole enhanced framework and the standard method. The multi-fidelity method has been tested with the hyperparameters pair $\eta_c^{\ell} = 2 \times 10^{-2}$ and $\Xi_{\eta} = 1/2D_c$. Such a combination entails no classification error and, therefore, no error in the fragility curve we are trying to obtain. The plot shows, however, that the multi-fidelity strategy offers additional gains compared with the enhanced method, thus significantly decreasing the numerical burden of the standard method. A factor of four is observed compared to the standard method. These results illustrate that substantial numerical gains can be obtained without compromising the quality of the prediction of the probability of failure of the structure.

The enhanced multi-fidelity strategy allows quick access to a response surface, *i.e.* a surrogate or meta-model. This model can then be accessed as a results library, thus allowing a rapid estimation of the maximum damage in the structure for a large range of inputs. Fragility curves construction is an example of an application that can greatly benefit from such charts. Once the response surface has been computed, assessing the probability of failure becomes a simple post-process of the latter.

3 Fragility curves

Fragility curves give access to the failure probability of the structure subjected to uncertain loading scenarios as a function of the scalar parameter α describing the severity of the loading. That parameter can, for instance, be the *peak displacement*, *i.e.* the maximum displacement $\alpha = U_d^{\max}$ in our study. A given set $\left\{U_d^{\max\,(i)}\right\}_{i\in[\![1,N_f]\!]}$ of loading severity defines the number of points in the curve. For each point, *i.e.* for each value of $U_d^{\max}$, N_s frequency realisations must be sampled according to a given probability distribution. Figure 5.9a shows the boolean surface obtained with the surrogate model. The construction of the fragility curve will be based on readings of that surface. Figure 5.9b shows how weight is associated with each point of the classification surface for the frequency sampling.

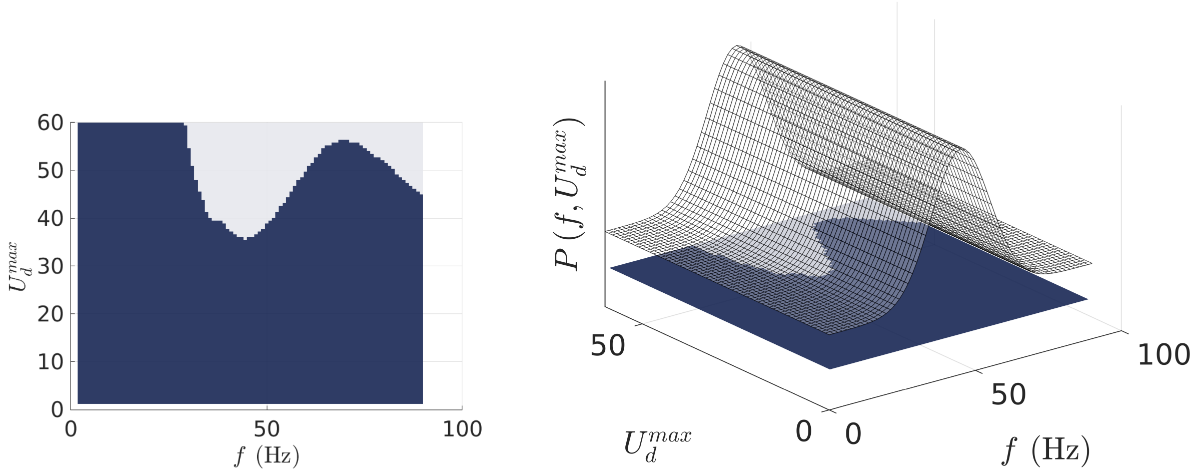

(a) Classification between computations leading to failure (grey) and safe results (dark blue).

(b) weighting procedure using a gaussian distribution.

Figure 5.9 • Classification and weight attributed to each point of the classification surface for the sampling procedure

For the fragility curve to converge, the number N_f of frequency samples for each displacement value must be very large. Using meta-models reduces the cost of constructing fragility curves since the numerous calls to the solver for each random frequency draw become a simple matter of reading the previously constructed virtual chart instead of new computations. Figure 5.10 shows the fragility curves obtained with a normal distribution for the frequency draws

$$f \sim \mathcal{N}\left(60\,\text{Hz}, 10\,\text{Hz}\right) \tag{5.7}$$

for different numbers of sample N_s. The influence of the number of draws for frequency sampling appears significant, justifying the need to consider a large number of draws. As the number of draws is less than a thousand, artefacts appear in the form of fluctuations along the fragility curve, indicating that the curve is not converged.

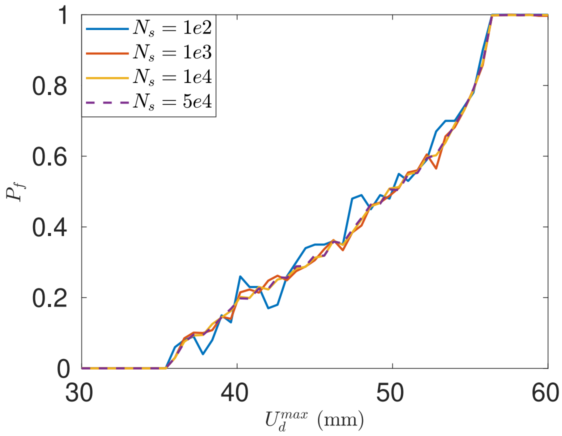

Figure 5.10 • Influence of the number of draws on the fragility curve

Chapter summary

The enhanced framework presented in Chapter 4 has been applied to a context where only specific quantities of interest are required. The goal of the present chapter was to extend the enhanced framework to classification study where coarse solutions suffice for some of the computation when there is little doubt about the outcome. Nonetheless, to ensure a precise classification, a multi-fidelity approach has been used where fine computations are performed on decisive computations only and coarser simulations are used elsewhere. This extension is straightforward based on the tools developed in Chapter 4 and allows significant numerical benefits without compromising the integrity of the classification outcome.

* * *

Perspectives

Such a framework should now be used on real non-parametrised seismic inputs. Several in-depth studies should also be carried out to robustly set the values of the new hyperparameters of the method, namely the range Ξ_{η_c} in which fine computations are required and the optimal value of the coarse stopping criterion η_c^{ℓ}. The gains shown in this chapter correspond to choices of method parameters that do not lead to any classification errors. The question of a possible acceptable error in classification can be raised. In such a case, the numerical gains could be greater at the cost of a less accurate classification. This discussion is complementary to implementing a robust method for the choice of parameters.

Conclusion & perspectives

This PhD dissertation focused on building an optimal multi-query framework for non-linear dynamics based on reduced-order model techniques. More specifically, the main objective of this work was to build virtual charts to predict the probability of failure of structures subjected to uncertain loading scenarios. The proposed framework, therefore, needed to be suited for tackling many non-parametrised loading scenarios in the most efficient manner possible, unlike many methods in the literature, which are adapted to explicitly parametric studies. Several theoretical and practical contributions were made to address these challenges, thereby removing some of the identified obstacles and opening the way to new perspectives to extend the work presented in this manuscript.

The proposed method's first brick consists of an efficient reduced-order model solver based on the LATIN-PGD method, where the dynamic computations are solved in the frequency domain while addressing the non-linear behaviour in the temporal domain. This solver can handle transient dynamics and compute non-periodic solutions with the FFT by relying on artificial damping to prevent Gibbs phenomena. The Proper Generalised Decomposition proved to be well-suited to describe the non-linear displacement corrections impacted by very localised damage effects. A comparison with a reduced-order basis comprising Linear Normal Modes revealed that the PGD provided a better solution approximation with fewer modes, particularly for highly localised patterns requiring high-frequency vibration modes for accurate representation. The chosen approach requires only a small number of PGD modes to represent solutions for various problems, minimising the computational cost.

Then, a new multi-query framework for non-linear dynamics, built on the LATIN solver, has been introduced. This framework effectively relies on computation similarities to substantially reduce the computational cost of multiple-loading studies. This enhanced methodology is built on three principles:

- **Principle I**: Smartly initialising the iterative solver with a parent-simulation,
- **Principle II**: Identifying a well-suited parent-simulation,
- **Principle III**: Designing an optimal sequence in which computations are performed.

The enhanced methodology has successfully decreased the number of iterations required for convergence in sequential computations. Moreover, when used with a reduced-order solver, this approach yields significant computational benefits by reducing the required number of modes to compute. Comparing this enhanced strategy with both full-order and reduced-order models revealed that reusing both the previous basis and converged solution significantly contribute to lowering numerical costs. Additionally, the sequence in which computations are executed notably impacts the method's performance. Introducing an extra step to determine an optimal computation sequence results in a robust framework that achieves optimal performance. The entire framework led to up to three times fewer iterations and twenty times less PGD modes generation compared to the standard LATIN scheme looped over the set of loadings in the case of a pool of 600 computations. The enhanced framework has proven very effective in a multi-query context and highlights increasingly good results as the number of queries increases.

Finally, the enhanced framework presented in Chapter 4 has been applied to a context where only specific quantities of interest are required. The goal of Chapter 5 was to extend the enhanced framework to classification studies where coarse solutions suffice for some of the computations when there is little doubt about the outcome. Nonetheless, to ensure a precise classification, a multi-fidelity approach has been used where fine computations are performed on decisive computations only and coarser simulations are used elsewhere. This extension allows significant numerical benefits without compromising the integrity of the classification outcome. Indeed, the illustration of the multi-fidelity method did not lead to any classification errors. The resulting fragility curves are, therefore, not affected by the coarse convergence of certain simulations. However, the additional numerical gain compared with the enhanced method increases from a factor of three to a factor of four.

* * *

The proposed framework paves the way for further developments that could significantly improve the current methodology. Although the proposed method has yielded highly satisfactory results, there is still significant room for improvement in several areas, namely the solver, multi-query considerations, and the model's aspects.

Enhancing the Numerical Solver

The number of modes generated during multi-query studies is always greater than the number of SVD modes required to describe the set of solutions. There is, therefore, room for improvement regarding the efficiency and frugality of the generation of PGD modes. To improve this point, it would seem judicious to implement and test the effectiveness of methods tried and tested in the literature for similar cases to those tackled in this work. The Gramm-Schmidt algorithm used to ortho-normalise the spatial modes when a new PGD pair is added could be changed to an (r)SVD. Indeed, doing so leads to orthonormal bases for both the spatial and temporal modes, which proved to significantly decrease the number of required PGD modes to reach a given convergence criterion [Giacoma et al., 2015; Alameddin et al., 2019]. With the same objective of reducing the number of PGD modes to be generated, a combination of vibration and PGD modes could be used to start the LATIN-PGD scheme. The number of vibration modes and the choice of the latter would require an in-depth study. However, such modes would make it possible to replace PGD modes for the more global corrections of the structure displacements, thereby further decreasing the number of PGD modes to compute.

A second point of potential improvement pertains to the frequency solver. While the introduction of artificial damping effectively mitigates the occurrence of Gibbs phenomena, the damped function's periodicity remains imperfect, as the decreasing exponential cannot entirely nullify the function at the end of the temporal widow. Fourier continuation methods [Lyon, 2011; Amlani & Bruno, 2016; Bruno et al., 2015] seem to offer a more elegant solution to the problem of the appearance of Gibbs phenomena due to the non-periodicity of the solution. Thus, comparing the artificial damping method proposed in this manuscript with Fourier continuation methods seems appropriate. While slightly increasing the numerical cost by adding a few imaginary points, these methods allow the FFT algorithm to be used on non-periodic fields, effectively mitigating the occurrence of Gibbs phenomena. This concept is used in the presented work for *a posteriori* frequency derivation. However, its usage for solving partial differential equations in the frequency domain directly is appealing and has proven very robust in the context of spatial differential equations.

This work has not addressed the numerical treatment associated with the computation of the local but non-linear constitutive equations. The prohibitive cost of the *local stage* of the LATIN method could be decreased using machine-learning or data-driven techniques. In both cases, the idea would be to bypass the need to solve the behaviour equations in the first stages of the LATIN scheme. Indeed, in the early stages of the method, the intermediate is far from the converged solution. Thus, the precise computation of the expensive solutions of the non-linear behaviour is wasteful. Conversely, using a rough approximation given by a trained neural network or a data-driven approach such as [Ladevèze et al., 2019; Gerbaud et al., 2022] for the first iterations allows to go through the iterative process at lower cost. The key idea would be to toggle back on the computation of the exact solution of the behaviour equations when the convergence criterion gets smaller. This way, the final solution satisfies both the global and local equation of the problem and is indeed the solution to all the equations of the problem. Doing so also ensures that even in cases where the machine learning approach fails to give satisfactory results, the converged solution would still be suitable.

Finally, the non-linearities could be tackled more locally. The structure could be paved with patches representing its details, and the PGD could be applied independently onto the different patches so that local modes would describe specifically localised non-linearities. Such an approach has been used jointly with a decomposition method to couple the different patches [Néron et al., 2016]. From one query to another, the library of modes of the different patches could also be reused in areas where similar non-linearities are expected. Such an approach falls into the scope of local-global methods that have shown good results for modelling localised phenomena that occur in cases of fatigue [Cardoso et al., 2018] or damage prediction [Nagaraj et al., 2021] for instance.

Areas for improvement in the multi-query framework

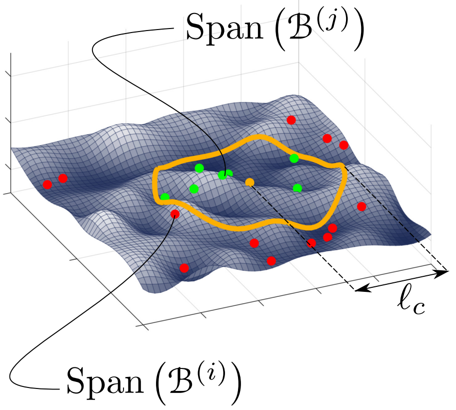
$\operatorname{Span}\left(\mathcal{B}^{(j)}\right)$
ℓ_c
$\operatorname{Span}\left(\mathcal{B}^{(i)}\right)$

Figure 5.11 • Selection of multiple PS using the Grassmann distance

In a multi-query framework, improving the initialisation of the PGD basis could involve incorporating PGD modes generated during multiple preceding computations rather than solely relying on the PGD modes from the parent-simulation. In this regard, the Grassmann distance between computations could be used to reuse the PGD modes from more than one previous calculation by adding a distance threshold ℓ_c. The initial PGD basis for the new simulations would include the spatial modes from all previous computations within this distance from the current calculation. Over the long term, in order to make the most out of the different PGD basis computed in a multi-query parametric context, relying on a bases interpolation method as proposed in [Mosquera et al., 2019; Friderikos et al., 2022] for POD basis might lead to better suited initial PGD basis, thus further decreasing the number of PGD modes to generate for the current computation.

Moreover, in a parametric context where the number of simulations is not fixed, relying on surrogate models and kriging methods coupled with the multi-fidelity framework detailed in [Nachar et al., 2020] would allow decreasing the number of computations needed to build the virtual chart, thereby decreasing the overall cost of the study.

Finally, the use of deep learning methods to interpolate the non-linear response of the structure for a new loading after learning its response for a large number of previously simulated loads could also be considered. This learned response could be used as a space-time initialisation for the LATIN scheme to speed up the calculation of the solution for a new load while ensuring that it satisfies the equations of the problem. In the case where only the loading changes from one calculation to another, graph neural network methods have shown good interpolation capacity for different loadings in a non-linear mechanics case [Hernandez et al., 2022].

Perspectives related to the damage model

This study's aim was not to assess damage phenomena but rather to develop and validate a computational framework capable of efficiently handling numerous non-linear dynamics calculations. It is worth noting that the damage model used in the work is inherently flawed as it does not provide a convergence propriety regarding the mesh size. Conversely, non-local damage models appear more realistic and consistent with experimental results. Those non-local models require solving additional equations and are computationally expensive. However, they can be put under the form of a *heat equation* [Azinpour et al., 2018; Marconi, 2022]. Therefore, implementing such a method would be identical to solving a multi-physics problem. The proposed methodology being based on the LATIN method, solving such a coupled problem with a reduced-order model for both physics appears straightforward. It has already been implemented in the case of standard multi-physics problems [Néron & Ladevèze, 2010b]. The extension of the LATIN-PGD to the non-local damage model treated as a coupled problem also appears appealing. We expect results in reducing the computational cost for non-local problems similar to those obtained in the case of multi-physics problems.

Appendix

Appendix A

Frequency derivation

In order to ensure consistency in the integration and differentiation schemes throughout the methodology, it is necessary to obtain the first and second derivatives of the temporal field, denoted as $f(t)$, through the frequency domain. However, when the function values at the boundaries of the temporal domain I are not equal, the non-periodicity of the function between $t = 0$ and $t = T$ can give rise to the occurrence of Gibbs phenomena. Therefore, careful attention must be given to the approach employed for deriving these derivatives. To address this issue, a technique is employed wherein the periodicity of the function is restored by extending the temporal domain of study with a buffer zone, where the initial and final values of the function are matched. This allows for a smoother transition and re-establishes periodicity within the extended temporal domain, facilitating the utilisation of Fourier analysis techniques. By following this procedure, the first and second derivatives of the original temporal field $f(t)$ can be accurately computed in the frequency domain and subsequently transformed back to the time domain for further analysis while mitigating the effects of the Gibbs phenomena.

1 Continuation method

The idea is based on the Fourier-based continuation method [Lyon, 2011; Amlani & Bruno, 2016; Bruno et al., 2015] that allows to artificially retrieve periodicity in cases where the target function is not periodic.

To do so, the domain $I = [0, T]$ is extended to $\tilde{I} = [0, T + a]$ where the zone $[T, T + a]$ is the buffer zone. The buffer zone is discretised in n_b time steps which allow to interpolate a matching function $\phi_b(t)$ so that

$$\begin{cases} \phi_b\left(t \in \left[T-k, T\right]\right) = f\left(t \in \left[T-k, T\right]\right) \\ \phi_b\left(t \in \left[T+a, T+a+k\right]\right) = f\left(t \in \left[0, k\right]\right) \end{cases} \tag{A.1}$$

The extended function $\phi(t)$ on which derivation will be applied then reads

$$\phi(t) = \begin{cases} f(t), \text{ if } t \in [0, T], \\ \phi_b(t), \text{ if } t \in [T, T+a]. \end{cases} \tag{A.2}$$

The resulting function exhibits periodicity, effectively mitigating the challenges arising from the non-periodic nature of the initial function $f(t)$. By introducing additional time steps within the buffer zone, periodicity is attained, albeit with minimal interpolation points. Consequently, this enables utilising the Fast Fourier Transform (FFT) technique without encountering the Gibbs phenomenon near the temporal window boundaries. Moreover, the computational overhead associated with incorporating the buffer zone remains reasonably low, ensuring that the overall additional computational cost remains manageable.

2 Example

This section illustrates the continuation method for the derivation of the function

$$f(t) = \exp\left(-\left(\frac{10t - T}{2T}\right)^2\right) \sin(2\pi f t) \tag{A.3}$$

for the following set of parameters

$$\begin{cases} f = 2\,\text{Hz} \\ T = 2.1\,\text{s}. \end{cases} \tag{A.4}$$

The continuation method is graphically explained in Figure A.1a, where the buffer zone is shown in blue, the initial function is plotted in green, and the interpolation points are shown in red. Figure A.1b shows the final extended function on which operations are performed.

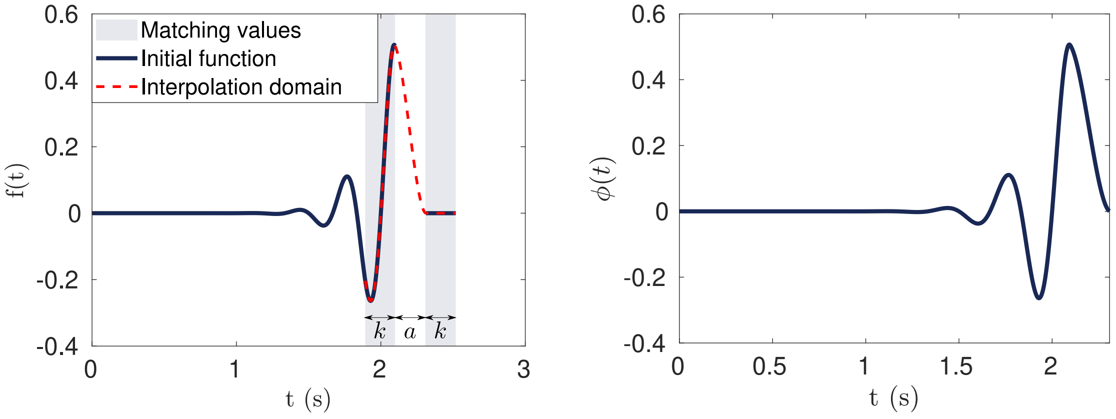

(a) Graphical illustration of the method

(b) Extended function $\phi(t)$

Figure A.1 • Continuation based method

The method has been applied to compute the first derivative of the function defined in Equation A.2, and the results are presented in Figure A.2. The first derivative obtained with the FFT is compared to the analytical derivative and the result given by a finite difference scheme (FD). Figure A.2a plots the results while Figure A.2b compares the influence of the number of time steps on the error of both methods compared to the analytical derivative. The Fourier-based derivation gives much closer results to the analytical function than the FD scheme.

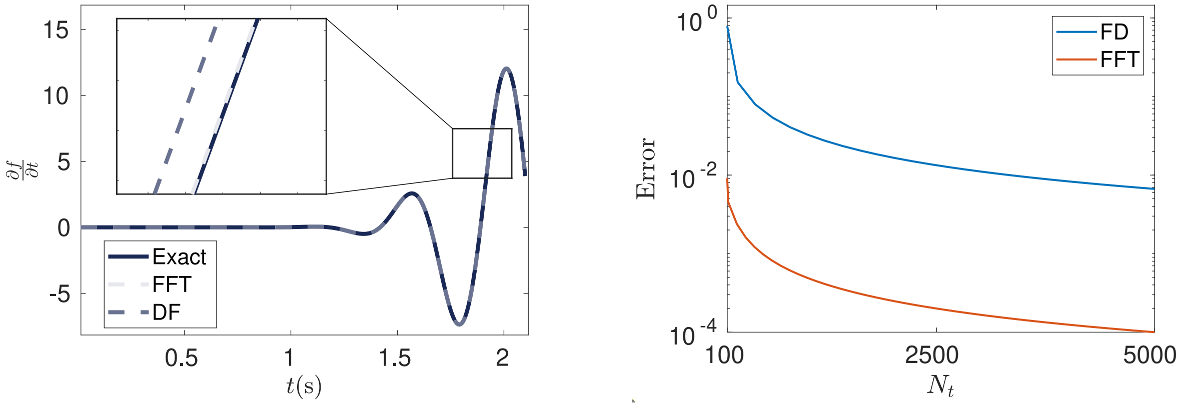

(a) Plot of the first derivative and comparison of the results

(b) Error as a function of the number of time steps

Figure A.2 • Comparison of Fourier and finite difference first order derivation

Appendix B

ROMlab

ROMlab is an *in-house* code written in MATLAB® language. It consists of a shared platform for reduced-order model and LATIN-based methods implementation. Throughout the years, the platform has been used as a demonstrator for new numerical tools, and its capabilities have been extended so that a wide range of physical problems can now be solved using that software.

1 History

The beginnings of ROMlab came from David Néron, and the development of the code has since been maintained by researchers of the LMPS lab (former LMT).

A non-exhaustive list of the main and most recent contributors to ROMlab is given in Figure B.1.

The numerical work and developments presented in this doctoral dissertation were carried out in parallel with work on domain decomposition in magnetostatics [Ruda et al., 2022] and on the strong coupling of different physics [Wurtzer et al., 2023]. The elementary blocks and the new operators introduced have been designed in a standard way to manage primal and dual fields generically in all these approaches, whatever the dimensions of the fields treated, for example.

2 Principles

One of the objectives is to mutualise as many steps and tools as possible across all applications. The pre-processing and post-processing stages are thus shared, regardless of the physics or behaviour being addressed. The assembly operations of different operators share the same core plug-ins as similarities between physics are utilised to minimise differentiating the code for each user.

The data input involves providing a mesh generated from GMSH, along with the physics and loading parameters and solver settings. Based on these data, the various operators are

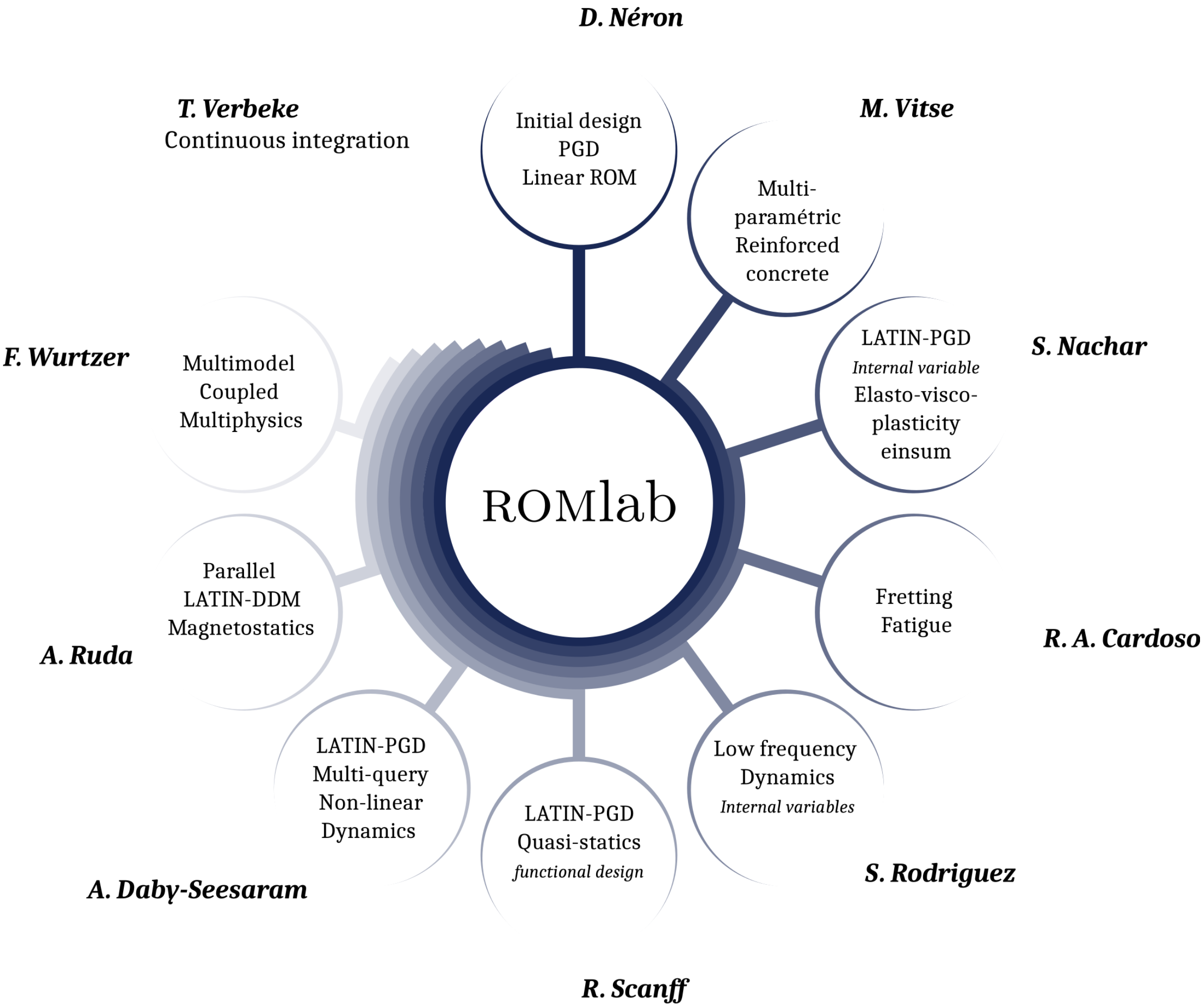
D. Néron
Initial design
PGD
Linear ROM
M. Vitse
Multi-
paramétric
Reinforced
concrete
S. Nachar
LATIN-PGD
Internal variable
Elasto-visco-
plasticity
einsum
R. A. Cardoso
Fretting
Fatigue
S. Rodriguez
Low frequency
Dynamics
Internal variables
R. Scanff
LATIN-PGD
Quasi-statics
functional design
A. Daby-Seesaram
LATIN-PGD
Multi-query
Non-linear
Dynamics
A. Ruda
Parallel
LATIN-DDM
Magnetostatics
F. Wurtzer
Multimodel
Coupled
Multiphysics
T. Verbeke
Continuous integration
ROMlab

Figure B.1 • ROMlab contributors, reproduced from [Ruda, 2023]

constructed during the pre-processing stage. Depending on the physics and chosen solver, the appropriate solving step is then executed, and the results can be exported in a file format compatible with the Paraview software.

One of the key challenges in developing ROMlab, which is capable of handling quasi-industrial cases, is paying particular attention to software optimisation, making the most of current multi-threaded parallel architectures. The entire code is thus vectorised, notably utilising the ‘einsum’ function developed in MATLAB® by Stéphane Nachar, which enables the use of Einstein summation.

3 Personal contributions

The work carried out during this doctoral thesis has expanded ROMlab’s capabilities. It can now handle non-linear dynamics. The damage behaviour driven by plasticity, accounting for crack closure effects as presented in Chapter 1, has also been implemented.

As mentioned in Chapter 3, numerous material behaviours can seamlessly be used in the local stage; therefore, the dynamics addition benefits from previously added behaviour in addition to the newly added damage model used in this thesis.

A full-order model LATIN-based solver, *i.e.* without PGD, has also been implemented for validation purposes. With either a frequency solver or Newmark schemes, ROMlab can now solve non-linear dynamics problems with and without reduced-order model techniques.

A portion of matrix operations has been modernised using the new vectorised functions in MATLAB®, which enable simultaneous processing across multiple matrices. Similarly, the utilisation of the MATLAB® “decomposition” function is now systematic. This function creates reusable matrix decompositions, consequently reducing the analysis time when performing a Cholesky decomposition multiple times on the different operators, for instance.

Appendix C

Industrial framework

This appendix presents the broader industrial framework for characterising failure prediction in piping components. The doctoral dissertation focuses on the final stage, which consists in predicting the damage evolution in the structure subjected to mechanical loading; however, damage levels in the structure evolve throughout its entire life cycle. The nominal operation of piping elements means they are subjected to high thermal stresses that fluctuate over time. This stress causes thermal fatigue, which in turn damages the pipe structure. The industrial framework must, therefore, account for prior damage existing before the occurrence of an earthquake or any other mechanical solicitation applied to the structure. Thus, preliminary high cycle fatigue (HCF) damage is assessed based on the thermo-mechanical loading due to the nominal behaviour of the power plant. In this context, the weakly coupled thermo-mechanical model employed is outlined, along with its numerical implementation. The coupled thermo-mechanical behaviour of the structure is solved for one cycle, and the result is post-processed to assess the fatigue damage over a given number of cycles N_c.

1 Isotropic thermo-mechanical formulation

A weak coupling is considered between thermal and mechanical aspects, where thermal effects influence mechanical behaviour, while the reciprocal interaction is neglected.

First, the temperature evolution in the pipe is computed by solving the heat equation in the domain Ω

$$\begin{cases} T = T_d, \ \forall \boldsymbol{x} \in \partial\Omega_1^{th} \\ T\left(\boldsymbol{x}, t=0\right) = T_0\left(\boldsymbol{x}\right), \ \forall \boldsymbol{x} \in \Omega \\ \rho c \dot{T} = -\nabla \cdot \boldsymbol{q} + r_d \ \forall \boldsymbol{x} \in \Omega \\ \boldsymbol{q} \cdot \boldsymbol{n} = j_{th} \ \forall \boldsymbol{x} \in \partial\Omega_2^{th} \\ \boldsymbol{q} = -k_{th} \nabla T, \ \forall \boldsymbol{x} \in \Omega. \end{cases} \tag{C.1}$$

The ensuing temperature field is used to compute a thermal preload as a strain

$$\boldsymbol{\varepsilon}^{th} = \alpha \mathbb{1} \left(T - T_0\right), \tag{C.2}$$

with k the conductivity of the material and α the dilatation parameter. When modelling the pipe's nominal operating condition, the mechanical equilibrium's inertial terms are neglected. The mechanical problem in weak form, therefore, becomes

$$\begin{cases} \boldsymbol{u} = \boldsymbol{u_d},\ \forall \boldsymbol{x} \in \partial\Omega_1 \\ \nabla \cdot \boldsymbol{\sigma} + \boldsymbol{f_d} = 0\ \forall \boldsymbol{x} \in \Omega \\ \boldsymbol{\sigma n} = \boldsymbol{F_d}\ \forall \boldsymbol{x} \in \partial\Omega_2 \\ \boldsymbol{\sigma} = \mathbb{K}\left(\varepsilon - \varepsilon^{th}\right) \end{cases} \tag{C.3}$$

Tacking the mechanical loading to be zero, *i.e.*

$$\begin{cases} \boldsymbol{u_d} = 0, \\ \boldsymbol{f_d} = 0, \\ \boldsymbol{F_d} = 0, \end{cases} \tag{C.4}$$

the resulting stress solely corresponds to thermal stress $\boldsymbol{\sigma}^{th}$, which can then be used to assess the damage due to thermal fatigue using post-processing based on S-N curves.

2 Thermal damage assessment

The thermal stress σ^{th} derived from elastic computations is further analysed through the use of Wöhler curves interpolation and HCF approaches, which provide a lifetime ratio that quantifies damage. This approach yields a specific damage increment value for each cycle, depending on the characteristics of the stress σ^{th}. Consequently, the provision of this stress value at each integration point can be employed to assess the corresponding level of thermal damage at various locations within the structure for a prescribed number of cycles N_c. A harmonisation of this damage value as a lifetime ratio with the notion of damage in continuum mechanics, used in the non-linear model presented in this manuscript, enables the lifetime ratio under thermal loading of the structure to be converted into a pre-damage value D_0 that accounts for the ageing of the structure. The pre-damage value can be used as an input of the non-linear solver, thus taking into account the nominal life cycles of the structure when assessing its failure probability under mechanical input. The CEA has studied the identification of the required parameters for the post-process stage and the harmonisation process in the context of the NARSIS project.

3 Fragility surfaces

It might be interesting to investigate the influence of the structure's lifespan, *i.e.* the number of nominal cycles N_c. To that aim, the number of cycles can be considered a new dimension in the fragility curves that become fragility surfaces. In this configuration, the first dimension gives the influence of the load on the probability of failure. In contrast, the second dimension gives information on the influence of the age of the structure on its probability of failure for a given load.

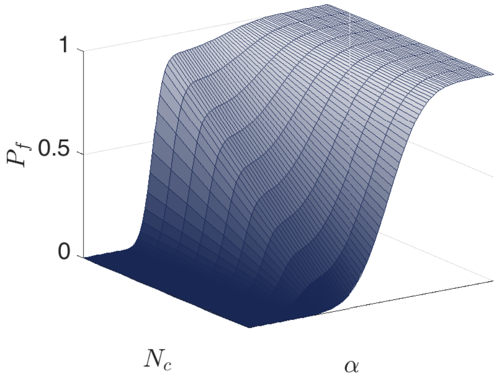

Figure C.1 • Example of a fragility surface

4 Overview of the framework

The industrial framework is graphically illustrated in Figure C.2.

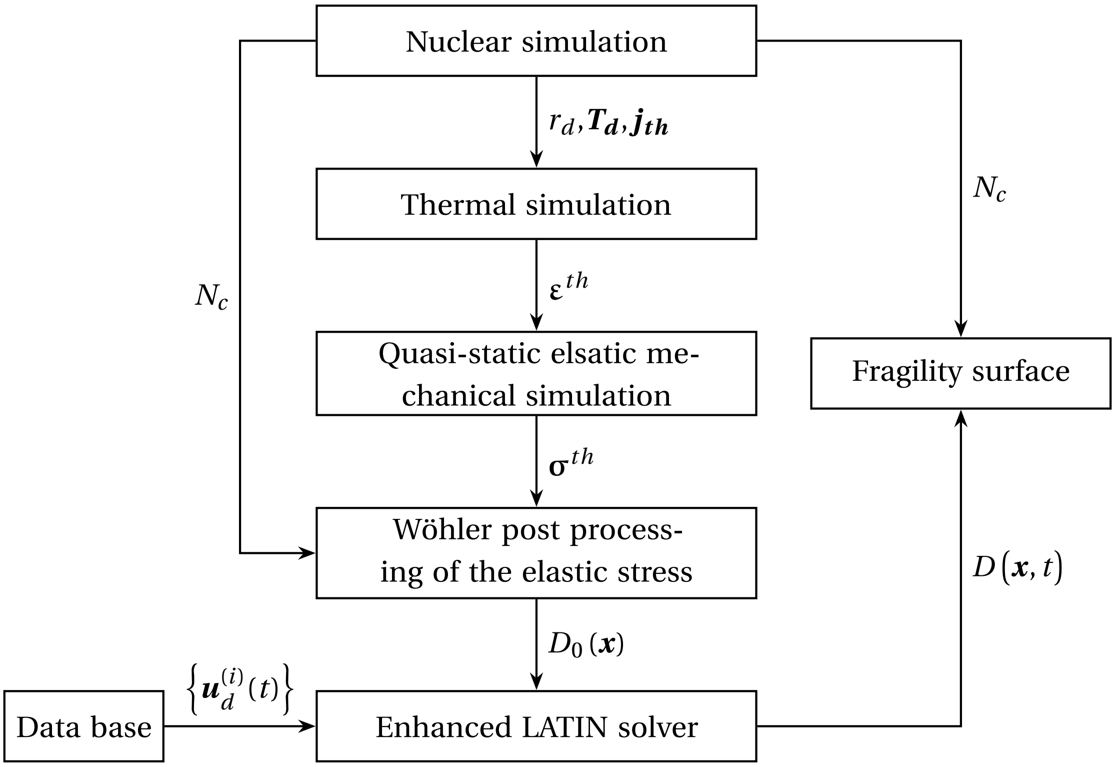
Nuclear simulation
$r_d, \boldsymbol{T_d}, \boldsymbol{j_{th}}$
Thermal simulation
$\boldsymbol{\varepsilon}^{th}$
Quasi-static elsatic mechanical simulation
$\boldsymbol{\sigma}^{th}$
Wöhler post processing of the elastic stress
$D_0(\boldsymbol{x})$
Enhanced LATIN solver
Data base
$\left\{\boldsymbol{u}_d^{(i)}(t)\right\}$
N_c
N_c
Fragility surface
$D(\boldsymbol{x}, t)$

Figure C.2 • Flow chart of the industrial damage assessment framework

Appendix D

Extended abstract in French

Les méthodes de réduction de modèles offrent un moyen efficace de réduire le coût de calcul associé aux larges simulations industrielles. Les méthodes *a posteriori*, telles que la POD, reposent sur une phase *offline* comprenant des calculs non linéaires complets préalables pour plusieurs jeux de paramètres [Chatterjee, 2000]. La base réduite construite à partir des *snapshots* est ensuite utilisée dans la phase *online* pour trouver des solutions à faible coût au problème non linéaire pour un nouvel ensemble de paramètres. L'automatisation de la sélection des *snapshots* a été proposée dans la méthode de la Base Réduite [Maday et al., 2002] qui s'appuie cependant toujours sur des calculs préalables possiblement coûteux. À l'inverse, les méthodes de réduction de modèles dites *a priori*, telles que la PGD [Néron & Ladevèze, 2010a; Chinesta et al., 2011], évitent la phase hors ligne en construisant la base réduite à la volée pendant les calculs. La PGD s'est révélée efficace pour les problèmes dynamiques linéaires [Boucinha et al., 2014] et non linéaires [Germoso et al., 2016; Quaranta et al., 2019]. Plusieurs choix sont possibles pour prendre en compte une dépendance paramétrique du problème avec la méthode PGD. D'une part, les études paramétriques peuvent inclure des paramètres en tant que coordonnées additionnelles du modèle réduit [Chinesta et al., 2011; Lu et al., 2018; Paillet et al., 2018], comme dans la méthode des éléments finis stochastiques [Anders & Hori, 1999]. Cette approche ne nécessite pas de multiples appels au solveur, mais un problème de plus grande dimension est construit. Cette approche nécessite également des solveurs spécifiques pour chaque nouveau problème paramétrique. Un autre choix consiste à séparer uniquement les variables espace-temps, laissant d'autres paramètres éventuels en dehors du solveur et à s'appuyer sur une stratégie multi-query spécifique pour gérer de manière optimale de multiples appels au solveur PGD espace-temps [Nachar et al., 2020; Néron et al., 2015]. Laisser les paramètres supplémentaires en dehors de la décomposition PGD permet de s'appuyer sur des solveurs PGD plus génériques, permettant le développement de solveurs non intrusifs [Scanff et al., 2022]. La base espace-temps PGD est construite explicitement pour le problème en cours. Par conséquent, la PGD garantit une base pertinente pour le problème courant et élimine le besoin de coûteux calculs amonts et de la sélection fastidieuse des *snapshots* [Tegtmeyer et al., 2017]. L'utilisation de la méthode PGD nécessite de manier des solutions globales sur l'espace et le temps. Dans un contexte non linéaire, l'utilisation d'un solveur non-incrémentale est donc requise. Aussi, la méthode LATIN [Ladevèze, 1999], solveur non-incrémental développé pour la résolution de problèmes mécaniques non linéaires, offre un cadre pertinent pour l'utilisation de la méthode PGD en cas de non linéarités. La méthode LATIN consiste en un schéma itératif au cours duquel la solution est alternativement cherchée dans l'espace des solutions aux équations globales et linéaires puis dans l'espace des solutions aux équations locales possiblement non linéaires. La solution exacte vérifiant à la fois les équations locales et globales, se trouve à l'intersection de ces deux espaces. Cette séparation des difficultés permet l'introduction naturelle de la PGD lors de la résolution des équations globales linéaires. La méthode LATIN-PGD a été appliquée à de nombreux contextes non linéaires, y compris pour l'évolution des dommages des matériaux quasi-fragiles soumis à des chargements de fatigue quasi-statiques à faible et grand nombre de cycles [Bhattacharyya et al., 2018b; Bhattacharyya et al., 2019] ou dans des conditions dynamiques [Iturra, 2021; Daby-Seesaram et al., 2023]. Deux points spécifiques ont amélioré la méthode LATIN-PGD dans le contexte multi-query pour des cas de variabilité des matériaux. Premièrement, en s'appuyant sur son caractère non-incrémental, le schéma itératif est initialisé avec la solution espace-temps d'un calcul précédent pour réduire le nombre d'itérations nécessaires à la convergence. Deuxièmement, la base réduite générée pour une simulation précédente est fournie à la nouvelle simulation comme dans le cadre de la POD. Ainsi, l'effort de calcul pour évaluer les modes spatiaux à ajouter à la volée est réduit dans un contexte paramétrique [Heyberger et al., 2012]. Certaines de ces propositions pourraient être utilisées dans le cas de la variabilité des chargements, mais le fait que les différentes simulations ne partagent pas la même admissibilité nécessite des développements supplémentaires.

Le gain numérique apporté par les méthodes de réduction de modèles peut de plus être couplé à la construction d'un méta-modèle pour réduire le nombre d'appels au solveur, diminuant ainsi le coût numérique global de l'étude. De plus, dans un contexte où les solutions complètes associées à chaque calcul ne sont pas utiles, mais où seules certaines quantités d'intérêt sont nécessaires, les simulations intermédiaires peuvent être effectuées avec un critère de convergence grossier. Cela est particulièrement pertinent pour les études d'optimisation, par exemple. Dans un tel contexte, des méthodes de krigeage multi-fidélité couplées à la PGD ont été employées avec succès pour une étude visco-plastique paramétrique [Nachar et al., 2020]. Cependant, l'utilisation de telles méthodes nécessite que le problème soit paramétré avec un nombre suffisamment faible de paramètres. Ces méthodes ne sont donc pas directement applicables au problème abordé dans cette thèse, étant donné que l'accent est mis sur la résolution de problèmes non paramétrés.

* * *

Cette thèse de doctorat présente un cadre multi-requête offrant une méthode efficace pour estimer la probabilité de défaillance structurale dans des conditions de chargement incertaines.

L'étude a été initialement motivée par le cas du risque sismique dans le contexte de la sûreté nucléaire, mais elle s'étend à diverses études nécessitant des calculs dynamiques non linéaires multiples. L'objectif est de développer une méthode efficace lorsque chaque calcul non linéaire est associé à un chargement fourni sous la forme d'un signal temporel indexé non paramétré. Le nombre de calculs à effectuer est donc fixé et ne peut pas être réduit pour atténuer le coût de l'étude. De plus, dans la suite, nous nous abstiendrons de nous appuyer sur des connaissances préalables de toute paramétrisation de la charge, car le cadre se veut utilisable de manière robuste dans des cas où une telle paramétrisation n'est pas immédiatement disponible.

Plus précisément, ce travail propose un cadre composé d'un solveur de dynamique non linéaire efficace associé à une nouvelle stratégie multi-query qui exploite les similitudes d'un calcul à l'autre et offre une procédure robuste pour déterminer un chemin optimal à travers l'espace des scénarios de chargement. Cette thèse est structurée en trois parties. La première partie donne un aperçu de l'état de l'art des calculs dynamiques non linéaires, tandis que la deuxième partie présente les nouveaux éléments au cœur de la méthodologie proposée. Enfin, la troisième partie propose une application de cette méthodologie pour prédire la probabilité de défaillance d'une structure soumise à des risques sismiques. Cette thèse de doctorat comprend un total de cinq chapitres.

1 Méthode de réduction de modèle hybride temps fréquence

Dans le chapitre 3, un cadre hybride original LATIN-PGD a été proposé pour les matériaux endommageables en dynamique. Les calculs liés à l'aspect dynamique sont effectués dans le domaine fréquentiel tout en résolvant toujours le comportement non linéaire dans le domaine temporel. Au cours de ce chapitre, la méthode hybride temps-fréquence couplée à une résolution PGD des équations d'admissibilité est validée sur plusieurs géométries et différents chargements. Il est important de noter que du fait des non-linéarité en jeux, des déplacements résiduels sont attendus en fin de simulation, empêchant ainsi la structure étudiée de revenir à son état initial. De fait la position finale de la structure diffère de sa position initiale ce qui occurre l'apparition de phénomènes de Gibbs lors de la résolution dans le domaine fréquentiel. Pour palier à ce problème, un problème auxiliaire basée sur l'utilisation d'amortissement artificiel est employé comme étape intermédiaire de résolution avant de retrouver par post-traitement la solution exacte initialement recherchée. Aussi, la stratégie est robuste et s'adapte aux simulations pour lesquels l'état final diffère de l'état initial, que ce soit dû à la présence de non-linéarités telles que la plasticité, ou à un faible amortissement de la structure. Les résultats mettent également en évidence la grande réductibilité des problèmes de dynamique à basse fréquence avec un comportement ductile endommageant. En effet, peu de modes PGD sont nécessaires pour représenter la solution des différents problèmes abordés dans ce chapitre. Enfin, il est intéressant de noter quand dans un tel cas, l'utilisation de la PGD semble plus adaptée que l'usage des modes propres de la structure dont la capacité à apporter des corrections locales est moins prononcée.

Ce chapitre présente donc une réponse partielle au problème général abordé dans cette thèse en fournissant un solveur efficace permettant de diminuer le coût de chaque calcul individuellement. Ce solveur tire parti à la fois des avantages apportés par la méthode de réduction de modèles PGD et des bénéfices numériques apportés par la résolution des équations dynamiques dans le domaine fréquentiel.

Afin de réduire davantage le coût numérique de l'étude multi-requête, il s'agit désormais de construire une méthode propice à de telles études reposant sur les spécificités du solveur choisi.

2 Cadre multi-requête proposé

Un cadre multi-query original pour la dynamique non linéaire est proposé dans le chapitre 4. Ce cadre tire avec succès parti des similitudes entre les calculs pour réduire significativement le coût de simulation d'une étude multi-requête. L'idée de ce chapitre est similaire à ce qui se retrouve dans la littérature pour des problèmes dont la variabilité est matérielle. L'idée est de s'appuyer sur le caractère non-incrémental de la LATIN pour venir initialiser le solveur itératif avec une solution espace-temps convergée issue d'une solution précédente dont le résultat est supposé proche du résultat attendu pour le calcul courant. Ainsi, le nombre d'itérations nécessaires à la convergence du schéma itératif pour le calcul courant est réduit. Dans cette thèse, cette idée a été étendue aux cas où la variabilité se trouve non plus dans le matériaux mais dans le chargement. Il a donc fallu adapter la méthode afin de pouvoir tirer parti d'une solution précédente calculée pour des conditions aux limites de type Dirichlet différentes de celles appliquées pour la solution courante, ces deux solutions ne partageant donc plus l'admissibilité. La méthode proposée est également pensée pour s'adapter à des cas pour lesquels une paramétrisation explicite du problème n'est pas accessible. Aussi la façon de choisir le calcul pertinent pour accélérer la simulation courante est basée sur un indicateur de proximité entre la solution élastique associée au calcul courant et l'ensemble des solutions associées aux calculs précédemment effectués. Enfin, les gain apportés par la méthode étant directement lié aux calculs présents dans la bibliothèque de calculs précédemment réalisés, l'ordre dans lequel sont chaînés les calculs influe significativement les résultats obtenus. Une proposition d'automatisation du choix de séquence de calcul est donc énoncée visant à rendre l'ensemble du cadre multi-query le plus robuste possible.

En résumé le cadre multi-query consiste en trois principes listés ci-après.

→ Principe I. Initialisation judicieuse de la solution espace-temps et de la base réduite

Ce premier principe permet de démarrer le schéma itératif plus près de la solution exacte, réduisant ainsi l'erreur initiale et le nombre d'itérations nécessaires pour atteindre la convergence. L'initialisation de la base réduite permet d'éviter les étapes redondantes de la LATIN qui seraient nécessaires au calcul de modes préexistants.

→ Principe II. Sélection d'une simulation parent pertinente

Le fait de s'appuyer sur des solutions élastiques pour trouver la simulation parent optimale permet de trouver de manière robuste un calcul préalable idéal pour initialiser le calcul actuel. Cette approche s'appuie sur des connaissances mécaniques solides, plutôt que sur des descriptions de chargement paramétrées par exemple, ce qui garantit la robustesse de la méthode pour les signaux de chargement non paramétrés.

→ Principe III. Trouver une séquence de calcul optimale

Cette dernière étape permet de s'assurer qu'une simulation parent appropriée est trouvée à travers l'ensemble des solutions antérieures, même au début de l'étude multi-requête, lorsque peu de calculs ont encore été effectués. Cette étape repose sur l'usage d'un algorithme génétique permettant de diminuer la distance cumulée totale entre toutes les simulations effectuées dans l'ordre de la séquence trouvée.

3 Extension multi-fidélité

Le cadre présenté dans le chapitre 4 a été appliqué à un contexte où seules des quantités spécifiques d'intérêt sont requises. L'objectif du chapitre 5 est d'étendre le cadre proposé à une étude de classification où des solutions grossières suffisent pour certaines des simulations pour lesquelles une légère erreur sur le résultat n'aurait aucun impact. Afin de tout de même assurer une classification précise, une approche multi-fidélité a été utilisée, dans laquelle des calculs fins sont effectués uniquement pour des simulations décisives et des simulations plus grossières sont utilisées ailleurs. Cette extension est directe grâce aux outils développés dans le chapitre 4 et permet d'obtenir d'importants avantages numériques sans compromettre l'intégrité du résultat de classification.

List of Figures

1 Human influence on the global surface temperature. (Reproduction of Figure 1 from [IPCC, 2021]) . . . 2

2 Global mean surface air temperature (GSAT) illustrated as warming stripes from blue (cold) to red (warm) over three different time periods. From 1750–1850 based on PAGES 2K reconstructions (PAGES 2k Consortium, 2017, 2019). (Reproduction of Figure 1.25 from [Chen et al., 2021]) . . . 2

3 Projected final energy consumption in the NLCS in France from 2020 to 2050. Reproduced from [RTE, 2021] . . . 3

5 Industrial framework . . . 4

4 Fragility curves and seismic ground motions examples . . . 5

6 Flow chart of the proposed methodology . . . 9

1.1 Reference problem . . . 14

1.2 Kinematic transformation of a continuum medium . . . 15

1.3 Kelvin-Voigt linear model . . . 18

1.4 Example of an S-N curve . . . 23

1.5 Kelvin-Voigt non-linear model . . . 24

1.6 Newton-Raphson scheme applied to mechanics . . . 27

1.7 Spherical Riks method, reproduced from [Crisfield, 1983]. . . . 29

1.8 Comparison between incremental and non-incremental schemes . . . 29

1.9 Graphical illustration of the LATIN method reproduced from [Ladevèze, 1999] . 30

2.1 Parametric manifold $\mathscr{M}$ and approximation of the solution associated to the parameter μ^*. Reproduced from [Rozza, 2014] . . . 39

2.2 Uncompressed image - Furfande, GR 58 . . . 42

2.3 Compressed images and their respective errors . . . 42

2.4 Error function of the number of PGD modes for each colour canal . . . 43

2.5 Wise initialisation strategy . . . 45

3.1 Working principle of the LATIN method, modified from [Ladevèze, 1999] 54

3.2 Scheme of the hybrid frequency-temporal strategy . . . 57

3.3 Frequency modes calculation strategy based on artificial damping . . . 63

3.4 Evolution of the damping rate as a function of the frequency. A Rayleigh damping matrix is used with a damping rate fixed at 5 % for the first two eigenfrequencies $f_1 = 30\,\text{Hz}$ and $f_2 = 78\,\text{Hz}$. 64
3.5 Two-dimensional fixed-end beam 65
3.6 Temporal load 1 - mono-frequency case 66
3.7 Evolution of the damage field for the beam solicited with load 1 - $f = 40\,\text{Hz}$ and $U_d^{\max} = 100\,\text{mm}$ 66
3.8 Damage evolution at different points of the beam (Figure 3.5) solicited with load 1 - $f = 40\,\text{Hz}$ at $U_d^{\max} = 100\,\text{mm}$ 67
3.9 Convergence of the error indicator and evolution of the number of PGD modes with LATIN iteration for the beam solicited with load 1 - $f = 40\,\text{Hz}$ and $U_d^{\max} = 100\,\text{mm}$ 67
3.10 Magnitude of PGD modes for the beam solicited with load 1 - $f = 40\,\text{Hz}$ and $U_d^{\max} = 100\,\text{mm}$ compared to energetically predominant eigenmodes 68
3.11 Modal Assurance Criterion Matrix of the PGD modes and the eigenmodes for the beam solicited with load 1 - $f = 40\,\text{Hz}$ and $U_d^{\max} = 100\,\text{mm}$ 69
3.12 Evolution of the error with LATIN iteration using an adaptive PGD basis or a fixed basis comprising the first 100 eigenmodes for the beam solicited with load 1 - $f = 40\,\text{Hz}$ and $U_d^{\max} = 100\,\text{mm}$ 70
3.13 Six estimated temporal PGD modes for the beam solicited with load 1 - $f = 40\,\text{Hz}$ and $U_d^{\max} = 100\,\text{mm}$ 70
3.14 Power spectral densities (PSD) of the six estimated frequential PGD modes for the beam solicited with load 1 - $f = 40\,\text{Hz}$ and $U_d^{\max} = 100\,\text{mm}$ 71
3.15 Numerical effect of the artificial damping: comparison of the temporal, non-dampened (showing unwanted artefacts) and dampened frequency computations for the elastic initialisation at point P_I of the beam solicited with load 1 - mono-frequency Gaussian load with $f = 40\,\text{Hz}$ and $U_d^{\max} = 100\,\text{mm}$ 72
3.16 Evolution of the overlapping error ζ for dampened frequency computation with regard to the damping coefficient d for the beam solicited with load 1 - mono-frequency Gaussian load with $f = 40\,\text{Hz}$ and $U_d^{\max} = 100\,\text{mm}$ 73
3.17 Temporal load 2 - bi-frequency Gaussian case 73
3.18 Power Spectral Density of the nine estimated PGD modes for the beam solicited with load 2 - bi-frequency load with $f_a = 40\,\text{Hz}$, $f_b = 80\,\text{Hz}$ at $U_d^{\max} = 30\,\text{mm}$ . . 74
3.19 Temporal load 3 - a complex load 74
3.20 Temporal PGD modes for the beam solicited with load 3 - a complex load . . . 75
3.21 Evolution of the error with LATIN iteration using an adaptive PGD basis or a fixed basis comprising the first 100 eigenmodes for the beam solicited with load 3 - a complex load 75
3.22 Modal Assurance Criterion (MAC) matrix comparing the basis of PGD modes with classical LNMs for the beam solicited with load 3 - a complex load 76
3.23 Three-dimensional structure with boundary conditions 77

3.24 Three-dimensional complex load applied to the pipe's boundary conditions . . 78
3.25 Evolution of the error indicator and the number of PGD modes for the three-dimensional pipe structure solicited with a complex load 78
3.26 Evolution of the damage field for the pipe solicited with a complex loading . . . 79
3.27 Damage field in the three-dimensional pipe structure solicited with a complex load at time $t = 2$ s and damage evolution at the T-junction between the tube and the middle branch over time 79

4.1 Non-parametrised indexed loading scenarios 82
4.2 Standard and enhanced non-linear LATIN-PGD schemes 85
4.3 Computation (k) enhanced from a chosen parent-simulation 87
4.4 Reference problem 93
4.5 Maximum damage as a function of the loading parameters 94
4.6 Comparison of the number of total iterations required for the semi-enhanced and the standard methods 95
4.7 Parent-simulation and enhanced current computations sequence compared with parent-simulation and standard current sequences 96
4.8 Comparison of the standard method with the enhanced strategy. 97
4.9 Optimal path strategy illustration 98
4.10 Indexes and distances indicators values of PS computations for the optimal path strategy compared with those of a random path 99
4.11 Comparison of Cumulative distribution function of the PS width for the optimal path and a random path 99
4.12 Number of generated modes in the parametric space 101
4.13 Number of iterations in the parametric space 102
4.14 Speed-up as a function of the number of computations in the multi-query study 103

5.1 Normalised response surface of damage in the structure with the critical damage D_c plane 110
5.2 Approximation error for different values of coarse stopping criterion η_c^ℓ 112
5.3 Influence of the stopping criterion on the classification precision between computations leading to failure (red) and safe results (black). 112
5.4 Difference in the number of iterations for different values of stopping criterion η_c. 113
5.5 Difference in the number of modes for different values of stopping criterion η_c. 113
5.6 Demarcation of low and high fidelity computations 115
5.7 Flow chart of the dynamic update of the stopping criterion methodology 115
5.8 Comparison of the number of iterations for the standard method, the enhanced method and the enhanced multi-fidelity method 116
5.9 Classification and weight attributed to each point of the classification surface for the sampling procedure 117
5.10 Influence of the number of draws on the fragility curve 117

5.11 Selection of multiple PS using the Grassmann distance 122

A.1 Continuation based method 128
A.2 Comparison of Fourier and finite difference first order derivation 129

B.1 ROMlab contributors, reproduced from [Ruda, 2023] 132

C.1 Example of a fragility surface 137
C.2 Flow chart of the industrial damage assessment framework 137

Bibliography

Alameddin, S., Fau, A., Nackenhorst, U., Néron, D., & Ladevèze, P. (2020). Semi-incremental model order reduction approach for fatigue damage computations. In *Virtual Design and Validation, Lecture Notes in Applied and Computational Mechanics* (pp. 229–247). Springer. https://doi.org/10.1007/978-3-030-38156-1_12. (Cit. on p. 85)

Alameddin, S., Fau, A., Néron, D., Ladevèze, P., & Nackenhorst, U. (2019). Toward optimality of proper generalised decomposition bases. *Mathematical and Computational Applications*, *24*(1). https://doi.org/10.3390/mca24010030 (cit. on pp. 45, 85, 88, 120)

Allemang, R. J., & Brown, D. L. (1987). *Experimental modal analysis and dynamic component synthesis, volume iii: Modal parameter estimation*. USAF Report: AFWAL-TR-87-3069. (Cit. on p. 68).

AL-Shudeifat, M. A., & Butcher, E. A. (2010). Order reduction of forced nonlinear systems using updated LELSM modes with new Ritz vectors. *Nonlinear Dynamics*, *62*(4), 821–840. https://doi.org/10.1007/s11071-010-9765-8 (cit. on p. 37)

Amlani, F., & Bruno, O. P. (2016). An FC-based spectral solver for elastodynamic problems in general three-dimensional domains. *Journal of Computational Physics*, *307*, 333–354. https://doi.org/10.1016/j.jcp.2015.11.060 (cit. on pp. 121, 127)

Ammar, A., Mokdad, B., Chinesta, F., & Keunings, R. (2007). A new family of solvers for some classes of multidimensional partial differential equations encountered in kinetic theory modelling of complex fluids: Part II: Transient simulation using space-time separated representations. *Journal of Non-Newtonian Fluid Mechanics*, *144*(2), 98–121. https://doi.org/10.1016/j.jnnfm.2007.03.009 (cit. on p. 40)

Anders, M., & Hori, M. (1999). Stochastic finite element method for elasto-plastic body. *International Journal for Numerical Methods in Engineering*, *46*(11), 1897–1916. https://doi.org/10.1002/(SICI)1097-0207(19991220)46:11<1897::AID-NME758>3.0.CO;2-3 (cit. on pp. 6, 139)

Avitabile, P. (2003). Twenty Years of Structural Dynamic Modification – A Review. *Journal of Sound and Vibration*, 12 (cit. on p. 36).

Azinpour, E., Ferreira, J. P. S., Parente, M. P. L., & de Sa, J. C. (2018). A simple and unified implementation of phase field and gradient damage models. *Advanced Modeling and*

Simulation in Engineering Sciences, *5*(1), 15. https://doi.org/10.1186/s40323-018-0106-7 (cit. on p. 123)

Barbarulo, A., Ladevèze, P., Riou, H., & Kovalevsky, L. (2014). Proper Generalized Decomposition applied to linear acoustic: A new tool for broad band calculation. *Journal of Sound and Vibration*, *333*(11), 2422–2431. https://doi.org/10.1016/j.jsv.2014.01.014 (cit. on p. 52)

Bhattacharyya, M., Fau, A., Desmorat, R., Alameddin, S., Néron, D., Ladevèze, P., & Nackenhorst, U. (2019). A kinetic two-scale damage model for high-cycle fatigue simulation using multi-temporal latin framework. *European Journal of Mechanics / A Solids*, *77* (cit. on pp. 6, 24, 52, 140).

Bhattacharyya, M., Fau, A., Nackenhorst, U., Néron, D., & Ladevèze, P. (2018a). A model reduction technique in space and time for fatigue simulation. In *Multiscale modeling of heterogeneous structures* (pp. 183–203). Springer International Publishing. (Cit. on p. 32).

Bhattacharyya, M., Fau, A., Nackenhorst, U., Néron, D., & Ladevèze, P. (2018b). A latin-based model reduction approach for the simulation of cycling damage. *Computational Mechanics*, *62*(4), 725–743 (cit. on pp. 6, 31, 52, 140).

Bishop, R. (1955). The treatment of damping forces in vibration theory. *Journal of the Royal Aeronautical Society*, *59*(539), 738–742 (cit. on pp. 22, 56).

Boisse, P., Bussy, P., & Ladeveze, P. (1990). A new approach in non-linear mechanics: The large time increment method. *International Journal for Numerical Methods in Engineering*, *29*(3), 647–663. https://doi.org/10.1002/nme.1620290312 (cit. on p. 30)

Boucard, P. A., & Champaney, L. (2003). A suitable computational strategy for the parametric analysis of problems with multiple contact. *International Journal for Numerical Methods in Engineering*, *57*(9), 1259–1281. https://doi.org/10.1002/nme.724 (cit. on pp. 31, 45, 52)

Boucard, P. A., Ladevèze, P., Poss, M., & Rougée, P. (1997). A nonincremental approach for large displacement problems. *Computers & Structures*, *64*(1), 499–508. https://doi.org/10.1016/S0045-7949(96)00165-4 (cit. on p. 31)

Boucard, P. A., & Ladevèze, P. (1998). A multiple-solution method for non-linear structural mechanics In *NMCM'98 - 7th International Conference on Numerical Methods in Continuum Mechanics*. Stará Lesná, Slovakia. (Cit. on pp. 82, 84, 86).

Boucinha, L., Ammar, A., Gravouil, A., & Nouy, A. (2014). Ideal minimal residual-based proper generalized decomposition for non-symmetric multi-field models – Application to transient elastodynamics in space-time domain. *Computer Methods in Applied Mechanics and Engineering*, *273*, 56–76. https://doi.org/10.1016/j.cma.2014.01.019 (cit. on pp. 6, 40, 139)

Boucinha, L., Gravouil, A., & Ammar, A. (2013). Space–time proper generalized decompositions for the resolution of transient elastodynamic models. *Computer Methods in Applied Mechanics and Engineering*, *255*, 67–88. https://doi.org/10.1016/j.cma.2012.11.003 (cit. on pp. 21, 40)

Bruno, O. P., Elling, T., & Sen, A. (2015). A Fourier Continuation Method for the Solution of Elliptic Eigenvalue Problems in General Domains. *Mathematical Problems in Engineering*, *2015*, e184786. https://doi.org/10.1155/2015/184786 (cit. on pp. 121, 127)

Cameron, T. M., & Griffin, J. H. (1989). An Alternating Frequency/Time Domain Method for Calculating the Steady-State Response of Nonlinear Dynamic Systems. *Journal of Applied Mechanics*, *56*(1), 149–154. https://doi.org/10.1115/1.3176036 (cit. on p. 52)

Cardoso, R. A., Néron, D., Pommier, S., & Araújo, J. A. (2018). An enrichment-based approach for the simulation of fretting problems. *Computational Mechanics*, *62*(6), 1529–1542. https://doi.org/10.1007/s00466-018-1577-6 (cit. on p. 121)

Carslaw, H. S. (1925). A historical note on Gibbs' phenomenon in Fourier's series and integrals. *Bulletin of the American Mathematical Society*, *31*(8), 420–424. https://doi.org/10.1090/S0002-9904-1925-04081-1 (cit. on p. 22)

Cauchy, A. (1827). De la pression ou tension dans un corps solide. *Ex. de Math*, *2* (cit. on p. 16).

Champaney, L., Cognard, J. Y., Dureisseix, D., & Ladevèze, P. (1997). Large scale applications on parallel computers of a mixed domain decomposition method. *Computational Mechanics*, *19*(4), 253–263. https://doi.org/10.1007/s004660050174 (cit. on p. 30)

Chartier, P., & Philippe, B. (1993). A parallel shooting technique for solving dissipative ODE's. *Computing*, *51*(3-4), 209–236. https://doi.org/10.1007/BF02238534 (cit. on p. 56)

Chatterjee, A. (2000). An introduction to the proper orthogonal decomposition. *Current Science*, *78*(7), 808–817 (cit. on pp. 5, 139).

Chen, D., Rojas, M., Samset, B., Cobb, K., Diongue Niang, A., Edwards, P., Emori, S., Faria, S., Hawkins, E., Hope, P., Huybrechts, P., Meinshausen, M., Mustafa, S., Plattner, G.-K., & Tréguier, A.-M. (2021). Framing, context, and methods. In V. Masson-Delmotte, P. Zhai, A. Pirani, S. Connors, C. Péan, S. Berger, N. Caud, Y. Chen, L. Goldfarb, M. Gomis, M. Huang, K. Leitzell, E. Lonnoy, J. Matthews, T. Maycock, T. Waterfield, O. Yelekçi, R. Yu, & B. Zhou (Eds.), *Climate change 2021: The physical science basis. contribution of working group* I *to the sixth assessment report of the intergovernmental panel on climate change* (pp. 147–286). Cambridge University Press. https://doi.org/10.1017/9781009157896.003. (Cit. on pp. 1, 2)

Chevreuil, M., Ladevèze, P., & Rouch, P. (2007). Transient analysis including the low- and the medium-frequency ranges of engineering structures. *Computers & Structures*, *85*(17), 1431–1444. https://doi.org/10.1016/j.compstruc.2006.08.091 (cit. on p. 18)

Chevreuil, M., & Nouy, A. (2012). Model order reduction based on proper generalized decomposition for the propagation of uncertainties in structural dynamics. *International Journal for Numerical Methods in Engineering*, *89*(2), 241–268. https://doi.org/10.1002/nme.3249 (cit. on p. 52)

Chinesta, F., Ladevèze, P., & Cueto, E. (2011). A short review on model order reduction based on proper generalized decomposition. *Archives of Computational Methods in Engineering*, *18*(4), 395–404 (cit. on pp. 5, 6, 40, 139).

Chouaki, A. T., Ladevèze, P., & Proslier, L. (1998). Updating structural dynamic models with emphasis on the damping properties. *AIAA journal*, *36*(1) (cit. on p. 18).

Clarke, L., Wei, Y.-M., Navarro, A. D. L. V., Garg, A., Hahmann, A., Khennas, S., Azevedo, I., Löschel, A., Singh, A., Steg, L., Strbac, G., & Wada, K. (2022). Energy systems. In P. Shukla, J. Skea, R. Slade, A. A. Khourdajie, R. van Diemen, D. McCollum, M. Pathak, S. Some, P. Vyas, R. Fradera, M. Belkacemi, A. Hasija, G. Lisboa, S. Luz, & J. Malley (Eds.), *Climate change 2022: Mitigation of climate change. contribution of working group* III *to the sixth assessment report of the intergovernmental panel on climate change* (pp. 147–286). Cambridge University Press. https://doi.org/10.1017/9781009157926.008. (Cit. on pp. 1, 3)

Cooley, J. W., & Tukey, J. W. (1965). An Algorithm for the Machine Calculation of Complex Fourier Series (cit. on p. 22).

Courard, A. (2016). *PGD-Abaques virtuels pour l'optimisation géométrique des structures* (Doctoral dissertation). Université Paris Saclay (COmUE). (Cit. on p. 6).

Craig, R. R., & Bampton, M. C. C. (1968). Coupling of substructures for dynamic analyses. *AIAA Journal*, *6*(7), 1313–1319. https://doi.org/10.2514/3.4741 (cit. on p. 36)

Crisfield, M. A. (1981). A FAST INCREMENTAL/ITERATIVE SOLUTION PROCEDURE THAT HANDLES "SNAP-THROUGH". In A. K. Noor & H. G. McCOMB (Eds.), *Computational Methods in Nonlinear Structural and Solid Mechanics* (pp. 55–62). Pergamon. https://doi.org/10.1016/B978-0-08-027299-3.50009-1. (Cit. on p. 28)

Crisfield, M. A. (1983). An arc-length method including line searches and accelerations. *International Journal for Numerical Methods in Engineering*, *19*(9), 1269–1289. https://doi.org/10.1002/nme.1620190902 (cit. on pp. 28, 29)

Daby-Seesaram, A., Fau, A., Charbonnel, P.-É., & Néron, D. (2023). A hybrid frequency-temporal reduced-order method for nonlinear dynamics. *Nonlinear Dynamics*, *111*(15), 13669–13689. https://doi.org/10.1007/s11071-023-08513-8 (cit. on pp. 6, 8, 84, 140)

de Brabander, P. (2021). *Sur la TVRC en dynamique transitoire: Approche large bande de fréquence et réduction de modèle* (Doctoral dissertation). Université Paris-Saclay. (Cit. on p. 52).

Deringer, V. L., Bartók, A. P., Bernstein, N., Wilkins, D. M., Ceriotti, M., & Csányi, G. (2021). Gaussian Process Regression for Materials and Molecules. *Chemical Reviews*, *121*(16), 10073–10141. https://doi.org/10.1021/acs.chemrev.1c00022 (cit. on p. 44)

Deutsch, F. (1995). The Angle Between Subspaces of a Hilbert Space. In S. P. Singh (Ed.), *Approximation Theory, Wavelets and Applications* (pp. 107–130). Springer Netherlands. https://doi.org/10.1007/978-94-015-8577-4_7. (Cit. on p. 89)

Eftekhar Azam, S., & Mariani, S. (2013). Investigation of computational and accuracy issues in POD-based reduced order modeling of dynamic structural systems. *Engineering Structures*, *54*, 150–167. https://doi.org/10.1016/j.engstruct.2013.04.004 (cit. on p. 37)

Eugeni, M., Saltari, F., & Mastroddi, F. (2021). Structural damping models for passive aeroelastic control. *Aerospace Science and Technology*, *118*, 107011. https://doi.org/https://doi.org/10.1016/j.ast.2021.107011 (cit. on p. 18)

Falini, A. (2022). A review on the selection criteria for the truncated SVD in Data Science applications. *Journal of Computational Mathematics and Data Science*, *5*, 100064. https://doi.org/10.1016/j.jcmds.2022.100064 (cit. on p. 88)

Farhat, C., & Li, J. (2005). An iterative domain decomposition method for the solution of a class of indefinite problems in computational structural dynamics. *Applied Numerical Mathematics*, *54*(2), 150–166. https://doi.org/10.1016/j.apnum.2004.09.021 (cit. on p. 5)

Friderikos, O., Baranger, E., Olive, M., & Neron, D. (2022). On the stability of POD basis interpolation on Grassmann manifolds for parametric model order reduction. *Computational Mechanics*, *70*(1), 181–204. https://doi.org/10.1007/s00466-022-02163-0 (cit. on p. 122)

Fuhg, J. N., & Fau, A. (2022). A classification-pursuing adaptive approach for Gaussian process regression on unlabeled data. *Mechanical Systems and Signal Processing*, *162*, 107976. https://doi.org/10.1016/j.ymssp.2021.107976 (cit. on pp. 44, 84)

Fuhg, J. N., Fau, A., & Nackenhorst, U. (2020). State-of-the-art and Comparative Review of Adaptive Sampling Methods for Kriging. *Archives of Computational Methods in Engineering*. https://doi.org/10.1007/s11831-020-09474-6 (cit. on p. 84)

Géradin, M., & Rixen, D. J. (2015). *Mechanical vibrations : Theory and application to structural dynamics* (Third). John Wiley. (Cit. on p. 63).

Gerbaud, P.-W., Néron, D., & Ladevèze, P. (2022). Data-driven elasto-(visco)-plasticity involving hidden state variables. *Computer Methods in Applied Mechanics and Engineering, 402*, 115394. https://doi.org/10.1016/j.cma.2022.115394 (cit. on p. 121)

Germoso, C., Aguado, J. V., Fraile, A., Alarcon, E., & Chinesta, F. (2016). Efficient PGD-based dynamic calculation of non-linear soil behavior. *Comptes Rendus Mécanique, 344*(1), 24–41. https://doi.org/10.1016/j.crme.2015.09.002 (cit. on pp. 6, 40, 139)

Giacoma, A., Dureisseix, D., Gravouil, A., & Rochette, M. (2015). Toward an optimal a priori reduced basis strategy for frictional contact problems with LATIN solver. *Computer Methods in Applied Mechanics and Engineering, 283*, 1357–1381. https://doi.org/10.1016/j.cma.2014.09.005 (cit. on pp. 45, 60, 120)

Gidaris, I., Taflanidis, A. A., & Mavroeidis, G. P. (2015). Kriging metamodeling in seismic risk assessment based on stochastic ground motion models. *Earthquake Engineering & Structural Dynamics, 44*(14), 2377–2399. https://doi.org/10.1002/eqe.2586 (cit. on p. 84)

Gravouil, A., & Combescure, A. (2003). Multi-time-step and two-scale domain decomposition method for non-linear structural dynamics. *International Journal for Numerical Methods in Engineering, 58*(10), 1545–1569. https://doi.org/10.1002/nme.826 (cit. on p. 5)

Guidault, P. A., Allix, O., Champaney, L., & Navarro, J. P. (2007). A two-scale approach with homogenization for the computation of cracked structures. *Computers & Structures, 85*(17), 1360–1371. https://doi.org/10.1016/j.compstruc.2006.08.085 (cit. on p. 30)

Gutiérrez, M. A. (2004). Energy release control for numerical simulations of failure in quasi-brittle solids. *Communications in Numerical Methods in Engineering, 20*(1), 19–29 (cit. on p. 28).

Halko, N., Martinsson, P. G., & Tropp, J. A. (2011). Finding Structure with Randomness: Probabilistic Algorithms for Constructing Approximate Matrix Decompositions. *SIAM Review, 53*(2), 217–288. https://doi.org/10.1137/090771806 (cit. on p. 88)

Hall, J. F. (1982). An FFT algorithm for structural dynamics. *Earthquake Engineering & Structural Dynamics, 10*(6), 797–811. https://doi.org/10.1002/eqe.4290100605 (cit. on pp. 22, 56)

Hansteen, O. E., & Bell, K. (1979). On the accuracy of mode superposition analysis in structural dynamics. *Earthquake Engineering & Structural Dynamics, 7*(5), 405–411. https://doi.org/10.1002/eqe.4290070502 (cit. on p. 36)

Hashin, Z., & Rotem, A. (1978). A cumulative damage theory of fatigue failure. *Materials Science and Engineering, 34*(2), 147–160. https://doi.org/10.1016/0025-5416(78)90045-9 (cit. on p. 23)

Hensman, J., Mills, R., Pierce, S. G., Worden, K., & Eaton, M. (2010). Locating acoustic emission sources in complex structures using Gaussian processes. *Mechanical Systems and Signal Processing, 24*(1), 211–223. https://doi.org/10.1016/j.ymssp.2009.05.018 (cit. on p. 44)

Hernandez, Q., Badias, A., Chinesta, F., & Cueto, E. (2022). Thermodynamics-informed Graph Neural Networks. *IEEE Transactions on Artificial Intelligence*, 1–1. https://doi.org/10.1109/TAI.2022.3179681 (cit. on p. 122)

Heyberger, C., Boucard, P.-A., & Néron, D. (2012). Multiparametric analysis within the proper generalized decomposition framework. *Computational Mechanics, 49*(3), 277–289 (cit. on pp. 6, 45, 65, 84, 85, 140).

Hulbert, G. M. (1992). Time finite element methods for structural dynamics. *International Journal for Numerical Methods in Engineering, 33*(2), 307–331. https://doi.org/10.1002/nme.1620330206 (cit. on p. 21)

Humar, J. L. (1990). *Dynamics of structures*. Prentice-Hall, Englewood Cliffs. (Cit. on p. 61).

Humar, J. L., & Xia, H. (1993). Dynamic response analysis in the frequency domain. *Earthquake engineering & structural dynamics, 22*(1), 1–12 (cit. on pp. 22, 52, 62).

Hussain, A., Muhammad, Y. S., Nauman Sajid, M., Hussain, I., Mohamd Shoukry, A., & Gani, S. (2017). Genetic Algorithm for Traveling Salesman Problem with Modified Cycle Crossover Operator. *Computational Intelligence and Neuroscience, 2017*, e7430125. https://doi.org/10.1155/2017/7430125 (cit. on p. 91)

Idelsohn, S. R., & Cardona, A. (1985). A reduction method for nonlinear structural dynamic analysis. *Computer Methods in Applied Mechanics and Engineering, 49*(3), 253–279. https://doi.org/10.1016/0045-7825(85)90125-2 (cit. on p. 37)

IPCC. (2021). Summary for policymakers. In V. Masson-Delmotte, P. Zhai, A. Pirani, S. Connors, C. Péan, S. Berger, N. Caud, Y. Chen, L. Goldfarb, M. Gomis, M. Huang, K. Leitzell, E. Lonnoy, J. Matthews, T. Maycock, T. Waterfield, O. Yelekçi, R. Yu, & B. Zhou (Eds.), *Climate change 2021: The physical science basis. contribution of working group* I *to the sixth assessment report of the intergovernmental panel on climate change* (pp. 3–32). Cambridge University Press. https://doi.org/10.1017/9781009157896.001. (Cit. on pp. 1, 2)

IPCC. (2022). Summary for policymakers. In H. O. Pörtner, D. C. Roberts, M. Tignor, E. S. Poloczanska, K. Mintenbeck, A. Alegrìa, M. Craig, S. Langsdorf, S. Löschke, V. Möller, A. Okem, & B. Rama (Eds.), *Climate change 2022: Impacts, adaptation, and vulnerability. contribution of working group* II *to the sixth assessment report of the intergovernmental panel on climate change* (In Press). Cambridge University Press. (Cit. on p. 1).

Iturra, S. R. (2021). *Abaques virtuelle pour le génie parasismique incluant des parametres associes au chargement* (Doctoral dissertation). Université Paris-Saclay. (Cit. on pp. 6, 52, 140).

Jakobsson, H., Bengzon, F., & Larson, M. G. (2011). Adaptive component mode synthesis in linear elasticity. *International Journal for Numerical Methods in Engineering*, *86*(7), 829–844. https://doi.org/10.1002/nme.3078 (cit. on p. 36)

Kappauf, J., Bäuerle, S., & Hetzler, H. (2022). A combined FD-HB approximation method for steady-state vibrations in large dynamical systems with localised nonlinearities. *Computational Mechanics*, *70*(6), 1241–1256. https://doi.org/10.1007/s00466-022-02225-3 (cit. on p. 52)

Ladevèze, P. (1985). Sur une famille d'algorithmes en mécanique des structures. *Comptes-rendus des séances de l'Académie des sciences. Série 2, Mécanique, physique, chimie, sciences de l'univers, sciences de la terre*, *300*(2) (cit. on p. 40).

Ladevèze, P. (1999). *Nonlinear computational structural mechanics: New approaches and non-incremental methods of calculation.* Springer. (Cit. on pp. 6, 30, 32, 52–54, 140).

Ladevèze, P., & Dureisseix, D. (1999). Une nouvelle stratégie de calcul micro/macro en mécanique des structures. *Comptes Rendus de l'Académie des Sciences - Series IIB - Mechanics-Physics-Astronomy*, *327*(12), 1237–1244. https://doi.org/10.1016/S1287-4620(00)88647-0 (cit. on p. 30)

Ladevèze, P., Néron, D., & Gerbaud, P.-W. (2019). Data-driven computation for history-dependent materials. *Comptes Rendus Mécanique*, *347*(11), 831–844. https://doi.org/10.1016/j.crme.2019.11.008 (cit. on p. 121)

Lee, J., & Fenves, G. L. (2001). A return-mapping algorithm for plastic-damage models: 3-D and plane stress formulation. *International Journal for Numerical Methods in Engineering*, *50*(2), 487–506. https://doi.org/10.1002/1097-0207(20010120)50:2<487::AID-NME44>3.0.CO;2-N (cit. on p. 54)

Leine, R. I., & Schreyer, F. (2016). A mixed shooting – harmonic balance method for unilaterally constrained mechanical systems. *Archive of Mechanical Engineering; 2016; vol. 63; No 2; 297-314* (cit. on p. 52).

Lemaitre, J., & Chaboche, J.-L. (1994). Mechanics of solid materials. *Cambridge university press* (cit. on pp. 23, 24).

Lemaitre, J., & Desmorat, R. (2005). *Engineering damage mechanics: Ductile, creep, fatigue and brittle failures.* Springer Berlin / Heidelberg. (Cit. on pp. 23, 25, 52).

Lemaitre, J. (1996). *A Course on Damage Mechanics.* Springer Berlin Heidelberg. https://doi.org/10.1007/978-3-642-18255-6. (Cit. on p. 23)

Lions, J.-L., Maday, Y., & Turinici, G. (2001). Résolution d'EDP par un schéma en temps "pararéel". *Comptes Rendus de l'Académie des Sciences - Series I - Mathematics*, *332*(7), 661–668. https://doi.org/10.1016/S0764-4442(00)01793-6 (cit. on p. 56)

Lu, Y., Blal, N., & Gravouil, A. (2018). Multi-parametric space-time computational vademecum for parametric studies: Application to real time welding simulations. *Finite Elements in Analysis and Design*, *139*, 62–72. https://doi.org/10.1016/j.finel.2017.10.008 (cit. on pp. 6, 139)

Lyon, M. (2011). A Fast Algorithm for Fourier Continuation. *SIAM Journal on Scientific Computing*, *33*(6), 3241–3260. https://doi.org/10.1137/11082436X (cit. on pp. 121, 127)

Maday, Y., Patera, A. T., & Turinici, G. (2002). A Priori Convergence Theory for Reduced-Basis Approximations of Single-Parameter Elliptic Partial Differential Equations. *Journal of Scientific Computing*, *17*(1), 437–446. https://doi.org/10.1023/A:1015145924517 (cit. on pp. 5, 139)

Maday, Y., & Rønquist, E. M. (2002). A Reduced-Basis Element Method. *Journal of Scientific Computing*, *17*(1), 447–459. https://doi.org/10.1023/A:1015197908587 (cit. on p. 39)

Malik, M. H., Borzacchiello, D., Aguado, J. V., & Chinesta, F. (2018). Advanced parametric space-frequency separated representations in structural dynamics: A harmonic–modal hybrid approach. *Comptes Rendus Mécanique*, *346*(7), 590–602. https://doi.org/10.1016/j.crme.2018.04.005 (cit. on p. 52)

Marconi, F. (2022). *Transition endommagement-fissuration par une formulation eikonale pour les modèles d'endommagement avec et sans plasticité* (Doctoral dissertation). Université Paris-Saclay. (Cit. on p. 123).

Marsh, G., Wignall, C., Thies, P. R., Barltrop, N., Incecik, A., Venugopal, V., & Johanning, L. (2016). Review and application of Rainflow residue processing techniques for accurate fatigue damage estimation. *International Journal of Fatigue*, *82*, 757–765. https://doi.org/10.1016/j.ijfatigue.2015.10.007 (cit. on pp. 5, 23)

Miao, J., & Ben-Israel, A. (1992). On principal angles between subspaces in Rn. *Linear Algebra and its Applications*, *171*, 81–98. https://doi.org/10.1016/0024-3795(92)90251-5 (cit. on p. 89)

Miner, M. A. (1945). Cumulative damage in fatigue. *Journal of Applied Mechanics*, *2*, 159–164. https://doi.org/10.1115/1.4009458 (cit. on p. 23)

Mohammadi, B. (2014). Principal angles between subspaces and reduced order modelling accuracy in optimization. *Structural and Multidisciplinary Optimization*, *50*(2), 237–252. https://doi.org/10.1007/s00158-013-1043-1 (cit. on p. 89)

Morin, B., Legay, A., & Deü, J.-F. (2018). Reduced order models for dynamic behavior of elastomer damping devices. *Finite Elements in Analysis and Design*, *143*, 66–75. https://doi.org/10.1016/j.finel.2018.02.001 (cit. on p. 5)

Mosquera, R., Hamdouni, A., El Hamidi, A., Allery, C., & ,Laboratoire LaSIE, Université de La Rochelle, Avenue M. Crépeau, 17042 La Rochelle, France. (2019). POD basis interpolation via Inverse Distance Weighting on Grassmann manifolds. *Discrete & Continuous Dynamical Systems - S*, *12*(6), 1743–1759. https://doi.org/10.3934/dcdss.2019115 (cit. on p. 122)

Nachar, S., Boucard, P.-A., Néron, D., & Rey, C. (2020). Multi-fidelity bayesian optimization using model-order reduction for viscoplastic structures. *Finite Elements in Analysis and Design*, *176*, 103400. https://doi.org/10.1016/j.finel.2020.103400 (cit. on pp. 6, 7, 31, 44, 122, 139, 140)

Nacivet, S., Pierre, C., Thouverez, F., & Jezequel, L. (2003). A dynamic Lagrangian frequency–time method for the vibration of dry-friction-damped systems. *Journal of Sound and Vibration*, *265*(1), 201–219. https://doi.org/10.1016/S0022-460X(02)01447-5 (cit. on p. 52)

Nagaraj, M. H., Petrolo, M., & Carrera, E. (2021). A global–local approach for progressive damage analysis of fiber-reinforced composite laminates. *Thin-Walled Structures*, *169*, 108343. https://doi.org/10.1016/j.tws.2021.108343 (cit. on p. 122)

Néron, D., Boucard, P.-A., & Relun, N. (2015). Time-space PGD for the rapid solution of 3D nonlinear parametrized problems in the many-query context. *International Journal for Numerical Methods in Engineering*, *103*(4), 275–292 (cit. on pp. 6, 31, 45, 139).

Néron, D., & Dureisseix, D. (2008). A computational strategy for poroelastic problems with a time interface between coupled physics. *International Journal for Numerical Methods in Engineering*, *73*(6), 783–804. https://doi.org/10.1002/nme.2091 (cit. on p. 31)

Néron, D., Dhia, H. B., & Cottereau, R. (2016). A decoupled strategy to solve reduced-order multimodel problems in the PGD and Arlequin frameworks. *Computational Mechanics*, *57*(4), 509–521. https://doi.org/10.1007/s00466-015-1236-0 (cit. on p. 121)

Néron, D., & Ladevèze, P. (2010a). Proper generalized decomposition for multiscale and multiphysics problems. *Archives of Computational Methods in Engineering*, *17*(4), 351–372 (cit. on pp. 5, 32, 40, 139).

Néron, D., & Ladevèze, P. (2010b). Proper Generalized Decomposition for Multiscale and Multiphysics Problems. *Archives of Computational Methods in Engineering*, *17*(4), 351–372. https://doi.org/10.1007/s11831-010-9053-2 (cit. on p. 123)

Newmark, N. M. (1959). A Method of Computation for Structural Dynamics. *Journal of the Engineering Mechanics Division*, *85*(3), 67–94. https://doi.org/10.1061/JMCEA3.0000098 (cit. on p. 20)

Newton, I. (1736). *The method of fluxions and infinite series.* (Cit. on p. 26).

Nouy, A. (2010). A priori model reduction through proper generalized decomposition for solving time-dependent partial differential equations. *Computer Methods in Applied Mechanics and Engineering, 199*(23-24), 1603–1626 (cit. on pp. 56, 67).

Oumaziz, P., Gosselet, P., Boucard, P.-A., & Guinard, S. (2017). A non-invasive implementation of a mixed domain decomposition method for frictional contact problems. *Computational Mechanics, 60*, 797–812 (cit. on p. 30).

Paillet, C., Néron, D., & Ladevèze, P. (2018). A door to model reduction in high-dimensional parameter space. *Comptes Rendus Mécanique, 346*(7), 524–531. https://doi.org/10.1016/j.crme.2018.04.009 (cit. on pp. 6, 139)

Proso, U., Slavič, J., & Boltežar, M. (2016). Vibration-fatigue damage accumulation for structural dynamics with non-linearities. *International Journal of Mechanical Sciences, 106*, 72–77. https://doi.org/10.1016/j.ijmecsci.2015.12.005 (cit. on pp. 5, 23)

Prud'homme, C., Rovas, D. V., Veroy, K., Machiels, L., Maday, Y., Patera, A. T., & Turinici, G. (2001). Reliable Real-Time Solution of Parametrized Partial Differential Equations: Reduced-Basis Output Bound Methods. *Journal of Fluids Engineering, 124*(1), 70–80. https://doi.org/10.1115/1.1448332 (cit. on p. 39)

Quaranta, G., Argerich Martin, C., Ibañez, R., Duval, J. L., Cueto, E., & Chinesta, F. (2019). From linear to nonlinear PGD-based parametric structural dynamics. *Comptes Rendus Mécanique, 347*(5), 445–454. https://doi.org/10.1016/j.crme.2019.01.005 (cit. on pp. 6, 40, 139)

Radermacher, A., & Reese, S. (2013). A comparison of projection-based model reduction concepts in the context of nonlinear biomechanics. *Archive of Applied Mechanics, 83*(8), 1193–1213. https://doi.org/10.1007/s00419-013-0742-9 (cit. on p. 37)

Ramm, E. (1981). Strategies for Tracing the Nonlinear Response Near Limit Points In *Nonlinear Finite Element Analysis in Structural Mechanics* (W. Wunderlich, E. Stein, & K.-J. Bathe, Eds.). Berlin, Heidelberg, Springer. 63–89. https://doi.org/10.1007/978-3-642-81589-8_5. (Cit. on p. 28)

Relun, N., Néron, D., & Boucard, P.-A. (2015). Multiscale elastic-viscoplastic computational analysis. *European Journal of Computational Mechanics, 20*(7-8), 379–409. https://doi.org/10.3166/ejcm.20.379-409 (cit. on p. 31)

Riks, E. (1979). An incremental approach to the solution of snapping and buckling problems. *International Journal of Solids and Structures, 15*(7), 529–551. https://doi.org/10.1016/0020-7683(79)90081-7 (cit. on p. 28)

Rixen, D. J. (2004). A dual Craig–Bampton method for dynamic substructuring. *Journal of Computational and Applied Mathematics*, *168*(1), 383–391. https://doi.org/10.1016/j.cam.2003.12.014 (cit. on p. 36)

Rodriguez, S., Néron, D., Charbonnel, P.-E., Ladevèze, P., & Nahas, G. (2019). Non incremental LATIN-PGD solver for nonlinear vibratoric dynamics problems In *14ème Colloque National en Calcul des Structures, CSMA 2019*. Presqu'Île de Giens, France. (Cit. on p. 52).

Rohmer, J., Gehl, P., Marcilhac-Fradin, M., Guigueno, Y., Rahni, N., & Clément, J. (2020). Non-stationary extreme value analysis applied to seismic fragility assessment for nuclear safety analysis. *Natural Hazards and Earth System Sciences*, *20*(5), 1267–1285. https://doi.org/10.5194/nhess-20-1267-2020 (cit. on p. 4)

Rozza, G., Huynh, D. B. P., & Patera, A. T. (2008). Reduced Basis Approximation and a Posteriori Error Estimation for Affinely Parametrized Elliptic Coercive Partial Differential Equations. *Archives of Computational Methods in Engineering*, *15*(3), 229–275. https://doi.org/10.1007/s11831-008-9019-9 (cit. on p. 39)

Rozza, G. (2014). Fundamentals of reduced basis method for problems governed by parametrized PDEs and applications. In F. Chinesta & P. Ladevèze (Eds.), *Separated Representations and PGD-Based Model Reduction* (pp. 153–227). Springer Vienna. https://doi.org/10.1007/978-3-7091-1794-1_4. (Cit. on p. 39)

RTE. (2021). Executive summary. In *Energy pathways to 2050 - key results*. (Cit. on pp. 1, 3).

Ruda, A., Louf, F., Boucard, P.-A., & Mininger, X. (2022). First Approach on a Mixed Domain Decomposition Method for 2-D Magnetostatic Simulation of Electrical Machines. *IEEE Transactions on Magnetics*, *58*(12), 1–8. https://doi.org/10.1109/TMAG.2022.3213190 (cit. on pp. 30, 131)

Ruda, A. (2023). *Méthode de decomposition de domaine mixte pour la simulation magnetostatique de machines tournantes* (Doctoral dissertation). Université Paris-Saclay. (Cit. on p. 132).

Ryckelynck, D., Missoum Benziane, D., Cartel, S., & Besson, J. (2011). A robust adaptive model reduction method for damage simulations. *Computational Materials Science*, *50*(5), 1597–1605. https://doi.org/10.1016/j.commatsci.2010.11.034 (cit. on p. 83)

Sainct, R., Feau, C., Martinez, J.-M., & Garnier, J. (2020). Efficient methodology for seismic fragility curves estimation by active learning on Support Vector Machines. *Structural Safety*, *86*, 101972. https://doi.org/10.1016/j.strusafe.2020.101972 (cit. on p. 4)

Scanff, R., Nachar, S., Boucard, P.-A., & Néron, D. (2020). A study on the latin-pgd method: Analysis of some variants in the light of the latest developments. *Archives of computational methods in engineering* (cit. on p. 63).

Scanff, R., Néron, D., Ladevèze, P., Barabinot, P., Cugnon, F., & Delsemme, J.-P. (2022). Weakly-invasive LATIN-PGD for solving time-dependent non-linear parametrized problems in solid mechanics. *Computer Methods in Applied Mechanics and Engineering, 396*, 114999. https://doi.org/10.1016/j.cma.2022.114999 (cit. on pp. 6, 139)

Shigenaka, R., Raytchev, B., Tamaki, T., & Kaneda, K. (2012). Face sequence recognition using grassmann distances and grassmann kernels In *The 2012 international joint conference on neural networks (ijcnn)*. 1–7. https://doi.org/10.1109/IJCNN.2012.6252731. (Cit. on p. 83)

Socie, D. (1992). Rainflow Cycle Counting : A Historical Perspective. In Y. Murakami (Ed.), *The Rainflow Method in Fatigue* (pp. 3–10). Butterworth-Heinemann. https://doi.org/10.1016/B978-0-7506-0504-5.50009-6. (Cit. on p. 23)

Tegtmeyer, S., Fau, A., Bénet, P., & Nackenhorst, U. (2017). On the selection of snapshot computation for proper orthogonal decomposition in structural dynamics In *Proceeding of the conference apm*. (Cit. on pp. 6, 139).

Van Blaricum, M., & Mittra, R. (1978). Problems and Solutions Associated with Prony's Method for Processing Transient Data. *IEEE Transactions on Electromagnetic Compatibility, EMC-20*(1), 174–182. https://doi.org/10.1109/TEMC.1978.303708 (cit. on p. 61)

Vandoren, B., De Proft, K., Simone, A., & Sluys, L. (2013a). A novel constrained LArge Time INcrement method for modelling quasi-brittle failure. *Computer Methods in Applied Mechanics and Engineering, 265*, 148–162. https://doi.org/10.1016/j.cma.2013.06.005 (cit. on pp. 30, 31)

Vandoren, B., De Proft, K., Simone, A., & Sluys, L. (2013b). A novel constrained LArge Time INcrement method for modelling quasi-brittle failure. *Computer Methods in Applied Mechanics and Engineering, 265*, 148–162. https://doi.org/10.1016/j.cma.2013.06.005 (cit. on p. 52)

Vitse, M., Néron, D., & Boucard, P.-A. (2019). Dealing with a nonlinear material behavior and its variability through PGD models: Application to reinforced concrete structures. *Finite Elements in Analysis and Design, 153*, 22–37. https://doi.org/10.1016/j.finel.2018.05.006 (cit. on p. 52)

Von Groll, G., & Ewins, D. (2001). The harmonic balance method with arc-length continuation in rotor/stator contact problems. *Journal of Sound and Vibration, 241*(2), 223–233. https://doi.org/10.1006/jsvi.2000.3298 (cit. on p. 52)

Wang, L., & Zhong, H. (2017). A time finite element method for structural dynamics. *Applied Mathematical Modelling, 41*, 445–461. https://doi.org/10.1016/j.apm.2016.09.017 (cit. on p. 21)

Wu, C., Liang, Y., Lin, W., Lee, H., & Lim, S. (2003). A note on equivalence of proper orthogonal decomposition methods. *Journal of Sound and Vibration*, *265*(5), 1103–1110 (cit. on p. 38).

Wu, H., Wu, P., Li, F., Shi, H., & Xu, K. (2019). Fatigue analysis of the gearbox housing in high-speed trains under wheel polygonization using a multibody dynamics algorithm. *Engineering Failure Analysis*, *100*, 351–364. https://doi.org/10.1016/j.engfailanal.2019.02.058 (cit. on pp. 5, 23)

Wurtzer, F., Boucard, P.-A., Ladevèze, P., & Néron, D. (2023). A first illustration of a multimodel strategy for coupled multiphysics problems In *VII ECCOMAS Young Investigators Conference*. Porto, Portugal. (Cit. on p. 131).

Yang, C., Liang, K., Rong, Y., & Sun, Q. (2019). A hybrid reduced-order modeling technique for nonlinear structural dynamic simulation. *Aerospace Science and Technology*, *84*, 724–733. https://doi.org/10.1016/j.ast.2018.11.008 (cit. on p. 40)

Zentner, I., Gündel, M., & Bonfils, N. (2017). Fragility analysis methods: Review of existing approaches and application. *Nuclear Engineering and Design*, *323*, 245–258. https://doi.org/10.1016/j.nucengdes.2016.12.021 (cit. on p. 4)

Zeoli, S., Balarac, G., Bénard, P., Georis, G., Houtin-Mongrolle, F., & Bricteux, L. (2020). Large eddy simulation of wind turbine wakes using adaptative mesh refinement. *Journal of Physics: Conference Series*, *1618*(6), 062056. https://doi.org/10.1088/1742-6596/1618/6/062056 (cit. on p. 5)

Zhang, P., Wang, J., Tian, Z., Sun, S., Li, J., & Yang, J. (2022). A genetic algorithm with jumping gene and heuristic operators for traveling salesman problem. *Applied Soft Computing*, *127*, 109339. https://doi.org/10.1016/j.asoc.2022.109339 (cit. on p. 91)

Zhu, T., Zhang, G., & Zang, C. (2022). Frequency-domain nonlinear model updating based on analytical sensitivity and the Multi-Harmonic balance method. *Mechanical Systems and Signal Processing*, *163*, 108169. https://doi.org/10.1016/j.ymssp.2021.108169 (cit. on p. 52)